

# **PHYSICAL AND MECHANICAL METALLURGY OF ZIRCONIUM ALLOYS FOR NUCLEAR APPLICATIONS: A MULTI-SCALE COMPUTATIONAL STUDY**

Michael Vasily Glazoff

October 2014

The INL is a U.S. Department of Energy National Laboratory  
operated by Battelle Energy Alliance



**PHYSICAL AND MECHANICAL METALLURGY OF  
ZIRCONIUM ALLOYS FOR NUCLEAR APPLICATIONS:  
A MULTI-SCALE COMPUTATIONAL STUDY**

PHYSICAL AND MECHANICAL METALLURGY OF ZIRCONIUM  
ALLOYS FOR NUCLEAR APPLICATIONS: A MULTI-SCALE  
COMPUTATIONAL STUDY

October 2014

**Idaho National Laboratory**

**Idaho Falls, Idaho 83415**

**<http://www.inl.gov>**

Prepared for the  
U.S. Department of Energy  
Office of Nuclear Energy  
Under DOE Idaho Operations Office  
Contract DE-AC07-05ID14517

**PHYSICAL AND MECHANICAL METALLURGY  
OF ZIRCONIUM ALLOYS FOR NUCLEAR APPLICATIONS:  
A MULTI-SCALE COMPUTATIONAL STUDY**

**A Dissertation**

**Presented in Partial Fulfillment of the Requirements for the  
Degree of Doctor of Philosophy**

**With a**

**Major in Nuclear Engineering**

**In the College of Graduate Studies**

**University of Idaho**

**By**

**Michael Vasily Glazoff**

**October 2014**

**Major Professor: Akira Tokuhiro, Ph.D.**

**Members of the Committee:**

**Robert Hiromoto, Ph.D.**

**Gabriel Potirniche, Ph.D.**

**Steven C. Marschman, Ph.D.**

## DISSERTATION

This dissertation of Michael Vasily Glazoff, submitted for the degree of Doctor of Philosophy with a major in Nuclear Engineering and titled " PHYSICAL AND MECHANICAL METALLURGY OF ZIRCONIUM ALLOYS FOR NUCLEAR APPLICATIONS: A MULTI-SCALE COMPUTATIONAL STUDY", has been reviewed in final form. Permission, as indicated by the signatures and dates given below, is now granted to submit final copies to the College of Graduate Studies for approval.

Major Professor	Akira Tokuhiko, Ph.D.	Date _____
-----------------	-----------------------	------------

Committee Members	Robert Hiromoto, Ph.D.	Date _____
-------------------	------------------------	------------

Gabriel Potirniche, Ph.D.	Date _____
---------------------------	------------

Steven C. Marschman, Ph.D.	Date _____
----------------------------	------------

Department Administrator	Lee Ostrom, Ph.D.	Date _____
--------------------------	-------------------	------------

Discipline's College Dean	Larry A. Stauffer, Ph.D.	Date _____
---------------------------	--------------------------	------------

Final Approval and Acceptance by the College of Graduate Studies

Dean of the College Of Graduate Studies	Jie Chen, Ph.D.	Date _____
---	-----------------	------------

## Abstract

In the post-Fukushima world, the thermal and structural stability of materials under extreme conditions is an important issue for the safety of nuclear reactors. Because the nuclear industry is going to continue using advanced zirconium cladding materials for the foreseeable future, it becomes critical to gain a fundamental understanding of several interconnected problems. First, what are the thermodynamic and kinetic factors affecting the oxidation and hydrogen pick-up by these materials at normal, off-normal conditions, and in long-term storage? Secondly, what protective coatings (if any) could be used in order to gain extremely valuable time at off-normal conditions, e.g., when temperature exceeds the critical value of  $\sim 1200^{\circ}\text{C}$  ( $2200^{\circ}\text{F}$ )? Thirdly, the kinetics of oxidation of such a protective coating or braiding needs to be quantified. Lastly, even if some degree of success is achieved along this path, it is absolutely critical to have in-service inspection algorithms allowing identifying defects of cladding as soon as possible.

This work attempts to explore these interconnected factors from a computational perspective, utilizing such modern techniques as first-principles atomistic simulations, computational thermodynamics of materials, plasticity theory development, and the morphological algorithms of image processing for defect identification. Consequently, it consists of the four parts dealing with these four problem areas preceded by the introduction and formulation of the studied problems. In the 1<sup>st</sup> part an effort was made to employ computational thermodynamics and *ab-initio* calculations to shed light upon the different stages of oxidation of zircaloy-2 and zircaloy-4, the role of microstructure optimization in increasing their thermal stability, and the process of hydrogen pick-up, both in normal working conditions and in long-term storage. The 2<sup>nd</sup> part deals with the need to understand

the influence and respective roles of the two different plasticity mechanisms in Zr nuclear alloys: twinning (at low T) and crystallographic slip (higher T's). For that goal, a description of the advanced plasticity model is outlined featuring the non-associated flow rule in HCP materials including Zr. The 3<sup>rd</sup> part describes the kinetic theory of oxidation of the several materials considered to be perspective coating materials for Zr alloys: SiC and ZrSiO<sub>4</sub>. In the 4<sup>th</sup> part novel and advanced projectional algorithms for defect identification in zircaloy coatings are described. The author's conclusions and recommendations are presented in the 5<sup>th</sup> part of this work, along with the list of used literature and the scripts for atomistic, thermodynamic, kinetic, and morphological computations.

Consequently, an integrative approach was adopted in this research effort. Its value is based upon developing multi-faceted understanding of complex processes taking place in nuclear fuel rods in-service and in storage. It helped identify a number of key problems pertaining to the safe operations with nuclear fuel: limits of temperature that should be strictly obeyed in storage to retard the hydriding of the zircaloy rod's bulk; understanding the benefits and limitations of the different kinds of coatings; developing an in-depth understanding of plasticity in Zr during normal and off-normal reactor conditions; develop original algorithms allowing identifying different kinds of defects in coated (SiC-braided) zircaloy-4.

The obtained results will hopefully be useful for the nuclear industry providing an improved understanding of the fundamental degradation processes taking place in Zr-based nuclear fuel retaining rod under normal, off-normal, and in-storage conditions.

## **Acknowledgements**

I would like to express my most sincere gratitude to my Advisor, Professor Akira Tokuhiro (University of Idaho) for encouragement, help, and valuable discussions. These discussions were, and continue to be, a rare privilege, and they significantly enhanced both the author's understanding of nuclear materials and enjoyment of his research.

The author is also very grateful to his Committee Members, Professors Robert Hiromoto, Gabriel Potirniche, and Steven C. Marschman (INL) for their continuous support.

The author's gratitude is extended to the Leadership of the Idaho National Laboratory – Manager Dr. Richard D. Boardman (Advanced Process and Decision Systems) and Deputy Director of the INL, Dr. Steven Aumeier. Without their help and encouragement this work would have never taken place.

A warm gratitude is expressed to my Professors and Instructors whose classes I have taken while working in the Graduate Program at the University of Idaho: Dr. Akira Tokuhiro, Dr. Indrajit Charit, Dr. Supathorn Phongikaroon, the late Prof. Michael Lineberry (Idaho State University), Dr. Mary Lou Dunzik-Gougar (Idaho State University), Dr. Majid Khalaf (Idaho State University), Dr. Ragunath Kanakala, Dr. Batric Pesic, and Dr. Fatih Aydogan.

A sincere gratitude is extended to Professors Jeong-Whan Yoon (Deakin University, Melbourne, Australia) who provided invaluable guidance in my plasticity studies, to Dr. Sergey N. Rashkeev (Qatar Scientific Foundation) for teaching the author the elements of first-principles atomistic calculations, and to Professor Yuri P. Pytyev (M.V.

Lomonosov Moscow University), - for his guidance in the morphological analysis and synthesis as applied to the problems of materials and nuclear engineering. The author would like to express his sincere gratitude to Drs. Sandra M. Birk and Steven C. Marschman (both of Idaho National Laboratory) for continuous support and encouragement, to Dr. Veena Tikare (Sandia National Laboratory, Albuquerque, NM, Computational Materials Science Program) for reviewing the manuscript and valuable comments and recommendations, and to Prof. Brent Heuser (University of Illinois Urbana-Champaign) for valuable discussions.

Last, but not least, a sincere gratitude is extended to Ms. Ashley Bogar, of the University of Idaho, Moscow (College of Graduate Studies) for her valuable comments and numerous recommendations on the proper formatting of this dissertation.

Our research was supported by the Next Generation Nuclear Power Plant (NGNP) program (U.S. Department of Energy, Office of Nuclear Energy, Science, and Technology under DOE Idaho Operations Office Contract DE-AC0799ID13727; Manager – Mr. Michael W. “Mike” Patterson). This support is gratefully acknowledged, as well as that of the Center for Advanced Energy Studies for providing the necessary computational resources.



## **Dedication**

The author dedicates this work, gratefully and respectfully,  
to his mother, *Prof. Valeria V. Vavilova*,  
and to the memory of his late father, *Prof. Vasily M. Glazov*

## Table of Contents

<b>Authorization to Submit Dissertation</b> .....	ii
<b>Abstract</b> .....	iii
<b>Acknowledgments</b> .....	v
<b>Dedication</b> .....	vii
<b>Table of Contents</b> .....	viii
<b>Appendices</b> .....	xiii
<b>List of Figures</b> .....	xiv
<b>List of Tables</b> .....	xx
<b>Chapter 1 Formulation of the Problem and its Significance</b> .....	1
1.1 Background.....	1
1.2 Goals and Motivation .....	6
1.3 Approach/Methodology.....	6
1.4 Organization of the Dissertation.....	8
1.5 References to Chapter 1 .....	17
<b>Chapter 2 Computational Thermodynamics and <i>Ab Initio</i> Atomistic Simulations of Zircaloy Oxidation and Hydriding in Normal Work Conditions and In Storage.</b> .....	18
2.1 Introduction.....	18
2.2 Oxidation and Hydrogen Uptake In Zirconium, Zircaloy-2 AND Zircaloy-4: Computational Thermodynamics and Ab Initio Calculations.....	19

<b>2.3 Computational Methods</b> .....	22
2.3.1 Ab Initio Calculations .....	22
2.3.2 Computational Thermodynamics of Materials .....	22
<b>2.4 Results and Discussion</b> .....	24
2.4.1 Zirconium Hydrides and Hydriding of Pure Zr, Zy-2, and Zy-4 .....	24
2.4.2 Oxidation .....	34
2.4.3 Suboxides of Zirconium .....	47
2.4.4 Interstitial Oxygen and Hydrogen Solid Solutions .....	49
2.4.5 Thermodynamic Data for Phase-Field Simulations of Zirconium Hydride Formation and Reorientation and Some Results .....	51
2.4.5.1 Equilibrium Thermodynamics of Concentrationally Non- Uniform Systems and Phase-Field Mesoscopic Approach .....	52
2.4.5.2 Adaptation of Hybrid Model to Simulate Hydride Formation .....	57
2.4.5.3 Simulation of Hydride Precipitation –Some Results [84] .....	58
2.4.5.4 Summary – Mesoscopic Work [84] .....	60
<b>2.5 Conclusions and Recommendations for Chapter 2</b> .....	61
<b>2.6 References to Chapter 2</b> .....	63

<b>Chapter 3 Materials and Methods for Zircaloy Cladding Protection against LOCA/RIA Accidents</b> .....	70
<b>3.1 Different Mechanisms of Zirconium Alloy Protection</b> .....	70
<b>3.2 Some Kinetic Aspects of Zr Cladding Oxidation in PWRs and BWRs</b> .....	71
<b>3.3 Ultra-High Temperature Steam Corrosion of Complex Silicates for Nuclear Systems</b> ....	77
3.3.1 Some Experimental Results .....	77

3.3.2	Brief Description of Complex Silicates .....	79
3.3.3	Paralinear SiC Oxidation in Water Vapor Environment.....	83
3.3.4	SiC Corrosion in Extreme Hot Steam Environment .....	87
3.3.4	Other Silica Based Ceramics in Hot Steam Environment.....	92
3.4.5	Specifics of Choosing Corrosion Resistant Ceramics for Nuclear Applications.....	96
3.4.6	Atomic-scale arguments .....	100
3.4.7	Some Conclusions .....	103
<b>3.4</b>	<b>The Concept of “Self-Healing” for Yttria-Stabilized Zirconia and Development of Protective Coatings for Zr-Based Cladding Materials .....</b>	<b>105</b>
3.4.1	Thermal Activation of Protection Mechanisms .....	105
3.4.2	Additions of Several PPM(s) of Beryllium .....	108
3.4.3	Zr Surface Modification with YSZ (Yttria-Stabilized Zirconia).....	111
<b>3.5</b>	<b>Computational Thermodynamics Assessment of Feasibility of Fe-Cr-Al Coatings for Zircalloys 2 and 4.....</b>	<b>114</b>
3.5.1	Introduction and Description of the Problem .....	114
3.5.2	Fe-Cr-Al Protective Coatings for Zircalloys: Selection of the Optimal Process Parameters .....	115
3.5.2.1	Fe-Cr-Al Composition “Window” and Deposition Process Temperature Mechanisms .....	116
3.5.2.2	Low-Temperature Incipient Melting Reactions in the Fe-Cr-Al-Zr Quaternary System.....	122
<b>3.6</b>	<b>Conclusions to Chapter 3 .....</b>	<b>126</b>
<b>3.7</b>	<b>References to Chapter 3 .....</b>	<b>128</b>

<b>Chapter 4 Development of Plasticity Model Using Non-Associated Flow Rule for Zirconium Nuclear Alloys</b> .....	134
<b>4.1</b> Brief Review of Plasticity Theory Development: Tresca, von Mises Plasticity, Schmid's Law, Normality and Deviations from Them. ....	134
<b>4.2</b> Development of Plasticity Model Using Non-Associated Flow Rule for HCP Materials Including Zirconium Alloys for Nuclear Applications.....	142
4.2.1 Plastic Potential for Non-Associated Flow Plasticity .....	142
4.2.2 A General Yield Function for the Tension Compression Asymmetry of Yield Strength (SD – Effect) .....	143
4.2.3 Extension of the Model for Orthotropic Functions.....	147
4.2.4 Modeling of Yield Surface Evolution for Zirconium Clocked-Rolled Plate.....	149
4.2.5 Application to High-Purity $\alpha$ -Titanium .....	152
<b>4.3</b> Conclusions to Chapter 4.....	154
<b>4.4</b> Recommendations and a Path Forward: Temperature Dependent Creep Surface under General Loading Conditions.....	155
<b>4.5</b> References to Chapter 4.....	162
 <b>Chapter 5 Morphological Analysis of Defects in SiC-Protected Zircaloy-4 Cladding</b> .....	164
<b>5.1</b> Introduction.....	164
<b>5.2</b> Formulation of the Problem.....	166
<b>5.3</b> What is Mathematical Morphology? .....	168
<b>5.4</b> Description of the Morphological Algorithm .....	176
<b>5.5</b> Results and Discussion .....	178

<b>5.6</b> Conclusions to Chapter 5 .....	182
<b>5.7</b> Literature to Chapter 5 .....	183

<b>Appendices</b> .....	185
<b>1</b> Thermodynamic Properties of different Zr-H Alloys at different temperatures.....	185

## List of Figures

<b>Figure 1</b> Hexagonal (hcp) Zr structure (different views): (a) in the direction perpendicular to the (0001) axes; (b) in the direction of the (0001) axes. Zr atoms are shown in cyan color; octahedral interstitials are indicated by arrows. ....	25
<b>Figure 2</b> Positions of single oxygen and hydrogen in hexagonal (hcp) Zr structure: (a) O in the octahedral interstitial; (b) H in the octahedral interstitial; (c) H in the middle of the Zr-Zr bond. Zr atoms are shown in cyan, oxygen – in red, hydrogen – in white. ....	26
<b>Figure 3</b> Relaxed crystalline structures of the three experimentally observed hydrides of zirconium: orthorhombic $\gamma$ -ZrH ( $a=4.592$ Å; $c=4.492$ Å); cubic $\delta$ -ZrH <sub>1.5</sub> ( $a=4.775$ Å) and tetragonal $\varepsilon$ -ZrH <sub>2</sub> ( $a=4.999$ Å; $c=4.433$ Å).....	27
<b>Figure 4 (a)</b> Calculation using ThermoCalc; <b>(b)</b> Experimental phase diagram [48].....	27
<b>Figure 5</b> The Gibbs free energy of the several co-existing phases in the Zr-H system as a function of the hydrogen mole fraction at 800 K .....	28
<b>Figure 6</b> Fragment of the diagram in Figure 4(a) for low values of $n_H$ .....	29
<b>Figure 7 (a)</b> Hydrogen isopleth for Zircaloy-2; <b>(b)</b> Same for Zircaloy-4.....	29
<b>Figure 8</b> Partial molar enthalpy of hydrogen in different phases as a function of the $x(H)/x(Zr)$ and its comparison to experiment [54] and the results of thermodynamic computations in [55].....	32
<b>Figure 9</b> Partial molar entropy of hydrogen: comparison of the results of modeling (left) and experimental data [16]; black solid line –the results of thermodynamic assessment in [55] and experimental work [54] .....	33
<b>Figure 10</b> Experimental [57] and computed phase diagram Zr-O .....	35
<b>Figure 11</b> Partial molar enthalpy of oxygen: experimental data [62, 63], the results of assessment in [64], and the present work .....	36
<b>Figure 12</b> Molar volume of Zircaloy-2 as a function of temperature .....	40
<b>Figure 13</b> Temperature dependence of the phase composition for Zircaloy-2 .....	41
<b>Figure 14</b> Temperature dependence of the phase composition for Zircaloy-4 .....	41
<b>Figure 15</b> Temperature dependence of the phase composition for ZIRLO™ .....	42



<b>Figure 16</b> Temperature dependence of the phase composition for alloy M5 .....	42
<b>Figure 17</b> Relaxed configuration for two hydrogen atoms that were initially put in one octahedral interstitial (as H <sub>2</sub> molecule). Zr atoms are shown in cyan, hydrogen—in white .....	44
<b>Figure 18</b> Relaxed configuration for H and O atoms. Initially oxygen atom was put in octahedral interstitial and H atom – in the middle of a neighboring Zr-Zr bond. Zr atoms are shown in cyan, O – in red, H – in white. ....	45
<b>Figure 19</b> The “checkerboard” configuration for O atoms in octahedral interstitials. Zr atoms are shown in cyan, O in the 1 <sup>st</sup> layer – in red, O in the 2 <sup>nd</sup> layer – in pink. Four non-equivalent groups of interstitials are indicated by numbers and yellow arrows. ....	46
<b>Figure 20</b> First-principles calculations [61] and experimental data illustrating the presence of suboxides of zirconium in the Zr-O phase diagram [75].....	48
<b>Figure 21</b> Free-energy curves for the Zr-H system at 300°C obtained using data in Appendix 1 [84, 85] .....	51
<b>Figure 22</b> Input microstructure with basal orientation for small simulations with seven grains. The grains are elongated in the X-direction, which is also the rolling direction for the purposes of this illustration [84] .....	59
<b>Figure 23</b> The distribution of hydrogen in the microstructure; hydrogen concentrations are highest in the $\delta$ -ZrH <sub>1.5</sub> precipitates and the matrix is depleted [84] .....	60
<b>Figure 24</b> Stages in the oxidation of Zr alloys modified in [7] after Gibert [12]. The kinetic equations for the two stages are shown ( $k_1$ and $k_2$ are the rate constants). ....	73
<b>Figure 25</b> Surface oxidation of Zy-702 tubing following one hour exposure to steam/air at ~1000°C, experimental data by McHough et al. [16].....	75
<b>Figure 26</b> SEM photomicrographs of Zy-702 tubing following one hour exposure in air/supersaturated steam at ~1000°C. (a) 100X, secondary electron mode. (b) 250X, secondary electron mode. (c) 500X, secondary electron mode. (d) 1000X, backscattered electron mode [16] .....	76
<b>Figure 27</b> Photographs of starting samples (above) and ruptured samples (below) of (a) Zy-702 tube, and, (b) Zy-702 tube fitted with a SiC CMC sleeve [16] .....	79
<b>Figure 28</b> The Si-C phase diagram calculated using ThermoCalc software and the TCBDIN database. Only the 2H-polytype ( $\alpha$ -SiC) relevant for our study is presented in this diagram .....	81
<b>Figure 29</b> Thermodynamic calculations of the total phase composition of the silicon carbide, oxygen, and water mixture as a function of temperature. ....	84

<b>Figure 30</b> SiC recession due to parabolic oxidation and volatilization in the “free-boiling” regime (reactor with collapsed roof). All the parameters used in these calculations are described in the text.....	88
<b>Figure 31</b> Steady-state linear SiC recession rate as a function of temperature.....	91
<b>Figure 32</b> The Si-Zr phase diagram calculated using ThermoCalc software and the TTZR1 database by ThermoTech LLC.....	97
<b>Figure 33</b> Pseudo-binary $\text{ZrO}_2\text{-SiO}_2$ phase diagram calculated using the FactSage codes.....	99
<b>Figure 34</b> Schematics of atomic structure for: (a) amorphous $\text{SiO}_2$ ; (b) amorphous $\text{ZrO}_2$ ; (c) regular stoichiometric zircon $\text{ZrSiO}_4$ . Zirconium is shown in cyan, Si – in grey; O – in red.....	101
<b>Figure 35 a.</b> Oxide growth by inward oxygen transport. White arrows represent the oxidation front at the oxide / metal, O/M interface; <b>b.</b> Oxide growth by outward metal cation transport. Black arrows represent the oxidation front at the oxide/gas, O/G interface; <b>c.</b> Oxide growth by mixed, inward oxygen and outward metal cation, transport [52, 53] .....	107
<b>Figure 36</b> Rectangular aluminum ingot (alloy of the 7xxx series) with addition of 12 ppm Be (left) and without additions of Be (right), [55] .....	110
<b>Figure 37 Left:</b> Atomic-scale models for YSZ surface: (a) a free (001) surface for oxygen saturated stabilized cubic $\text{ZrO}_2$ structure; <b>Right:</b> YSZ (001) surface, schematics of Y (a), Mn (b), and La (c) subsurface substitutional defects. In each case, two subsurface Zr atoms are substituted by dopant impurity atoms and one oxygen vacancy is added. Oxygen atoms are shown in red, Zr – in light blue balls, Y – in yellow [66] .....	113
<b>Figure 38</b> Binary phase diagram Fe-Cr computed using ThermoCalc ver. S. Green lines represent connodes (tie-lines).....	116
<b>Figure 39</b> Fe-Cr-Al isothermal cross-section diagram at 850°C .....	117
<b>Figure 40</b> Fe-Cr-Al isothermal cross-section diagram at 800°C .....	117
<b>Figure 41</b> Fe-Cr-Al isothermal cross-section diagram at 700°C .....	118
<b>Figure 42</b> Fe-Cr-Al isothermal cross-section diagram at 600°C .....	118

<b>Figure 43</b> Fe-Cr-Al isothermal cross-section diagram at 550°C .....	119
<b>Figure 44</b> Fe-Cr-Al isothermal cross-section diagram at 500°C .....	119
<b>Figure 45</b> Fe-Cr-Al isothermal cross-section diagram at 400°C .....	120
<b>Figure 46</b> Cr isopleth for the Al-Cr-0.8Fe system .....	110
<b>Figure 47</b> Al isopleth for the Al-Cr-0.8Fe system .....	121
<b>Figure 48</b> Binary Zr-Fe phase diagram .....	121
<b>Figure 49</b> Binary Zr-Cr phase diagram .....	122
<b>Figure 50</b> Binary Zr-Al phase diagram .....	123
<b>Figure 51</b> Liquidus projection and the ternary eutectic in the Fe-Cr-Al system: L $\rightarrow$ FCC + BCC + HCP .....	124
<b>Figure 52</b> Monovariant equilibrium lines in the Fe-Cr-Al system .....	125
<b>Figure 53</b> Liquidus projection in the Fe-Zr-Cr system .....	125
<b>Figure 54</b> The von Mises yield surfaces in principal stress coordinates circumscribes a cylinder with radius $\sqrt{2/3}\sigma_y$ around the hydrostatic axis. Also shown is Tresca's hexagonal yield surface ( <a href="http://en.wikipedia.org/wiki/Von_Mises_yield_criterion">http://en.wikipedia.org/wiki/Von_Mises_yield_criterion</a> ) [13] ....	136
<b>Figure 55</b> Intersection of the von Mises yield criterion with the $(s_1, s_2)$ plane, where $s_3=0$ [13] .....	136
<b>Figure 56</b> Deviations from normality and associated flow rule as illustrated by the concept of the so-called “Lode angle”[14] .....	137
<b>Figure 57</b> The results of the tension and compression tests at 1 atm (0.1 MPa) and at superimposed pressures of 138, 414 and 828 MPa, after Spitzig and Richmond [12].....	138
<b>Figure 58</b> Effect of the pressure sensitive parameter $b$ on the yield surface of the proposed yield function constructed in the three-dimensional space of principal stresses: (a) negative $b$ ; (b) positive $b$ . .....	146
<b>Figure 59</b> Effect of the pressure sensitive parameter $b$ on the yield surface of the proposed yield function constructed in the space of principal stresses under plane stress condition with $\sigma_3 = 0$ .....	147
<b>Figure 60</b> Effect of the third stress invariant on the yield surface adjusted by the material parameter $c$ for materials under spatial loading.....	150

<b>Figure 61</b> Comparison of yield surface evolution predicted by the proposed yield function with those computed by the VPSC model for a zirconium clock-rolled plate during in-plane compression for various levels of pre-strain. (units: MPa) .....	150
<b>Figure 62</b> Comparison of yield surface evolution predicted by the proposed yield function with those computed by the VPSC model for a zirconium clock-rolled plate pre-strained in through-thickness compression for various levels of pre-strain. (units: MPa) .....	151
<b>Figure 63</b> Comparison the yield surfaces of high-purity $\alpha$ -titanium constructed by the proposed yield function on the $\pi$ -plane with experimental results (units: MPa) .....	153
<b>Figure 64</b> Comparison the yield surfaces of high-purity $\alpha$ -titanium constructed by the proposed yield function under plane stress with experimental results (unit: MPa) .....	156
<b>Figure 65</b> Comparison of yield surface evolution predicted by the proposed yield function with those computed by the VPSC model for a zirconium clock-rolled plate during in-plane compression for various levels of pre-strain. (units: MPa) .....	
<b>Figure 66</b> True stress behavior of Zirconium under compression under various high temperatures.....	157
<b>Figure 67</b> Schematic view of a proposed general methodology .....	159
<b>Figure 68</b> SEM photomicrographs of cross sections of C fibers filaments during conversion to SiC. <b>(a)</b> As-received (unconverted) PAN-based carbon fibers. <b>(b)</b> Partially converted carbon filament with ~200 nm thick SiC shell. <b>(c)</b> Partially converted C filament with 1 $\mu$ m thick SiC shell. <b>(d)</b> Fully converted SiC tube. SEM/EDS analysis of a partially converted filament (right) indicates stoichiometric conversion of C to SiC, [8] .....	165
<b>Figure 69</b> ZY-4 tube with composite fiber outer wrap. Off-normal braided features are highlighted in red circles .....	166
<b>Figure 70</b> General view of the analyzed sample (optical - digital photography).....	167
<b>Figure 71</b> Local defects (blue ovals) and global defects (lateral shifts of the vertical filaments) .....	167
<b>Figure 72</b> Three-dimensional (3D) representation of the surface height function $f(x, y)$ for original rolled and formed aluminum alloy, AA6022. Total surface height function <b>(a)</b> and its morphological decomposition into OP (“orange peel”, or grain roughening) <b>(b)</b> , and RGI (roll-grin imprint) <b>(c)</b> components. The size of the imaged area is 1.2*1.2	

mm <sup>2</sup> , [20]. The original quantitative surface height data for analysis were obtained using confocal microscopy .....	176
<b>Figure 73</b> The effects of non-uniformity of illumination were removed using a morphological algorithm.....	179
<b>Figure 74</b> Equalizing “cylinder of brightness” allowing introducing the non-uniform illumination correction (see Figure 70 above).....	179
<b>Figure 75</b> Minima correspond to the points in which morphological difference between the analyzed sample and the etalon (reference sample) were minimal .....	180
<b>Figure 76</b> Major defects are highlighted with green color.....	180
<b>Figure 77</b> This Figure corresponds to Figure 73 but illustrates just the defects themselves.....	181
<b>Figure 78</b> General view of the <i>MorphoHawk</i> platform and of the images generated by the developed MEX modules (the results of morphological processing).....	181

## List of Tables

<b>Table 1</b> Material constraints in the proposed yield function in equation (4.13) for a zirconium clock-rolled plate during in-plane compression for various levels of pre-strain .....	160
<b>Table 2</b> Material constants in the proposed yield function in equation (4.13) for a zirconium clock-rolled plate during through-thickness compression for various levels of pre-strain .....	161

## Chapter 1 Formulation of the Problem and Its Significance

1. Michael V. Glazoff, Jeffrey O. Brower, Tammy L. Trowbridge, Marat Khafizov, Analysis of Corrosion of the Dummy “EE” Plate 19 in Type YA ATR Fuel Elements, INL External Report, August 2014 (in preparation)
2. Kevin M. McHugh, John E. Garnier, Sergey N. Rashkeev, Michael V. Glazoff, George W. Griffith, and Shannon Bragg-Sitton, “High Temperature Steam Corrosion of Cladding for Nuclear Applications: Experimental”, *Ceramic Engineering and Science Proceedings* (special volume: Ceramic Materials for Energy Applications III), vol.34, issue 9, pp.149-160 (2013)
3. Veena Tikare, Philippe Weck, Peter Schultz, Blythe Clark, Michael V. Glazoff, Eric Homer, Milestone 2 Report on Integration of the Hybrid Hydride Model into INL’s MBM, Joint Sandia/INL Report, FCRD-UFD-2014-00068 Rev.0, August 2014
4. Veena Tikare and Michael V. Glazoff, Model for Simulation of Hydride Precipitation in Zr-Based Used Fuel Claddings: A Status Report on Current Model Capabilities, Joint Sandia/INL Report, FCRD- UFD-2014-000068, SAND2013-10834P, August 30 (2013)
5. Veena Tikare, John Scaglione, Jeremy Busby, Robert Howard, Michael V. Glazoff, and Jason Hales, Roadmap for Developing a Computation Tool for Prediction of Hydride Precipitation and Reorientation during Long-Term Dry-Storage, Prepared for U.S. Department of Energy Campaign or Program, FCRD- UFD-2013-000068, SAND2012-10834P, December 15 (2012)

### 1.1 Background

In order to consistently analyze severe accidents such as the March 11, 2011 Fukushima nuclear plant accident, Tokuhiro proposed a multi-scale approach that is known under the abbreviation of “LENDIT” [1, 2]. The term LENDIT stands for “length, energy, number, distribution, information and time”, and the concept provides convenient scales for characterization of a given phenomenon. In particular, it was further developed to propose linear constraints that are used to guide the branch-and-bound algorithm to limit the number of possible states to be analyzed [2].

In this work, an approach was taken via to use a modified LENDIT approach for multiscale analysis of different phenomena taking place in zirconium-based nuclear alloys in the fuel clad, first in reactors and subsequently in long-term storage. This, therefore, spans the whole lifecycle of a zirconium alloy for nuclear applications. Atomistic modeling provides the smallest

length scale (of the order of nanometers), mesoscopic phase field simulations yield valuable information on scales of the order of 10 to 100 micrometers, computational thermodynamics, plasticity theory give results applicable on the scale of a material coupon (i.e., of the order of centimeters and more). Finally, the kinetics of oxidation provides valuable time scale (1<sup>st</sup> order kinetics) for the processes of oxidation of the Zr-based clad relative to off-normal condition timescales. Below, these LENDIT-base phenomena are investigated in application to a number of scenarios (normal, off-normal regimes of reactor work and in storage). As a result, it becomes possible to develop a more coherent picture of the complex processes taking place inside the “first engineered barrier”; that being the nuclear fission-product bearing Zr-based cladding.

The United States Nuclear Regulatory Commission (NRC) in its “Standard Review Plan” document [3] (Section 4.2, Fuel System Design) specifically requires that the areas of review include: 1. Design Bases; 2. Description and Design of Drawings; 3. Design Evaluation; 4. Testing, Inspection, and Surveillance Plans; 5. Inspections, Tests, Analyses, and Acceptance Criteria (ITAAC); and 6. COL (Combined License) Action Items and Certification Requirements and Restrictions. In particular, “Fuel System Damage” section of the Design Bases stipulates that the following damage criteria must be addressed:

1. Stress, strain, or loading limits for spacer grids, guide tubes, thimbles, fuel rods, control rods, channel boxes, and other fuel system structural members should be provided;
2. Oxidation, hydriding, and the buildup of corrosion products (crud) should be limited, with a limit specified for each fuel system component;

In Part B of the “Design Bases” Section, the following criteria are defined: 1. Hydriding; 2. Cladding collapse; 3. Overheating of cladding; 4. Pellet / cladding interaction; 5. Bursting; 6. Mechanical fracturing.



In this dissertation, a research effort was undertaken to view these undesirable degradation mechanisms from a technical perspective. This holistic interdisciplinary approach defined the selection of topics for research: thermodynamics and atomistic mechanisms of hydriding; kinetics of oxidation; design of coatings; development of advanced plasticity approach to Zr nuclear alloys in service and in storage; methods of inspection of Zr fuel retaining rods for defect identification.

Light Water Reactor (LWR) Zr-based clad behavior during normal and off-normal reactor operation and in storage represents a complex problem calling for an inter-disciplinary integrative approach. In particular, the LENDIT time, length, and energy scale(s) change about 15 orders of magnitude. Indeed, one has to consider such physical, chemical and mechanical phenomena as oxidation and hydriding of clad [3]; its plastic and creep behavior in a broad temperature range (from ambient temperature to 1100°C and above); compatibility of Zr nuclear alloys with potential protective coatings and their thermal stability; development of capabilities for monitoring and rapid identification of stress-corrosion cracking in the clad. Experiment-based, scientific approach to all these issues is a very significant problem. In this situation, the interdisciplinary, integrative computational approach adopted in the present work, presents itself as a viable, original alternative to empirical, costly, and lengthy studies.

Nuclear materials science [4, 5] supports the basis of material nuclear reactor design. Indeed, to be of value for the nuclear industry, the obtained results need to be capable of explaining a number of phenomena of ultimate complexity. Although access to specialized nano-scale atomistic simulations is of value, the reality of long-term used fuel storage demands an unprecedented integration of phenomena. However, if successful, it is of much needed significance and relevance to the nuclear industry.

Consequently, the extremely complex problems of today's nuclear industry require that researchers specialize in very narrow areas of engineering but be able to understand the large scales and new demands successfully. It is for this reason that a research effort was made in this work to demonstrate such an integrative approach to the complex interdisciplinary problem of Zr-based nuclear fuel clad behavior under different in- and ex-vessel conditions.

Light water nuclear reactor (LWR) cladding performance during normal, off-normal conditions, in wet and in dry storage, were studied quite extensively during the last 30 years [5-9]. Indeed, cladding is the critically-important engineering barrier preventing the release of gaseous products (hydrogen, radioactive gases –products of fission). At the present time the nuclear industry uses mostly such Zr-based alloys as Zircaloy-2 (Zy-2) for boiling water reactors (BWRs) and Zircaloy 4 (Zy-4), -in the case of Pressurized Water Reactors (PWRs)<sup>1</sup>. However, a transition is rapidly taking place toward more oxidation- and hydrogen uptake- resistant materials such as ZIRLO<sup>TM</sup> and M5<sup>TM</sup>.

Thermodynamic calculations clearly indicate that zirconium is unstable with respect to oxidation by water even at room temperature [10]. The only reason why this process does not attain catastrophic proportions in service conditions is the formation of a thin protective layer of oxide  $ZrO_2$  on the top. It is also a very slow process. However, at temperatures around 800°C and above, zirconium will be oxidized very rapidly in steam environments [11, 12] leading to significant hydrogen gas production in abnormal conditions. Typically, such events are accompanied by the nuclear reactor core uncovering. Subsequent core re-flooding [11, 12] is needed to restore cooling (if at all possible).

---

<sup>1</sup> With time, Zy-2 has evolved as well. GE uses a (near) pure Zr liner in BWR clad and AREVA adds  $Cr_2O_3$  to their clad for HBU (High Burn-Up) service. The author is grateful to Dr. Marschman for this comment.

During significant temperature excursions (LOCA, RIA)<sup>2</sup>, a cascade of interrelated events will take place. First, there will be oxide growth on the surface of the clad accompanied by the HCP  $\rightarrow$  BCC phase transformation in zirconium. Secondly, as a result of the oxidation of zirconium by the superheated water vapor, the release of hydrogen gas will follow accompanied by enhanced hydriding of the clad itself. Thirdly, as a result of the two processes discussed above, stress-corrosion cracking will eventually be initiated accompanied by the release of fission gases. When the temperature excursion is precipitous enough and of high enough amplitude to cause Zr melting on the fuel side of the clad, it will eventually fill the fuel/clad gap and come into direct contact with the uranium oxide fuel. Moreover, in HBU service, there is a rim that grows into the pellet-clad space and there is little to no gap left; the fuel and clad are essentially in contact.

Due to the presence of the several low-melting eutectics in the  $\alpha$  -Zr(O)/ZrO<sub>2</sub>-UO<sub>2</sub> system, the process may become self-sustaining even at temperatures significantly below the temperature of Zr melting in the  $\alpha$  -Zr(O)/ZrO<sub>2</sub>-UO<sub>2</sub> system [15]. This sequence of events represents a highly plausible scenario of the molten core accident at both Three-Mile Island and Fukushima nuclear power plants, [13-15]

In normal reactor working conditions, the UO<sub>2</sub> ceramic fuel always swells as a result of the formation of gaseous fission products [13, 14]. The gas atoms/molecules tend to migrate toward the center of the fuel pellet, eventually resulting in the formation of the center void. In the case of higher burnup levels, contact between the UO<sub>2</sub> fuel and Zr cladding will be established. While this contact may result in a partial reduction of the fuel by the Zr-based solid solution [15],

---

<sup>2</sup> In general, this might be any event resulting in the loss of flow transfer that induces boiling to an extent that a dry spot develops in the cladding surface. The author is grateful for this rectification to Prof. Tokuhiko, his Advisor.

this process in itself does not represent any significant danger in the normal working conditions. Given the phase field of the  $\alpha$ -Zr(O) is much broader and higher temperature-wise than that of pure Zr (see Chapter 2), the  $\alpha$ -Zr(O) solid solution will be forming on the fuel-side of the element out of  $\beta$ -Zr. However, while in normal service conditions these processes are kept under control, the situation may quickly become worse during sustained power excursions [15].

In wet storage of spent nuclear fuel there is the need to very rigorously control the chemistry of the cooling water (as even minor deviations from the optimal values of pH may result in rapid uncontrollable corrosion development) and minimize the overall amounts of the dissolved impurities. Otherwise, localized corrosion of the fuel elements may take place [3], e.g., pitting, crevice, or even erosion-corrosion. In dry storage, some critical issues include understanding the nature of (relatively low temperature) long-term creep, and the issues arising from the redistribution of zirconium hydrides that may result in the potential cracking of the element in storage [6].

While a completely accident tolerant fuel form does not exist (since severe unchecked LOCA/RIA events will always lead to coolant blockage and fuel rod melting [15]), it was our goal to explore both thermodynamic and kinetic mechanisms of Zr oxidation, and develop potential approaches to its protecting e.g. with SiC braiding or coating(s). These approaches are outlined in the next two Sections.

## **1.2 Goals and Motivation.**

As a result of the Fukushima accident [16], the work aimed at developing a safer, accident-tolerant nuclear fuel components significantly accelerated during the last two years. It involves both the exploration of the principally novel materials (e.g., ceramics such as silicon

carbide and zircon), studies of the thermodynamics and kinetics of the zircaloy oxidation and of their respective ceramic coatings, efforts to better understand hydrogen uptake in these materials as well as work aimed at developing reliable automated algorithms of early defects identification in the clad materials.

### 1.3 Approach and Methodology

In this work, a multi-scale, multi-physics computational approach was adopted for solving the problem described above. We thus aim to consider and establish understanding of linkages that impact the state of the fuel clad during normal, off-normal reactor work and in storage. In so doing, the following computational techniques were used:

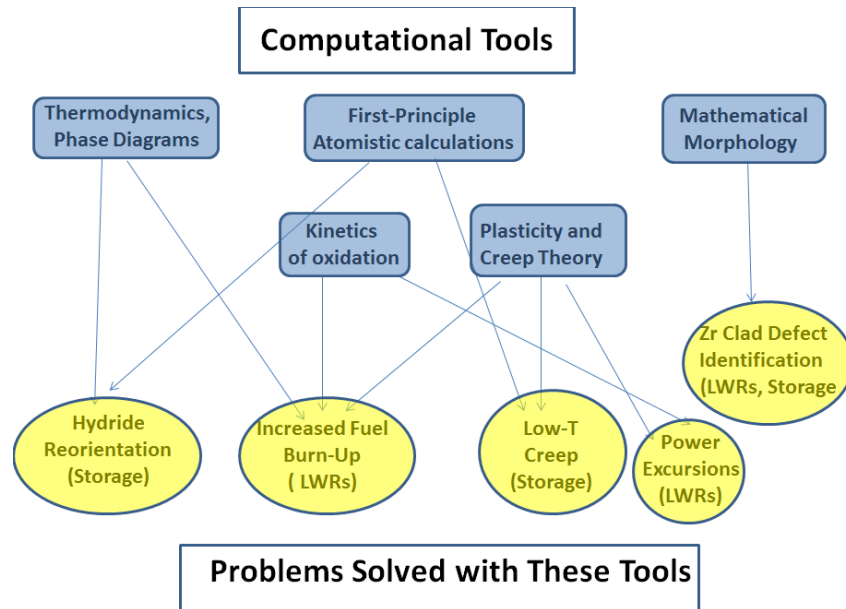
- Computational thermodynamics and phase equilibria (Thermo-Calc v.3.0.1) in order to understand the character of phase equilibria of Zr and its nuclear alloys with hydrogen and oxygen, (Chapter 2) and provide data for thermodynamic stability of complex silicates (Chapter 3) and for meso-scale phase-field calculations of microstructure evolution in the Zr-H system (hydride precipitation and reorientation, together with Sandia, Chapter 2). The importance of this work is in providing the necessary quantitative information about the state of, and potential processes in the clad;
- First-principles atomistic calculations in order to shed light upon the atomic structure of sub-oxides of zirconium and hydrogen diffusion pathways (Chapter 2), and atomistic modeling of complex silicates in support of the conducted kinetic calculations using software VASP (Chapter 3). This is a very important part of the work as it allows understanding the potential pathways of hydrogen atoms in zirconium clad and compare

disordered solid solutions  $\alpha$ -Zr(O) vs. ordered sub-oxides  $Zr_3O$ , the latter being much more efficient in retarding the hydriding process;

- Phenomenological calculations of the “microstructure – property” type (using software *JMatPro* v.8.1, Chapter 2, in order to understand the evolution of phase composition of zirconium alloys and their density with temperature). These calculations have critical importance for proper development of different coatings, which should be compatible with zircalloys (physical properties, phase composition, mechanical properties);
- Advanced plasticity modeling with non-associated flow rule to understand the nature of plastic response of zirconium and its alloys (Zy-2 and Zy-4), its anisotropy, pressure dependence of the yield strength, crystallographic slip and twinning;
- To monitor and identify different types of defects in Zr cladding, we developed innovative morphological modeling methods allowing conducting the monitoring in real time or using stand-alone snapshots of the cladding.

In other words we have tried to shed new light for a very ambitious agenda of achieving in-depth multi-physics understanding of zirconium alloys “from cradle to grave”, i.e., from their fabrication to normal / off-normal work in a light water nuclear reactor to used fuel disposition and storage.

Finally, the tools that were used to solve the problems named above are conveniently presented in the diagram below:



## 1.4 Organization of the Dissertation

Consequently, this dissertation consists of the four inter-connected parts. In the 1<sup>st</sup> part an effort was made to employ computational thermodynamics and ab initio calculations to shed light upon the different stages of oxidation of zircaloy (2 and/or 4), the role of microstructure optimization in increasing their thermal stability, and the process of hydrogen pick-up, both in normal working conditions and in long-term storage. The 2<sup>nd</sup> part deals with the need to understand the influence and respective roles of the two different plasticity mechanisms in Zr nuclear alloys: twinning (at low T) and crystallographic slip (higher T's). For that goal, a description of the advanced plasticity model is outlined featuring the non-associated flow rule in hcp materials including Zr. The 3<sup>rd</sup> part describes the kinetic theory of oxidation of the several materials considered to be perspective coating materials for Zr alloys: SiC and ZrSiO<sub>4</sub>. In the 4<sup>th</sup> part novel and advanced projectional algorithms for defect identification in zircaloy coatings are described. In so doing, the author made use of his applied industrial research experience in this

area. Our conclusions and recommendations are presented in the 5<sup>th</sup> part of this work, along with the list of used literature and the scripts for thermodynamic and morphological computations.

Each Chapter begins with a brief list of the original publications in which the author participated during the last 4 years. All atomistic *ab-initio* computations, computational thermodynamics and phase equilibria, kinetics of oxidation and morphological analysis results represent the original contributions of the author. In his plasticity studies, the author was guided and mentored by Prof. Jeong-Whan Yoon (Deakin University, Melbourne, Australia), the late Dr. Owen Richmond (Alcoa Technical Center, Alcoa Center, PA), and by Prof. John L. Bassani (University of Pennsylvania, Philadelphia), while working as a graduate research assistant at the University of Pennsylvania some 20 years ago. Collaborations with Dr. Vasily V. Bulatov (Edward Teller Fellow, LLNL) and Dr. Sergey N. Rashkeev (Principal Investigator and Project Lead, Qatar Foundation, Doha, Qatar) on the atomistic nature and non-equilibrium thermodynamics of plastic flow are also gratefully acknowledged. The meso-scale modeling results presented in Chapter 1 was completed by Dr. Veena Tikare using the author's expertise for calculating the thermodynamic driving forces for the hybrid "Phase-Field – Potts" simulations of zirconium hydriding. The list of publications in each area is presented below.

### Computational Thermodynamics and Phase Equilibria

1. M.V. Glazoff, I. Charit, and P. Sabharwall, Computational Thermodynamic Modeling of Hot Corrosion of Alloys *Haynes 242* and *Hastelloy<sup>TM</sup> N* for KF-ZrF<sub>4</sub> Molten Salt Service, submitted to *SciTech* (June 2014)
2. M.V. Glazoff, A. Tokuhito, S.N. Rashkeev, and P. Sabharwall, Zirconium, Zircaloy-2, and Zircaloy-4: Computational Thermodynamics and Atomistic Perspective on Hydrogen Uptake and Oxidation, *Journal of Nuclear Materials*, vol.444, pp.65-75 (2014)
3. M. V. Glazoff, Modeling of Some Physical Properties of Zirconium Alloys for Nuclear Applications in Support of UFD Campaign, INL Report # INL/EXT-13-29581 (July 2013)
4. R.E. Mizia, D.E. Clark, M.V. Glazoff, T.E. Lister, T.L. Trowbridge, Optimizing the Diffusion Welding Process for Alloy 800H: Thermodynamic, Diffusion Modeling, and Experimental Work, *Metallurgical and Materials Transactions A*, vol.44A, pp. S154-S161 (January 2013)



5. Vadim S. Zolotarevsky, Nicholas A. Belov, and Michael V. Glazoff, **Casting Aluminum Alloys (monograph)**, 546pp., Elsevier, Amsterdam (November 2007)
6. M.V. Glazoff, F. Barlat and H. Weiland, Continuum Physics of Phase and Defect Microstructures: Bridging the Gap between Physical Metallurgy and Plasticity of Aluminum Alloys, *International Journal of Plasticity*, vol.20, #3, pp. 363-402 (2004). This paper was used at MIT, Dept. of Materials Science and Engineering, as “recommended reading” for graduate-level course “Physical Metallurgy” by Professors Russell and Van Vliet in 2003/2004
7. M.V. Glazov, M.V. Braginsky, C. Laird, J.L. Bassani and M.A. Jameel, On Increased Variance of Coherent Solids, *Materials Science and Engineering A*, vol.271, No.1-2 (1999) pp.291-297
8. M.V. Glazov, G.S. Burkhanov, V.G. Ivanchenko and E.A. Shishkin, Phase Equilibria and Calculation of the Thermodynamics Properties of Alloys in the Systems Nb-Sn, Nb-Al and Nb-Ge, *J. of Metals Physics (Russian)*, vol.11, No.5 (1989) pp.32-35
9. M.V. Glazov and G.S. Burkhanov, Thermodynamics of Superconducting Phase Transition in Multi-Component Systems, *J. of Physical Chemistry (Russian)*, vol.63, No.2 (1989) pp.230-231
10. L.N. Galkin, M.V. Glazov, V.V. Vavilova and Yu.K. Kovneristy, Rapid Quenching and Stabilization of the Phase with the  $\delta$ -Mn Structure in the “Re-Ta” Binary System, *Reports of the Soviet Academy of Sciences*, vol.300, No.5 (1988) pp.1157-1161.
11. M.V. Glazov (Glazoff), Phase Equilibria and Calculation of the Thermodynamic Properties Alloys in Binary Systems with Intermediate Superconducting A15-Phases, *Ph.D. Dissertation (Chemistry)*, Russian Academy of Sciences, Moscow Institute of Metallurgy (1987)
12. E.M.Savitsky, M.V.Glazov and Yu.V.Efimov, Amorphous Metallic Alloys as Mesophases, *Journal of Non-Crystalline Solids*, vol.85 (1986) pp.133-137
13. E.M. Savitsky, M.V. Glazov and Yu.V. Efimov, Amorphous Metallic Alloys and the Problem of Thermodynamic Stability of Phases, *Reports of the Soviet Academy of Sciences*, v. 280, No.5 (1985) pp.1117-1121
14. E.M. Savitsky, M.V. Glazov and Yu.V. Efimov, Thermodynamics of Superconducting Phase Transition in Two-Component Systems, *J. of Physical Chemistry (Russian)*, v.59, No.2 (1985), pp.499-502
15. M.V. Glazov, On the Concentration Dependence of Chemical Potentials in Two-Component Systems, *J. of Physical Chemistry (Russian)*, v.57, No.2 (1983) pp.489-491
16. L.M. Pavlova, M.V. Glazov, V.Ya. Shevchenko, The Evaluation of the Dissociation Degrees of some  $A^{II}B^V$  Compounds Using a Simple Asymmetrical Solution Model, *Reports of the Soviet Academy of Sciences*, v.238, No.1 (1978) pp.108-111.

### Studies on the Atomic Structure of Matter

1. M.V. Glazoff, S.N. Rashkeev and J. Stephen Herring, Mechanisms of Chromium Vaporization Reduction from Metallic Interconnects in Solid Oxide Devices by Nickel Coatings, published online, *Int. Journal of Hydrogen Energy* (2014), <http://dx.doi.org/10.1016/j.ijhydene.2014.07.023>
2. M.V. Glazoff, A. Tokuhiro, S.N. Rashkeev, and P. Sabharwall, Zirconium, Zircaloy-2, and Zircaloy-4: Computational Thermodynamics and Atomistic Perspective on Hydrogen Uptake and Oxidation, *Journal of Nuclear Materials*, vo.444, pp.65-75 (2014)

3. S.N. Rashkeev, M.V. Glazoff, and A. Tokuhiro, Ultra-High Temperature Steam Corrosion of Complex Silicates for Nuclear Applications: Theory/Modeling Study, ***Journal of Nuclear Materials***, vol. 444, pp.56-64 (2014)
4. S.N. Rashkeev and M.V. Glazoff, Fischer-Tropsch Synthesis over Supported Pt-Mo Catalyst: Towards Bimetallic Catalyst Optimization, ***Journal of Physical Chemistry (C)***, vol.117, pp.4450-4458 (February 2013)
5. S.N. Rashkeev and M.V. Glazoff, Atomic-Scale Mechanisms of Oxygen Electrode Delamination in Solid Oxide Electrolyzer Cells, ***International Journal of Hydrogen Energy***, pp.1280-1291, vol.37, issue 2 (January 2012)
6. M.V. Glazoff and S.N. Rashkeev, Beryllium Adsorption at Transition Aluminas: Implications for Environmental Science and Oxidation of Aluminum Alloys, ***Journal of Physical Chemistry C***, vol.114, pp. 14208–14212 (2010)
7. A.Y. Borisevich, S. Wong, S.N. Rashkeev, M.V. Glazoff, S.J. Pennycook, S.T. Pantelides, Dual Nano-Particle/Substrate Control of Dehydrogenation Catalysis, ***Advanced Materials***, vol.19, pp. 2129-2133 (2007)
8. J.C. Idrobo, A. Halabica, S. Rashkeev, M.V. Glazoff, L.A. Boatner, R.F. Haglund, S.J. Pennycook, and S.T. Pantelides, Atomic-Scale Characterization and Optical Properties of Metal Nanoparticles Embedded in Alumina Matrices, ***Microscopy and Microanalysis***, vol.13 (Suppl. 2), p.1190 (2007)
9. S. Wang, A.Y. Borisevich, S.N. Rashkeev, M.V. Glazoff, K. Sohlberg, S.J. Pennycook, and S.N. Pantelides, Dopants Adsorbed As Single Atoms Prevent Degradation of Catalysts, ***Nature Materials***, vol.3 (3), pp.143-146 (2004)
10. S.N. Rashkeev, K. Sohlberg, M.V. Glazoff, J.W. Novak, S.J. Pennycook, and S.T. Pantelides, Transition Metal Atoms on Different Alumina Phases: The Role of Subsurface Sites on Catalytic Activity. ***Physical Review B (Condensed Matter)***, vol.67, 115414 (2003)
11. V.V. Bulatov, O. Richmond and M.V. Glazov, An Atomic Dislocation Mechanism of Pressure-Dependent Plastic Flow in Pure Aluminum, ***Acta Materialia***, vol.47/12 (1999) pp.3507-3514
12. C.S. Becquart, P.C. Clapp, M.V. Glazov and J.A. Rifkin, Molecular Dynamics Simulations of Amorphization in Al and Ni<sub>3</sub>Al, ***Computational Materials Science***, vol.1 (1993), pp.411-418
13. P.C. Clapp, M.V. Glazov and J.A. Rifkin, Dislocation Dynamics and Multiplication via Atomistic Simulations, ***Journal de Physique IV***, vol.3 (1993) pp.2005-2014
14. N.A. Palii, M.V. Glazov, Yu.V. Barmin and V.V. Vavilova, X-Ray Diffraction Studies of the Short-Range Order Structure of Some Amorphous Alloys in the Re-Ta and Re-W Binary Systems, ***Reports of the Russian Academy of Sciences***, vol.318 (1991) pp.144-147
15. M.M. Eliseeva, M.V. Glazov, Yu.K. Kovneristy and A.I. Landa, Computer Simulation of Structure of Amorphous Metallic Alloys Using Different Modifications of Regularization Technique, ***Journal of Melts (Russian)***, vol.4 (1993), pp.62-67
16. M.V. Glazov and V.M. Glazov, Development of Molecular-Statistical Concepts in Application to Solutions in the Works of Professor I.R. Prigogine, ***Introduction to the Russian Translation of I. Prigogine's Monograph "The Molecular Theories of Solutions"***, Moscow, Metallurgy (1990), pp.9-14

## Kinetics, Nonlinear Non-Equilibrium Thermodynamics and Diffusion

1. M.V. Glazov (Glazoff), Self-Organization and Spatio-Temporal Dissipative Structures in Fatigued Metals, **Ph.D. Dissertation (Materials Science and Engineering)**, University of Pennsylvania, Department of Materials Science and Engineering (1995)
2. S.N. Rashkeev, M.V. Glazoff, and A. Tokuhiro, Ultra-High Temperature Steam Corrosion of Complex Silicates for Nuclear Applications: Theory/Modeling Study, **Journal of Nuclear Materials**, vol. 444, pp.56-64 (2014)
3. Michael V. Glazoff, Advanced High Temperature Reactor: Computational Thermodynamics Study of Materials, Their Diffusion Welding, and Corrosion, **M.S. Thesis (Nuclear Engineering)**, University of Idaho (Idaho Falls), Department of Nuclear Engineering (2013)
4. R.E. Mizia, D.E. Clark, M.V. Glazoff, T.E. Lister, T.L. Trowbridge, Optimizing the Diffusion Welding Process for Alloy 800H: Thermodynamic, Diffusion Modeling, and Experimental Work, **Metallurgical and Materials Transactions A**, vol.44A, pp. S154-S161 (January 2013)
5. Piyush Sabharwall, Denis E. Clark, Ronald E. Mizia, Michael V. Glazoff, and Michael G. McKellar, Diffusion Welded Micro-Channel Heat Exchanger For Industrial Processes, **Journal of Thermal Science and Engineering Applications**, vol.5, pp.011009 -01100912 (March 2013)
6. S.N. Rashkeev and M.V. Glazoff, Current “Pulsing” as a Mechanism for Potential Dramatic Working Life Extension of Solid Oxide Electrolysis Cells, **Applied Physics Letters**, vol.99, issue 17, article 173506 (24 October 2011)
7. S.N. Rashkeev, M.V. Glazoff and F. Barlat, Strain Rate Sensitivity Limit Diagrams and Plastic Instabilities in a 6xxx Series Aluminum Alloy Part I: Analysis of Temporal Stress-Strain Serrations, **Computational Materials Science**, vol. 24, pp.295-309 (2002)
8. F. Barlat, M.V. Glazoff, J.C. Brem and D.J. Lege, A Simple Model for Dislocation Behavior, Strain and Strain Rate Hardening Evolution in Deforming Aluminum, **International Journal of Plasticity**, vol.18, pp.919-939 (2002)
9. G.H. Bray, M.V. Glazov, R.J. Rioja, R.P. Gangloff and C. Li, Effect of Artificial Aging on Fatigue Crack Growth Resistance of 2xxx Series Aluminum Alloys, **International Journal of Fatigue**, vol.23, pp. S265-S276 (2001)
10. S.N. Rashkeev, M.V. Glazov and F. Barlat, The Eckhaus Instability –a Possible Wavelength Changing Mechanism in the Evolution of Dislocation Patterns, **Computational Materials Science**, vol.21, pp.230-242 (2001)
11. M. Zaiser and M.V. Glazov, Some Remarks on the Classification of Plastic Instabilities, **Journal of the Mechanical Behavior of Materials (London)**, vol.11, Nos.1-3, pp.243-249 (2000)
12. S.N. Rashkeev, M.V. Glazov and O. Richmond, Irregularities and Modulated Dislocation Patterns in Plastically Deformed Metals: the Eckhaus Instability, **Journal of the Mechanical Behavior of Materials (London)**, vol.10, No.1 (1999), pp.7-30.
13. M.V. Glazov, D.J. Lege, F. Barlat and O. Richmond, Computer Simulation of Annealing and Recovery Effects on Serrated Flow in Some Al-Mg Alloys, **Metallurgical and Materials Transactions**, vol.30A (1999) pp.387-397
14. M.V. Glazov, D.R. Williams and C. Laird, Temporal Dissipative Structures in Cyclically Deformed Metallic Alloys, **Applied Physics A (Springer-Verlag)**, vol.64, (1997) pp.373-381

15. M.V. Glazov, Temporal Instabilities and Dissipative Structures in Fatigued Metals, *Journal of Metals (JOM)*, No.4 (1996) p.61
16. M.V. Glazov, L. Llanes and C. Laird, Self-Organized Dislocation Structures (SODS) in Fatigued Metals, *Phys. Stat. Solidi (A)*, vol.149 (1995) pp.297-321
17. M.V. Glazov and C. Laird, Size Effects of Dislocation Patterning in Fatigued Metals, *Acta Metall. Mater.*, vol.43, No.7 (1995) pp.2849-2857
18. M.V. Glazov and M.D. Adamenkova, On the Physico-Chemical Criterion for Detecting Protein Aggregates on Adsorbing Surfaces, *J. of Physical Chemistry (Russian)*, v.56, No.7 (1982) pp.1813-1814
19. M.V. Glazov and M.D. Adamenkova, Calculation of Mobility Times for Some Protein Globules on Adsorbent Surfaces, *J. of Physical Chemistry (Russian)*, v.56, No.5 (1982) pp.1307-1309.

### Dislocations and Plasticity

1. M.V. Glazov, M.V. Braginsky, L.A. Lalli and O. Richmond, On the Derivation and Analysis of the "Machine Equation" in Finite Deformations, *Applied Physics A (Springer-Verlag)*, vol.67, No.5 (1998) pp.571-578
2. **Influences of Interface and Dislocation Behavior on Microstructure Evolution**, MRS Symposium Proceedings, vol.652, Edited by Mark Aindow, Mark D. Asta, Michael V. Glazov et al., MRS, Warrendale, PA (2001)
3. J.-W. Yoon, F. Barlat, H. Weiland, M.V. Glazoff, and R. Dick, State of the Art for Crystal Plasticity-Based Modeling, ATC Internal Report # 07-201, 2007-11-15
4. M.V. Glazoff, F. Barlat and H. Weiland, Continuum Physics of Phase and Defect Microstructures: Bridging the Gap between Physical Metallurgy and Plasticity of Aluminum Alloys, *International Journal of Plasticity*, vol.20, #3, pp. 363-402 (2004)
5. J.-W. Yoon, Ya. Lou, J.H. Yoon, and M.V. Glazoff, Asymmetric Yield Function Based on the Stress Invariants for Pressure Sensitive Metals, *International Journal of Plasticity*, vol.56, pp.184-202 (2014)
6. Jeong-Whan Yoon and Michael V. Glazoff, Development of Plasticity Model Using Non-Associated Flow Rule for HCP Materials Including Zirconium for Nuclear Applications, INL Report # INL/EXT-13-29737, August 2013
7. M.V. Glazoff, S.N. Rashkeev, Yu.P. Pyt'ev, J.-W. Yoon, and S. Sheu, Interplay Between Plastic Deformations and Optical Properties of Metal Surfaces: a Multiscale Study, *Applied Physics Letters*, volume 95, issue 8, article 084106 (August 24, 2009)
8. S.N. Rashkeev, M.V. Glazoff and F. Barlat, Strain Rate Sensitivity Limit Diagrams and Plastic Instabilities in a 6xxx Series Aluminum Alloy Part I: Analysis of Temporal Stress-Strain Serrations, *Computational Materials Science*, vol. 24, pp.295-309 (2002)
9. F. Barlat, M.V. Glazoff, J.C. Brem and D.J. Lege, A Simple Model for Dislocation Behavior, Strain and Strain Rate Hardening Evolution in Deforming Aluminum, *International Journal of Plasticity*, vol.18, pp.919-939 (2002)
10. M. Zaiser and M.V. Glazov, Some Remarks on the Classification of Plastic Instabilities, *Journal of the Mechanical Behavior of Materials (London)*, vol.11, Nos.1-3, pp.243-249 (2000)
11. S.N. Rashkeev, M.V. Glazov and O. Richmond, Irregularities and Modulated Dislocation Patterns in Plastically Deformed Metals: the Eckhaus Instability, *Journal of the Mechanical Behavior of Materials (London)*, vol.10, No.1 (1999), pp.7-30
12. V. Bulatov, O. Richmond and M.V. Glazov, An Atomic Dislocation Mechanism of Pressure-Dependent Plastic Flow in Pure Aluminum, *Acta Materialia*, vol.47/12 (1999) pp.3507-3514

13. M. Zaiser, M.V. Glazov, L.A. Lalli and O. Richmond, On the Relations Between Strain- and Strain-Rate Softening Phenomena in Some Metallic Materials: a Computational Study, *Computational Materials Science*, vol.15 (1999) pp.35-49
14. M.V. Glazov, M.V. Braginsky, L.A. Lalli and O. Richmond, On the Derivation and Analysis of the “Machine Equation” in Finite Deformations, *Applied Physics A (Springer-Verlag)*, vol.67, No.5 (1998) pp.571-578
15. M.V. Glazov and C. Laird, Size Effects of Dislocation Patterning in Fatigued Metals, *Acta Metall. Mater.*, vol.43, No.7 (1995) pp.2849-2857
16. P.C. Clapp, M.V. Glazov and J.A. Rifkin, Dislocation Dynamics and Multiplication via Atomistic Simulations, *Journal de Physique IV*, vol.3 (1993) pp.2005-2014

### **Applied Mathematics and Morphological Analysis**

1. Michael V. Glazoff, Akira Tokuhiko, and Robert Hiromoto, Morphological Analysis of Zirconium Nuclear Fuel Rods Braided with SiC: Quality Assurance and Defect Identification, *Journal of Nuclear Materials* vol. 451, pp. 216-224 (2014)
2. Eric Dufek, Michael V. Glazoff, Lucia Petkovic, and Kevin Gering, “Morphological analysis and evaluation of electrode structures”, *224<sup>th</sup> ECS Meeting*, B10-1194, San Francisco, October 31 (2013)
3. S.N. Rashkeev and M.V. Glazoff, Letter-Report to J. Lehner and J.M. Kerkhoff, Development of the Ginzburg-Landau Theory of Armor Penetration: Brief Discussion of the Initial Theoretical Results and Planned Theory Verification Work in 2008, ATC Internal Report # 08-020, 2008-01-28 (*ITAR Export Controlled*)
4. Michael V. Glazoff and Sergey N. Rashkeev, Advanced Armor, Part II. Hydro-Codes and Modeling of Penetration: Potential Next Steps for the Alcoa Defense Organization, ATC Internal Report # 07-078, May 15, 2007 (*ITAR Export Controlled*)
5. M.V. Glazoff, S.N. Rashkeev, Yu.P. Pyt’ev, J.-W. Yoon, and S. Sheu, Interplay Between Plastic Deformations and Optical Properties of Metal Surfaces: a Multiscale Study, *Applied Physics Letters*, volume 95, issue 8, article 084106 (August 24, 2009)
6. Yu.P. Pyt’ev and Michael V. Glazoff, Development of the New Version of Alcoa Proprietary Software *MorphoSurf* v. 2.0 with Open Architecture: Functionalities for Analysis, Synthesis, and Design of Material Surfaces with required properties, ATC Internal Letter-Report # 07-126, 2007-07-19
7. Yuri P. Pyt’ev, Michael V. Glazoff, and Vyacheslav Markelov, Conventional and Adaptive Morphological Filters for Synthesis of Rolled Aluminum Surfaces with Required Optical Properties and Visual Appearance: a New Approach to a Complex Problem, ATC Internal Report # 07-096, 2007-06-15
8. M.V. Glazoff and Yu.P. Pyt’ev, Correction for Illumination Fall-Off in Optical Image Acquisition for *MorphoSurf* Processing, ATC Internal Letter-Report to J.M. Kerkhoff # 07-036, March 12 (2007)
9. M.V. Glazoff, Yu.P. Pyt’ev, and J.M. Epp, Adaptive Morphological Filtering of Complex Images for Feature Extraction: EDT Steel Rolls and Texture-Rolled Aluminum Alloys Surfaces ATC Internal report # 07-083, 2007-06-02

10. M.V. Glazoff, Advanced Armor. Part I: Metallic Armor – Calculations of Its Protective Ability and Factors that Affect It Under Different Conditions of Impact, ATC Internal Report #06-154, July 30 (2006) (*ITAR Export Controlled*)
11. M.V. Glazoff and Ch. Bailey, Analysis of Numerical Operations in Precipitation Modeling for Bayer Process: Part II. New Algorithms and Results – Robust, Reliable, and Easy to Use, ATC Internal Report #06-255, December 13 (2006)
12. M.V. Glazoff and S.N. Rashkeev, 3D Computer Simulation of Light Scattering from Rough Aluminum Surfaces: a New Functionality of the “*MorphoSurf*”: Alcoa Proprietary Software, ATC Internal Report #05-128. June 21 (2005)
13. M.V. Glazoff, Analysis of Numerical Operations in Precipitation Modeling for Bayer Process: Part 1. Description of Computational Algorithms, ATC Internal Report #05-188, September 07 (2005).
14. M.V. Glazoff, D.E. Coleman, J.M. Epp, and N.C. Whittle, Morphological Analysis of Different Surface Features Using The *MorphoSurf* Software: Standard Operating Procedures. ATC Internal Report No. 04-054, March 22 (2004)
15. M.V. Glazoff, H. Weiland, D.E. Coleman, J.M. Epp, N.C. Whittle, *MorphoSurf*: Computational Platform for Morphological Analysis of Rolled Aluminum Surface Features. Applied Mathematics. ATC Internal report No. 04-027, April 06 (2004)
16. S.N. Rashkeev, M.V. Glazoff and F. Barlat, Strain Rate Sensitivity Limit Diagrams and Plastic Instabilities in a 6xxx Series Aluminum Alloy Part I: Analysis of Temporal Stress-Strain Serrations, *Computational Materials Science*, vol. 24, pp.295-309 (2002)
17. S.N. Rashkeev, M.V. Glazov and F. Barlat, The Eckhaus Instability –a Possible Wavelength Changing Mechanism in the Evolution of Dislocation Patterns, *Computational Materials Science*, vol.21, pp.230-242 (2001)
18. M.V. Glazov and S.N. Rashkeev, Light Scattering from Rough Metallic Surfaces with Superimposed Periodic Structures, *Applied Physics B*, vol. 66(2) (1998) pp.217-223
19. M.V. Glazov, D.R. Williams and C. Laird, Temporal Dissipative Structures in Cyclically Deformed Metallic Alloys, *Applied Physics A (Springer-Verlag)*, vol.64, (1997) pp.373-381
20. M.V. Glazov, Regularized Algorithms of Image Processing and Feature Extraction in Scanning Electron Microscopy, *Proc. 2<sup>nd</sup> Int. Conf. On Inverse and Ill-Posed Problems*. Ed by A.M. Denisov, the University of Moscow (1996), p.69
21. M.V. Glazov (Glazoff), Self-Organization and Spatio-Temporal Dissipative Structures in Fatigued Metals, *Ph.D. Dissertation (Materials Science and Engineering)*, University of Pennsylvania, Department of Materials Science and Engineering (1995)
22. M.V. Glazov and C. Laird, Size Effects of Dislocation Patterning in Fatigued Metals, *Acta Metall. Mater.*, vol.43, No.7 (1995) pp.2849-2857
23. M.M. Eliseeva, M.V. Glazov, Yu.K. Kovneristy and A.I. Landa, Computer Simulation of Structure of Amorphous Metallic Alloys Using Different Modifications of Regularization Technique, *Journal of Melts (Russian)*, vol.4 (1993), pp.62-67
24. V.A. Somenkov, A.V. Irodova, N.A. Palii, V.V. Vavilova and M.V. Glazov, Regularized Algorithms of Diffraction Data Processing for Amorphous Metallic Alloys. II. Neutron Diffraction Data for Amorphous Alloy Re<sub>90</sub>Ta<sub>10</sub>. *Physics of Metals and Metals Science (Great Britain)*, vol.71, No.2 (1991) pp.137-140

25. M.V. Glazov, N.A. Palii and A.S. Krylov, Regularized Algorithms of Diffraction Data Processing for Amorphous Metallic Alloys. I. Description of Regularizing Algorithms and Programs, *Physics of Metals and Metals Science (Great Britain)*, vol.71, No.2 (1991) pp.130-136s
26. M.V. Glazov and T.A. Bolokhova, Solution of the Raleigh's Reduction Problem in Spectroscopy Using Different Modifications of Regularization Technique, *Optics and Spectroscopy (Russian)*, vol.67, No.3 (1989) pp.553-557

### **Phase-Field and Mesoscale Simulations**

1. V. Tikare, Ph. Weck, P. Schultz, B. Clark, M. V. Glazoff, Eric Homer, Milestone 2 Report on Integration of the Hybrid Hydride Model into INL's MBM, Joint Sandia/INL Report, FCRD-UFD-2014-00068 Rev.0, August 2014
2. V. Tikare and M.V. Glazoff, Model for Simulation of Hydride Precipitation in Zr-Based Used Fuel Claddings: A Status Report on Current Model Capabilities, Joint Sandia/INL Report, FCRD-UFD-2014-000068, SAND2013-10834P, August 30 (2013)
3. V. Tikare, J. Scaglione, J. Busby, R. Howard, M.V. Glazoff, and J. Hales, Roadmap for Developing a Computation Tool for Prediction of Hydride Precipitation and Reorientation during Long-Term Dry-Storage, Prepared for U.S. Department of Energy Campaign or Program, FCRD-UFD-2013-000068, SAND2012-10834P, December 15 (2012)
4. M.V. Glazoff, F. Barlat and H. Weiland, Continuum Physics of Phase and Defect Microstructures: Bridging the Gap between Physical Metallurgy and Plasticity of Aluminum Alloys, *Int. J. of Plasticity*, vol.20, #3, pp. 363-402 (2004). This paper was used at MIT, Dept. of Materials Science and Engineering, as "recommended reading" for graduate-level course "Physical Metallurgy" by Professors Russell and Van Vliet in 2003/2004

### **1.5 References to Chapter 1**

1. A. Tokuhiro, Fukushima, LENDIT and Reactor Safety R&D, Seminar at Purdue University, School of Nuclear Engineering, April 23, 2012
2. Joseph Nielsen, Akira Tokuhiro, Robert Hiromoto and Jivan Khatri, Optimization method to branch-and-bound large SBO state spaces under dynamic probabilistic risk assessment via use of LENDIT scales and S2R2 sets, *J. Nucl. Sci. Technol.*, Vol. 51, No. 10, pp.1212–1230 (2014)
3. Gary S. Was, Fundamentals of Radiation Materials Science, Springer -Verlag, Berlin (2007)
4. Robert W. Cahn, The Coming of Materials Science, Pergamon, Cambridge (2001)
5. Michael V. Glazoff, Jeffrey O. Brower, Tammy L. Trowbridge, Marat Khafizov, Analysis of Corrosion of the Dummy "EE" Plate 19 in Type YA ATR Fuel Elements, INL External Report, August 2014
6. Kevin M. McHugh, John E. Garnier, Sergey N. Rashkeev, Michael V. Glazoff, George W. Griffith, and Shannon Bragg-Sitton, "High Temperature Steam Corrosion of Cladding for

Nuclear Applications: Experimental”, *Ceramic Engineering and Science Proceedings* (special volume: Ceramic Materials for Energy Applications III), vol.34, issue 9, pp.149-160 (2013)

7. Veena Tikare, Philippe Weck, Peter Schultz, Blythe Clark, Michael V. Glazoff, Eric Homer, Milestone 2 Report on Integration of the Hybrid Hydride Model into INL’s MBM, Joint Sandia/INL Report, FCRD-UFD-2014-00068 Rev.0, August 2014

8. T. Alam, M.K. Khan, M. Pathak., K. Ravi, R. Singh, and S.K. Gupta, *Nucl. Engin. Design*, vol.241 (2011) 3658

9. P. Hofmann, *J. Nucl. Mater.*, vol.270 (1999) 194

10. M.V. Glazoff, A. Tokuhiro, S.N. Rashkeev, and P. Sabharwall, Zirconium, Zircaloy-2, and Zircaloy-4: Computational Thermodynamics and Atomistic Perspective on Hydrogen Uptake and Oxidation, *J. Nucl. Mater.*, vo.444, pp.65-75 (2014)

11. T. Arima, K. Moriyama, N. Gaja, H. Furuya, K. Idemitsu, and Y. Inagaki, *J. Nucl. Mater.*, vol.257 (1998) 67

12. W.F. Hsieh, J.J. Kai, C.H. Tsai, and X.J. Guo, *Mater. Chem. and Phys.*, vol.50 (1997) 37

13. Samuel Glesstone, Alexander Sesonske, Nuclear Reactor Engineering, XanEdu Publ. (2010)

14. E.E. Lewis, Nuclear Reactor Power Safety, John Wiley & Sons, New York (1977)

15. B. Heuser, G. Was, M. Preuss, M.V. Glazoff, P. Sabharwall, J. Hales, et al., **Funded DOE IRP Proposal (\$3,500,000.00)** by INL, UIUC, University of Michigan, University of Florida, University of Manchester, Engineered Zircaloy Cladding Modifications for Improved Accident Tolerance of LWR Fuel (September 29, 2012)

16. [http://en.wikipedia.org/wiki/Fukushima\\_Daiichi\\_nuclear\\_disaster](http://en.wikipedia.org/wiki/Fukushima_Daiichi_nuclear_disaster)



## Chapter 2 Computational Thermodynamics and *Ab Initio* Atomistic

### Simulations of Zircaloy Oxidation in Hydriding in Normal

#### Working Conditions and In Storage

1. M.V. Glazoff, A. Tokuhiro, S.N. Rashkeev, and P. Sabharwall, Zirconium, zircaloy-2, and zircaloy-4: Computational Thermodynamics and Atomistic Perspective on Hydrogen Uptake and Oxidation, *Journal of Nuclear Materials*, vo.444, pp.65-75 (2014)
2. M. V. Glazoff, Modeling of Some Physical Properties of Zirconium Alloys for Nuclear Applications in Support of UFD Campaign, INL Report # INL/EXT-13-29581 (July 2013)
3. Veena Tikare and Michael V. Glazoff, Model for Simulation of Hydride Precipitation in Zr-Based Used Fuel Claddings: A Status Report on Current Model Capabilities, Joint Sandia /INL Report, FCRD-UFD-2014-000068, SAND2013-10834P (August 30 2013)

### 2.1 Introduction

Zirconium-based alloys zircaloy-2 (Zy-2) and zircaloy-4 (Zy-4) are widely used in nuclear industry as cladding materials for BWRs and PWRs, respectively. Over more than 60 years these materials displayed a very good combination of properties such as low neutron absorption, creep behavior, stress-corrosion cracking resistance, reduced hydrogen uptake, corrosion, and/or oxidation, especially in the case of Zy-4, [1-3]. However, over the last couple of years energetic efforts were undertaken to improve their oxidation resistance during off-normal temperature excursions, as well as to further improve upon the already achieved levels of mechanical behavior and reduced hydrogen uptake [1-3]. In order to facilitate the development of such novel materials, it is very important to achieve not only engineering control, but also scientific understanding of the underlying material degradation mechanisms, both in working conditions and in storage of spent nuclear fuel.

This Chapter strives to contribute to these efforts by constructing the thermodynamic models of both alloys, constructing of the respective phase diagrams, and oxidation mechanisms. A special emphasis was placed upon the role of zirconium suboxides [4] in hydrogen uptake reduction and the

atomic mechanisms of oxidation. To that end, computational thermodynamics calculations were conducted concurrently with first-principles atomistic modeling.

## **2.2 Oxidation and Hydrogen Uptake In Zirconium, Zircaloy-2 and Zircaloy-4: Computational Thermodynamics and Ab Initio Calculations**

Zircaloy-2 (hereafter referred to as Zy-2) was originally developed in order to improve upon the level of corrosion resistance of the zircaloy-1 (i.e., Zr-2.5%Sn) [1-3, 5]. This goal was achieved via the additions of minor amounts of Cr, Ni, and Fe. It was used, with significant success, as the material out of which nuclear fuel retaining rods were fabricated, for the work in boiling water reactors (BWRs) and, to a lesser extent, pressurized water reactors (PWRs). To avoid using very expensive “iodide” zirconium, zirconium sponge was recommended for alloying purposes; the Zy-2 chemical composition and the maximum level of allowable impurities (specified for reactor-grade material), are presented below [1, 6]:

Zy-2: Zr (1.2-1.7) %Sn (0.07-0.2) %Fe (0.03-0.08) %Ni (0.05-0.15) %Cr. The following level of impurities is allowed for Zy-2: Al -0.0075%; B – 0.00005%; C -0.0270%; Cd – 0.00005%; Co: 0.0020%; Cu -0.0050%; H – 0.0025%; Hf – 0.0200%; Pb – 0.0130%; Mg – 0.0200%; Mn – 0.0050%; N -0.0080%; Na -0.0020%; Si -0.0120%.

The principal goal of these alloying elements in Zy-2 was to neutralize the detrimental effect on corrosion resistance of the impurities, especially —nitrogen, aluminum, and carbon, [1, 6]. However, this alloy had the hydrogen uptake higher than the level required for work in pressurized light water reactors, [1]. It is mostly for this reason that the Zy-4 alloy was developed, [1]. The principal thought was to eliminate nickel as it demonstrated the highest

ability to serve as a hydrogen getter. Consequently, its alloy composition window was selected as follows:

Zy-4: Zr (1.2-1.7 )%Sn (0.18-0.24) %Fe (0.07-0.13) %Cr., [7]. As a result, the hydrogen uptake was reduced almost by a factor of four.

One important issue which did not receive attention in the literature is this: what does the expression “hydrogen uptake” actually mean? Is this the amount of hydrogen that could be dissolved in the Zr-based solid solution at a given temperature, or the overall hydrogen distributed among solid solution, precipitates of second phases (typically  $Zr_2M$ , C1\_FCC, and hexagonal C14 Laves phases [8, 9]), and the hydride phase? If the former definition is correct, then the hydride solvus curve should be different for Zy-2 and Zy-4 as a function of temperature. If, on the other hand, the term “hydrogen uptake” is related to the rate of sorption of hydrogen in a given alloy, then one needs to understand the mechanism of such adsorption impediment for Zy-4.

The issue of hydrogen is closely connected to that of zirconium alloys oxidation. As it will be demonstrated below with atomistic simulations, the formation of certain oxygen bearing zirconium compounds, especially monoclinic  $ZrO_2$  and suboxide  $Zr_3O$  [10-12], at the interface “cooling water –alloy surface” is critical to preventing hydrogen pickup. Under normal working conditions the primary source of hydrogen is radiolysis of water. Under catastrophic temperature excursions above 800°C, zirconium will be oxidized by water forming  $ZrO_2$  and hydrogen. We will be concerned mostly with the conditions realized during spent nuclear fuel storage, so the temperature range of interest will be below 400°C.

In general, zirconium is thermodynamically unstable with respect to its oxidation process even at room temperatures [13, 14]. The necessary condition for the  $ZrO_2$  formation is that the

partial pressure of  $O_2$  must be higher than the dissociation pressure of the  $ZrO_2$  at a given temperature, [13]. Since this condition is satisfied even in deep vacuum, there will always be a thin layer of oxide on the surface, of the order of 2nm to 5nm. Another source of potential problems is the metastability of Zr and its alloys with respect to oxidation by fresh and/or spent nuclear fuel,  $UO_2$ , [14].

Consequently, in this paper a research effort was made to understand the following issues: (1). Construction of self-consistent thermodynamic models of hydrides for pure Zr, Zy-2, and Zy-4; (2). Understanding the phase equilibria and thermodynamic properties in the Zr-O system and interaction of Zy-2 and Zy-4 with oxygen, paying special attention to the role of zirconium suboxides in the overall reduction of hydrogen pickup; (3). Elucidating the role of microstructure in the reduction of hydrogen uptake; and (4). Providing specific recommendations on safe dry storage of spent nuclear fuel (SNF).

This Chapter is organized as follows. In Section 2, the employed computational methods, i.e., first principles atomistic simulations and computational thermodynamics of materials are described. Section 3 describes the equilibrium aspects of hydride formation in pure Zr, Zy-2, and Zy-4. Section 3 is devoted to the Zr-O system, its thermodynamic properties and phase equilibria. Special emphasis was made upon the protective role of  $Zr_3O$  in reducing the hydrogen uptake in Zr and its alloys. In Section 4 conclusions and recommendations for future research are provided.

## 2.3 Computational Methods

In this work, *ab initio* first-principles, density functional theory (DFT) – based calculations and computational thermodynamics of materials (CALPHAD approach) were used. Their brief descriptions are given below.

### 2.3.1 *Ab Initio Calculations*

The supercell total energy calculations were based on the generalized gradient approximation (GGA) for exchange and correlation, and plane waves [15]. We used the GGA functional of Perdew, Burke, and Ernzerhof (PBE) [16], which gives good results for chemisorption of molecules on transition-metal surfaces and similar processes. Projected Augmented Wave (PAW) scalar relativistic pseudopotentials [17, 18], and the VASP code [19] were used. The energy cutoff for the plane-wave basis was set at 500 eV, and all integrations over the Brillouin zone were done using the Monkhorst-Pack scheme with four  $\mathbf{k}$  points in the relevant irreducible wedge [20]. Inclusion of additional  $\mathbf{k}$  points was found to have minimal effect on the total energy differences of interest.

We used two hcp supercells containing 54 atoms (3 x 3 x 3 hcp unit cells) and 200 atoms (5 x 5 x 4 unit cells). For each supercell, we relaxed all the atomic positions until the quantum-mechanical force on each atom became smaller than 0.02 eV / Å. Activation barriers were calculated using the nudged-elastic-band method [21].

### 2.3.2 Computational Thermodynamics of Materials

The goal of computational thermodynamics is to establish a bridge between phase equilibria and thermodynamic properties of materials. To achieve that, one needs the conditions of equilibrium, as well as certain models for all solid, liquid, and gaseous phases participating in

a given equilibrium. Even if such models are reliable and physically consistent, the problem of global optimization of the system free energy has to be solved. In turn, such problems require that significant computational power and efficient optimization algorithms are available to the researcher.

All of these conditions started to be realized in the beginning of the 1980s. Mats Hillert in Sweden (KTH) [22] supervised the development of the ThermoCalc and DICTRA software. Also, Hillert made very significant contributions to a number of useful thermodynamic models (theory of sub-lattices [22], energy compound formalism, the concept of para-equilibrium, etc. [22]). Other models were developed for different types of systems, including model of ionic liquids used in this work. Lukas et al. [23], Saunders and Miedownik [24] developed the generalized equilibrium conditions, (software BINGGS for binary systems). Liu used first-principles approach to obtain data necessary for thermodynamic simulations, [25]. Similar work developed, concurrently and independently, in Canada (Prof. A.D. Pelton and software FactSage) and in the US (the late Prof. Austin Chen, software PANDAT). As a result, it became possible to provide self-consistent descriptions of phase equilibria in multi-component systems and thermodynamic properties of materials [22].

In this work, commercial databases for zirconium alloys TTZR1 (ThermoTech Ltd.) and Binary alloys TCBIN (ThermoCalc AB) were used. These databases and the ThermoCalc ver. S software were used to generate data on the thermodynamic properties of hydrides, in particular, partial molar enthalpy and entropy of hydrogen. The obtained results were consistent with the constructed phase diagrams and property diagrams. All results were critically evaluated in light of the existing experimental data.

## 2.4 Results and Discussion

### 2.4.1. Zirconium Hydrides and Hydriding of Pure Zr, Zy-2, and Zy-4

The formation of hydrides and the problem of hydriding were studied very extensively, [1-3, 26, First principles calculations of the equilibrium crystalline lattice parameters, free energy of formation at different temperatures, and the phonon density of states were discussed by Blomquist and by Zhu et al., [35, 36]. A detailed overview of the problem of hydrogen solubility in Zr and its alloys was provided by Anghel [13]. The principal reason of this interest is that the formation of zirconium hydrides may cause such undesirable phenomena as hydrogen embrittlement and reorientations of hydride blisters during storage and transportation phase of spent nuclear fuel storage, [37-45]. Consequently, efforts were made to reduce hydrogen uptake via changes in alloy chemical composition, development of different coatings, thermo-mechanical treatments optimizing alloy microstructure (size distribution and number density of second phase particles, or SPPs) etc. [13], This becomes even more critical given new requirements to higher degree of burn-up of nuclear fuel, both in BWRs and PWRs (in the latter case –from older value of below 45 MWd/kgU and up to 60 MWd/kgU (HBU case), [46].

Zhang and Norton [47] have concluded that the maximal hydrogen uptake sites are located on grain boundaries and/or interfaces that facilitate heterogeneous nucleation of hydride compounds. Hydrogen tends to segregate to surfaces and interfaces (grain boundaries, cracks and other defects) in Zr. These hydrogen-rich areas are possible nucleation sites for hydrides. Moreover, oxygen in the  $\alpha$ -Zr matrix facilitates hydrogen segregation to the surfaces, [47]. Understanding the role of the different zirconium oxides and suboxides in the reduction of hydrogen uptake was the most important goal formulated in this study.

The equilibrium crystalline structures of hcp-Zr and its three hydrides are depicted in Figures 1 and 2, respectively. In all cases, the equilibrium lattice parameter(s) were determined by total energy relaxation technique of the lattice parameters and corresponding atomic positions.

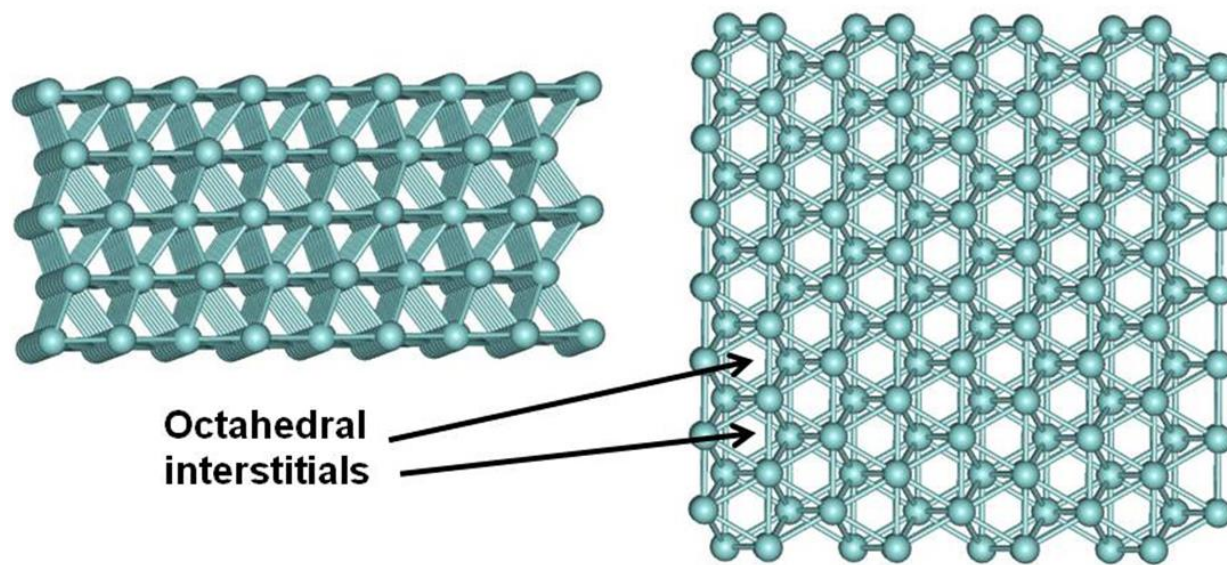


**Figure 1** Hexagonal (hcp) Zr structure (different views): (a) in the direction perpendicular to the (0001) axes; (b) in the direction of the (0001) axes. Zr atoms are shown in cyan color; octahedral interstitials are indicated by arrows.

The low-temperature  $\alpha$ -phase of Zr has hcp structure characterized by the 2/1 ratio of tetrahedral and octahedral interstitial positions per unit cell. The lattice parameters were determined in this work as  $a = 3.2276 \text{ \AA}$  and  $c = 5.1516 \text{ \AA}$ , space group P63/mmc, see Figure 1.

The transport properties (diffusion) of hydrogen and oxygen atoms in Zr are directly related to relatively large interstitial space that could be occupied by these atoms which are nearly “free” energetically there. Figure 2 shows the relaxed atomic structures for the equilibrium positions of O and H atoms in the Zr hcp structure. Oxygen always goes into octahedral interstitials because any other possible location will inevitably damage the Zr



crystalline network and cause local rearrangement of Zr atoms. Neutral hydrogen atoms may also go into octahedral interstitials (interaction energy of H atom with Zr network is below 0.1 eV, i.e., almost negligible). However, it can also position itself in the middle of Zr-Zr bonds. In the latter case, hydrogen damages the Zr network by forming asymmetric Zr-H-Zr bridges or even attaching itself to only one Zr atom and leaving dangling bond defect at another Zr atom. However, this “damage” is not that significant as it would be if oxygen atom were placed in a similar position – the energy of Zr-H-Zr configuration is only 0.5 eV higher than that of the interstitial configuration. It means that although H would energetically prefer to be located at an interstitial position, metastable Zr-H-Zr configurations are also possible if the process is driven kinetically.

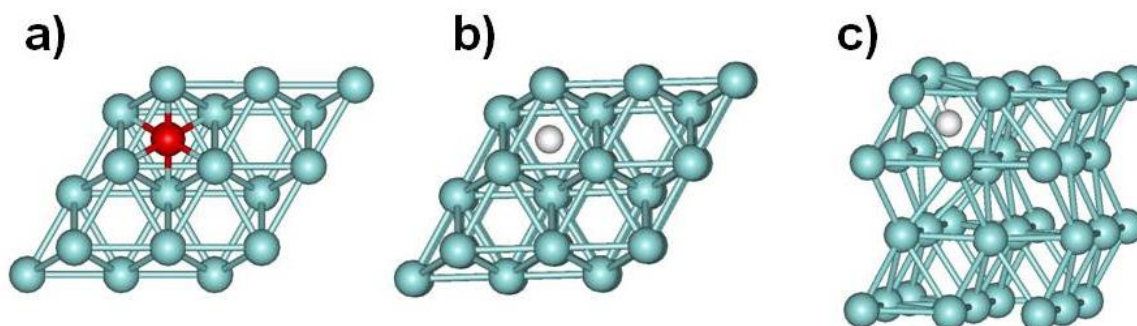


**Figure 2** Positions of single oxygen and hydrogen in hexagonal (hcp) Zr structure: (a) O in the octahedral interstitial; (b) H in the octahedral interstitial; (c) H in the middle of the Zr-Zr bond. Zr atoms are shown in cyan, oxygen – in red, hydrogen – in white.

There are three distinctly different types of zirconium hydride structures described in the literature:  $\gamma$ -ZrH;  $\delta$ -ZrH<sub>1.66</sub> (which was modeled in this work as ZrH<sub>1.5</sub>) and  $\epsilon$ -ZrH<sub>2</sub> [35]. In Figure 3 we present the results of our first-principles calculations yielding the three energy-relaxed crystal lattice structures.

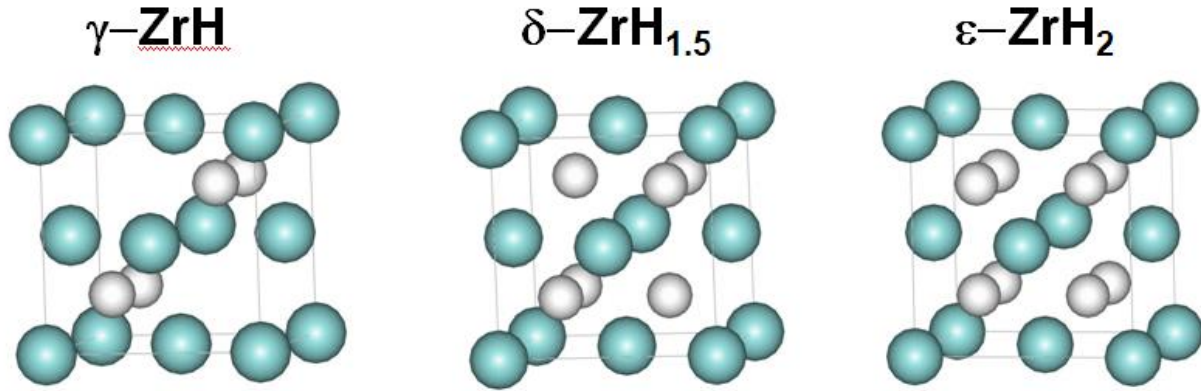


**Figure 3** Relaxed crystalline structures of the three experimentally observed hydrides of zirconium: orthorhombic  $\gamma$ -ZrH ( $a=4.592 \text{ \AA}$ ;  $c=4.492 \text{ \AA}$ ); cubic  $\delta$ -ZrH<sub>1.5</sub> ( $a=4.775 \text{ \AA}$ ) and tetragonal  $\epsilon$ -ZrH<sub>2</sub> ( $a=4.999 \text{ \AA}$ ;  $c=4.433 \text{ \AA}$ ).

The space groups of these hydrides are Cccm; Fm3m; and I4/mmm, respectively. It can be seen that very minor lattice distortions caused by the hydrogen atoms result in the change of the symmetry group(s) and in the value(s) of the lattice parameter(s) as one moves from one hydride to another. These results were obtained using a standard energy minimization procedure and agree well with the existing experimental data.

In Figure 4 the results of our thermodynamic modeling of the Zr-H phase diagram are presented and compared to the existing literature data, [48].

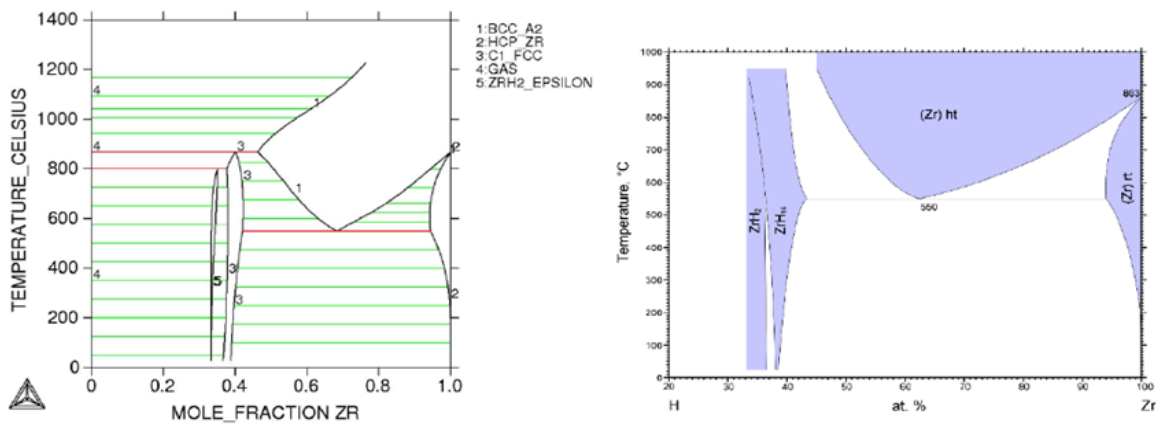


**Figure 4 (a)** Calculation using ThermoCalc; **(b)** experimental phase diagram [48]

Both diagrams agree well in establishing the phase fields of the  $\delta$ - and  $\epsilon$ -hydrides with homogeneity ranges on the basis of the stoichiometric compounds  $\text{ZrH}_{1.5}$  (experimentally established value is  $\text{ZrH}_{1.66}$ , [35]).

The values of the Gibbs free energy computed at  $T=800$  K are illustrated by Figure 5; these values lie in the range from  $-20,000$  J/mol to  $\sim 8,000$  J/mol. This reference range will be useful when we discuss existing data on partial molar enthalpy of hydrogen in different zirconium alloys, as well as for determining the driving forces of hydride formation, - the corresponding look-up tables could be used for phase-field calculations of zirconium hydride microstructure evolution.

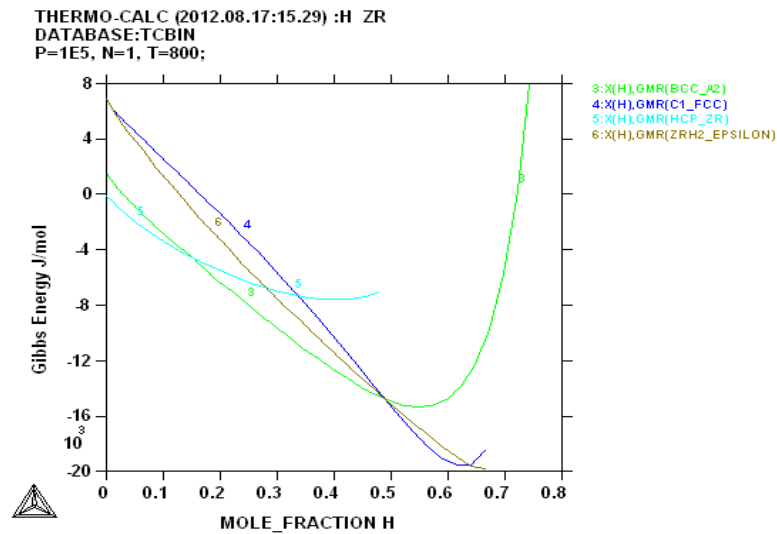


**Figure 5** The Gibbs free energy of the several co-existing phases in the Zr-H system as a function of the hydrogen mole fraction at 800 K.

The zoomed-in diagram for the hydrogen mole fraction varying from 0 to 0.1 is given in Figure 6. It provides an estimate of the hydride dissolution temperature as  $550^{\circ}\text{C}$  corresponding to  $\sim 0.054$  mole fraction of hydrogen. Also, a distinctive feature of this diagram is the retrograde

solubility above 550°C, with a minimum corresponding to ~600°C. Again, these results correspond well to the existing experimental data [28, 30, and 48].

Proceeding in a similar way, we constructed the quasi-binary Zy-2 – hydrogen and Zy-4 –hydrogen property diagrams. Sometimes such diagrams are called isopleths as they correspond to the case of constant sum of concentrations: ( $n_{Zr} + n_H = \text{const}$ ), thus allowing to vary the hydrogen concentration at the expense of zirconium, the principal alloying element.

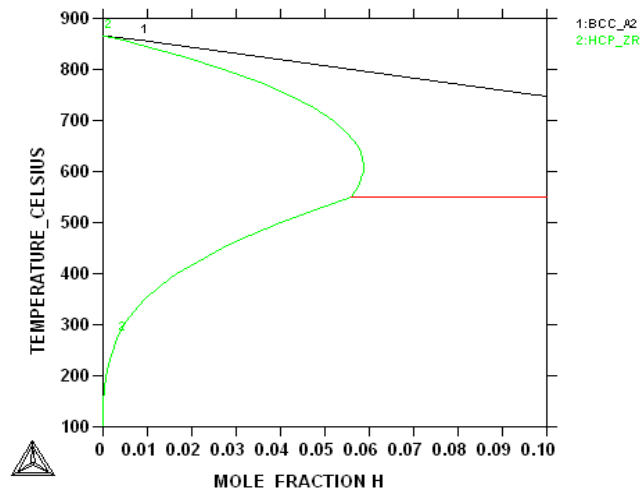


**Figure 6** Fragment of the diagram in Figure 4(a) for low values of  $n_H$

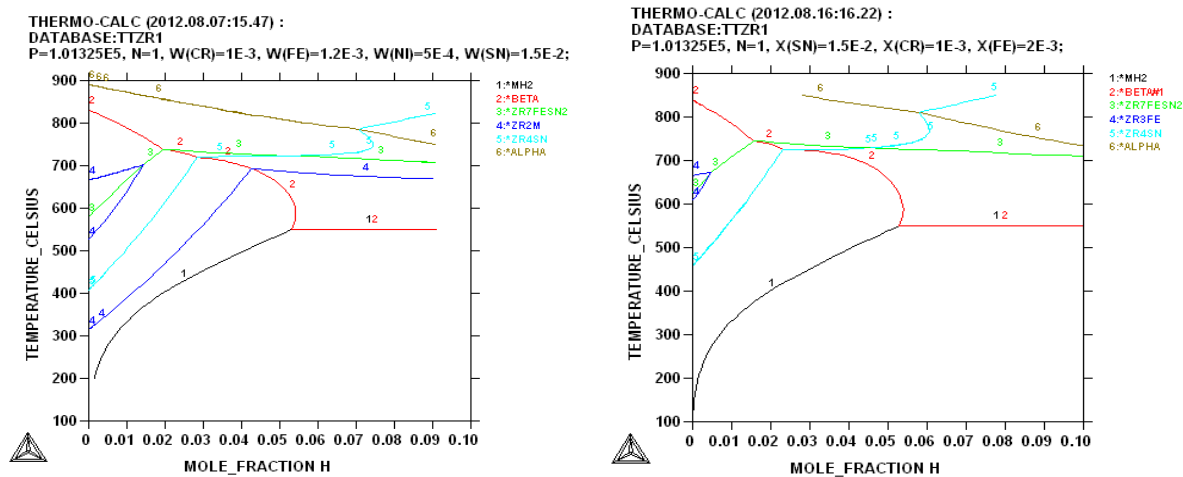


**Figure 7** (a) Hydrogen isopleth for zircaloy-2; (b) Hydrogen isopleth for zircaloy-4

It is important to mention that in both equilibrium diagrams there are such phases present as  $Zr_4Sn$ ,  $Zr_7FeSn_2$ , and  $Zr_3Fe$ , in addition to  $Zr_2M$  and hydride phase. However,  $Zr_4Sn$  and  $Zr_3Fe$  were never discovered in the equilibrium microstructure of both alloys.

Experimentally, microstructural characterization of alloy Zy-4 was conducted by Vandersande and Bement [49]. These researchers identified the second phase particles in an annealed Zircaloy4 sample to be primarily the hexagonal, Laves-phase C14  $Zr(Fe, Cr)$ , type. Krasevec [50] found both hexagonal and fcc Zr- and Cr-bearing precipitates, in an annealed Zy-2 sample. Mukhopadhyay et al. [51] observed fine precipitates of the two types: cubic  $Zr_2(Cr, Fe)$  with a hexagonal C14 type structure (structural type  $MgZn_2$ ) and the cubic C15-structure (prototype  $MgCu_2$ ).

Rao and Bangaru [52] studied the microstructures of heat treated samples of Zy-4 to understand the microstructural basis of nodular corrosion. These workers used samples annealed from the beta-phase field, as-received, and samples with microstructure on the basis of the alpha-Zr. It was established that the first group of the samples possessed the best corrosion response. An advanced synchrotron study of second-phase particles (SPPs) in bulk zirconium alloys was conducted recently by Erwin et al., [53].

The list of equilibrium phases that can be taken into consideration in the TTZR1 database includes both the hexagonal C14 Laves phase and the C15 cubic phases, but these phases were not observed in the equilibrium calculations conducted in this work.

The presence of the several compounds not found in experimental phase diagrams poses a question: should we determine the hydrogen solubility from these diagrams, or from metastable diagrams in which such phases as  $Zr_3Fe$ ,  $Zr_7FeSn_2$ ,  $Zr_4Sn$  get the status of “suspended”? We studied both possibilities. In fact, as far as the hydride solvus and the temperature of hydride

dissolution reaction are concerned, we get results almost identically similar to those for the pure Zr-H phase diagram. The temperature of the hydride dissolution reaction was 551°C for Zy-2 and 552°C – for Zy-4. Given the experimental error in determining the temperature of phase transformation is of the same order, we can conclude that these results are identical.

On the other hand, if we construct metastable phase diagrams as described above, then the highest solubility point (for hydrogen in Zr) shifts toward lower values, i.e., for both alloys ~0.034 hydrogen mole fraction. The temperature of the non-variant reaction remains the same, i.e., ~550°C.

This latter assumption contradicts the experimental evidence presented in [28] and in [30] that the equilibrium solubility maximum for Zr, Zy-2, and Zy-4 remains practically the same. In our calculations, it was around 0.058 hydrogen mole fraction for pure Zr; 0.056 – for Zy-4; and 0.054 – for Zy-2.

The thermodynamic properties evaluation for the Zr-H system was limited to the partial molar enthalpy of hydrogen in the alpha- and beta-phases. This property is very sensitive to the formation of different complexes and tendency to atomic ordering or segregation. Besides, it was evaluated experimentally and reported in at least two articles [30, 54, and 55].

The partial molar enthalpy of hydrogen in the binary Zr-H system was assessed according to the well-known expression [22]:

$$H_H = H_m + \left( \partial H_m / \partial x(\text{Zr}) \right)_{T,P} - x(\text{Zr}) \cdot \left( \partial H_m / \partial x(\text{Zr}) \right)_{T,P} \quad (1)$$

In expression (1),  $H_m$  stands for the molar enthalpy of the system;  $x(\text{Zr})$  represent the molar fraction of zirconium, and  $H_H$  is the partial molar enthalpy of hydrogen for different phase fields of the diagram at 650°C

The values of partial molar entropy of hydrogen were calculated using the following expression:

$$S_H = -\frac{\partial \mu(H)}{\partial T} \quad (2)$$

In expression (2) the chemical potential of hydrogen,  $\mu(H)$ , is assessed with respect to its references state [22].

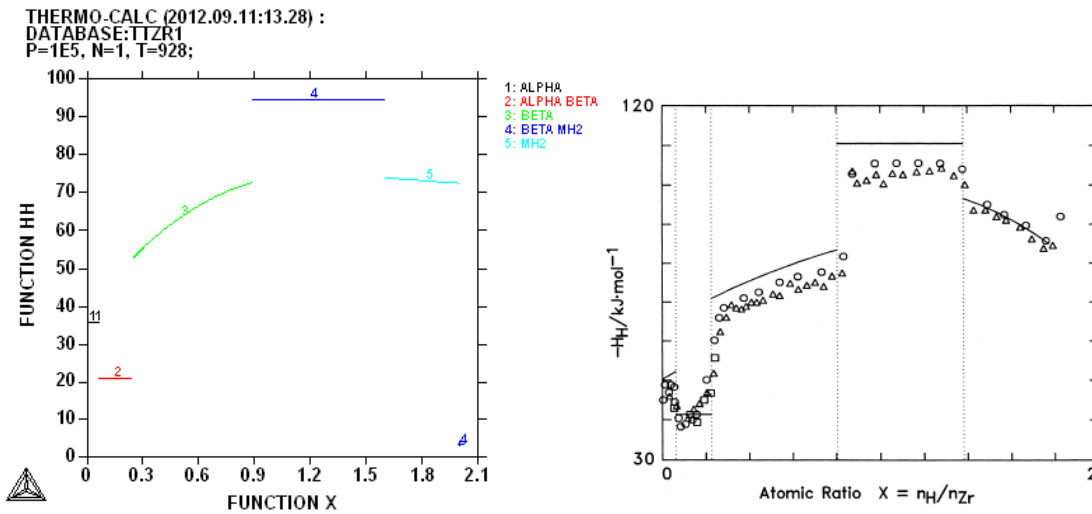


**Figure 8** Partial molar enthalpy of hydrogen in different phases as a function of the  $x(\text{H})/x(\text{Zr})$  and its comparison to experiment [54] and the results of thermodynamic computations in [55]

The agreement between our results and the results reported in [54, 55] is quite good. At the same time, the experimental results reported in [30] give values of  $H_H$  one order of magnitude lower. For example, it was reported that for pure Zr, at temperature 650°C,  $H_H$  is

around -260 kJ/mol. These results are different from the ones reported in [54] and in this study. The most probable source of the discrepancy for partial molar enthalpy (and entropy, see below), is the choice of a different standard state for hydrogen in [30]. As stated in [30] on page 318, these quantities have been defined "referring to the standard state of hydrogen atoms at rest in a vacuum", whereas molecular hydrogen gas is used as the standard state in the present paper<sup>3</sup>.

For alloys Zy-2 and Zy-4 somewhat lower values were obtained in [30]: -250 kJ/mol for Zy-4; and 240 kJ/mol for Zy-2. In this work, it was problematic to conduct the assessment of thermodynamic properties because of the presence of equilibrium phases that were not observed experimentally in past work.

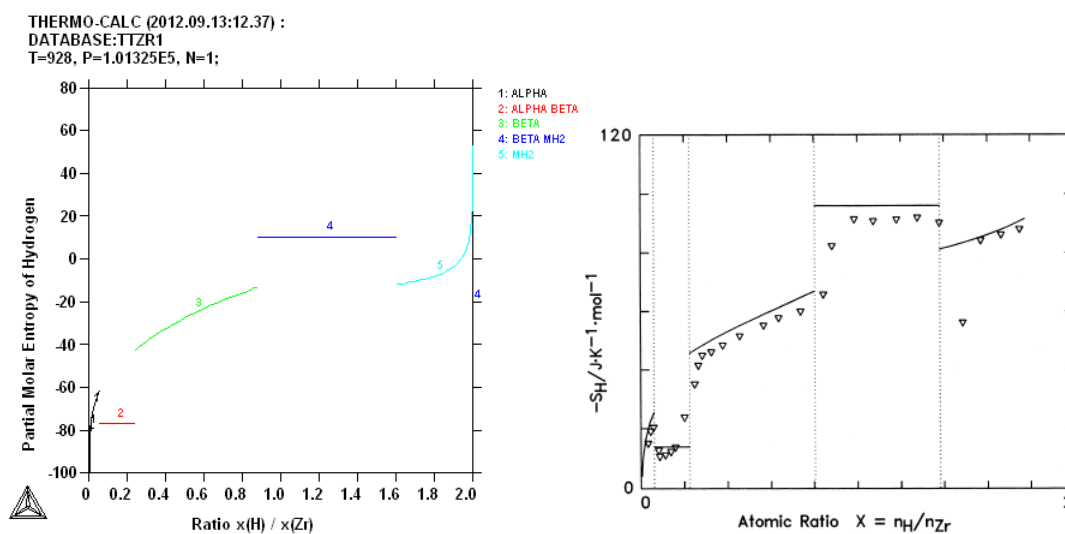


**Figure 9** Partial molar entropy of hydrogen: comparison of the results of modeling (left) and experimental data [16]; black solid line –the results of thermodynamic assessment in [55] and experimental work [54]

The results for partial molar entropy of hydrogen are presented in Figure 9 below. There is a qualitative agreement between the experimental data reported in [54] and our calculations.

<sup>3</sup> The authors are very grateful to the Referee of this paper who had brought this argument to our attention.



There is a significant shift in the absolute value of  $(-S_H)$ . However, partial molar entropy, being a second derivative of the Gibbs free energy with respect to concentration and to temperature, is notoriously unstable with respect to small errors in the input experimental information. Suffice it to say that in [23] the *values of different sign* were reported for the partial molar entropy of hydrogen of the alpha-phase. This implies only that the reassessment of the Zr-H diagram should be done to get a better agreement for nuclear Zr-bearing alloys.

#### 2.4.2. Oxidation

Zirconium-based alloys represent the main structural materials used in light water cooled nuclear reactors (PWRs and BWRs). For these materials, the formation of a thin oxide layer with long-term kinetic stability in working reactor conditions is very important [1]. A detailed study of the diffusion of oxygen in zirconium was published by Cox [56].

When atoms of hydrogen or oxygen occupy interstitial lattice positions between atoms of a zirconium, they form solid solution(s). In the case of oxygen, its solubility in zirconium is quite large, about 29 at.% at ambient temperature [57]. This is a consequence of the relatively large size of the octahedral sites in the hcp lattice, see Figure 1. These 29 atomic % of oxygen approximately correspond to filling from 1/4 to 1/3 of interstitials in each layer of the hcp structure. One could expect that when this critical concentration of dissolved oxygen is reached, oxygen atoms and remaining interstitials will start to form some ordered structures which results in significant reconstruction of hcp network and the onset of zirconium oxide formation. This is indeed the case [4, 58-60], and the significance of such order-disorder transformations for the reduction of hydrogen uptake will be discussed below.

There are several crystallographic modifications of  $\text{ZrO}_2$ . One is monoclinic, with the space group  $P2_1/c$  and four atoms per unit cell. The lattice parameters (in Å) are  $a = 5.1501(2)$ ;  $b = 5.2077(2)$ ; and  $c = 5.3171(2)$ . It does not have oxygen deficiency, i.e., the monoclinic modification is stoichiometric. This is the low temperature modification of  $\text{ZrO}_2$  present in nature as a rare mineral called *baddeleyite*. Tetragonal modification is characterized by the space group  $P4_2/nmc$ , [60] and lattice parameters  $a=3.6067$  Å;  $b = 3.6067$  Å; and  $c = 5.1758$  Å, [61]. The occupancy factor for oxygen atoms in it is  $\sim 0.984(4)$ . This implies that tetragonal modification  $\text{ZrO}_{2-\delta}$  has oxygen deficiency  $\delta=0.031(7)$ . It is for this reason that stabilization of zirconia is necessary with lower valence oxides such as  $\text{Y}_2\text{O}_3$ . Finally, there is a cubic zirconia modification, FCC\_C1, with space group  $Fm-3m$ , and lattice parameter  $a = 5.09$  Å. The experimental and calculated Zr-O phase diagrams are presented in Figure 10 below.

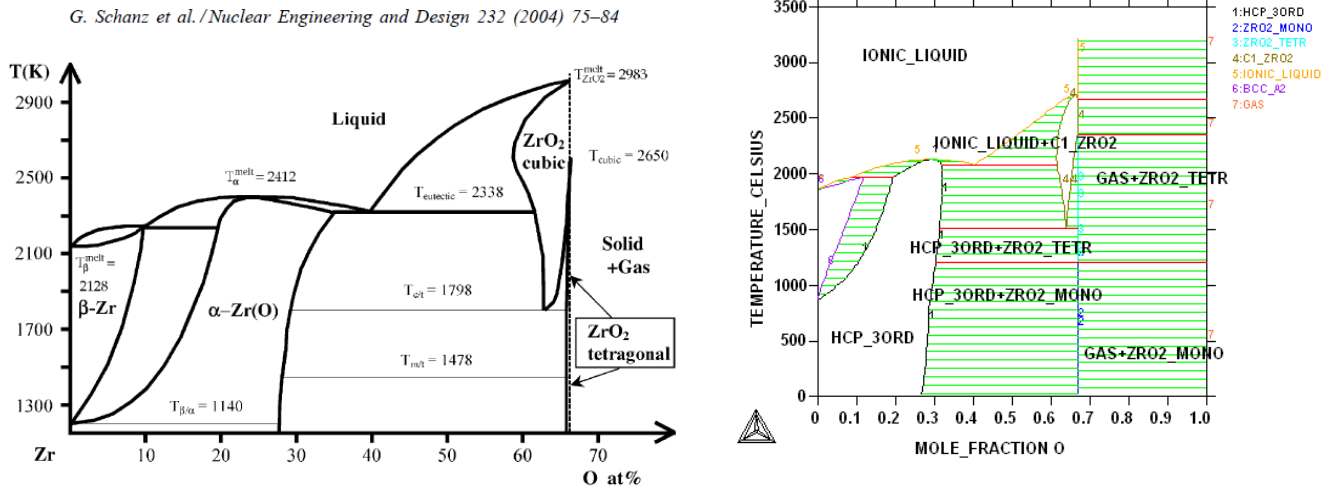
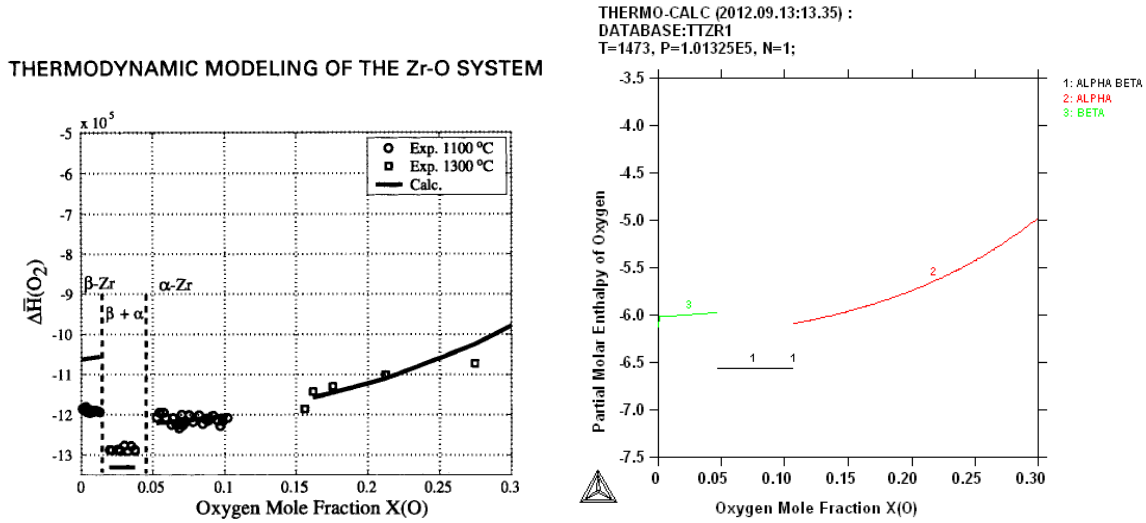


Fig. 5. Binary phase diagram Zr-O, assessed in (Abriata et al., 1986).

### Figure 10 Experimental [57] and computed phase diagram Zr-O

We computed this phase diagram with the ThermoCalc software and using the TTZR1 and TCBIN databases by ThermoTech Inc. and ThermoCalc AB, respectively. It can be seen that

there is practically one to one correspondence between the two diagrams. It should also be noted that the model of ionic liquids was used in this work to represent the behavior of the liquid phase. The results of calculation of the partial molar enthalpy of oxygen in different phases at 650°C are presented in Figure 11.



**Figure 11** Partial molar enthalpy of oxygen: experimental data [62, 63], the results of assessment in [64], and the present work

This last calculation is a good test for the physical sense of the model. Indeed, the partial molar enthalpy of the beta-phase is higher than that of the (alpha + beta) phase field. As it was demonstrated in [64], if Henry's law is followed for the beta phase, then the following relation must hold up to the point of maximum oxygen solubility (saturation):

$$\mu(O)_{\beta} = \mu(O)_{\beta/\alpha} + RT \ln \left( \frac{x(O)}{x(O)_{sat.}} \right) \quad (3)$$

Then, for the partial molar enthalpy of oxygen within the beta phase we will get [64]:

$$\bar{H}_{O_2, \alpha} = \frac{2 \frac{\partial \mu(O)_{\beta/\alpha}}{\partial T}}{\partial (1/T)} = \bar{H}_{O_2, \beta/\alpha} + 2RT^2 \frac{dX_O/dT}{X_O}$$

Looking at the experimental and computed phase diagram of the Zr-O system, we observe that  $dX_O / dT > 0$ , i.e., the partial molar enthalpy of oxygen for the (beta + alpha) region must be smaller (more negative) than that of the alpha-region, [64].

As described in literature, two distinct corrosion periods have been observed for Zr, pre-transition and post-transition [1]. The pre-transition period is characterized by a decreasing corrosion rate and an adherent, protective film with a shiny black appearance. During the post-transition period a constant but greater corrosion rate was observed, and a less protective film formed that had a white flaky appearance. The time required to reach transition is both temperature and time dependent [1].

This change in coloration could serve a possible qualitative indicator of the undesirable transition from  $ZrO_2$  to  $Zr(OH)_4 \cdot nH_2O$ . Indeed, in the precious and semi-precious stone industry a process of blackening of metallic zirconium is described, which results in beautiful shiny black coloration [65]. The raw piece is made of pure zirconium, which is then subjected to heating in a controlled oxidizing atmosphere. During this process the color changes to bronze, then to blue, then to yellow and other colors as the heat-up continues according to a prescribed thermal schedule. The initial very pure blue color is caused by the constructive interference of the light waves. As the process continues, the continuing oxidation results a second order of colors that is formed over the first, and so on. Eventually, as the oxide layer gets thicker, shiny black surface appears. These changes in coloration could be explained similar to an earlier effort by the authors to describe omni-directional coloration of metals via light scattering from textured metallic surfaces, [65]

On the other hand, hydroxides of  $\text{Zr}(\text{OH})_4 \cdot n\text{H}_2\text{O}$  are more flaky and white, [66]. This provides a possibility to measure the degree of oxidation of the underlying Zr-alloy nuclear rod using a photo colorimeter.

While the phenomenon of zirconium oxidation / corrosion is very complex, the factors affecting it have been studied extensively. In particular, it is known [1] that *impurities* such as nitrogen, carbon, and aluminum have a pronounced deleterious effect on the corrosion resistance of Zircaloy-2.

*Heat treatment and irradiation* also affect corrosion of Zr quite substantially [13]. Detailed synchrotron studies of SPP precipitation and dissolution as a function of irradiation dose were reported in [67, 68] For example, Rudling and Wikmark established that there is an optimum range for size distribution and composition of SPPs, which is correlated with the exposure conditions. They reported optimum size distributions for SPPs in the range of approximately 25-175 nm for BWR conditions. Optimum SPP Fe/Cr ratios of 0.6-1.2 and Fe/Ni ratios of 0.9-1.0 have also been found [69].

*Porosity development* in the oxide layers generates easy diffusion pathways for molecules during oxidation [13]. A significant contribution of molecular oxygen to total oxygen transport in zirconia has been observed at temperatures up to 800°C. Effective pore sizes in the nanometer range were found for pre-transition oxides on Zircaloy-2. Inward oxygen transport can be enhanced by the Fe-containing second phase particles, which promote the dissociation of oxygen. These results suggest furthermore that a proper choice of the second-phase particles composition and size distribution can lead to the formation of dense oxides, which are characterized by low oxygen and hydrogen uptake rates during oxidation.

Concerning *oxygen diffusion via grain boundaries*, differences of several orders of magnitude between grain boundary conductivity and the conductivity inside the grains have been reported (grain boundary diffusion  $\gg$  diffusion via/in grains) [13, 70]. For oxide scales grown on Zr-based alloys at temperatures around 400°C, two crystallographic phases of zirconia have been reported: monoclinic and tetragonal. The monoclinic phase is stable at low temperatures and is, as expected, the dominating phase in the oxide scale (see our computed Zr-O phase diagram in Figure. 10). The tetragonal phase can also be found close to the oxide/Zr(O) interface (stabilized by the high compressive stress and grain size  $< 30\text{nm}$ ) and within the oxide scale near the interface between the partially oxidized intermetallics and the bulk oxide. It is important that the oxygen vacancy concentration in zirconia is higher in the tetragonal phase (2-3 mol %) than in the monoclinic phase ( $< 2$  mol %), thereby allowing for enhanced oxygen transport in the former. The tetragonal  $\rightarrow$  monoclinic phase transformation takes place with a volume increase of about 7% and has a significant impact on the corrosion behavior of Zr-based alloys [71]. Using the JMatPro v.7 software package (and thermodynamic database for zirconium alloys, the TTZR1, this effect was confirmed below, Figure 12.

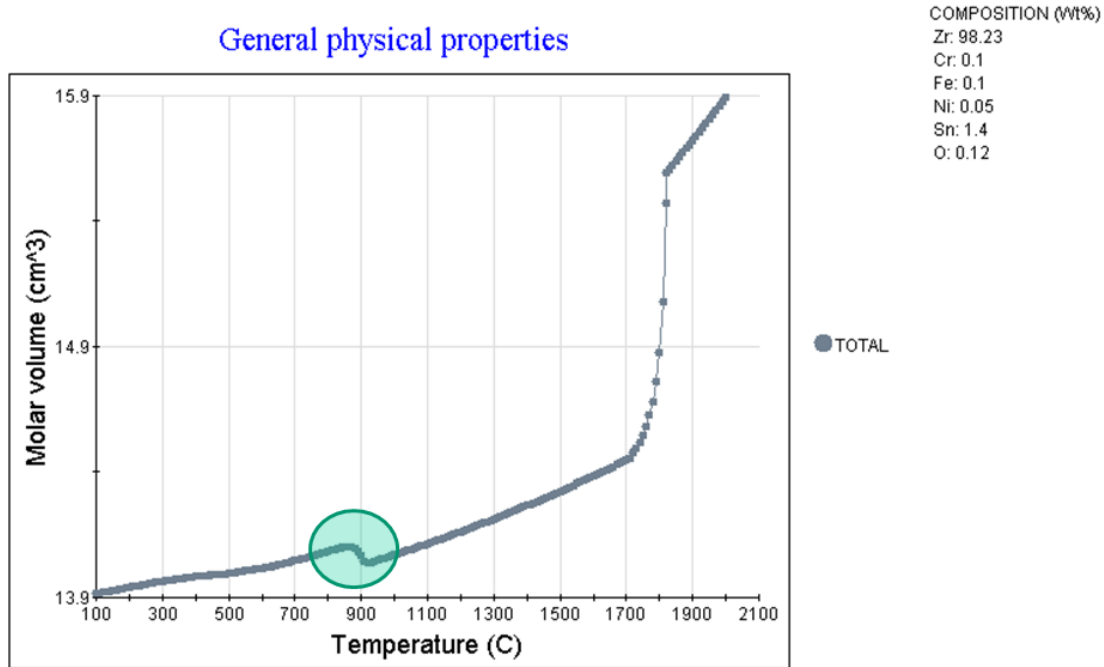


**Figure 12** Molar volume of zircaloy-2 as a function of temperature

In [72], it was established that the second-phase particles, or SPPs, have a high affinity for hydrogen and act as short-circuit pathways for hydrogen transport through the oxide protective layers. Hydrogen can easily diffuse through these thin oxide scales via metallic SPPs. Depending upon a given alloy's chemical composition, its phase composition might be quite different. Again, using the JMatPro v.7, the following temperature dependencies of the alloy phase compositions were obtained for zircaloy-2, zircaloy-4, ZIRLO<sup>TM</sup>, and M5<sup>TM</sup>, see Figures 13 to 16.

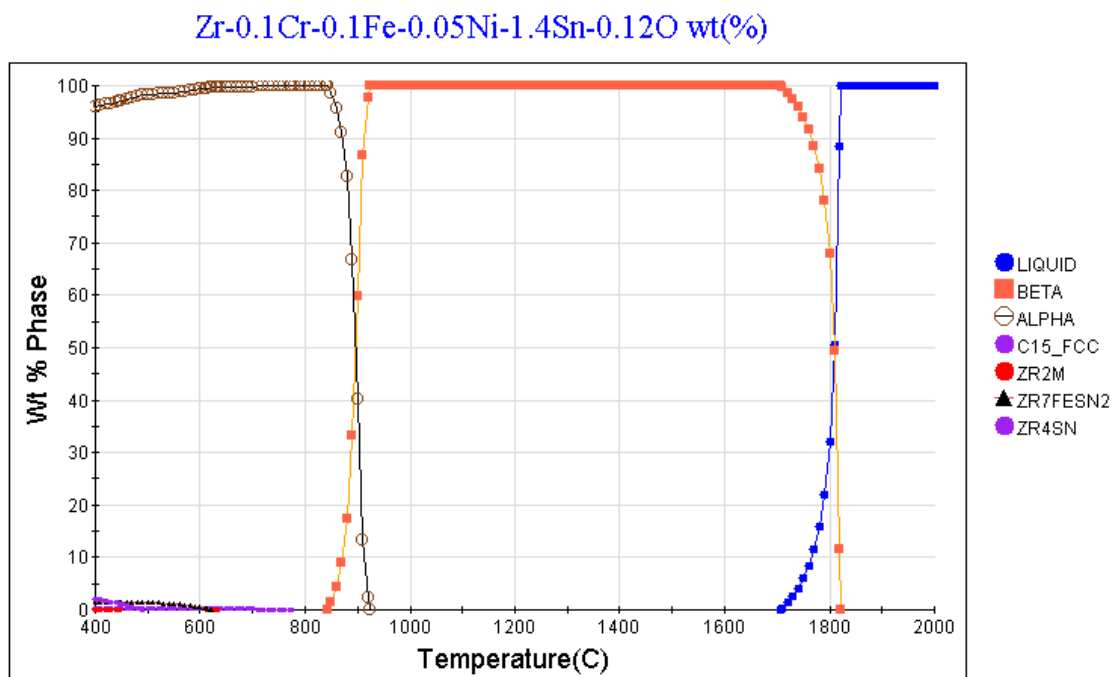


**Figure 13** Temperature dependence of the phase composition for the alloy zircaloy-2

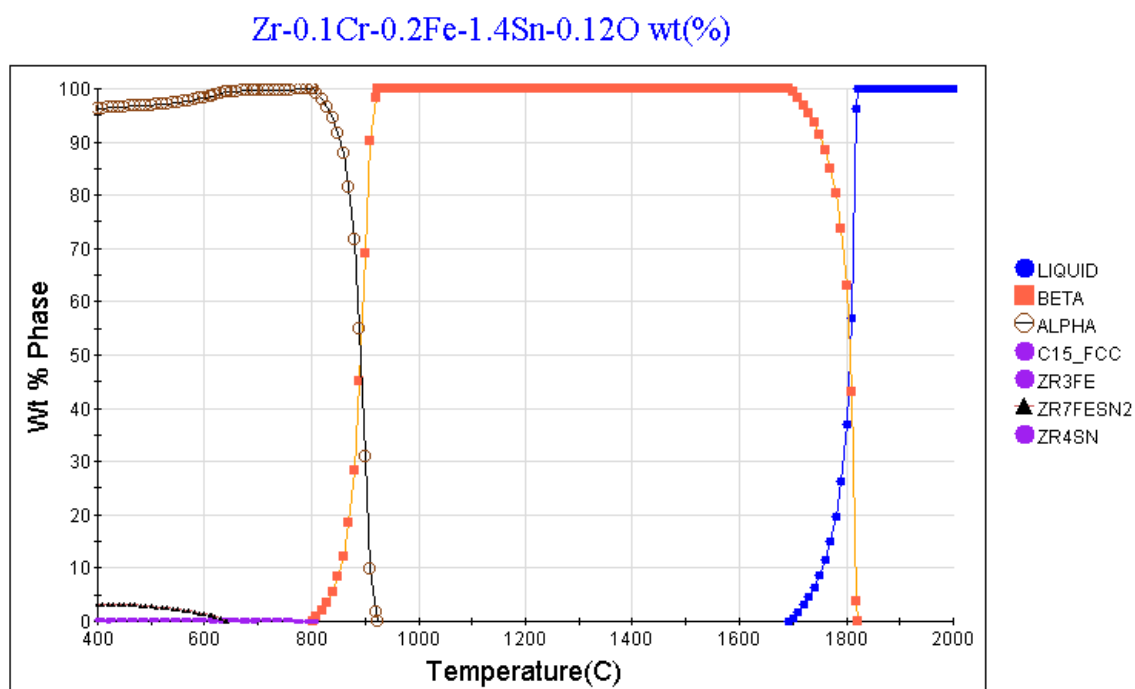


**Figure 14** Temperature dependence of the phase composition for zircaloy-4



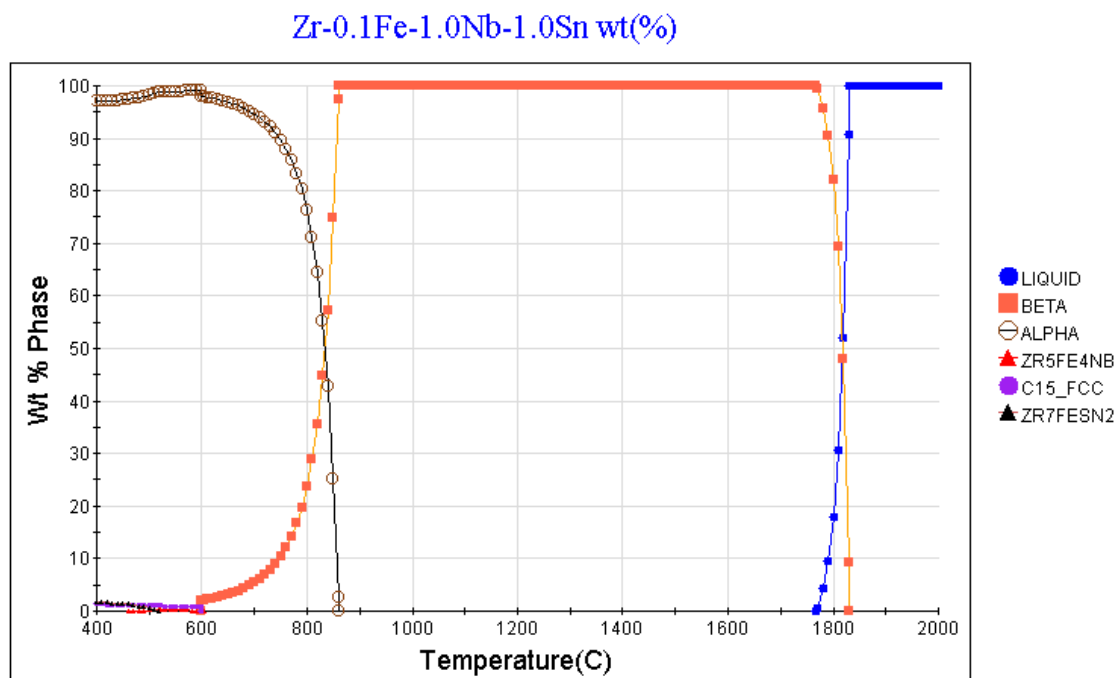


**Figure 15** Temperature dependence of the phase composition for ZIRLO™

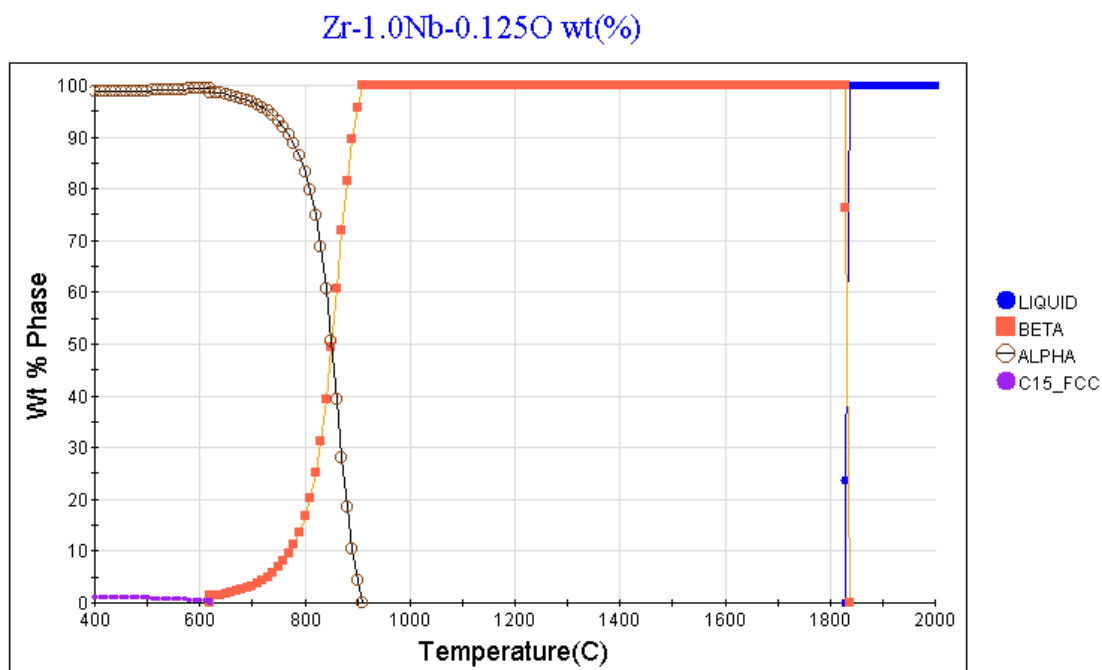


**Figure 16** Temperature dependence of the phase composition for the alloy M5™.

An interesting feature of the crystalline Zr at room temperature is an efficient repelling of interstitial atoms (H or O) from each other. Collective behavior of interstitial oxygen atoms in hcp- Zr was recently described by Ruban et al. [73]. Their calculations indicated that although interstitial oxygen atom produces just a minimal shift of the surrounding Zr atoms, it is energetically unfavorable (by about 0.5 eV) when two O atoms occupy any neighboring interstitial positions. The authors of [73] later used these atomic-scale energies in their Monte Carlo simulations of thermodynamically preferred interstitial configuration(s). We repeated these calculations and confirmed their validity. On this basis one could hypothesize that before the complete reconstruction of Zr network, oxygen might form an intermediate “checkerboard” configuration within one Zr layer with (0001) orientation (this minimal energy configuration corresponds to the maximal concentration of O atoms within the layer in which O atoms do not occupy neighboring positions), and in each layer the maximal atomic concentration of oxygen would be 25 %. This is quite close to the experimental value of 29 at.%, and to the  $\text{Zr}_3\text{O}$  stoichiometric suboxide [4, 58-60]. The discrepancy in the numbers may be explained by the kinetic effects which were not taken into account in this study. For even larger oxygen concentrations, the Zr-O structure should undergo a total reconstruction, and further oxidation will eventually result in the formation of the  $\text{ZrO}_2$ .

Another interesting feature of the  $\alpha$ -Zr structure is an impossibility of more than one atom (hydrogen or oxygen) to stay in one interstitial position. Figure 17 shows the relaxed atomic configuration for hydrogen molecule placed in a Zr octahedral interstitial – the two hydrogen atoms could not “coexist” in one octahedral interstitial position and eventually move to different interstitials. Therefore, one cannot expect hydrogen gas formation and/or hydrogen blistering as is observed at Al/ $\text{Al}_2\text{O}_3$  interfaces; also, one cannot expect that hydrogen molecule

could be positioned as a whole (as in Si and/or  $\text{SiO}_2$ ) into hcp Zr crystalline lattice. At low oxygen concentrations hydrogen is unlikely to form any additional complexes except reconfiguring Zr network by forming asymmetric or broken Zr-H-Zr bonds.

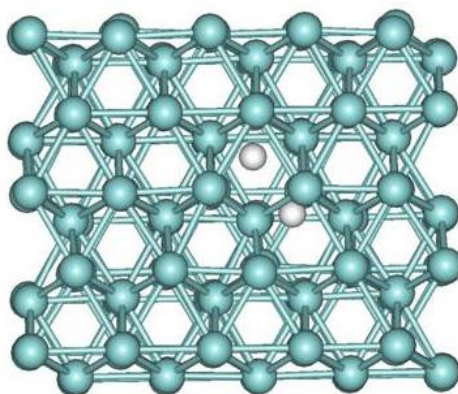


**Figure 17** Relaxed configuration for two hydrogen atoms that were initially put in one octahedral interstitial (as  $\text{H}_2$  molecule). Zr atoms are shown in cyan, hydrogen – in white.

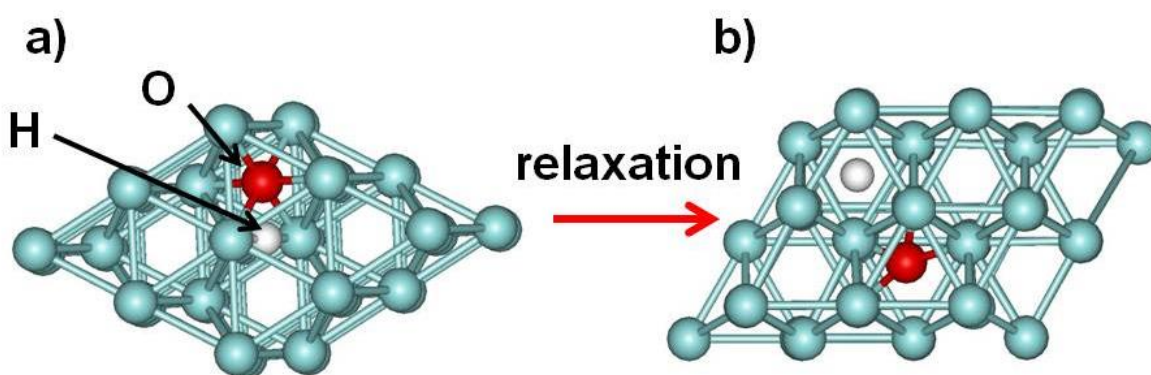


**Figure 18** Relaxed configuration for H and O atoms. Initially oxygen atom was put in octahedral interstitial and H atom – in the middle of a neighboring Zr-Zr bond. Zr atoms are shown in cyan, O – in red, H – in white.

Oxygen and hydrogen atoms also repel in the Zr hcp network. Figure 18 demonstrates how the energy relaxation of the original configuration for H and O complex actually takes place. Initially, oxygen atom was positioned in the middle of an octahedral interstitial, while the H atom – close to of the neighboring Zr-Zr bonds. Relaxation forces these two atoms to move into the neighboring interstitial position instead of forming a complex within one interstitial. This is understandable – oxygen is strongly electronegative and has tendency to oxidize Zr (pull electrons away from neighboring metal atoms). Hydrogen in Zr solid solution exhibits negative valence and tends to form zirconium hydrides. Apparently, oxygen is a much stronger oxidant than hydrogen, and when oxygen is present in some interstitial, hydrogen positioned in the vicinity has no chance to find electrons at the surrounding Zr atoms. Therefore, it cannot attach itself to surrounding metal atoms and redirects itself into a neighboring interstitial that is still not occupied by oxygen.

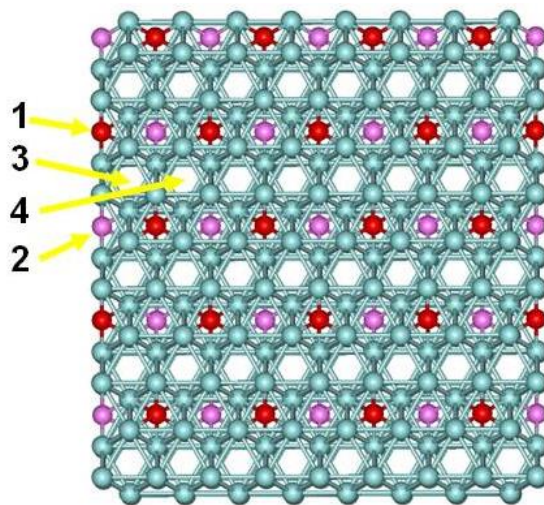


**Figure 19** The “checkerboard” configuration for O atoms in octahedral interstitials. Zr atoms are shown in cyan, O in the first layer – in red, O in the second layer – in pink. Four non-equivalent groups of interstitials are indicated by numbers and yellow arrows.

Figure 19 illustrates the formation of the “checkerboard” configuration. In the first layer (oxygen atoms are shown in red), O is arranged in such a way that it does not occupy any two nearest neighboring interstitials. In the second layer (O atoms shown in pink), the intra-layer configuration should be similar. However, it has to shift with respect to the configuration in the first layer because we should avoid neighboring O atoms in the direction parallel to the (0001) axis of the hcp structure. In the second layer, oxygen could occupy interstitials of the type 3 and 4 with the same probability. In the third layer, several possibilities to arrange O atoms in checkerboard structure become available again, and so on. An important conclusion that comes from such a construction is that after several layers of octahedral interstitial are occupied with oxygen in concentration close to the critical (at which 25% of octahedral interstitials are occupied), all the direct paths through hcp structure oriented along the (0001) direction for hydrogen atoms will be blocked by shifted checkerboard oxygen layers, and in order to migrate in the structure, any additional hydrogen atom will need to migrate not only in the (0001) direction but also laterally within the hcp Zr layers.

### 2.4.3 Suboxides of zirconium

Suboxides of transition metals such as titanium, zirconium, vanadium, etc., were discovered in early sixties of the past century, [4, 58-60]. At temperatures between about 900°C and 300°C various ordered phases have been reported [5]. Octahedral interstitial ordering of oxygen increases microhardness [58] and embrittlement [74], and therefore, promotes stress corrosion cracking. However, as it will be demonstrated later, it is very beneficial for reducing the hydrogen uptake under certain conditions, [71].

Order-disorder transitions in the zirconium – oxygen system were studied using heat capacity measurement for alloys with O/Zr ratios of 0.16 and 0.24 at 473K-973K [75]; and alloys

with O/Zr ratios of 0.0, 0.10, 0.13, and 0.24, at 325K-905K, Figure 20. In particular, a high degree of long-range ordering was achieved in samples that were cooled from 350°C to 250°C, during a period of about one month. This clearly indicates that a high mobility of oxygen is observed in the  $\alpha$ -Zr matrix even at such modest temperatures [61]. These temperatures are directly relevant to the conditions of the spent nuclear fuel (SNF) storage and so is the formation of sub-oxides.

Inside the metal, oxygen is randomly distributed in octahedral interstitial positions up to a concentration of 0.33 mole fraction of O. Yilmazbayhan et al. [76] identified the formation of ordered suboxides ( $\text{Zr}_3\text{O}$ ) at the oxide /  $\alpha$ -Zr interface underneath the oxide and ahead of the oxidation front, by using microbeam synchrotron radiation diffraction. Oxygen uptake has a hardening effect on the Zr matrix, -this effect is actually used in one of the novel Zr-Nb-O nuclear alloys, “M5<sup>TM</sup>”<sup>4</sup>. Cox [5] established that at temperatures around 400°C, less than 10% of the reacting oxygen is expected to dissolve into the metal substrate. He proved experimentally that preferential dissolution of oxygen, from the already formed oxide layer, takes place along the grain boundaries of Zr accompanied by the formation of arrays of pores in the oxygen-depleted grain boundaries (oxide) just above the metal substrate. These defective grain boundaries are possible open porosity development sites.

A clear correlation was found between oxide-metal interfacial microstructure and protective nature of the oxide (when interfacial structure is present, oxide is protective, when it is not present, - not protective) [10-12, and 76].

---

<sup>4</sup> C. Bataillon, C., D. Feron, L. Marchetti, et al. E-DEN Monograph, “Corrosion” Commissariat à l’Energie Atomique; 2008. M5 is the trademark of the AREVA Corporation (France)

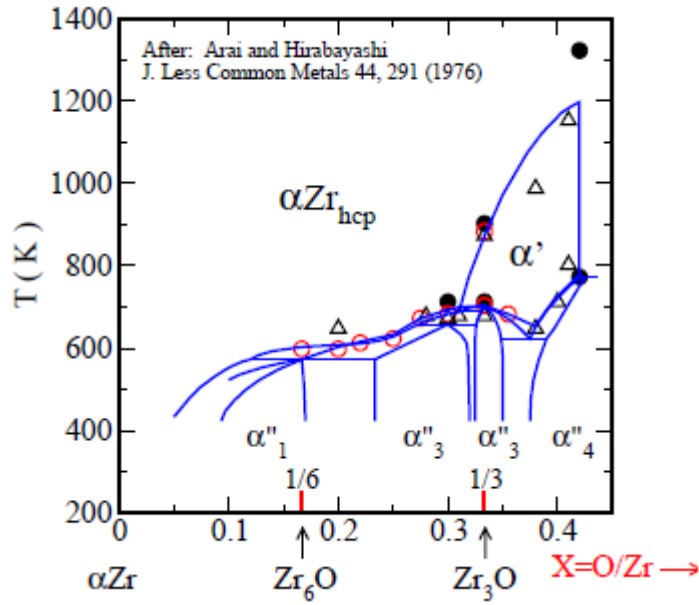


**Figure 20** First-principles calculations [61] and experimental data illustrating the presence of suboxides of zirconium in the Zr-O phase diagram [75]

The structure of the oxide–metal interface is of great interest to understanding the mechanism of oxide growth and the differences between the protective and non-protective oxides. As it was demonstrated in [10-12], the protective alloys always exhibit extra peaks in the diffraction scans obtained near the oxide–metal interface region. These peaks have been associated with two different phases found in that region in the protective oxides:

- (i) A highly oriented tetragonal phase that has been hypothesized to be a crystallographic precursor of the monoclinic phase observed in the bulk of the oxide.
- (ii) The formation of the sub-oxide phase  $\text{Zr}_3\text{O}$ . This phase has also been seen at the oxide–metal interface by various researchers in oxides formed in Zr alloys at low temperature [77-82]. In particular, the diffraction pattern from synchrotron radiation shows strong  $\text{Zr}_3\text{O}$  peaks in a two to three micron region next to the oxide–metal interface corrosion.

Summarizing these results, characteristic differences seem to exist in the oxide–metal interface regions of protective and non-protective oxides. In particular, the presence of the two interfacial oxide phases, a highly oriented tetragonal phase and a sub-oxide phase was associated with protective behavior uniform appears to be important for the reduction in hydrogen pick-up. These results stimulated further first-principles calculations aimed at understanding the atomic mechanisms of such protection. These results are presented in the next Section.

#### **2.4.4. Interstitial oxygen and hydrogen solid solutions**

To understand the migration mechanisms of hydrogen in zirconium suboxides, migration barriers for oxygen and hydrogen in interstitial solid solutions were calculated using nudged elastic bands approach [21,83]. It was established that, unlike in pure Zr, inside the zirconium suboxide lattice the migration barrier for moving oxygen atom from one octahedral interstitial to another is very high ( $>2$  eV). In turn, this implies that oxygen atoms are not mobile at moderate temperatures (below 600 – 800°C). High migration barrier for oxygen in suboxide is not surprising – it follows immediately from the simple geometric arguments (comparison between Zr-O and Zr-Zr bond lengths). Indeed, while an oxygen atom is put in some octahedral interstitial, it will stay there before either the temperature increases or the hcp Zr network significantly changes due to increase of oxygen atoms concentration above the critical value that hcp network can still tolerate. From the thermodynamics point of view, the checkerboard oxygen ordering (Figure 14) is energetically favorable. However, if because of kinetic reasons two oxygen atoms will become neighbors, their rearrangement towards energetically favorable configuration will develop on a very slow time scale. Therefore, because of kinetics we could expect checkerboard distortions in the “real” suboxide systems.



Apparently, ordering of low-mobile oxygen atoms in  $\text{Zr}_3\text{O}$  changes dynamics of hydrogen propagation through this class of materials. Assuming that the gradient of hydrogen concentration is directed along the (0001) axis, the following two modifications of the original hcp Zr matrix by oxygen are realized. First, the oxygen checkerboard arrangement shuts down “vertical” channels for hydrogen propagation along the (0001) axis. Moving along each of these, originally preferable migration paths, hydrogen will interact inevitably with oxygen atoms (this interaction is repulsive) positioned along this path. It means that the trajectory will become different from straight line, i.e., it will become longer by necessity. Secondly, migration barriers for hydrogen between two octahedral interstitials increase when oxygen atom is present in the neighboring interstitial. In the absence of oxygen, migration barrier between two interstitials was determined to be about 0.6 eV, in agreement with earlier calculations. On the other hand, when oxygen is present in the neighboring interstitial, this barrier increases to 0.9 eV. Therefore, in addition to increasing the length of hydrogen migration paths, a presence of oxygen increases hydrogen migration barriers. Both factors are unfavorable for hydrogen migration and it explains why hydrogen will propagate slower in  $\text{Zr}_3\text{O}$  than in pure zirconium.

Another interesting observation is that in the vicinity of oxygen atoms trapped in octahedral interstitials, hydrogen might migrate by another mechanism, namely through the middle of Zr-Zr bonds. In such a case, H atom distorts the Zr-Zr bond, forms the asymmetric Zr-H-Zr configuration, and eventually may break the original Zr-Zr bond. This process might be considered a precursor to the formation of a stoichiometric hydride.

### 2.4.5 Thermodynamic Data for Phase-Field Simulations of Zirconium Hydride

#### Formation and Reorientation and Some Results

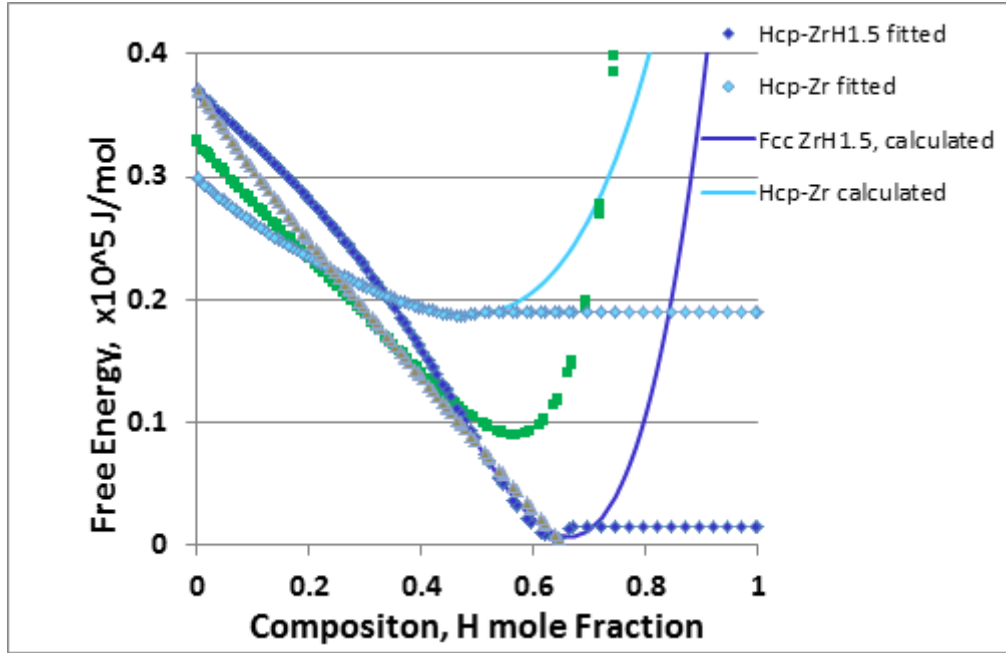


**Figure 21** Free-energy curves for the Zr-H system at 300 °C obtained using data in Appendix 1 [84, 85]

In order to use the obtained thermodynamic data (on the free energy of all competing phases as a function of temperature and hydrogen concentration) in phase-field calculations of microstructure evolution conducted by Dr. Veena Tikare of Sandia [84], the data needed to be represented in the fitted form (polynomials of the 5<sup>th</sup> degree were used for that goal). For example, the fitted free energy functions at 300°C were determined to be

$$E_{\alpha-Zr} = 2.135026x^5 - 16.96998x^4 + 7.119466x^3 - 1.541714x^2 - 0.297439x + 0.3679003 \quad (2.1)$$

for the  $\alpha$ -Zr phase, and

$$E_{\delta\text{-ZrH}_{1.5}} = 2.135026x^5 - 0.6183701x^4 - 0.6586253x^3 + 0.6083004x^2 - 0.4182968x + 0.2992497 \quad (2.2)$$

for the  $\delta\text{-ZrH}_{1.5}$  phase. The free energies for the  $\gamma\text{-ZrH}$  and  $\varepsilon\text{-ZrH}$  are included for completeness, but were not used for the demonstration purposes in [84]. The reason is that in storage of spent nuclear fuel only  $\delta\text{-ZrH}_{1.5}$  phase was detected.

In order to understand how the calculations were made, we provide a brief description of the phase-field approach of microstructure evolution in materials science following Glazoff et al. [86, 87]

#### **2.4.5.1 Equilibrium thermodynamics of concentrationally non-uniform systems and Phase-Field Mesoscopic Approach**

Approximately in the mid-1950s Hillert [88] at MIT worked on understanding the thermodynamics and kinetics of nucleation in some metallic systems. He realized that in order to describe the problem adequately, the thermodynamic formalism should incorporate characteristic length scale(s). However, instead of a rigorous continuum approach, Hillert chose to solve systems of coupled difference equations in order to obtain equilibrium interface width - a cumbersome procedure which does not allow one to write out a close-form solution of the problem. As a result, his formalism did not properly reveal the general underlying problem [89-91].

Sometime later the fundamental papers on equilibrium thermodynamics of concentrationally non-uniform system were published by Cahn and Hilliard [88-90]. These workers' main idea was that of a "diffuse interface," that is in order to understand systems with interfaces of some finite width (and all real interfaces are usually diffuse, rather than sharp), it is necessary to employ the concentration gradient (or, more, broadly, the gradient of an order parameter),  $\nabla c$ , as an

*independent variable*. Below a brief derivation of the key expression for free energy functional will be given, which later became the basis of “phase-field” theory. For concentrationally non-uniform systems the local free energy of a particle should depend not only on concentration itself, but also on its gradient(s). In order to work in the continuum approximation, it is necessary to assume that the composition gradient is small compared to the reciprocal distance between the particles [89]. Following Cahn and Hilliard [89], one can write down:

$$f(c, \nabla c, \nabla^2 c, \dots) = f_0(c) + \sum_i L_i \left( \frac{\partial c}{\partial x_i} \right) + \sum_{i,j} k_{ij}^{(1)} \left( \frac{\partial^2 c}{\partial x_i \partial x_j} \right) + \sum_{i,j} k_{ij}^{(2)} \left( \frac{\partial c}{\partial x_i} \right) \left( \frac{\partial c}{\partial x_j} \right) + \dots \quad (2.3)$$

For the phenomenological coefficients one gets [88]

$$L_i = \left[ \frac{\partial f}{\partial \left( \frac{\partial c}{\partial x_i} \right)} \right]_0 \quad (2.4a)$$

$$K_{ij}^{(1)} = \left[ \frac{\partial f}{\partial \left( \frac{\partial^2 c}{\partial x_i \partial x_j} \right)} \right]_0 \quad (2.4b)$$

$$K_{ij}^{(2)} = \left[ \frac{\partial^2 f}{\partial \left( \frac{\partial c}{\partial x_i} \right) \partial \left( \frac{\partial c}{\partial x_j} \right)} \right]_0 \quad (2.4c)$$

These phenomenological coefficients are components of a polarization vector in a polar crystal ( $L_i$ ), and tensors reflecting the crystal symmetry  $k_{ij}^{(1)}$  and  $k_{ij}^{(2)}$ . In the case of a cubic crystal or an isotropic medium there are certain symmetry operations which can be imposed to obtain the correct form of the free energy functional: it must be invariant with respect to the symmetry operations of reflection ( $x_i \rightarrow -x_i$ ) and of rotation around a fourfold axis ( $x_i \rightarrow x_j$ ). As a result of the application of these requirements it becomes possible to write down for a cubic lattice [90]:

$$f(c, \nabla c, \nabla^2 c, \dots) = f_0(c) + k_1 \nabla^2 c + k_2 (\nabla c)^2 + \dots \quad (2.5)$$

Integrating over the volume  $V$  and using the divergence theorem for the second term of decomposition (2.3), one can get the key expression for the free energy functional of a concentrationally non-homogeneous system:

$$F = N_V V [f_0 + k (\nabla c)^2 + \dots] dV \quad (2.6)$$

In equation (2.4),

$$k = -dk_1/dc + k_2 = -[\partial^2 f / \partial c \partial \nabla^2 c]_0 + [\partial^2 f / \partial (\nabla c)^2]_0.$$

The resulting expression for the free energy (i.e., the free energy functional) in the simplest variant of phase-field approach this expression looks as follows:

$$F[c] = V \{ f_0 + k (\nabla c)^2 \} dV \quad (2.7)$$

In equation (2.7)  $f_0$  is the free energy density for a concentrationally *uniform* system. The coefficient “ $k$ ” is necessary on the dimensional grounds, *and it is via this coefficient that a length scale comes into the constitutive equation(s) naturally*. This is the key expression because it provides one with an ability to create equilibrium systems with microstructure. Originally, this approach was used to describe microstructure arising as a result of spinodal decomposition. Specifically, the dynamics of spinodal decomposition could be considered within the framework of partial differential equations that describe such gradient systems with the potential function  $F[c]$  as a Lyapunov functional. Thus, in a sense, although the problem is dynamical, the final (steady-state) solution will minimize  $F$  [87, 88].

The most impressive demonstration of this statement was the successful modeling of kinetics of spinodal decomposition by Cahn and Hilliard described in detail by Hilliard [91]. For a “traditional” flux problem the potential for diffusion is determined by the derivative  $df/dc$ ; in the case when the free energy of the system is defined, one needs to

solve a variational problem of minimization of the functional (2.5) subject to condition that the average composition of the system as a whole remains constant, that is

$$(c - c_0) dx = 0.$$

This results in the following modified diffusion equation [90]:

$$\partial c / \partial t = -(1/N_V) \partial J / \partial x = (1/NV) k_1 \cdot f'' \{ \partial^2 c / \partial x^2 - k_2 \partial^4 c / \partial x^4 \} k \quad (2.8)$$

If  $k_1 f$  and  $k_2$  are constants, expression (2.6) represents the linearized yielding the famous Cahn–Hilliard equation. Microstructure, or “phase patterning”, arises as a result of competition of the second and the fourth gradient terms, and the resulting pattern undoubtedly minimizes the free energy functional [91]. The only order parameter in this case is concentration, a conserved value. Experimental data indicates that microstructure morphology typical of spinodal decomposition is highly nontrivial, its most important feature being the periodic modulation of composition inside the miscibility gap [91].

Summing up, it is useful to outline the main steps in the description of phase microstructures with phase-field approach [92]. Microstructures are described by a set of space- and time-dependent variables (“fields”). These variables are called “order parameters”. The latter can be “conserved” and “non-conserved”. An example of a conserved order parameter is concentration in the problem of solidification of a two component alloy. The word “conserved” used in the description of such parameters implies that a conservation law must be obeyed, that is:  $\partial c / \partial t = -\nabla J$ . The flux  $J$  can be determined as a gradient of chemical potential, a variational derivative of the Landau free energy functional. If a field variable  $\eta$  is not conserved, as in the case of solidification of one- and multicomponent alloys [93- 95], then its evolution can be

described by a relaxation-type time-dependent Ginzburg–Landau equation, sometimes also called the “Allen–Cahn equations”:

$$\partial \eta / \partial t = -L \cdot \delta F / \delta \eta (r, t) \quad (2.9)$$

For example, in the case of a two-component heterogeneous system one has to solve a set of equations:

$$d\eta_i^\alpha(r, t) / dt = -L^\alpha (\delta F / \delta \eta(r, t)); \quad i = 1, 2, \dots, p \quad (2.10a)$$

$$dC(r, t) / dt = \nabla \{ L_C \nabla [\delta F / \delta c(r, t)] \} \quad (2.10b)$$

In this equations  $F$  stands for the Lyapounov functional,  $\alpha$  denotes a particular phase, and  $L$  is the “relaxation” constant. For a two-component system, the maximum number of coexisting phases is equal to 3. The derivatives in the right-hand side of expressions (2.7) and (2.8) should be understood as “variational.”

The developed approach, in a sense, brought microstructure into thermodynamics of heterogeneous systems and turned out to be remarkably applicable to a broad variety of problems dealing with microstructure evolution in complex solids and in liquids. Below a brief description is given illustrating how this approach was adapted to the problem of zirconium hydride re-orientation in Zr alloys for nuclear applications [84].

#### 2.4.5.2 Adaptation of Hybrid Model to Simulate Hydride Formation [84]

The hybrid Potts-phase field model was applied to simulate the nucleation and growth of  $\delta$ -ZrH<sub>1.5</sub> precipitates. The equation of state used by the hybrid is

$$E_{hyb} = \sum_{i=1}^N \left( E_v(q_i, C) + \frac{1}{2} \sum_{j=1}^n J(q_i, q_j) \right) + E_i \quad (2.11)$$

In this expression, the volumetric free energy is given by Equations 1 and 2 for the  $\alpha$ -ZrH solid solution and  $\delta$ -ZrH<sub>1.5</sub> compound  $q$ , and follows directly from our thermodynamic calculations. The model is called “hybrid” because the interfacial energy is given in the Potts formulation and compositional gradients - in the phase field formulation  $E_i$ . The evolution of composition is given by equation (2.10b), with energy represented by equation (2.7), and the mobility is represented equations (2.4a). For the two-component system, there will be just one mobility coefficient.

“Traditional” phase field models contain, in addition to the volumetric free energy, an interfacial free energy  $E_i$  term,  $E_i = \kappa(\nabla C)^2$ . The microstructures of the zircaloy and hydride precipitates are evolved using Monte Carlo Potts techniques [96]. The microstructural feature or state is identified by a unique integer identifier  $q$  that designates a discrete quantum of material of a particular orientation and phase occupying that site. This set of states  $q$ ’s evolves to simulate microstructural evolution to minimize the overall free energy of the system along particular microstructural paths. Individual changes to the state  $q$  at all the sites are attempted. The change is carried out using the Metropolis algorithm [96]. The probability of the change  $P$  is calculated using Boltzmann statistics, where the probability of change is a function of the change in energy  $\Delta E$ , i.e.,

$$P = \begin{cases} \exp\left(-\frac{\Delta E}{k_B T}\right) & \text{for } \Delta E > 0 \\ 1 & \text{for } \Delta E \leq 0 \end{cases} \quad (2.12)$$



The change in energy,  $\Delta E = E_{final} - E_{initial}$ , is calculated using the adopted equation of state. If the probability  $P = I$ , the change is carried out. If  $P < I$ , then a random number  $R$  that is evenly distributed from 0 to 1 is chosen. If  $R \leq P$ , then the site is changed to its new state. In this way, the microstructure is evolved, while it is directly coupled to the compositional evolution through the equation of state given by Eq. 4. The units of time in the simulations are Monte Carlo steps, MCS; 1 MCS is when each site in the simulation has attempted a change. The model was modified in [84] to account for the preferred crystallographic orientations of zirconium hydride precipitation. The results are briefly discussed below.

#### **2.4.5.3 Simulation of Hydride Precipitation –Some Results [84]**

The objective in [84] was to simulate the precipitation of hydrides following the drying cycle. Following the drying cycle the temperature immediately drops and then decays very slowly over many months and years. For demonstration purposes, we simulate this condition by starting the simulation at 300°C with a zirconium matrix supersaturated with hydrogen. The temperature is held constant while the hydrides precipitate. A variety of microstructures for the underlying cladding were used. The composition was over-saturated with all the hydrogen dissolved to mimic the drying cycle. The sample temperature is then reduced to 300°C and held here to simulate precipitation. Nucleation of precipitates could occur under any stress condition. A more evolved model that can couple the local micro-stresses may be able to answer these questions.

For demonstration purposes, we present the results obtained for “rolled” zirconium plate subjected to further hydriding and precipitation of zirconium hydride<sup>5</sup>. In these simulations the

---

<sup>5</sup> Of course, this is a significant oversimplification. In fuel, the quantity of hydrogen dissolved in the clad is limited by the solubility limit. So, when fuel is loaded into a cask, the clad is kept cool by the water and the hydrogen solubility is low in the clad. When the water is pumped out and the cask evacuated, heat transfer is poor and the

grains had an average elongation of 2 times in the rolling direction as compared to the transverse and normal directions and the  $\alpha$ -Zr grains have orientation with preferred orientation of the basal poles. The starting composition was over-saturated with all the hydrogen dissolved in the  $\alpha$ -Zr matrix; the temperature was reduced to 300°C and held at this temperature for the subsequent simulation [84].

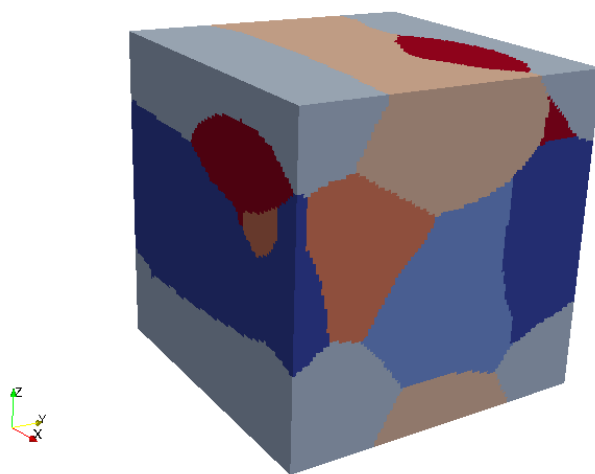


**Figure 22.** Input microstructure with basal orientation for small simulations with seven grains. The grains are elongated in the X-direction, which is also the rolling direction for the purposes of this illustration [84].

The distribution of hydrogen in the rolled microstructure corresponding to precipitates is shown in Figure 23. The hydrogen concentration is highest in the precipitates and corresponds to a stoichiometry of  $\text{ZrH}_{1.6}$ , which is very close to that observed experimentally. The hydrogen content in the matrix is depleted with the highest depletion close to the precipitate surface and

---

fuel rods heat up by gamma heating. That process is about 12 hours long. As the temperature rises, the hydrogen solubility of the base clad increases, and some of the existing hydrides dissociate. Once the fuel is dried, helium is added to the cask and convective heat transfer is reestablished. Now that the temperature can go down, the solubility of hydrogen in the clad becomes lower, and new hydrides precipitate. The driving force for the hydride orientation is the hoop stress from the rod internal pressure. Thus, the new hydrides precipitate perpendicular to that stress field.

increasing in the matrix away. This is expected in diffusion-controlled phase changes such as in the one being simulated here.

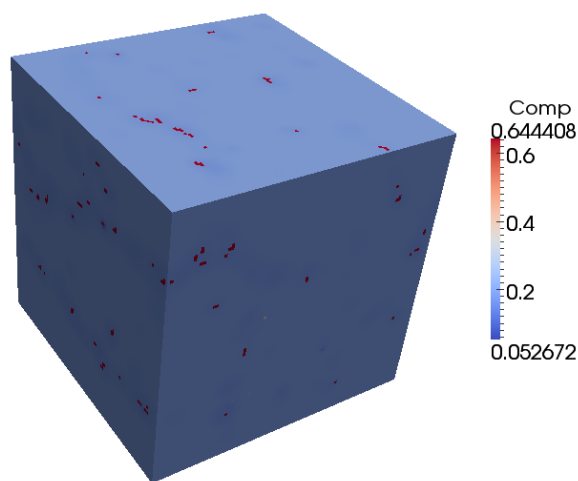


**Figure 23** The distribution of hydrogen in the microstructure; hydrogen concentrations are highest in the  $\delta$ -ZrH<sub>1.5</sub> precipitates and the matrix is depleted [84].

#### 2.4.5.4 Summary on Mesoscopic Work [84]

The precipitation of  $\delta$ -ZrH<sub>1.5</sub> in  $\alpha$ -Zr matrix by nucleation and growth in a Zircaloy-4 microstructure has been demonstrated. All the basic microstructural evolution processes necessary to simulation hydride precipitation were incorporated into the model and demonstrated. The results of the model show good qualitative agreement with experimental observations. The underlying microstructures of Zr-based claddings can be computationally generated to match the available experimental data on the specific systems; this capability was demonstrated on rolled zircaloy-4 microstructure with geometric elongation and crystallographic orientation to match the data available about these features. The thermodynamic free energies were obtained using CALPHAD-type calculations for  $\alpha$ -Zr,  $\delta$ -ZrH<sub>1.5</sub>,  $\gamma$ -ZrH and  $\epsilon$ -ZrH<sub>2</sub> phases. The calculated free energies for  $\alpha$ -Zr and  $\delta$ -ZrH<sub>1.5</sub> phases were used for the hydride precipitate formation simulations. The model uses the full chemical potential of the two phases with both

components in preparation for the more complex compositions that will be simulated in the near future. The phase transformation from  $\alpha$ -Zr to  $\delta$ -ZrH<sub>1.5</sub> leading to precipitation by nucleation and growth of precipitates can be simulated. The nucleation rate and subsequent growth of the precipitates is controlled by diffusion of hydrogen. The growth of the precipitates occurred in energetically favorable crystallographic directions. While it is not clear that the growth occurs in particular directions due to thermodynamics of the precipitate growth, this method was chosen for demonstration. However, should the kinetics of precipitate growth prove to be the controlling factor that determines the precipitate growth, the model can be modified to simulate the kinetic mechanism. The nucleation sites of the precipitates, dislocation loops or other defects can be distributed to match those in the actual materials. We have demonstrated this by allowing nucleation to occur with equal probability anywhere in the grains or predominantly near grain boundaries.

## 2.5 Conclusions and Recommendations on Chapter 2

In this Chapter we presented the results of computational thermodynamics and first-principles atomistic studies of the processes of hydrogen uptake and corrosion of zirconium and its alloys that are so important for nuclear industry and spent nuclear fuel disposition and storage problem. It was established computationally that for pure Zr, alloys Zy-2 and Zy-4 the differences in hydrogen uptake could not be explained using thermodynamic arguments as the hydrogen solvi and hydrogen saturation points were practically the same in all of these three materials: temperature of hydride dissolution 550°C and ~0.056 hydrogen molar fraction. On this basis, a conclusion was made that to understand the mechanisms of the hydrogen uptake slowing down it was necessary to understand the kinetics of the hydrogen diffusion process and the role of the Zr<sub>3</sub>O suboxide forming underneath the layer of ZrO<sub>2</sub> at the depth of about 2 to 3 microns.

This work was done using the first principles calculations, which demonstrated why the formation of  $\text{Zr}_3\text{O}$  seems to be important for the slowing down of hydrogen diffusion inside the bulk of Zr alloy. In turn, this implies that the spent fuel storage temperature should never exceed some  $360^\circ\text{C}$  when the disordering reaction takes place accompanied by the formation of the disordered Zr-O solid solution.

The obtained results could find direct application in phase-field calculations of the zirconium hydride microstructure evolution and reorientation (data on the driving forces for hydride formation in the form of a look-up table).

In the future research efforts, it would be advantageous to perform more accurate modeling kinetic Monte Carlo simulations of these order-disorder transformations and their role in slowing down the hydrogen uptake in nuclear zirconium alloys. Also, a detailed work on the development of self-consistent phase diagram region corresponding to these transformations should be constructed on the base of data generated from first-principles calculations on the temperature dependence of the free energy of the suboxide formation and not the semi-empirical Miedema rules, as it was done in the excellent assessment conducted by the authors of [64].

## 2.6 References to Chapter 2

1. L. Whitmarsh, Review Of Zircaloy-2 and Zircaloy-4 Properties Relevant to N.S. Savannah Reactor Design, ORNL-3281, Oak Ridge National Laboratory (1962)
2. G.P. Sabol in: Zirconium in the Nuclear Industry: 14th International Symposium, Stockholm, Sweden, ASTM International, STP 1467, p.3 (2004)
3. K.L. Murty, I. C. *Progress in Nuclear Energy*, 48, p. 325 (2006)
4. I.I. Kornilov, V.V. Glazova (Vavilova), and E.M. Kenina, Reports of the USSR Academy of Sciences, vol.169, p.343 (1966)
5. B. Cox, *Journal of Nuclear Materials*, vol. 336, p. 331 (2005)
6. G.E. Zima, A Review of the Properties of Zircaloy-2, HW-60908, (October 14, 1959)
7. B. Lustman and F. Kerze, The Metallurgy of Zirconium, McGraw-Hill, New York (1955)
8. D. Setoyama, *Journal of Nuclear Materials*, vol. 344, p. 291 (2005)
9. D. Arias; T. Palacios; C. Turillo, *Journal of Nuclear Materials*, vol.148, p.227 (1987)
10. A. Motta, A. Yilmazbayhan, M. Gomes da Silva, R. J. Comstock, G. Was, J. Busby, E. Gartner, Q. Peng, Y.H. Jeong, and J. Y. Park, "Zirconium Alloys for Supercritical Water Reactor Applications: Challenges and Possibilities," *Journal of Nuclear Materials* vol. 371 (2007) pp.61-75.
11. A. Yilmazbayhan, Microstructural Basis, of Uniform Corrosion in Zr Alloys, Ph.D. Thesis in Nuclear Engineering, Pennsylvania State University (2004)
12. A. Motta, A. Yilmazbayhan, R.J. Comstock, J. Partezana, G.P. Sabol, Z. Cai and B. Lai, Microstructure and Growth Mechanism of Oxide Layers Formed in Zr Alloys Studied with Micro-Beam Synchrotron Radiation, *Journal of ASTM International*, vol.2, Paper # JAI 12375 (2005)
13. Klara Anghel, Modified Oxygen and Hydrogen Transport in Zr-Based Oxides, Doctoral Thesis, Division of Corrosion Science, Department of Materials Science and Engineering Royal Institute of Technology (KTH) Stockholm, Sweden (2006).
14. Benjamin P. Burton, Axel Van der Valle, Harold T. Stokes, First Principles Phase Diagram Calculations for the Octahedral-Interstitial System  $\text{ZrO}_x$ ,  $0 < x < 0.5$ ; NIST preprint, July 11 (2011)
15. M.C. Payne, M.P. Teter, D.C. Allan, T.A. Arias, J.D. Joannopoulos, *Rev. Mod. Phys.*, vol. 64, 1045-1097 (1992)

16. J.P. Perdew, K. Burke, M. Ernzerhof, *Phys. Rev. Lett.*, vol.77, 3865-3868 (1996)
17. P.E. Blöchl, *Phys. Rev. B*, vol.50, 17953-17979 (1994)
18. G. Kresse, J. Joubert, *Phys. Rev. B*, 59, 1758-1775 (1999)
19. G. Kresse, J. Hafner, *Phys. Rev. B*, vol.48, 13115-13118 (1993); also see G. Kresse, J. Furthmüller, *Phys. Rev. B*, vol.54, 11169-11186 (1996)
20. D.J. Chadi, M.L. Cohen, *Phys. Rev. B* vol.8, 5747-5753 (1973)
21. H. Jonsson, G. Mills, K.W. Jacobsen, *Classical and Quantum Dynamics in Condensed Phase Systems*; World Scientific, Singapore, p 385 (1998)
22. M. Hillert: *Phase Equilibria, Phase Diagrams, and Phase Transformations*, Cambridge University Press, Cambridge, UK (2007)
23. H.L. Lukas, S.G. Fries, and Bo Sundman, *Computational Thermodynamics (The CALPHAD Method)*, Cambridge University Press, Cambridge (2007)
24. N. Saunders and A.P. Miodownik, *CALPHAD – Calculation of Phase Diagrams. A Comprehensive Guide*, Pergamon, London (1998)
25. Zi-Kui Liu, First-Principles calculations and CALPHAD Modeling of Thermodynamics, *Journal of Phase equilibria and Diffusion*, published online 03 September (2009)
26. L.J. Siefken, Preliminary Design Report for Modeling of Hydrogen Uptake in Fuel Rod Cladding during Severe Accidents, INEEL, September 14 (1998)
27. A. Sawatsky, the Diffusion and Solubility of Hydrogen in the Alpha Phase of Zircaloy-2, *Journal of Nuclear Materials*, vo.2, No.1, pp.62-68 (1960)
28. G. Ostberg, Determination of Hydride Solubility in Alpha Phase Zirconium, Zircaloy-2, and Zircaloy-4, *Journal of Nuclear Materials*, vol.5, No.2, pp.208-215 (1962)
29. J.J. Kearns, Terminal Solubility and Partitioning of Hydrogen in the Alpha Phase of Zirconium, Zircaloy-2, and Zircaloy-4, *Journal of Nuclear Materials*, vol.22, pp.292-303 (1967)
30. S. Yamanaka, M. Miyake, M. Katsura, Study on the Hydrogen Solubility in Zirconium Alloys, *Journal of Nuclear Materials*, vol.247, pp.315-321 (1997)
31. O. Zanellato, M. Preuss, J.-Y. Buffiere, F. Ribeiro, A. Stewer, J. Desquines, J. Andrieux, B. Krebs, Synchrotron Diffraction Study of Dissolution and Precipitation Kinetics of Hydrides in Zircaloy-4, *Journal of Nuclear Materials*, vo. 420, pp.537-547 (2012)
32. J. Xu, and S.-Q Shi, Investigation of Mechanical Properties of  $\epsilon$ -Zr hydride Using Micro- and Nano-Indentation Techniques, *Journal of Nuclear Materials*, vol.327, pp.165-170 (2004)
33. D. G. Westlake, The Habit Planes of Zirconium Hydride in Zirconium and Zircaloy, *Journal of Nuclear Materials*, vol.26, pp.208-216 (1968)

34. V.S. Arunachalam, B. Lenthinen, and G. Ostberg, The Orientation of Zirconium Hydride on Grain Boundaries in Zircaloy-2, *Journal of Nuclear Materials*, vol.21, pp.241-248 (1967)
35. J. Blomquist, J. Oloffson, A.-M. Alvarevol.z, C. Bjerken, Structure and Thermodynamic Properties of Zirconium Hydrides from First Principles, Preprint, University of Malme, Sweden (2010)
36. W. Zhu, R. Wang, G. Shu, P. Wu, H. Ziao, First-Principles Study of Different Polymorphs of Crystalline Zirconium Hydride, *Journal of Physical Chemistry C*, vol.114 (50), pp.22361-22368 (December 23, 2010)
37. Ma, X. Q., Shi, S. Q. et al., "Effect of Applied Load on Nucleation and Growth of gamma-Hydrides in Zirconium," *Comput. Mater. Sci.*, Vol. 23, 2002, p. 283.
38. Domizzi, G., Enrique, R. A. et al., "Blister Growth in Zirconium Alloys: Experimentation and Modeling," *J. Nucl. Mater.*, Vol. 229, p. 36 (1996)
39. Carpenter, G. J. C., "The precipitation of Gamma-Zirconium Hydride in Zirconium," *Acta Metall.* Vol. 26, p. 1225 (1978)
40. Bradbrook, J. S., Lorimer, G. W. et al., "The Precipitation of Zirconium Hydride in Zirconium and Zircaloy-2," *J. Nucl. Mater.*, vol. 42, p. 1 (1972)
41. Kearns, J. J., "Terminal Solubility and Partitioning of Hydrogen in the Alpha Phase of Zirconium, Zircaloy-2 and Zircaloy-4," *J. Nucl. Mater.*, vol. 22, p. 292 (1967)
42. Bailey, J. E., "Electron Microscope Observations on the Precipitation of Zirconium Hydride in Zirconium," *Acta Metall.*, Vol. 11, p. 267 (1963)
43. Z. Zhao, M. Blat-Yrieix, J.-P. Morniroli, A. Legris, L. Thuinet, Y. Kihn, A. Ambard, and L. Legras, Characterization of Zirconium Hydrides and Phase Field Approach to Mesoscopic Scale Modeling of Their Precipitation, *Journal of ASTM International*, vol. 5, No. 3 Paper ID JAI101161
44. X.Q. Ma, S.Q. Shi, C.H. Woo, and L.Q. Chen, The phase field model for hydrogen diffusion and c-hydride precipitation in zirconium under non-uniformly applied stress, *Mechanics of Materials*, vol. 38, pp. 3–10 (2006)
45. Z. Zhao, M. Blat-Yrieix, J.-P. Morniroli, A. Legris, L. Thuinet, Y. Kihn, A. Ambard, L. Legras, Characterization of Zirconium Hydrides and Phase Field Approach to a Mesoscopic-Scale Modeling of Their Precipitation, *Journal of ASTM International*, vol. 5, Issue 3 (March 2008)
46. James H. Saling and Audeen W. Fentiman, Radioactive Waste Management, 2<sup>nd</sup> edition, Taylor and Francis, New York (2001)
47. C. -S. Zhang; B. Li; P.R. Norton, *Journal of Alloys and Compounds*, vol.231, p. 354 (1995)



48. E. Zuzek, J.P. Abriata, A. San Martin, and F.D. Manchester, H-Zr (Hydrogen-Zirconium), Binary Alloy Phase Diagrams, II Ed., Ed. T.B. Massalski, Vol. 2, p 2078-2080 (1990)
49. Van der Sande, J.B. and A.L. Bement, "An Investigation of Second Phase *Particles in Zircaloy-4 Alloy*", *Journal of Nuclear Materials*, vol. 52. pp. 115-134 (1974)
50. Krasevec, V, "Transmission Electron Microscopy Study of Second *Phase Particles in Zircaloy- 2*," *Journal of Nuclear Materials*, vol. 98, p. 235 (1981)
51. P. Mukhopadhyay and V. Raman, *Metallography*, vol.11, p.481 (1978)
52. N.(Rao)V. Bangaru, An investigation of the microstructures of heat-treated Zircaloy-4, *Journal of Nuclear Materials*, vol. 131, issues 2–3, pp.280–290 (1985)
53. K.T. Erwin, O. Delaire, A.T. Motta, R.C. Birtcher, Y. Chu, and D. Mancini, "Observation of Second Phase Particles in bulk Zirconium Alloys Using Synchrotron Radiation," *Journal of Nuclear Materials*, vol.294, pp.299-304 (2001).
54. P. Dantser, W. Luo, T.B. Flanagan, J.D. Clewley, *Metallurgical Transactions A*, vol.24, p.1471 (1993)
55. E. Konigsberger, G. Eriksson, and W.A. Oates, Optimization of the Thermodynamic Properties of the Ti-H and Zr-H Systems, *Journal of Alloys and Compounds*, vol. 299, pp.148-152 (2000)
56. B. Cox; J.P. Pemsler, *Journal of Nuclear Materials*, vol.28, p. 73 (1968)
57. J.P. Abriata, J. Garces, R. Versaci, The O–Zr (Oxygen– Zirconium) System, *Bull. Alloy Phase Diagrams*, vol. 7 (2), p.116 (1986); also see D. Setoyama and S. Yamanaka, Phase Diagram of Zr-O-H ternary system, *J. Alloys Compd.*, vol. 370, p 144-148 (2004)
58. A. Dubertret and P. Lehr, *Compt. Rendus Acad. Sc. Paris*, vol. 262, p. 1147 (1966).
59. L.M. Kovba, E.M. Kenina, I.I.Kornilov, and V.V. Glazova, Investigation into Ordered Structures of  $Zr_6O$  and  $Zr_3O$  Suboxides, Reports of the USSR Academy of Sciences, vol. 180, issue 2, p. 360 (1968)
60. I.I. Kornilov and V.V. Glazova, Formation Of  $Ti_6O$  and  $Ti_3O$  Compounds In Titanium-Oxygen System, Reports of the USSR Academy of Sciences, vol. 150, iss. 2, p.313 (1963)
61. B.P. Burton, A. van de Walle, H.T. Stokes, First Principles Phase Diagram Calculations for the Octahedral-Interstitial System  $ZrO_x$ ,  $0 < x < 1/2$ , *J. of the Physical Society of Japan*, vol. 81., iss. 1, art. 014004 (January 2012)

62. G. Boreau and P. Gerdanian, High Temperature Thermodynamics of Solutions of Oxygen in Zirconium and Hafnium, *J. Phys. Chem. Solids*, vol.45, pp.141-145 (1984)
63. G. Boreau and P. Gerdanian, Use of Tian-Valve Micro-Calorimeter at 1300°C for Direct Measurement of Partial Molar Enthalpy of Oxygen in the Metal-Oxygen Systems, *Can. Metall. Q.*, vol.13 pp.339-343 (1974)
64. R. Arroyave, L. Kauffman, and T.W. Eagar, Thermodynamic Modeling of the Zr-O System, *Calphad*, vo.26,, no.1, pp. 95-118 (2002)
65. <http://www.titaniumstyle.com/black-zirconium-ring.html>
66. Chuanyong Huang, Zilong Tang, Zhongtai Zhang, Differences between Zirconium Hydroxide ( $\text{Zr}(\text{OH})_4 \cdot n\text{H}_2\text{O}$ ) and Hydrous Zirconia ( $\text{ZrO}_2 \cdot n\text{H}_2\text{O}$ ), *Journal of the American Ceramic Society*, vol. 84, iss. 7, pp. 1637–1638 (July 2001)
67. P. Vizcaíno, A. D. Banchik, J. P. Abriata. “Synchrotron x-ray Diffraction Evidences of the Amorphization / Dissolution of the Second Phase Particles (SPPs) in Neutron Irradiated Zircaloy-4”, *Materials Letters*, vol.62, pp. 491–493 (2008)
68. P. Vizcaíno , A. D. Banchik, J. P. Abriata. “Hydrogen in Zircaloy-4: Effects of the Neutron Irradiation on the Hydride Formation”, *Journal of Materials Science*, vol. 42, pp.6633-6637 (2007)
69. P. Rudling; G. Wikmark, *Journal of Nuclear Materials*, vol. 265, p.44 (1999)
70. K. R. Lawless, *Rep. Prog. Phys.* vol. 37, p. 231 (1974)
71. A. Yilmazbayhan, A.T. Motta, R.J. Comstock, G.P. Sabol, B. Lai, Z.H. Cai, Structure of zirconium alloy oxides formed in pure water studied with synchrotron radiation and optical microscopy: relation to corrosion rate, *Journal of Nuclear Materials*, vol.324, p.6 (2004)
72. C. Andrieu; S. Ravel; G. Ducros; C. Lemaignan, *Journal of Nuclear Materials*, 347, p. 12 (2005)
73. A.V. Ruban, V.I. Baikov, B. Johansson, et al., Oxygen and nitrogen interstitial ordering in hcp Ti, Zr, and Hf: An *ab-initio* study, *Physical Review B*, vol.82, iss.13, art.134110 (October 14, 2010)
74. A. W. Cronenberg, M. S. El-Genk *J. Nucl. Materials* 78, 390 (1978).
75. T. Arai and M. Hirabayashi, *Journal of the Less-Common Metals*, vol. 44, p.291 (1976)

76. A.Yilmazbayhan, E. Breval, A.T. Motta, R.J. Comstock, *Journal of Nuclear Materials*, vol. 349, p.265 (2006).
77. I.G. Ritchie, A. Atrens, *J. Nucl. Mater.* 67 (1977) 254.
78. Yoshitaka Nishino, A.R. Krauss, Yuping Lin, D.M. Gruen, *J. Nucl. Mater.*, vol.228, p. 346 (1996).
79. C. Morant, J.M. Sanz, L. Galan, L. Soriano, F. Rueda, *Vacuum* 39 (1989) 860.
80. M.C. Deibert, B.P. Thiesen, R. Kahraman, *Appl. Surf. Sci.*, 35 (1989) 302.
81. C.O. De Gonzalez, E.A. Garcia, *Appl. Surf. Sci.*, vol.44, p.211 (1990).
82. T. Ericsson, G. Ostberg, B. Lehtinen, *J. Nucl. Mater.*, vol.25, p.322 (1968).
83. G. Mills and H. Jonsson, *Phys. Rev. Letts*, vol.72, p.1124 (1994)
84. Veena Tikare and Michael V. Glazoff, Model for Simulation of Hydride Precipitation in Zr-Based Used Fuel Claddings: A Status Report on Current Model Capabilities, Joint Sandia/INL Report, FCRD- UFD-2014-000068, SAND2013 10834P (August 30 2013)
85. M.V. Glazoff, A. Tokuhiro, S.N. Rashkeev, and P. Sabharwall, Zirconium, Zircaloy-2, and Zircaloy-4: Computational Thermodynamics and Atomistic Perspective on Hydrogen Uptake and Oxidation, *Journal of Nuclear Materials*, vo.444, pp.65-75 (2014)
86. M.V. Glazoff, F. Barlat and H. Weiland, Continuum Physics of Phase and Defect Microstructures: Bridging the Gap between Physical Metallurgy and Plasticity of Aluminum Alloys, *International Journal of Plasticity*, vol.20, #3, pp. 363-402 (2004). This paper was used at MIT, Dept. of Materials Science and Engineering, as “recommended reading” for graduate-level course “Physical Metallurgy” by Professors Russell and Van Vliet in 2003/2004
87. Vadim S. Zolotarevsky, Nicholas A. Belov, and Michael V. Glazoff, Casting Aluminum Alloys (*monograph*), 546pp., Elsevier, Amsterdam (November 2007)
88. M. Hillert, A theory of nucleation for solid metallic solutions, D.Sc. Dissertation, Massachusetts Institute of Technology, Cambridge, MA (1956).
89. J.W. Cahn and J.E. Hilliard, Free Energy of a Non-uniform System: I. Interfacial free energy, *J. Chem. Phys.*, vol. 28, p. 258 (1958)
90. Cahn J.W., and Hilliard, J.E., Free energy of a Non-uniform system, III. Nucleation in a two-component incompressible fluid. In: *J. Chem. Phys.*, vol. 31, p. 688 (1959)
91. Hilliard, J.E. Spinodal Decomposition, Phase Transformations, Chapter 12, American

Society for Metals, Metals Park, OH, 1970.

92. L.-Q. Chen, Phase-Field Models of Microstructure Evolution, *Annual Rev. Mater. Res.*, vol. 32, p.113 (2002)
93. L.-Q. Chen and Y. Wang, The continuum field approach to modeling micro-structural evolution. In: *J. of Metals*, vol. 48, No. 12, pp. 13-18 (1996)
94. W.J. Boettinger, J.A. Warren, C. Beckermann C., and A. Karma, Phase-Field Simulation of Solidification, *Annual Rev. Mater. Sci.*, vol. 32, pp.163-194 (2002).
95. D. Lewis, T. Pusztai, L. Gránásy, J. Warren, and W. Boettinger, Phase-Field Models for Eutectic Solidification, *JOM*, pp. 34-39 (2004)
96. E.R. Homer, V. Tikare, and E.A. Holm, Hybrid Potts-Phase Field Model for Coupled Microstructural-Compositional Evolution, *Comp. Mater. Sci.*, 69, 414–423 (2013).

## Chapter 3 Materials and Methods for Zircaloy Cladding Protection against LOCA/RIA Accidents

1. B.Heuser, G. Was, M. Preuss, M.V. Glazoff, P. Sabharwall, J.Hales, et al., **Funded DOE IRP Proposal (\$3,500,000.00)** by INL, UIUC, University of Michigan, University of Florida, University of Manchester, Engineered Zircaloy Cladding Modifications for Improved Accident Tolerance of LWR Fuel (September 29, 2012)
2. S.N. Rashkeev, M.V. Glazoff, and A. Tokuhiro, Ultra-High Temperature Steam Corrosion of Complex Silicates for Nuclear Applications: Theory/Modeling Study, *Journal of Nuclear Materials*, vol. 444, pp.56-64 (2014)
3. Kevin M. McHugh, John E. Garnier, Sergey N. Rashkeev, Michael V. Glazoff, George W. Griffith, and Shannon Bragg-Sitton, “High Temperature Steam Corrosion of Cladding for Nuclear Applications: Experimental”, *Ceramic Engineering and Science Proceedings* (special volume: Ceramic Materials for Energy Applications III), vol.34, issue 9, pp.149-160 (2013)
4. John E. Garnier, Michael V. Glazoff, Sergey Rashkeev, George W. Griffith, Composite materials, bodies and nuclear fuels including metal oxide and silicon carbide and methods of forming same, US Patent Application #20 130,010,914 A1 (January 10, 2013)

### 3.1 Different Mechanisms of Zirconium Alloy Protection

A completely accident-free nuclear fuel form is not feasible because severe LOCA or RIA accidents will inevitably result in fuel rod melting [1-5]. Consequently, six potential approaches could be considered for protection of zirconium clad in order to ensure its extended longevity and gain additional time for the mitigation/alleviation of such accidents:

1. Advanced ceramics cladding based upon SiC, ZrSiO<sub>4</sub>, or Zircaloy cladding braided / coated with selected ceramic materials;
2. Temperature-activated zircaloy protection with yttria-stabilized zirconia [6,7]
3. Zircaloy cladding coated with metallic materials (e.g. Fe-Cr-Al) forming a layer of protective oxide on the surface;
4. Further work on improvement of zirconium based cladding materials, e.g., the introduction of such advanced and relatively novel alloys as ZIRLO<sup>TM</sup> and M5<sup>TM</sup>;

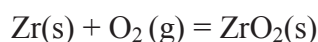
5. Ancillary additions of beryllium into zircaloy ingot in order to protect its surface from runaway oxidation (in analogy with practices used by the aluminum industry worldwide) [8];
6. Using completely different materials like stainless steel instead of Zircaloy-2 and/or Zircaloy-4 in cladding.

The success of any of these approaches will depend upon a number of factors, including technical feasibility, cost/benefit analysis, and the relative ease with which NRC and other regulatory authorities could approve this new technology for use in nuclear industry. Below, we provide a quantitative approach to solving the first of these problems that estimates the oxidation rate of complex ceramics such as SiC and  $\text{ZrSiO}_4$ . For other approaches, a more general description is provided coupled to the technical assessment when feasible (this includes approaches 2 and 4 above). This work is precluded below by a brief review of oxidation of zirconium and its alloys in normal and off-normal conditions. It should be considered a supplement to the extensive overview of the oxidation problem presented in Chapter 2 of this work. The difference between the two is that the former is mostly a discussion of the kinetic aspects of oxidation, while the latter deals mostly with the thermodynamics aspects of these complex processes.

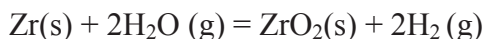
### **3.2 Some Kinetic Aspects of Cladding Oxidation in PWRs and BWRs**

A primary requirement of advanced nuclear fuel cladding designs is to contain the nuclear fuel inside the fuel rods in the event of a loss-of-coolant accident (LOCA). This needs to be achieved without diminishing heat transfer characteristics or impairing coolant flow during

normal operation. While Zr-based alloys are currently used as cladding in most nuclear reactor designs, a variety of advanced cladding materials including metals, ceramics and metal/ceramic composites are being considered as replacements and/or coatings (see above). The corrosion behavior of these materials depends on many factors, including the chemical nature of the cladding material, the reaction temperature, and the type and concentration of the oxidizing agent. For example, corrosion of Zr in air follows a different oxidation pathway than it does in steam. In air, the predominant reaction is:



In steam, oxidation is accompanied by the evolution of hydrogen gas which can potentially ignite:



Today, it is well established that zirconium is thermodynamically unstable with respect to oxidation even at room temperatures, see Chapter 2. However, in ambient conditions the Zr rate of oxidation is practically negligible because of the formation of a protective layer of  $\text{ZrO}_2$  on the top. This passivation property is well known and documented for many metals, including Zr, Al, Be, Mg, and others (see Chapter 5). As a result, one could discuss only at which conditions these processes become sufficiently fast to become a danger for the Zr cladding in LWR nuclear reactors.

In the case of zircaloy-2 (used mostly for older BWRs, but also used with almost pure Zr liner by GE today) it was established that cubic rate oxidation kinetics is observed between 400 and 600°C [5, 9, 10, and 15]. Zircaloy-4 was used mostly in PWRs (now also being replaced by advanced materials such as ZIRLO and M5); it does not contain Ni as an alloying element (mostly responsible for the hydrogen uptake in Zr-2) and obeys quasi-parabolic or parabolic

rate(s) of oxidation between 600°C and 950°C [11, 15]. It is important to emphasize that the oxidation of zirconium is a reaction – diffusion process, which can display a tremendous richness of nonlinear oxidation behaviors with bifurcations from the primary thermodynamic branch of solutions corresponding to dynamic “phase transitions” from one type of rate dependency to another. For diffusion-limited processes, parabolic rate is typical in the case when oxide layers are dense already. The role of point defects will be highlighted when Approach #2 is reviewed.

Linear oxide growth in Zy-4 is observed at or below 800°C [11, 15]; it is typical of solid materials with significant porosity. In this case, because of the continuous exposure to oxidation of fresh areas of the metal, we will observe linear kinetics of oxidation. According to Gibert [12], the general schematic of Zr oxidation could be presented by the graph:

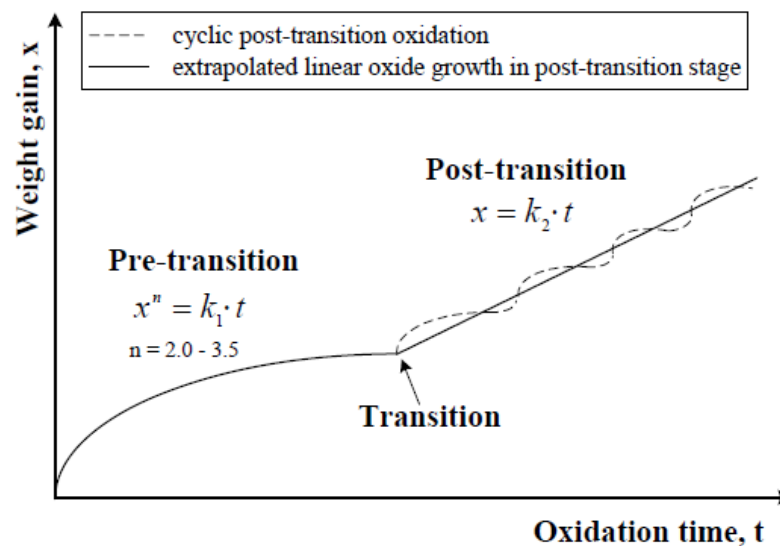


**Figure 24** Stages in the oxidation of Zr alloys modified in [7] after Gibert [12]. The kinetic equations for the two stages are shown ( $k_1$  and  $k_2$  are the rate constants).



This transition from a complex “quasi-parabolic” power law to linear rate at elevated temperature could be related to the structural change from tetragonal to monoclinic zirconia ( $t\text{-ZrO}_2$ )  $\rightarrow$  ( $m\text{-ZrO}_2$ ) in Zy-4 [6, 11, 13, 15].

The breakaway transition described above represents a distinctive danger factor in the case of off-normal power and temperature excursions because of the accelerated oxide growth. In particular at temperatures higher than 1000°C this can result in oxygen starvation, accompanied by the formation of Zr oxynitride thereby facilitating further porosity-mediated corrosion of the clad [14, 15].

In the case of Zy-2, the  $t^{1/3}$  kinetics is attributed to the  $m\text{-ZrO}_2$  phase [14, 15]. Typically, at least at temperatures less than 600°C, this does not result in breakaway oxidation transition [6, 9, and 16]. At the same time, Zy-2 is susceptible to localized or nodular corrosion in service. This effect is attributed to the precipitation of different Fe-, Cr-, and Ni-bearing phases [5, 9]. In the literature these phases are often called by the general term “ $\chi$ –phase. However, in reality the situation is more complex. The accurately modeled temperature dependencies of phase composition for Zy-2, Zy-4, ZIRLO<sup>TM</sup>, and M5<sup>TM</sup> was considered in detail in Chapter 2, see Figures 13-16.

The corrosion response of novel Zr-based materials, M5<sup>TM</sup> and ZIRLO<sup>TM</sup>, was studied under LOCA conditions (ambient pressure, temperature in the range from 900 to 1200 °C, up to 4000 seconds) by the authors of [14, 15]. These materials had oxidation rates characterized by the parabolic kinetics. The M5<sup>TM</sup> oxidation rate constant was smaller than Zy-4. Neither M5<sup>TM</sup> nor ZIRLO were prone to breakaway oxidation. It was concluded that the oxidation of M5 and ZIRLO is smaller than that of Zy-4 under LOCA conditions described above [6, 14, and 15].

The authors of [16] studied the oxidation behavior of zirconium alloy Zr-704. The following experimental data provide a clear illustration to the discussion above:

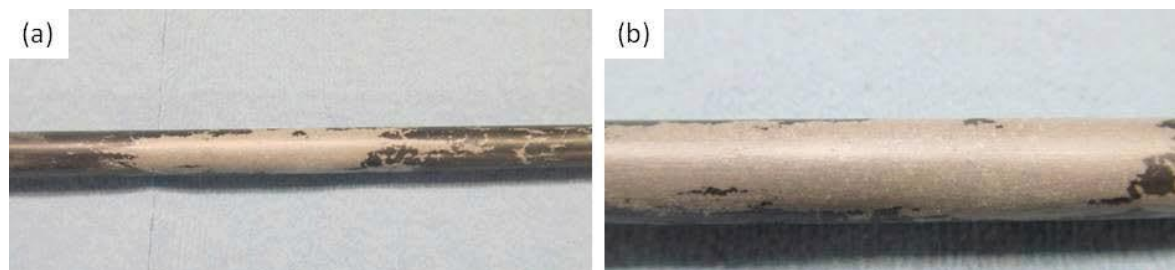


**Figure 25** Surface oxidation of Zy-702 tubing following one hour exposure to steam/air at  $\sim 1000^{\circ}\text{C}$  ([16], experimental data by McHugh et al.)

The mottled surface was characterized by a white, flaky, fully-converted  $\text{ZrO}_2$  oxide and a tenacious black transitional zirconium oxide layer [16]. As described in Chapter 2, these oxides correspond to the pre-transitional period oxidation (black) and to the post-transitional oxidation period (white flaky appearance), see Figure 24.

Figure 25 shows representative SEM photomicrographs of the cross-section of tubing, at various magnifications. Three main microstructure zones were observed as oxygen diffuses into the alloy at  $1000^{\circ}\text{C}$ : an outer, fully-converted zirconium oxide layer; a partially converted underlying zone of oxygen-stabilized  $\alpha$ -Zr phase; and a minimally oxidized  $\beta$ -Zr phase of the base metal. The fully converted zirconium oxide layer was about  $65\text{ }\mu\text{m}$  thick and was interlaced with axial and transverse cracks of various lengths that resulted from tensile loading due to volumetric expansion. Use of a vCD detector (BSE mode) in Figure 25d clearly revealed these cracks as well as transverse cracks that initiated in the brittle, oxygen-stabilized  $\alpha$ -Zr phase of the metal. The oxygen-stabilized Zr phase was less well resolved but appeared to be about  $30\text{ }\mu\text{m}$  thick. Similar trends have been observed by other investigators in steam-oxidized zircaloy-2 [17,

18] and zircaloy-4, [19, 20, 21]. The relative thickness of the fully converted oxide layer and oxygen-stabilized  $\alpha$ -Zr phase will depend upon temperature and time. Weight gain measurements in these studies indicated that the total oxygen uptake for samples tested at 1000°C obeys a parabolic rate law,  $W^2 = K_p * t$  where  $K_p$  is the temperature dependent rate constant,  $W$  denotes oxygen weight gain, and  $t$  is time. The current study was conducted in acidified steam (simulating a LOCA at INL's ATR reactor). It is not clear to what extent this affected the oxidation behavior.

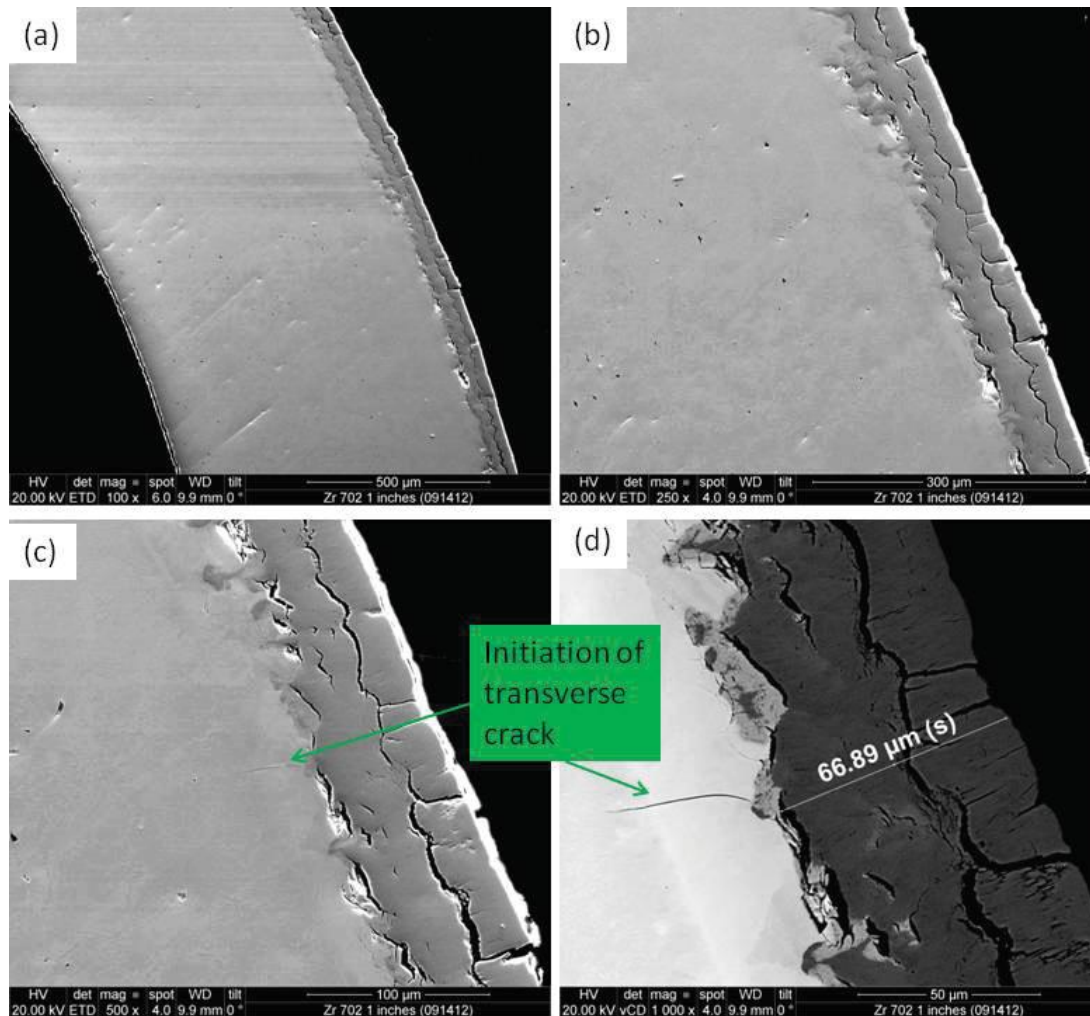


**Figure 26** SEM photomicrographs of Zy-702 tubing following one hour exposure in air/supersaturated steam at ~1000°C. (a) 100X, secondary electron mode. (b) 250X, secondary electron mode. (c) 500X, secondary electron mode. (d) 1000X, backscattered electron mode [16]

### **3.3 Ultra-High Temperature Steam Corrosion of Complex Silicates for Nuclear Applications: A Computational Study**

#### **3.3.1 Some Experimental Results [16]**

Nuclear fuel rods used in a PWR are internally pressurized with He to about 2 MPa during manufacture. Helium is added to improve thermal conductivity at the pellet-cladding interface, and to reduce interaction between pellet and cladding during service. As the tubes are heated, the pressure rises. As the fuel burnup increases, gaseous fission products further increase the pressure. The internal pressure is largely offset by the water pressure in the reactor's primary coolant loop. During a LOCA, as primary coolant is lost, the rise in differential pressure can cause the cladding to strain and rupture. Advanced materials such as SiC CMC could increase the reactor's safety margin by providing containment for the nuclear fuel, preventing it from entering the primary coolant. Deformation of fuel cladding during a LOCA is very complicated. Stress, temperature, and creep strength influence deformation. In greater detail, different aspects of the plastic behavior of zirconium are considered in Chapter 4 of this dissertation.

Azimuthal (circumferential) temperature variations due to fuel movement and eccentricity can play an important role in local temperature and strain behavior. Manufacturing flaws and small differences in microstructure also influence creep. Various studies have been conducted worldwide to study the deformation and ballooning behavior of zirconium alloys in steam, for example, at the PROPAT facility in the UK [22], the EDGAR-1 [23] and EDGAR-2 [24] facilities in Canada and at CEA in France, also at the Korean Atomic Energy Institute [25], in Japan [26] and elsewhere. Preliminary experiments were conducted in steam/air on

pressurized tubes of Zy-702 measuring 9.5 mm OD x 356 mm long. As-received Zy-702 tubes and Zy-702 tubes reinforced with a ~ 38 mm long tubular sleeve of SiC CMC, as shown in Figure 2a, were tested. The composite tube consisted of single-ply Hi Nicalon  $\beta$ -SiC woven fibers that were polymer infiltrated with polycarbosilane and pyrolyzed to form a matrix of  $\beta$ -SiC. Tubes were pressurized with He to 3.4 MPa and induction heated to the point of rupture by coupling the induction field to a 254 mm long Mo rod susceptor inserted inside the Zy-702 tubes at the center<sup>6</sup>. Temperature of the susceptor was monitored with a grounded type K thermocouple inserted 25 mm from the end of the susceptor. Tubes were heated at an average rate of 37°C/min. Figure 8a shows an as-received (starting) Zy-702 tube, and ruptured sample, while Figure 8b shows a starting Zy-702 tube with a 11 mm ID x 11.3 mm OD x 38 mm long SiC CMC sleeve. The sleeve fit loosely over the Zy-702 tube with about 1.5 mm clearance. Since the tubes were vertically oriented, a small ring of a ZrO<sub>2</sub>-based adhesive was applied to the Zy-702 tube to center the SiC CMC sleeve and hold it in place. The coating ring appears white in Figure 27b, to the left of the SiC CMC.

In summary, tests were conducted using Zy-702 and SiC ceramic materials. As expected, SiC exhibited improved oxidation resistance over Zy-702 in dry oxygen and steam/air at 1000°C. Oxygen and steam readily attacked Zy-702 forming a brittle ZrO<sub>2</sub> layer at the exposed surface interlaced with axial and transverse cracks. Oxygen diffusion through this layer resulted in the formation of an oxygen-stabilized  $\alpha$ -Zr phase with intermittent transverse cracks. The interior of the Zy-702 transformed to the  $\beta$ -Zr phase which coarsened with exposure time at elevated temperature [16]. The SiC materials formed a thin layer of relatively stable SiO<sub>2</sub>. Preliminary

---

<sup>6</sup> Sandvik Zr 702 is a zirconium grade containing less than 4.5% Hf, 99.2% (Zr+Hf), and ~0.2% (Fe+Cr). It is characterized by immunity to stress corrosion cracking and high resistance to pitting and crevice corrosion. In this study, it was used in lieu of Zy-4 because it was unavailable for us at that time.

experiments were also conducted in steam/air on pressurized (3.4 MPa He) tubes of Zy-702 and Zy-702 tubes reinforced with a tubular sleeve of SiC CMC. The tubes were induction heated to the point of rupture by coupling the induction field to a Mo susceptor inserted inside the Zy-702 tubes. Rupture occurred as the Zr- field. Ballooning was observed for all samples with a maximum circumferential strain of about 80%. At the location of the reinforcing SiC CMC sleeve, metal expansion was significantly constrained. The OD increased about 2%, indicating the 1-ply braided SiC CMC fabric stretched but did not fail under the test conditions [16].



**Figure 27** Photographs of starting samples (above) and ruptured samples (below) of (a) Zy-702 tube, and, (b) Zy-702 tube fitted with a SiC CMC sleeve [16].

### 3.3.2 Brief Description of Complex Silicates

Computational research work reported in this Section was conducted in support of the experimental program briefly described above. In particular, broad intervals of thermal stability

and the oxidation rates that could not be achieved at INL experimentally were of paramount interest to us.

Nuclear fuel rods in water reactors are contained in sealed tubes (cladding) made of zircaloy-2 (BWRs) and zircaloy-4 (BWRs and PWRs). In a recent accident at the Fukushima nuclear plant, during the LOCA accident, the fuel rods inside the reactors overheated due to the release of decay heat. The heat generated steam inside the core increasing the reactor pressure. While zirconium reacts with water vapor even at ambient temperature, this process becomes significantly accelerated at  $\sim 800^{\circ}\text{C}$  and higher, resulting in the formation zirconium oxides, hydroxides, and hydrogen, - an explosive gas. In turn, the mixture of overheated steam with hydrogen exploded when it came into contact with air. These explosions caused serious damage to the reactor buildings at the Fukushima nuclear plant.

To avoid such accidents in the future, research work is in progress to develop a suitable coating or replace zirconium alloys altogether with ceramic materials in nuclear reactors. In particular, silicon carbide (SiC) is being studied as a cladding material candidate for fuel rods in water-cooled reactors. Silicon carbide is a refractory ceramic with the numerous commercial applications. It has excellent strength, significantly lower chemical reactivity, very low neutron absorption, and resistance to radiation damage. The material's combination of high strength and hardness, chemical inertness, and attractive thermal properties (high conductivity, low thermal expansion, and thermal shock resistance) makes it useful for a variety of applications such as abrasives and wear components, high temperature semiconductors, armor, and reinforcement in composites.

As it follows from the Si-C phase diagram constructed using ThermoCalc, silicon carbide melts incongruently, according to the peritectic reaction:  $\text{SiC} + \text{Graphite} \rightarrow \text{Liquid}$  at  $1404^\circ\text{C}$ , Cupid and Seifert [27].

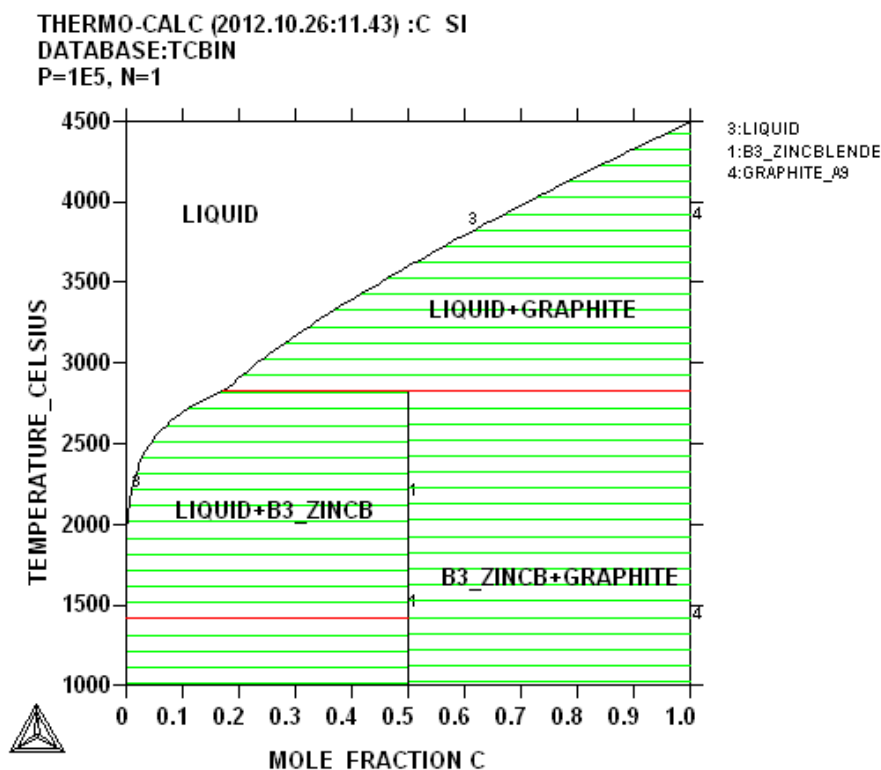


**Figure 28** The Si-C phase diagram calculated using ThermoCalc software and the TCBIN database.

Only the 2H-polytype ( $\alpha$ -SiC) relevant for our study is presented in this diagram.

Therefore, the SiC has potentially better properties as a cladding material than zircaloy(s), which will start reacting with water vapor producing appreciable amounts of hydrogen around  $800^\circ\text{C}$ . Unlike most ceramic materials, it also performs well in a nuclear reactor environment as it exhibits excellent radiation stability, is composed of low activation elements, and retains its strength and shape even after a long period of irradiation in a nuclear reactor [28, 29].



SiC exhibits polymorphism, and more than 250 polytypes have been identified. One crystal stacking arrangement results in the cubic 3C-SiC ( $\beta$ ) structure. All hexagonal stacking arrangements (2H, 4H, 6H, etc.) are grouped together as  $\alpha$ -SiC with the 6H polytype being the most prevalent [30, 31]. Different technical solutions may be proposed for developing the SiC ceramic fuel cladding. Recently, it was proposed at the INL to strengthen and protect the underlying zircaloy cladding tubing with braided fiber outer wrap [32, 33]. The method provides for an additional layer of protection, thereby avoiding the direct contact of the cooling water with a zircaloy tube. At least in principle, this technical solution might have helped to avoid the Fukushima catastrophe had it been in place at the time of the LOCA accident.

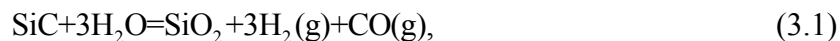
In this work, we present our modeling/simulation results for the corrosion rate of SiC in a very high temperature water vapor environment. Our goal was to understand how fast different SiC based reactor components will degrade in such condition and how long time it will take for the ceramic-modified reactor core to melt. Such estimates are important for the Light Water Reactor Sustainability (LWRS) program.

This section is organized as follows. Section 3.3.1 contains the main equations related to the two-step SiC oxidation in water vapor environment and relation of the main parameters of the theory on the change of the environmental conditions (pressure, temperature, viscosity, surface quality, etc.). Using this theory (originally developed for the process of combustion), we provide estimates of the corrosion rate of SiC ceramics in Section 3.3.2. We found that it would take a significant time for a typical SiC fiber (which contains  $\sim 50,000$  individual filaments of 5 – 10  $\mu\text{m}$  in diameter) to completely degrade even in the vapor environment with temperatures up to  $2200^\circ\text{C}$  imitating emergency LWR conditions. In Section 3.3.4 we discuss possibilities for using other silica-based ceramics in order to find materials with even higher water resistance

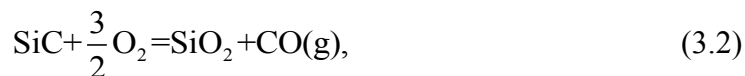
than SiC. Section 3.3.5 contains a general discussion of the specifics of ceramics used in nuclear applications and special requirements that are needed to be satisfied, while Section 3.3.6 provides some atomic scale arguments in favor of the conclusions made in this part of the dissertation. In particular, we found that zircon ( $\text{ZrSiO}_4$ ) is a very promising material for nuclear applications. Section 6 contains atomic-scale arguments based on the first-principles calculations explaining why zircon is extremely water resistant at high temperatures. Main conclusions of this work are included in Section 3.3.7.

### 3.3.3 Paralineer SiC oxidation in water vapor environment

Silicon carbide based composites were developed for use in heat engines. Currently, this material is actively studied as a potential replacement / liner of the existing zircaloy-2 and zircaloy-4 alloys used for manufacturing reactor rods. In both cases, water vapor is a major component of the environments of interest. In particular, it was calculated that the products of combustion contain at least 10% water vapor independent of the fuel-to-air ratio [34]. Simple thermodynamic calculations conducted in 1997 indicated that in an environment containing water vapor, reaction that occurs for the oxidation of SiC is [35]:



the symbol ‘g’ means a gas phase. Our thermodynamic calculations (see Figure 26) generally confirm this statement. However, the ratio of CO to  $\text{CO}_2$  in the mixture will depend upon temperature and the initial conditions in the mixture (see Figure 26). In the oxygen-enriched environment, corresponding to a combustion process, the following reaction has to be considered [36]:



However, these conditions are not met in a nuclear reactor and will not be discussed further.

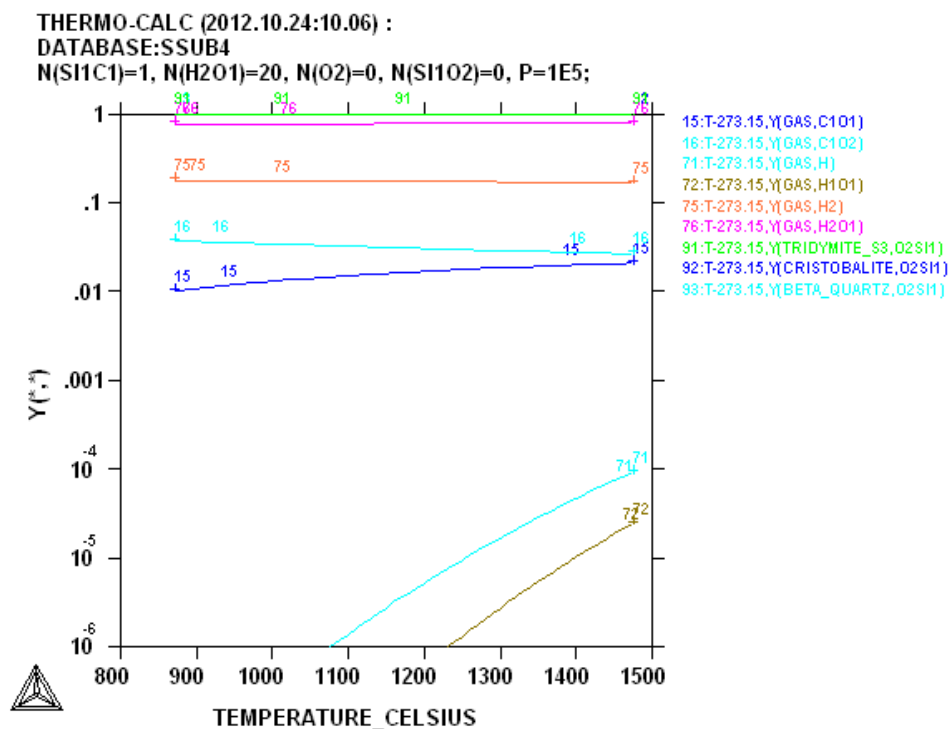
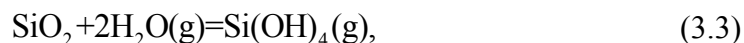


**Figure 29** Thermodynamic calculations of the total phase composition of the silicon carbide, oxygen, and water mixture as a function of temperature.

In the literature, a possibility of the  $\text{SiO}_2$  volatilization was discussed, accompanied by the formation of such hydroxides and/or oxy-hydroxides as  $\text{Si(OH)}_4$  (gas),  $\text{SiO(OH)}_2$  (gas), and  $\text{Si}_2\text{O(OH)}_6$ . It was demonstrated in [37] that SiC undergoes parilinear oxidation in an environment containing 50% $\text{H}_2\text{O}$ /50% oxygen at 1 atm total pressure and temperatures between 1200° and 1400°C, and the silica scales volatilize mainly as  $\text{Si(OH)}_4(\text{g})$ :



In a pure hot water vapor environment (without oxygen), the parabolic oxidation process should be described by Eqs. (3.2) and (3.4). The kinetics of the oxidation reaction are described by the parabolic rate constant for oxide formation,  $k_p$ , whereas the kinetics of the volatilization reaction are described by the linear rate constant for oxide volatilization,  $k_l$ . These reactions occur simultaneously and are described by the equation [3.4]:

$$\frac{dx}{dt} = \frac{k_p}{2x} - k_l \quad (3.4)$$

In Eq. (3.4)  $x$  stands for the oxide thickness, and  $t$  represents time. At long times or high volatility rates, a steady state is achieved in which oxide is formed at the same rate it is volatilized. SiC layer undergoes linear recession in time, given by the rate  $\dot{y}_L$ , when this steady state is achieved, which is directly related to the volatility rate of the oxide,  $k_l$ . Dimensional changes because of parabolic oxidation are shown as a function of time for SiO<sub>2</sub> growth on SiC. At the steady state, the limiting oxide thickness  $x_L$  is achieved, which is given by

$$x_L = \frac{k_p}{2k_l}. \quad (3.5)$$

The subscript L here and below refers to the steady-state limit. The parabolic oxidation kinetics of SiC in water vapor and combustion environments have been studied under a wide variety of conditions, and the model has been shown to be valid in a majority of cases.

The analytic solution of Eq. (3.4) is presented below in Eq. (3.6):

$$t = \frac{k_p}{2k_l^2} \left[ -\frac{2k_l}{k_p} x - \ln \left( 1 - \frac{2k_l}{k_p} x \right) \right], \quad (3.6)$$

It is also important to understand how the oxidation/volatilization processes depend upon more fundamental parameters (pressure, water vapor partial pressure ( $P_{H_2O}$ ), gas velocity, and

temperature) that describe any given environment, rather than on the empirical kinetic rate constants that may or may not be known.

The parabolic rate constant,  $k_p$ , describes the kinetics of Eq. (3.4) for moderately thick scales (diffusion limited growth). This rate constant varies with  $P_{H_2O}$  and temperature but is independent of gas velocity in combustion system. The temperature dependence is discussed later. The water-vapor dependence can be described using a power law:

$$k_p \propto \exp\left(-\frac{\Delta G_0^{SiO_2}}{RT}\right) * P_{H_2O}^n, \quad (3.7)$$

where  $n$  is the power-law exponent,  $\Delta G_0^{SiO_2}$  is the change of the Gibbs free energy for the reaction (2) where  $SiO_2$  is formed (i.e., SiC is oxidized by water). This power law should be identical for all  $SiO_2$  formers, because parabolic oxide growth is rate limited by transport of oxidant through the  $SiO_2$  scale. Deal and Grove [37] have observed a power-law exponent of unity for the parabolic oxidation of silicon by water vapor, indicating that the oxidation reaction is limited by the diffusion of molecular water, rather than a charged species, through the  $SiO_2$  scale. Studies on the oxidation of SiC in water vapor have found power-law exponents varying between 0.76 and 0.91 [38].

The linear volatilization rate constant describes the kinetics of Eq. (3.4). This rate constant varies with  $P_{H_2O}$ , total pressure (other gases are always present in the system), temperature, and gas velocity. Under combustion conditions, the volatilization of  $SiO_2$  to form  $Si(OH)_4$  is limited by transport of  $Si(OH)_4$  through a laminar gaseous boundary layer.

$$k_l \propto \exp\left(-\frac{\Delta G_0^{Si(OH)_4}}{RT}\right) * v^{1/2} \frac{P_{H_2O}^2}{P_{total}^{1/2}}, \quad (3.8)$$

where  $\Delta G_0^{Si(OH)_4}$  is the change of the Gibbs free energy for the reaction (3.3) where  $Si(OH)_4$  is formed (heat of volatilization),  $v$  is the gas velocity in the boundary layer [39].

In other publications the equation for  $k_l$  was written in another form [40]:

$$k_l = 0.664 \left( \frac{Lv\rho}{\eta} \right)^{1/2} \left( \frac{\eta\rho}{D} \right)^{1/3} \frac{D\rho_v}{L}, \quad (3.9)$$

where  $D$  the inter-diffusion coefficient of  $Si(OH)_4$  in the boundary layer gas,  $\rho_v$  the equilibrium concentration of the volatile  $Si(OH)_4$ ,  $L$  a characteristic length,  $\eta$  and  $\rho$  are the viscosity and concentration of the boundary layer gas. This expression then can be simplified if one notices that expression in the parentheses of Eq. (3.9) are simply the dimensionless Reynold's number ( $Re$ ) and the dimensionless Schmidt number ( $Sc$ ). This equation does not directly show the temperature dependence of the linear volatilization rate constant but clearly indicates that  $SiO_2$  vaporization from the surface decreases when the boundary layer viscosity increases.

### 3.3.4 SiC corrosion in extreme hot steam environment

Although at normal reaction operation conditions, SiC ceramic parts and components are not expected to be exposed to temperatures much higher than 300°C, and their corrosion is not expected to be significant, it is extremely important to understand how these elements will operate in the case of emergency situation. In a situation similar to the 2011 Fukushima reactor

accident, these parts could be potentially exposed to very hot steam (up to 2000°C) flowing with high speed due to partial meltdown of fuel rods and collapse of the reactor roof.

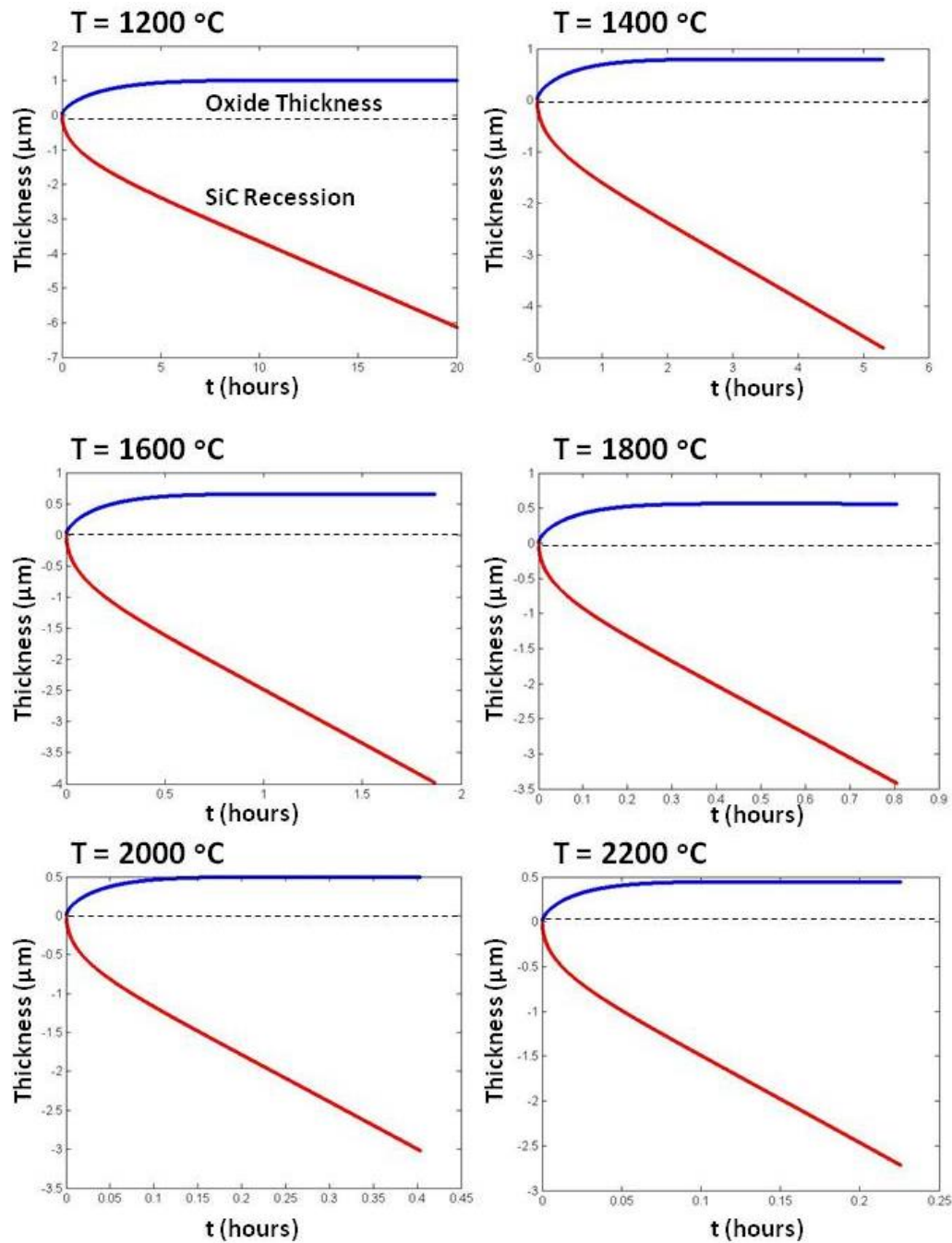


**Figure 30** SiC recession due to parabolic oxidation and volatilization in the “free-boiling” regime (reactor with collapsed roof). All the parameters used in these calculations are described in the text.

To perform this estimate, we used the data from [35], namely:  $k_p = 0.50 \mu\text{m}$  and  $k_l = 0.02 \mu\text{m}$  in an environment containing 50% $\text{H}_2\text{O}$ /50% oxygen at 1 atm total pressure and temperatures between 1200 and 1400 °C, and for the gas flowing with the speed 4.4 cm/s. Eqs. (3.8) and (3.9) allow to rescale the two kinetic parameters  $k_p$  and  $k_l$  to other temperature and gas speed if the parameters  $\Delta G_0^{\text{SiO}_2}$  (heat of oxidation),  $\Delta G_0^{\text{Si(OH)}_4}$  (heat of volatilization), and  $v$  (gas flow velocity) are known. If we assume that reactor roof is collapsed and water is boiling at the reactor bottom, we can estimate gas flow velocity using the formula for the velocity of gas flowing from chimney pipe,

$$v = C \sqrt{2gh \frac{T_i - T_o}{T_i}}, \quad (3.10)$$

where  $T_i$  is the average inside temperature (K),  $T_o$  is outside air temperature,  $g$  is gravitational acceleration,  $9.81 \text{ m/s}^2$ ,  $h$  is the chimney height (we take is of the order of the length of the fuel rode,  $h \sim 20 \text{ ft.} \sim 6 \text{ m}$ ).  $C$  is the so-called discharge coefficient that is usually taken between 0.65 and 0.7. For the standard free energy of volatilization  $\Delta G_0^{\text{Si(OH)}_4}$ , we took the value of 108 kJ/mole obtained for the lean-burn environment [39].

We did not find any accurate experimental information for  $\Delta G_0^{\text{SiO}_2}$ , the standard free energy of  $\text{SiO}_2$  oxidation by water. This is probably related to the fact that interaction of amorphous  $\text{SiO}_2$  network with water is quite complicated and depends on many factors. In our previous theoretical paper, we considered different water migration mechanisms in silica, and found that in open  $\text{SiO}_2$  networks that contain multi-atom rings, water molecule may migrate as a whole, while in more dense environments,  $\text{H}_2\text{O}$  molecule may split, and more sophisticated



migration mechanisms may turn on [41]. For estimates, we took the barrier of  $0.9 \text{ eV} = 86.4 \text{ kJ/mol}$  corresponding to the migration of water molecule as a whole through six-fold  $-\text{Si-O-Si-O} \dots$  rings (with six Si atoms) calculated in this paper as an estimate for the heat of silica oxidation by water,  $\Delta G_0^{\text{SiO}_2}$ . Then one can write out the scaling relations for the coefficients  $k_p$  and  $k_l$  that allow estimating them at different temperatures. Namely,

$$\begin{aligned} k_{l,T_i} &= k_{l,T_{i0}} \cdot \left( \frac{(T_i - T_o)}{(T_{i0} - T_o)} \cdot \frac{T_{i0}}{T_i} \right)^{1/4} \cdot \exp \left( - \frac{\Delta G_0^{\text{Si(OH)}_4}}{R} \cdot \left( \frac{1}{T_i} - \frac{1}{T_{i0}} \right) \right) \\ k_{p,T_i} &= k_{p,T_{i0}} \cdot \exp \left( - \frac{\Delta G_0^{\text{SiO}_2}}{R} \cdot \left( \frac{1}{T_i} - \frac{1}{T_{i0}} \right) \right) \end{aligned} \quad (3.11)$$

where  $T_{i0}$  is the temperature (in our case,  $T_{i0} = 1200^\circ\text{C}$ ) for which we have experimental data for the coefficients  $k_p$  and  $k_l$ . Also, before estimating these coefficients for other temperatures, we rescaled the original experimental coefficients to the flow velocity given for the temperature  $T_{i0}$  by Eq. (3.11).

Figure 3 compares the kinetics of  $\text{SiO}_2$  layer formation and SiC recession for different temperatures starting at  $1200^\circ\text{C}$ . In all of the cases we used a “free-boiling” regime (“collapse of the reactor roof”), water boils inside and vapor goes away from the system with the velocity described by the chimney pipe formula of Eq. (3.11). It is obvious that the shape of all the curves is self-similar, and the temperature effects can be described using the rescaling of the vertical and horizontal axes. The rescaling coefficients will be defined by the temperature. One can observe a very strong horizontal compression of the curves (or the reduction of the characteristic time scale) that means that all of the recession processes accelerate with temperature.

Figure 4 shows the steady-state linear SiC recession rate (which is reached when the thickness of the SiO<sub>2</sub> layer saturates due to the two processes: (i) its growth due to SiC oxidation by water, and (ii) its evaporation at the external surface. Although the recession rate increases fast with temperature, even at 2200°C it does not exceed 10µm/h that is of the order of individual SiC filament thickness in the SiC fiber. This means that even in the worst-case scenario (2200°C and the steam velocity is defined by Eq. (3.11) which does not take into account the turbulence near the surface caused by the surface roughness), we do not expect that the fiber recession will be larger than one the thickness of one filament per hour. On the other hand, the standard fiber contains 50,000 such filaments, i.e., its radius is of the order of 200 filament radii. Consequently, the fiber network will reach the state of a complete collapse not earlier than after some 200 hours (8 – 9 days). This is a very reasonable time to perform emergency operations accurately and without any rush. Of course, this estimate is valid if one assumes that the water vapor attacks the fiber from outside only, i.e., water molecules do not penetrate between the filaments of the fiber when they will have a possibility to attack many filaments simultaneously from both inside and outside the fiber which could significantly accelerate the recession processes. This implies that the space between filaments should be such as to prevent penetration of water molecules in between the filaments.

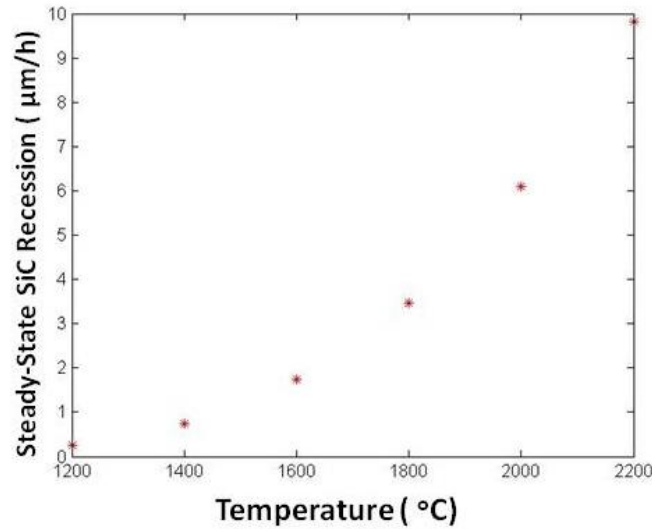


**Figure 31** Steady-state quasi- linear SiC recession rate as a function of temperature

In reality, the steam velocity near the SiC walls should be much lower than in the estimate performed above because: (i) at the interfacial layer between the gas and the surface of the fiber, gas velocity will be lower due to ‘sticking’ effects (especially when the surface is rough); (ii) turbulence processes should be quite significant (especially near the surface of the fiber) which will slow down the gas motion even more. Therefore, the estimate above should be considered as the upper limit for the SiC fiber recession (performed for the laminar flow of an ideal gas and neglecting any “sticking” effects at the surface). In a real situation, the recession should be significantly lower.

### 3.3.5 Other silica based ceramics in hot steam environment

The extensive recession tests for silicon carbide [36] and silicon nitride [42] ceramics in actual combustion environments indicate that the recession rate of these ceramics is extremely large. To overcome this problem, environmental barrier coating (EBC) systems for non-oxides

ceramics were proposed by several research groups [36, 43-45]. The EBC materials must sustain under combustion field and protect the substrate from the oxidation and corrosion for the anticipated lifetime. Because the EBC layer coated on the non-oxide substrate, the coefficient of thermal expansion (CTE) of EBC materials must be compatible to that of the substrate. Hence, the low CTE materials such as rare earth di-silicates ( $\text{Ln}_2\text{Si}_2\text{O}_7$ , Ln = rare earth), mullite ( $\text{Al}_6\text{Si}_2\text{O}_{13}$ ), zircon ( $\text{ZrSiO}_4$ ), and hafnion ( $\text{HfSiO}_4$ ) could be potential candidates for EBC materials for silicon carbide and silicon nitride ceramics. In particular, volatility data in high steam environments indicate that rare earth monosilicates ( $\text{RE}_2\text{SiO}_5$ ; RE: rare earth element) have lower volatility than the currently used barium strontium aluminum silicate (BSAS) EBC topcoat in combustion environments [35]. Rare earth silicates also exhibit superior chemical compatibility compared to BSAS. The superior chemical compatibility and low volatility are key attributes to achieve higher temperature capability. The chemical compatibility is especially critical for EBCs on  $\text{Si}_3\text{N}_4$  because of the high chemical reactivity of some of the oxide additives in  $\text{Si}_3\text{N}_4$ . In simulated combustion environments, EBCs with a rare earth mono-silicate top coat exhibit superior temperature capability and durability compared to the current state-of-the art EBCs with a BSAS top coat.

The phase stability and recession mechanisms of some silicates were examined in a high speed steam jet environment at 1300 and 1600° C for a for different exposure time intervals. The phase stability and recession mechanism of  $\text{Lu}_2\text{Si}_2\text{O}_7$  were examined in a high speed steam jet environment at 1300 and 1500 8C for a 100 h exposure time test [46]. In was found that after high temperature steam jet exposure of  $\text{Lu}_2\text{Si}_2\text{O}_7$  for 100 h, a porous microstructure was formed on the exposed samples surface. Microstructural analysis indicated that the grain size of the 1500°C sample was slightly larger than that of the 1300°C sample. At 1300°C,  $\text{Lu}_2\text{Si}_2\text{O}_7$

completely decomposed to form a  $\text{Lu}_2\text{SiO}_5$ . On the other hand, both  $\text{Lu}_2\text{SiO}_5$  and  $\text{Lu}_2\text{Si}_2\text{O}_7$  phases were observed in the 1500° C test sample.

X-ray studies of recession behavior of  $\text{Lu}_2\text{SiO}_5$  phase indicated that no phase change was observed for all samples after 100 h steam exposure [47]. Detailed scanning electron microscopy examinations showed some cracks formation on the bulk surface for the samples at 1400 and 1500°C. Also, porous structure was formed on the bulk surface for the samples of 1300 and 1400°C. As for the 1500°C sample, the porous structure disappeared after the exposure test. The high magnification images of the 1300°C sample showed the depletion of grain boundary glassy phase. However, for 1400°C sample, boundary phase was formed again, and the grain growth can be identified for the sample of 1500°C. The recession mechanism can be explained by a mass transfer of evaporated species from the bulk surface, and the weight loss rate measured can be interpreted by Arrhenius plot.

In the development of environmental barrier coating system for silicon nitride ceramic, a corrosion behavior of mullite was examined under static state water vapor environment at elevated temperatures [48]. Results showed that a small amount of sodium, which was present in mullite bulk as an impurity, accelerated the water vapor corrosion of silica component and decomposition of mullite into alumina phase. To improve the selective corrosion of the boundary phase in silicate compounds, a mullite /  $\text{Lu}_2\text{Si}_2\text{O}_7$  eutectic system without boundary glassy phase was developed. The eutectic composition was  $\text{Al}_2\text{O}_3:\text{SiO}_2:\text{Lu}_2\text{O}_3 = 27.3:54.6:18.1$  in molar ratio and the eutectic temperature was estimated to be ~1500–1520°C. No weight loss was measured after the static state water vapor corrosion test at 1300°C for 100 h. However, the recession of mullite phase in the eutectic oxide occurred after exposure to high speed steam-jet environment at 1200°C.

For  $\text{Yb}_2\text{Si}_2\text{O}_7$ ,  $\text{Yb}_2\text{SiO}_5$  phase was formed on the bulk surface by the decomposition of the initial phase and the elimination of silica component at elevated temperatures [49]. The phase ratio of  $\text{Yb}_2\text{SiO}_5/\text{Yb}_2\text{Si}_2\text{O}_7$  increased up to  $1400^\circ\text{C}$  and then decreased above  $1400^\circ\text{C}$ . Fine grains were generated on the bulk surface at  $1300^\circ\text{C}$ . The phase decomposition caused on the grain interior. A porous structure was formed on the bulk surface during the test at  $1400^\circ\text{C}$ . Surface cracks were generated for  $1400^\circ\text{C}$  test sample, and a smooth surface was generated on the surface of  $1500^\circ\text{C}$  test sample. The triple points of the grains were bridged with a glassy phase.

A corrosion test in static state water vapor environment and a recession test in high velocity steam jet environment for zircon bulk were performed at  $1300^\circ\text{C}$  [50]. The trace of the water vapor corrosion could be recognized on the grain surfaces and at the grain boundaries for the sample after the static state corrosion test. Sand ripple-like morphology was generated on the grain surfaces and etch pits with less than  $0.1\text{ }\mu\text{m}$  size were formed at the grain boundaries. A porous structure was formed on the bulk surface of the sample after the steam jet test. A glassy phase enriched with silica could be recognized on the surface of the sample after the test. Cracks were induced on the bulk surface during the test. The zircon phase at the bulk surface decomposed into monoclinic zirconia phase and the fraction of silica component at the bulk surface decreased by the steam jet test. The monoclinic zirconia phase was observed to regenerate and grow on the bulk surface.

These references clearly indicate that interaction between silicates and hot steam are quite complicated and involve many different factors including chemical reactions, phase transformations, diffusion, and dimensional stability. Typically, when the EBC layer is attacked and corroded by water vapor, many cracks are induced in the EBC layer during the test and thus the silicon carbide or silicon nitride substrate continues to be oxidized by water vapor and/or

oxygen to some extent. These cracks are caused by the CTE differences between EBC materials and the substrate. In the case of silicon nitride with  $\text{Lu}_2\text{Si}_2\text{O}_7$  EBC, the silica scale formed on the entire surface of the substrate. On the other hand, in the case of silicon nitride with zircon, the silica phase only generated at the region near the cracks and the zircon layer and the substrate remained adherent during the test [51]. As results, zircon is considered to be a very promising material for the EBC applications.

### **3.3.6 Specifics of choosing corrosion resistant ceramics for nuclear applications**

The EBC layers for additional protection of SiC ceramics that could be potentially for designing different components of light water reactor (LWR) should satisfy several additional requirements that are insignificant for combustion systems. The main requirement is that any EBC material not exhibit high absorption cross section for thermal neutrons, in order not to significantly interfere into the reactor operation regimes and neutron economy. Although at normal reaction operation conditions, SiC ceramic parts and components are not expected to be exposed to the temperature much higher than  $300^\circ\text{C}$ , these elements are quite stable, and their corrosion should not be very significant, i.e., they could operate for a long time without additional protection. However, in the case of emergency situation similar to the 2011 Fukushima reactor accident, these parts could be exposed to a very hot steam (up to  $2000^\circ\text{C}$ ) flowing with high speed due to partial meltdown of fuel rods and the reactor roof collapse.

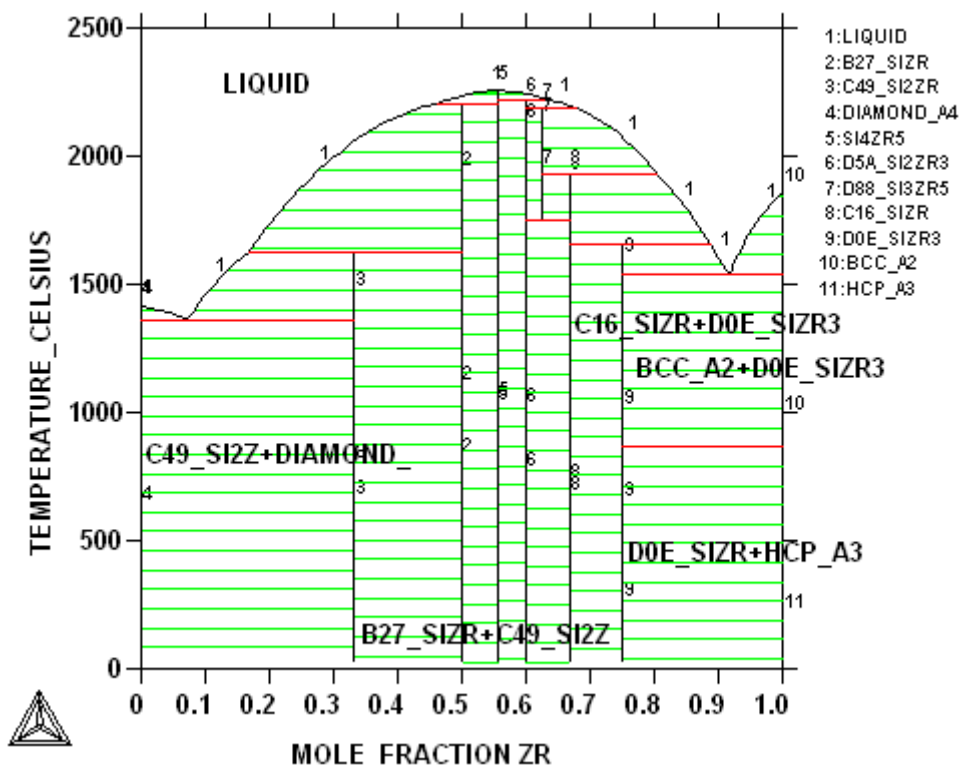


**Figure 32** Si-Zr phase diagram calculated using ThermoCalc software and the TTZR1 databases by ThermoTech, Inc.

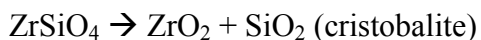
Therefore, most of silicates reviewed in the previous section (e.g., Hf and La based ceramics) cannot be used in LWRs because these elements have extremely high neutron absorption. Silicate ceramics that include only Be, Al, Mg, and Zr atoms should be preferable for using in reactors because these elements have much lower cross section for neutron absorption. Although these metals may form different silicates including known minerals beryllium silicate ( $\text{Be}_2\text{SiO}_4$ ) and beryllium aluminum silicate ( $\text{Be}_3\text{Al}_2\text{Si}_6\text{O}_{18}$ ), here we analyze the case of zircon ( $\text{ZrSiO}_4$ ) only because zirconium metal is widely used for different components (including fuel rods) in LWRs.

Figure 32 shows the Si-Zr phase diagrams calculated by using the ThermoCalc computational thermodynamics codes and the TCBIN database [36]. This figure indicates that



zirconium can form several different silicides (SiZr –B27\_SiZr; Si<sub>4</sub>Zr<sub>5</sub> - D0E\_SiZr<sub>3</sub>, Si<sub>2</sub>Zr<sub>3</sub> – D5A\_Si<sub>2</sub>Zr<sub>3</sub>; and Si<sub>3</sub>Zr<sub>5</sub> - D88\_Si<sub>3</sub>Zr<sub>5</sub>) that may stay solid for temperatures up to 2100 – 2200°C. If a layer of zirconium is positioned on top of silicon substrate, one could imagine that at higher temperatures when diffusion processes become intensive, Si and Zr layers will interpenetrate into each other, and their interfacial region will contain several different silicides. The crystal structure of material at a given spatial point is a function chemical composition at this point and the temperature. It is quite logical to imagine that in the interfacial areas with comparable concentrations of Zr and Si, silicides like SiZr, Si<sub>4</sub>Zr<sub>5</sub>, Si<sub>2</sub>Zr<sub>3</sub>, and Si<sub>3</sub>Zr<sub>5</sub> (most likely, all of them) will be formed. Also, a formation of multilayer structure in which each level represents a silicide with a given chemical composition is very likely as well. These silicides will avoid melting up to very high temperatures.

Now consider that the Si-Zr system discussed above is exposed to oxygen or water steam at very high temperatures. Figure 8 shows the ZrO<sub>2</sub>-SiO<sub>2</sub> pseudo-binary phase diagrams calculated by using the FactSage computational thermodynamics codes and FactSage FACT oxide database 2010 [53]. This diagram definitely indicates that zircon, ZrSiO<sub>4</sub>, will be thermodynamically stable until temperature T=1530°C, when it decomposes into ZrO<sub>2</sub> and cristobalite according to the following eutectoid reaction:



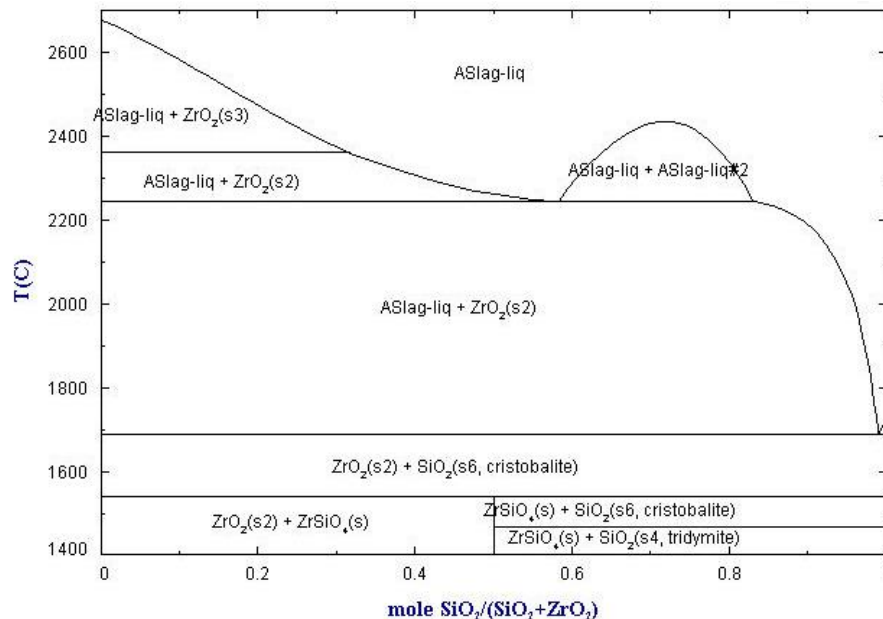


**Figure 33** Pseudo-binary ZrO<sub>2</sub>-SiO<sub>2</sub> phase diagram (FactSage oxide database, 2010, [51])

How this phase transformation could affect the protective properties of zircon remains to be established experimentally. However, the critical temperature for this system is that of the eutectic nonvariant reaction at 1692°C, when the SiO<sub>2</sub> in the physical mixture formed at T=1530°C, will be subjected to incipient melting.

In the literature, the effect of “softening” of zircon was discussed between 1600°C and 1800°C, accompanied by very little shrinkage up to 1750°C. The high grade zircon sand is largely used in foundry as mold. It does not wet the molten metal, thus rendering a better and smoother surface to the castings. It is estimated that about 75% of the total world zircon production is used as molding sand and in the manufacture of refractory bricks, zirconium compounds and ceramics. Only 25% is used for the extraction of metal or in the manufacture of alloys. Zircon exhibits many characteristics that make it very suitable for super refractory purposes. In addition to a high melting point it was very low thermal expansion and good

resistance to abrasion. Zircon is used when acidic refractory is required while zirconia refractories are considered to be basic.

In summary, experimental research that needs to be conducted on these two substances, the SiC and  $\text{ZrSiO}_4$ , should emphasize two clear goals: 1. To understand the effects of the  $\text{Si(OH)}_4$  (volatilization of  $\text{SiO}_2$ ) formation upon the kinetics of the SiC recession (if any) at the temperature range of interest; 2. To understand how the peritectoid reaction of the  $\text{ZrSiO}_4$  decomposition into  $\text{ZrO}_2$  and cristobalite affects the  $\text{ZrSiO}_4$  protective properties; and 3. To explore the behavior of  $\text{ZrSiO}_4$  up to the temperature of incipient melting and obtain clear data on the influence of the latter upon the  $\text{ZrSiO}_4$  protective properties.

### **3.3.7 Some atomic-scale arguments**

To understand the difference in steam corrosion of silica and zircon, we performed self-consistent, first-principles atomic-scale calculations for: (i) amorphous Si phase; (ii) amorphous zirconia phase; (iii) pure stoichiometric zircon. The calculations the amorphous  $\text{SiO}_2$  were performed for 72-atom amorphous  $\text{SiO}_2$  supercells. These structures were initially generated by using the Monte Carlo bond-switching method, and relaxed until the total energy was minimized (see [41] for more details).

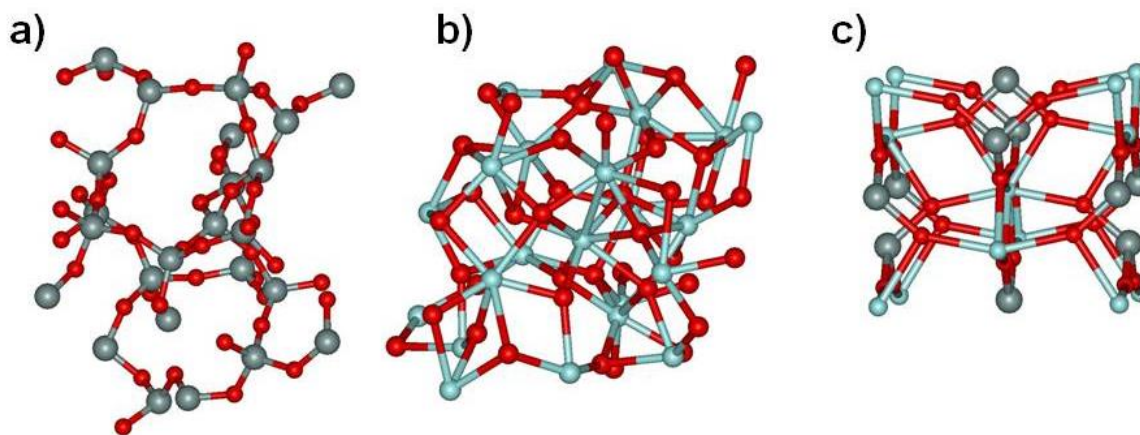


**Figure 34** Schematics of atomic structure for: (a) amorphous  $\text{SiO}_2$ ; (b) amorphous  $\text{ZrO}_2$ ; (c) regular stoichiometric zircon  $\text{ZrSiO}_4$ . Zirconium is shown in cyan, Si – in grey; O – in red

The self-consistent electronic structure calculations were based on the generalized gradient approximation (GGA) for exchange and correlation, and plane waves [44]. We used the GGA functional of Perdew, Burke, and Ernzerhof (PBE) [55], which gives good results for chemisorption of molecules at transition-metal surfaces. Projected Augmented Wave (PAW) scalar relativistic pseudopotentials [56, 57], and the VASP code [58] were used. The energy cutoff for the plane-wave basis was set at 500 eV, and all integrations over the Brillouin zone were done using the Monkhorst-Pack scheme with four  $\mathbf{k}$  points in the relevant irreducible wedge [59]. Inclusion of additional  $\mathbf{k}$  points was found to have minimal effect on the total-energy differences of interest here. For each supercell, we relaxed all atoms until the quantum-mechanical force on each atom became smaller than 0.02 eV/Å.

The relaxed structures of a single “amorphous”  $\text{SiO}_2$  and  $\text{ZrO}_2$  supercell are shown in Figure 31a and 31b. The structure for  $\text{ZrO}_2$  was obtained from a relaxed  $\text{SiO}_2$  structure by substitution all Si atoms by Zr atoms with subsequent relaxation of supercell parameters (lattice vectors) and

all atomic coordinates. The first interesting thing to notice is that amorphous  $\text{SiO}_2$  and amorphous  $\text{ZrO}_2$  phases have nearly the same volume density per unit (i.e., any fixed volume contains same number of units of both materials). It means that in amorphous  $\text{SiO}_2$  some Si atoms could be substituted with Zr atoms without significant change of the volume. Second, atomic network of the two amorphous oxides is very different. In  $\text{SiO}_2$ , the structure is quite open, and it contains many large  $-\text{Si-O-Si-O}-\dots$  rings (six-fold or even larger). This is the reason why amorphous  $\text{SiO}_2$  oxide is so vulnerable to the attack of oxygen and/or water vapor – the molecules may migrate through the large ring network with quite low migration energy barrier [41].  $\text{SiO}_2$  oxide may be attacked not only at the surface but in the bulk also which significantly accelerates oxide recession in hot steam and its evaporation through the formation of volatile  $\text{Si}(\text{OH})_4$  species. Evaporation will further increase the porosity and further accelerate the degradation process.

Amorphous zirconia forms a much denser network which is related to the fact that Zr-O interatomic distance ( $\sim 2.1\text{-}2.2 \text{ \AA}$ ) is much longer than the Si-O distance ( $\sim 1.6\text{-}1.7 \text{ \AA}$ ). Also, each Si atom in  $\text{SiO}_2$  is 4-fold coordinated and O – 2-fold coordinated while in zirconia the coordination of both type of atoms is higher (in regular phases Zr is 8-coordinated, and O is 4-coordinated). This results in the formation of the four atom Zr-O-Zr-O rings which fill all the space and which present a much stronger obstacle for migrating water molecules than large rings in amorphous silica. Therefore, the steam corrosion attack may occur only at the zirconia surface (or grain boundaries, cracks, dislocations, or other structural defects) which significantly slows down the corrosion process. Another important issue is that  $\text{Zr}(\text{OH})_4$  hydroxide is not volatile – once formed at the surface it will likely remain there and provide the additional barrier against the migrating water molecules, i.e., the steam corrosion of zirconia is a much slower process.

In the case of periodic zircon structure (a unit cell is shown in Figure 31c), we still have a rather dense network with Zr-O-Zr-O rings, i.e., water penetration will be slow. According to [44], zircon corrosion starts at grain boundaries with the process of eliminating Si from the grains through the formation of volatile silicon hydroxide. Grains are becoming more and more abundant with zirconium, and eventually form a rough  $\text{ZrO}_2$  surface covered with cracks which are forming due to lattice incompatibility of zirconia with remaining zircon substrate and different CTEs of the two materials. Our structures shown in Figure 7 provide a qualitative explanation of such a degradation mechanism. Let us assume that we have an amorphous oxide structure where Si and Zr atoms are alternating. This structure should be denser than a pure amorphous  $\text{SiO}_2$  because of presence of Zr-O bonds. With removing Si from the network, the remaining structure is becoming more and more compact and dense before it forms amorphous zirconia shown in Figure 7b, and further water diffusion in the bulk becomes suppressed. The corrosion of zirconia still continues at grain boundaries but oxide recession is much slower than in silica because zirconium hydroxide is not volatile.

### 3.3.8 Some Conclusions

Summing up, the results obtained in the present computational study allow for making some preliminary conclusions about the possibilities of using complex silicates ( $\text{SiC}$  and  $\text{ZrSiO}_4$ ) in nuclear reactors and their protection against high-temperature steam corrosion:

1. Most of silicates used in combustion systems are hardly useful for nuclear applications because they contain atoms with high neutron absorption cross sections. Silicate ceramics useful for the nuclear applications should contain only Be, Al, Zr, and/or Mg metal atoms. Although many different silicate ceramics made of these atoms (such as beryllium

silicate, beryllium aluminum silicate, etc.) are known as nature minerals or artificially made ceramics, their use is predicated upon conducting additional experimental research.

2. The best studied silicate is  $\text{ZrSiO}_4$  which is could be useful for nuclear applications because of several reasons:

- (i) First, it is one of least corrosive ceramics in hot steam. Additional experimental research is needed because all of the previous studies were performed at temperatures below  $1600^\circ\text{C}$ , while nuclear applications require ceramics to be stable at  $2000^\circ\text{C}$  (at least for some noticeable period of time). The phase reactions of the  $\text{ZrSiO}_4$  decomposition and incipient melting should be studied and understood in detail
- (ii) Secondly, the zircon thermal properties open up a possibility of using the SiC ceramics in LWR with greater confidence. While a detailed modeling and experimental work is warranted to make this statement with certainty, a possibility exists that interaction between the SiC and the zircaloy in the rod coating at extremely high temperatures will form zircon layer that, in turn, could provide additional protection for different reactor components.
- (iii) Thirdly, it seems plausible to use the mixed  $\text{ZrC-SiC}$  ceramics instead of pure SiC. In such a case, during oxidation zircon is also likely to be formed.

At the present, work is continuing in the following directions:

1. Calculations of water migration barriers in amorphous oxide networks with alternating Si and Zr atoms. This will provide opportunity to make quantitative predictions for different

Zr concentration in the network and use these predictions for calculating the oxide recession rates for different Zr concentration using Eqs. (3.8) - (3.10).

2. Modifying the analysis to take into account the grain boundaries, surface roughness, etc., etc. which appears which Si is washed out from the network.

This analysis will give an opportunity to provide realistic estimates for the reactor protection time in the case of emergency and/or a major LOCA accident.

### **3.4 The Concept of “Self-Healing” for Yttria-Stabilized Zirconia and Development of Protective Coatings for Zr-Based Cladding Materials**

#### **3.4.1 Thermal Activation of Protection Mechanisms**

It is important to remind the reader that tetragonal zirconia is a non-stoichiometric compound. The occupancy factor for oxygen atoms in the crystalline lattice in  $\text{ZrO}_2$  is  $\sim 0.984(4)$ . This implies that tetragonal modification  $\text{ZrO}_{2-\delta}$  has oxygen deficiency  $\delta=0.031(7)$ . It is for this reason that stabilization of zirconia is necessary with lower valence oxides such as  $\text{Y}_2\text{O}_3$  (see Chapter 2).

In [60, 61], we proposed to conduct experimental and modeling research aimed at developing the concept of a self-healing zirconium surface to increase the ability of a zircaloy rod surface to withstand high temperatures [62, 63]. The self-healing effect is achieved at high temperatures (around  $\sim 800^\circ\text{C}$ ) via the optimization of cation and anion transport through the protective layer of YSZ. Additional protection is supposed to be achieved via ancillary additions of Be (several ppm) to the Zircaloy solidifying metal in the process of ingot casting. Both



materials (Be and YSZ) have been demonstrated to render protection against Zr oxidation at elevated temperatures and to achieve the balanced flux of metal cations to the surface, and oxygen anions – inside the bulk of the Zr material. As a result of thus optimized ion diffusion, surface attains a property to self-heal in the case of a crack/defect formation. Following [7, 62, and 63], let's discuss briefly this very important “concept of self-healing”, or “self-repairing”.

There *are two types of transport in zirconia*: the inward oxygen transport, and the outward metal transport. In the first case, if the volume of the newly formed oxide is larger than the volume of the base metal (the so-called “Pilling-Bedworth ratio”  $> 1$  [64, 65]), the oxide scale will be in the state of compression [7]. In turn, this will induce the formation of cracks in the bulk of these oxide scales parallel to the interface between oxide and gas, which appear at certain thicknesses, see Figure 32a, [62, 63]. In the second case, i.e. during oxidation, one could expect that a significant number of vacancies forming as a result of the metal cations moving outward will coalesce at the interface, thereby creating crack/pores [63], Figure 32b. However, when the compressive stress in the oxide scale at the interface between oxide and gas is reduced by the outward cation transport and the cavity formation is avoided by inward transport of oxygen and oxide formation. The overall result of this “mixed” transport mode is the formation of a thinner and more protective, gas-tight oxide scale, Figure 32c [7].

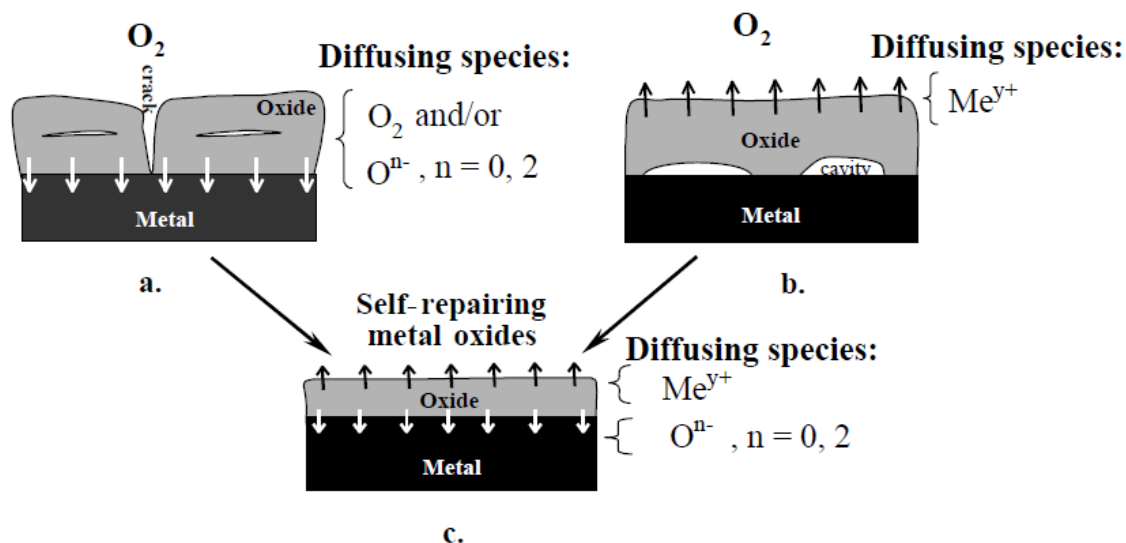


**Figure 35 a.** Oxide growth by inward oxygen transport. White arrows represent the oxidation front at the oxide / metal, O/M interface.

**b.** Oxide growth by outward metal cation transport. Black arrows represent the oxidation front at the oxide/gas, O/G interface.

**c.** Oxide growth by mixed, inward oxygen and outward metal cation, transport [62, 63]

In the case of water cooled zirconium alloy cladding, there is obviously no gas because the cooling water is conditioned and purified using meticulous protocols to a very high standard of electric conductivity and very low amount of impurities. So the original concept was modified in this work [60] in the following way. Under the conditions of neutron irradiation, water molecules dissociate forming ions (“radiolysis” of water). Consequently, oxygen ions are available for inward diffusion. At ambient temperatures, the overall rate of transport of oxygen anions and metal cations inside the  $ZrO_2$  surface layer will be very low. However, when temperature goes up, e.g., as a result of a LOCA/RIA accident, then the metal cation transport will be higher (exponential growth with temperature), and the mechanism of self-healing will be “turned on”. In fact, it is thermally activated protection, but it can be achieved only in zirconia doped with yttria (or other  $3^+$  - valent cation), because in this case there will be a potential for the release of

multiple cations and vacancies at the same time. Additionally, it was proposed to employ ancillary additions of beryllium when casting zircaloy ingot assuming that its protective behavior (against oxidation) will be similar to that observed in aluminum and other metals [8]. Both concepts are analyzed in greater detail below. The modified samples of yttria-stabilized zirconia coated zircaloy clad could be obtained using the technique of modified CVD (Chemical Vapor Deposition) and/or physical vapor deposition (PVD).

Here, it is important to mention that the concept of “thermally-activated protection” was envisioned and formulated for the first time by Heuser (UIUC) [60]. More specifically, his original idea was to cause precipitation of a protective phase crystallites, tentatively going to the surface of the Zr cladding and protecting it against high-temperature oxidation and the release of hydrogen gas. Here, it was modified slightly to achieve thermal activation via other mechanisms such as the formation of BeO on the Zr clad surface, and use the concept of “self-healing” yttria-stabilized zirconia coating for protection.

### **3.4.2 Additions of Several PPM(s) of Beryllium**

It is planned to use ancillary additions of Be from 1ppm up to 10ppm's. In spite of its toxicity, beryllium was used by aluminum industry for the production of both cast and wrought aluminum alloys [66]. In the case of aluminum alloys, it is a very interesting additive. It creates on the surface of molten and even solid aluminum a strong oxide film, which protects the alloy surface from further oxidation. This is particularly important for Al–Mg alloys. In addition, beryllium is the most effective morphology modifying agent for iron-bearing constituent particles [8]. The reason is that beryllium can form compact particles of complex phases with Al and Fe and to a significant extent neutralize the harmful effects of iron upon formability and

fracture toughness. There is also substantial information about the influence of Be upon processes at elevated temperatures, but their interpretation is inconclusive. More specifically, beryllium is used by the aluminum industry worldwide at least for three reasons:

1. It is well known in the aluminum casting art that various surface imperfections such as pits, vertical folds, oxide patches and the like, which form during ingot casting, can develop into cracks during casting or in later processing [66]. A crack in an ingot or slab propagates during subsequent rolling, for example, leading to expensive remedial rework or outright scrapping of the cracked material. Most ingots are worked in some manner; however, working will not heal a cracked ingot. For rectangular ingots of wrought aluminum alloys, during solidification the atoms of Be rapidly move to the mold-metal interface and prevents the formation of excessive oxides that which create stress risers (eventually initiating cracks). Be modifies oxide properties and/or behavior and oxide thickness such that stress risers do not create unacceptable cracking. This is illustrated by Figure 33 below [66]:

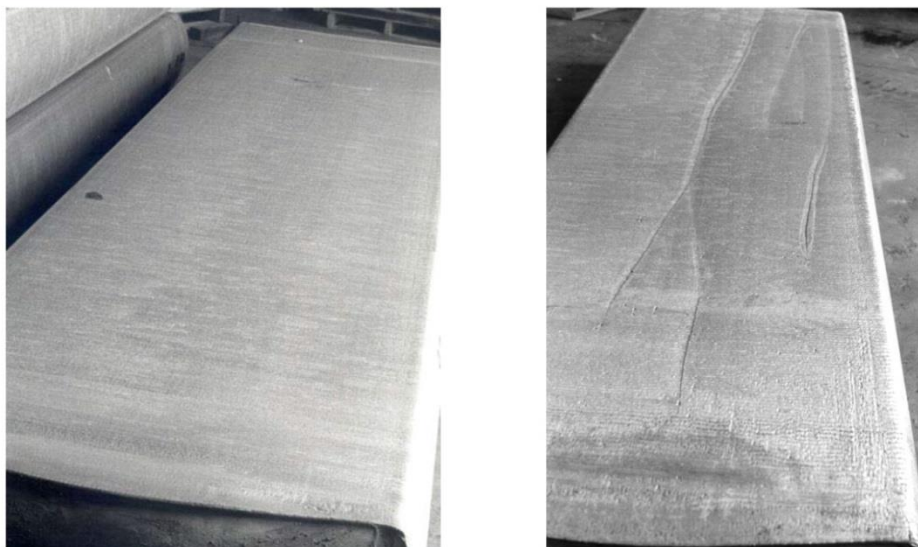


**Figure 36** Rectangular aluminum ingot (alloy of the 7xxx series) with addition of 12 ppm Be (left) and without additions of Be (right), [66]

In the past, beryllium has been added, usually at part per million by weight (ppm) levels to some of these alloys to control surface defects. Beryllium is effective at controlling surface defects in aluminum cast ingots [66]

2. For castings, Be reduces the kinetics of oxide formation such that alloy composition can be maintained longer (i.e., Mg burn off is averted) and the formation of dross is greatly reduced;

3. For aerospace castings, scrap results from flow-line defects which are thought to be the results of reduced fluidity. The true root cause is unknown but thought to be related to surface tension or increased oxides in the metal [60].

Our hypothesis, which is being verified experimentally at UIUC, is that addition of 1 to 10 ppm Be to Zr alloys will result in obtaining similar benefits.

### **3.4.3 Zr Surface modification with YSZ**

Surface modification of core structural components is not a new concept; in particular, MAX ( $M_{n+1}AX_n$ , where M is an early transition metal, A is one of elements in groups 13–16, and X is C and/or N) phases have been considered for high temperature fast neutron reactors because of very good compatibility with molten Pb and Na coolants [12]. Some MAX phases form self-terminating oxides in high-temperature oxidizing environments and may be suitable for LWR applications. Obviously, TRISO fuel forms involve coatings as well, in particular SiC and pyrolytic graphite. This experience forms the basis of the potential use of SiC as LWR cladding.

In [6, 60] we proposed to utilize the exceptionally well-studied (in electrochemical applications) YSZ to achieve modification of the surface of existing LWR cladding material that

can be scaled to industrial throughput requirements. The goal of surface modification will be to shift the  $M+O \rightarrow MO$  reaction away from oxide formation and  $H_2(g)$  generation, thereby leading to accident tolerance. Our confidence in success of the proposed approach is based upon the fact that YSZ possesses excellent chemical inertness, hardness, and it is used as a refractory in jet engines. Additionally, depending on the overall amount of  $Y_2O_3$  (typically from 0.5 to 8 at%) it has thermal expansion coefficient very close to that of monoclinic or tetragonal modifications of  $ZrO_2$ . The ionic conductivity mechanism (due to oxygen anions) is temperature activated and attains non-zero values around  $800^\circ C$ . This is precisely what we need to balance out the fluxes of metal cations to the surface and avoid the onset of crack formation eventually resulting in the exposure of zirconium metal to superheated water vapor resulting in the formation of hydrogen gas.

Thus, combining the ideas of 1 to 10 ppm Be additions to Zr ingot, YSZ as coating material, and self-healing surfaces of zirconium alloys, we can say confidently that the level of protection against the onset of hydrogen evolution will be raised at least  $200^\circ C$  to  $300^\circ C$ .

Fabricated specimens of Be-doped Zr coated with YSZ will need to be tested under  $T-\sigma-p(O_2)$  conditions relevant to off-normal scenarios. Fabrication of the YSZ coating containing different amounts of yttria is generally available via the MO-CVS process. Exceptionally inert YSZ layer will ensure protection, if not altogether elimination, of accelerated zirconium oxide growth.

Pure  $ZrO_2$  displays three polymorphs at atmospheric pressure: cubic (c-), tetragonal (t-), and monoclinic (m-) [52]. At ambient pressure, the ground-state  $ZrO_2$  has a monoclinic structure up to a temperature of 1450 K [53] when the m- to t-phase transition occurs accompanied by a

decrease in unit-cell volume. The cubic fluorite phase of zirconia is only thermodynamically stable at temperatures higher than 2650 K. A simple explanation of this fact is that  $\text{Zr}^{4+}$  ions appear to be too large for an efficiently packed rutile structure and too small to form the fluorite structure [54]. Stabilization of c- $\text{ZrO}_2$  down to room temperature can be achieved by doping with  $\text{Y}^{3+}$  [55] which forms the YSZ ceramics used in practical applications. The overall amount of  $\text{Y}_2\text{O}_3$  necessary to achieve the optimal combination of properties will be established in the proposed study. The lattice constant for this structure obtained from our first-principles, self-consistent electronic structure calculations is 5.17 Å (corresponding to the Zr-Zr distance of 3.65 Å between two nearest Zr neighbors), in a good agreement with the experimental value of 5.07 Å [56], see Figure 34 below.

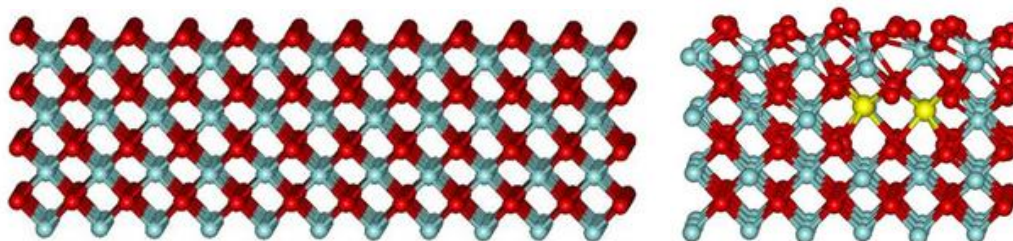


**Figure 37 Left:** Atomic-scale models for YSZ surface: (a) a free (001) surface for oxygen saturated stabilized cubic  $\text{ZrO}_2$  structure; **Right:** YSZ (001) surface, schematics of Y (a), Mn (b), and La (c) subsurface substitutional defects. In each case, two subsurface Zr atoms are substituted by dopant impurity atoms and one oxygen vacancy is added.

Oxygen atoms are shown in red, Zr – in light blue balls, Y – in yellow [66]

All calculations are based on the generalized gradient approximation (GGA) for exchange and correlation, and plane waves [32]. We used the GGA functional of Perdew, Burke, and Ernzerhof (PBE) [33], which gives good results for chemisorption of molecules at transition-metal surfaces. Projected Augmented Wave (PAW) scalar relativistic pseudopotentials [34, 35], and the VASP code [36] were used. The energy cutoff for the plane-wave basis was set at 500

eV, and all integrations over the Brillouin zone were done using the Monkhorst-Pack scheme with eight  $\mathbf{k}$  points in the relevant irreducible wedge [47]. Inclusion of additional  $\mathbf{k}$  points was found to have minimal effect on the total-energy differences of interest here. The total number of atoms varied between 200 and 350 for different periodic supercells. For each supercell, we relaxed all atoms until the quantum-mechanical force on each atom became smaller than 0.02 eV/Å. All the calculations were spin-polarized. Activation barriers were calculated using the nudged-elastic-band method [48].

The formation energies and migration barriers for several different loadings of  $\text{ZrO}_2$  with yttria will be determined, and the role of different defects- clearly elucidated. In particular, we will investigate the role of different point defects (oxygen vacancies, interstitials, substitutional defects, etc.) in degradation of bulk materials, surfaces, and interfaces and in the processes of transport and trapping of different atoms at interfaces. We plan to use the values calculated from first-principles for parameterization the Kinetic Monte Carlo (KMC) codes for calculating transport coefficients.

### **3.5 Computational Thermodynamics Assessment of Feasibility of Fe-Cr-Al Coatings for Zircalloys 2 and 4**

#### **3.5.1 Introduction and Description of the Problem**

There are growing efforts to replace zirconium based alloys as clad materials by some other, less-oxidation prone materials. The basic idea is to eliminate deficiencies of Zr-based alloys and achieve a more reliable performance both under design-basis and beyond-design-basis accident scenarios [67]. However, due to the well-known conservatism of the NRC and other



regulatory bodies, one can envision that a faster way to arrive at a feasible solution is to use coatings. One effort to develop a oxidation resistant coating for Zr alloys Zircaloy-2 and Zircaloy-4 was documented in [6], via the application of the Fe-Cr-Al coatings forming a very thin protective layer of alumina scale on the clad surface. Coating of the general composition  $M\text{Cr}$  and  $M\text{CrAl}$ , where  $M=\text{Fe}, \text{Ni}$ , or  $\text{Co}$ , have been used extensively in energy-producing steam and gas turbine components [67]. Operate in a severe environment at elevated temperatures. A large number of oxidation-resistant Ni–Cr–Al coatings are available for protection of gas turbine protection at service temperatures of up to about 1100°C [68-76]. For these Ni-based coatings, the Cr content ranges from 3 wt. % to 22 wt. % and the Al content ranges from 2 wt. % to 20 wt. % with no or little Fe. Most of the Ni–Cr–Al coatings are processed using conventional methods and exhibit normal grain sizes. Recently, some investigators processed Ni–Cr–Al coatings with a nanoscaled grain structure [68-76]. Several Fe–Cr–Ni–Al coatings with nanoscaled grain structure are also reported in literature [69]. Liu and co-workers [77, 78] reported the oxidation characteristics of sputtered-deposited nanocrystalline Fe–Cr–Ni–Al coatings with 25–26 wt. % Cr, 19.3 wt. % Ni, and 3.4–4.2 wt. % Al with and without 1.8 wt. %Mn.

### **3.5.2 Fe-Cr-Al Protective Coatings for Zircalloys: Selection of the Optimal Process**

#### **Parameters**

In this part of the dissertation, a computational thermodynamics approach has been undertaken to design and assess potential Fe–Cr–Al systems to produce stable nano-structured corrosion-resistant coatings that form a protective, continuous scale of alumina at elevated temperatures on zircaloy cladding. In so doing, it was important to answer the following two questions:

1. What is the optimal composition window for this kind of coating on the surface of Zr cladding?
2. What are any potential “show-stoppers” for this approach to improving Zr cladding’s thermal stability?

In order to answer both questions, a computational thermodynamics approach was used. In the first case, it is necessary to determine the concentrations of alloying elements and the temperature of the deposition process that would allow avoiding the formation of very brittle particles of the  $\sigma$ -phase. In the second, it is necessary to develop a detailed understanding whether low-temperature incipient melting is possible due to the existence of a eutectic or peritectic reactions. The results of this computational research are provided below.

#### **3.5.2.1 Fe-Cr-Al Composition “Window” and Deposition Process Temperature**

Binary Fe-Cr and ternary Fe-Cr-Al phase diagrams were calculated to help identify compositional ranges without the undesirable brittle phases. The computational results identified a series of Fe-Cr-Al coating compositions that maintain long-term stability at elevated temperatures. First, it was necessary to understand how much Cr and Al such a coating should contain. We started with the binary Fe-Cr phase diagram, Figure 35. As it can be seen, it exhibits a miscibility gap in the temperature range from  $\sim 500^{\circ}\text{C}$  to  $\sim 810^{\circ}\text{C}$ . This gives us a tentative range of temperatures to avoid in the sputtering process if we are to avoid the appearance of the  $\sigma$ -phase. Of course, it will change for the Fe-Cr-Al system.

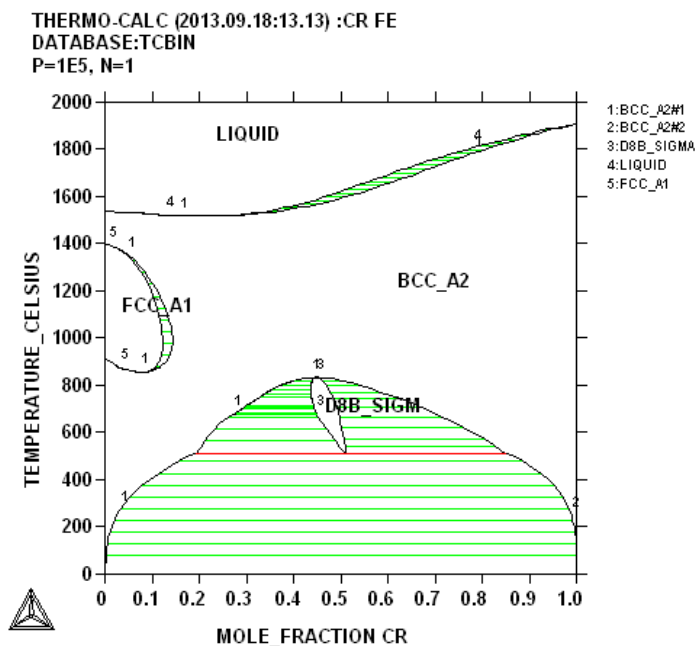


**Figure 38** Binary phase diagram Fe-Cr computed using ThermoCalc ver. S. Green lines represent connodes (tie-lines).

To understand how significant this change might be, we constructed a series of isothermal cross-sections for the Fe-Cr-Al system beginning with  $T=1123\text{K}$  ( $850^{\circ}\text{C}$ ) and down to  $673\text{K}$  ( $400^{\circ}\text{C}$ ), Figures 35 -42.

THERMO-CALC (2013.08.20:10.31) :FE-CR-AL at T=1123 K  
 DATABASE:TCFE6  
 T=1123, P=1E5, N=1;

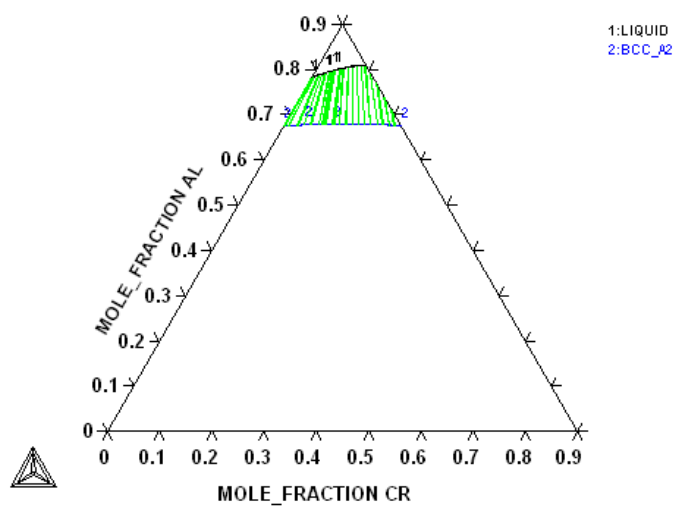


**Figure 39** Fe-Cr-Al isothermal cross-section diagram at 850°C

THERMO-CALC (2013.09.18:12.21) :FE-CR-AL at T=973 K  
 DATABASE:TCFE6  
 T=973, P=1E5, N=1;

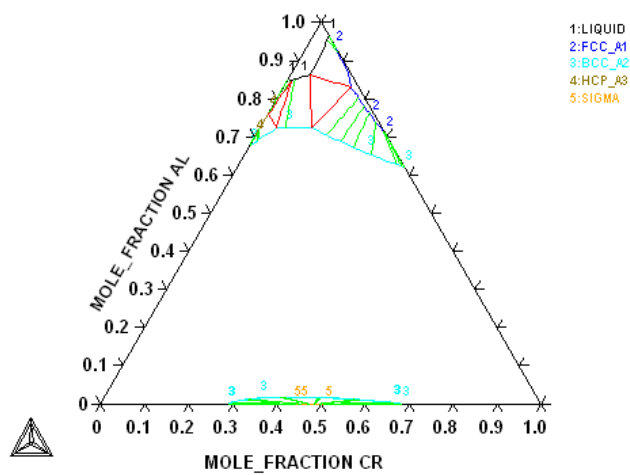


**Figure 40** Fe-Cr-Al isothermal cross-section diagram at 800°C

THERMO-CALC (2013.09.18:12.25) :FE-CR-AL at T=923 K  
 DATABASE:TCFE6  
 T=923, P=1E5, N=1;

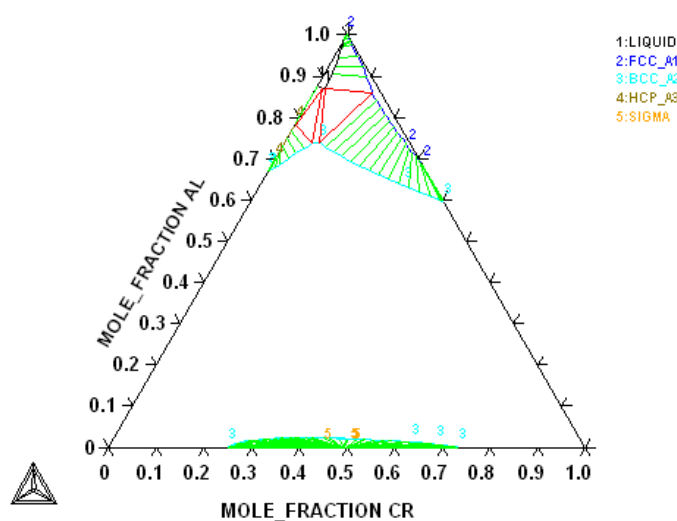


Figure 41 Fe-Cr-Al isothermal cross-section diagram at 700°C

THERMO-CALC (2013.09.18:12.28) :FE-CR-AL at T=873 K  
 DATABASE:TCFE6  
 T=873, P=1E5, N=1;

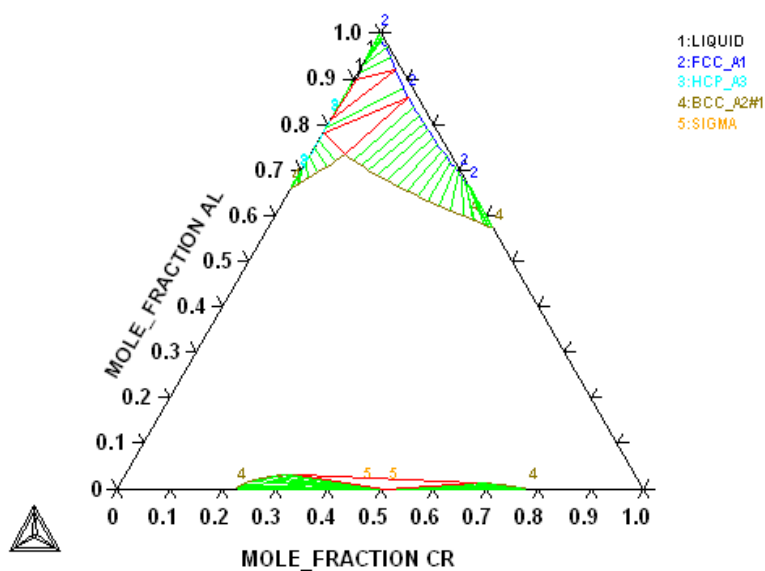


Figure 42 Fe-Cr-Al isothermal cross-section diagram at 600°C

THERMO-CALC (2013.09.18:12.44) :FE-CR-AL at T=823 K  
 DATABASE:TCFE6  
 T=823, P=1E5, N=1;

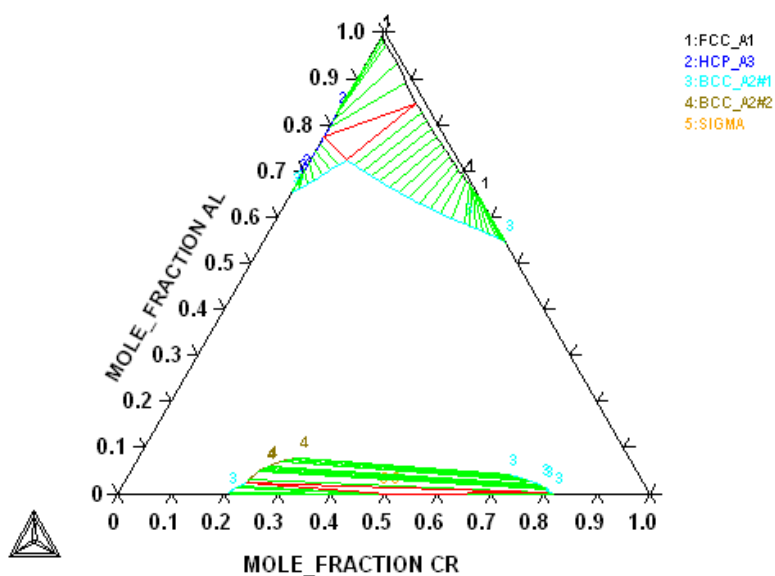


Figure 43 Fe-Cr-Al isothermal cross-section diagram at 550°C

THERMO-CALC (2013.09.18:13.19) :FE-CR-AL at T=773 K  
 DATABASE:TCFE6  
 T=773, P=1E5, N=1;

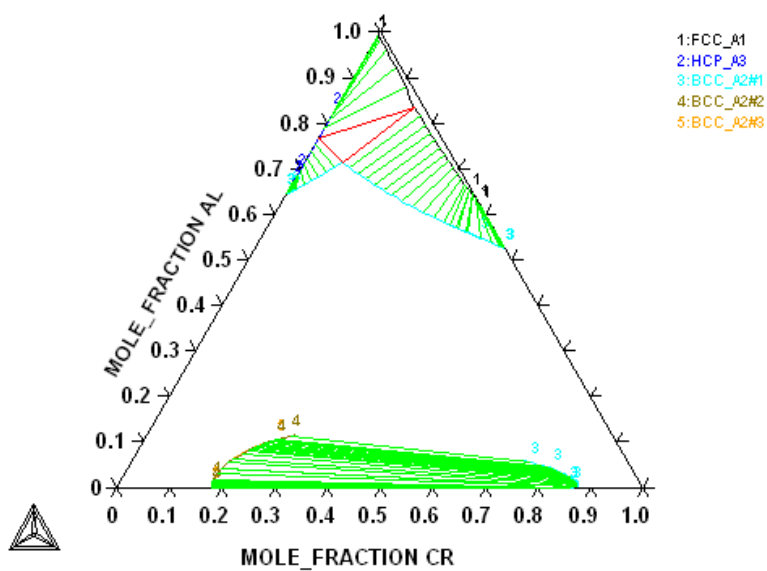
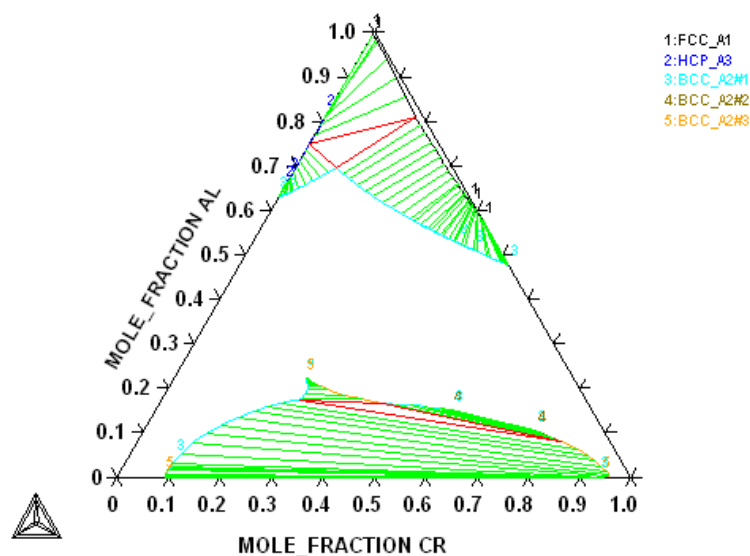


Figure 44 Fe-Cr-Al isothermal cross-section diagram at 500°C

THERMO-CALC (2013.09.18:13.22) :FE-CR-AL at T=673 K  
 DATABASE:TCFE6  
 T=673, P=1E5, N=1;



**Figure 45** Fe-Cr-Al isothermal cross-section diagram at 400°C

From the analysis of these diagrams it becomes clear that the temperature interval of the  $\sigma$ -phase existence is approximately in between 550°C and 800°C for all concentration ranges of the Fe-Cr-Al system (it is for this reason that we decided to avoid constructing a polythermal cross-section diagram). Consequently, for the sputtering process to avoid the formation of the brittle and extremely undesirable  $\sigma$ -phase, the process should be conducted either below 550°C or above 800°C. Probably a higher temperature would be preferable if it is technically feasible.

Another question that needs to be answered is about the preferred chemical composition of the Fe-Cr-Al coating. Using the same criterion as above (the avoidance of the  $\sigma$ -phase) we constructed the two isopleths below, Figures 43 and 44. One gives the idea how much aluminum we need, the other-how much chromium needs to be used in the optimal coating composition.

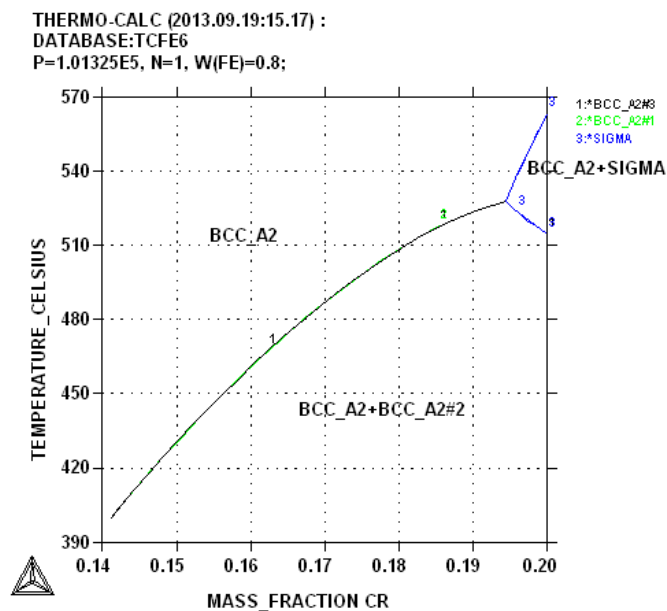


**Figure 46** Cr isopleth for the Al-Cr-0.8Fe system

This property diagram clearly indicates that the overall amount of chromium should be less than some 19%, while the amount of aluminum should be not less than 0.7 wt.%.

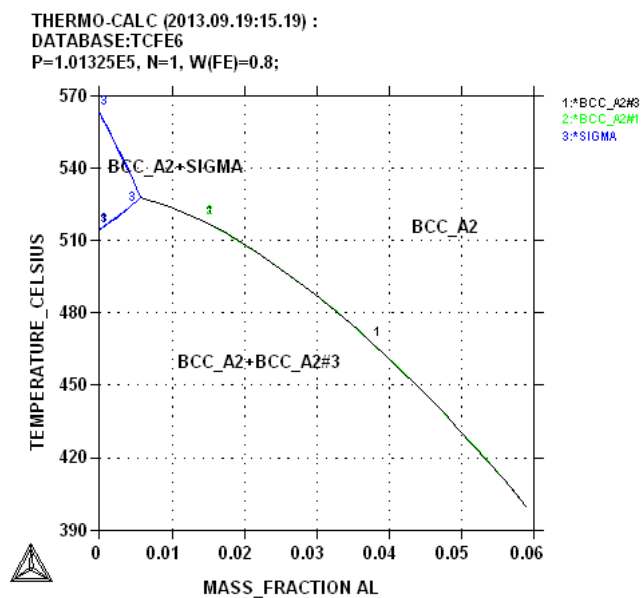


**Figure 47** Al isopleth for the Al-Cr-0.8Fe system

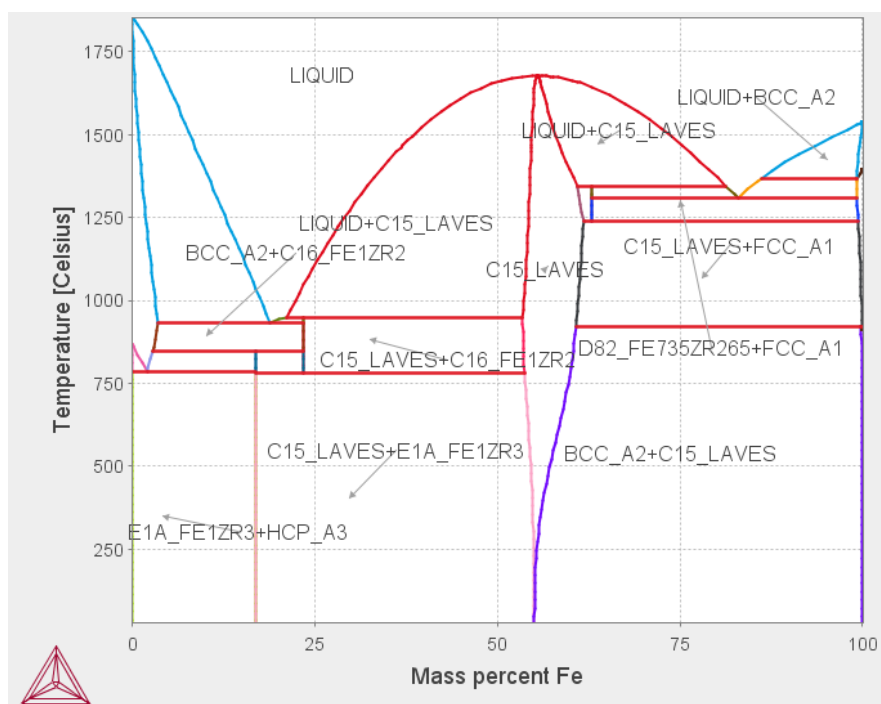
In practice, however, the amount of aluminum should be at least 4 to 5wt. % to allow for the formation of a contiguous layer of protective oxide,  $\text{Al}_2\text{O}_3$ . The reasonable amount of chromium



is probably in the 15wt. % range, so that the recommended composition of the Fe-Cr-Al is **80wt. % Fe - 15 wt. % Cr – 5 wt. % Al**.

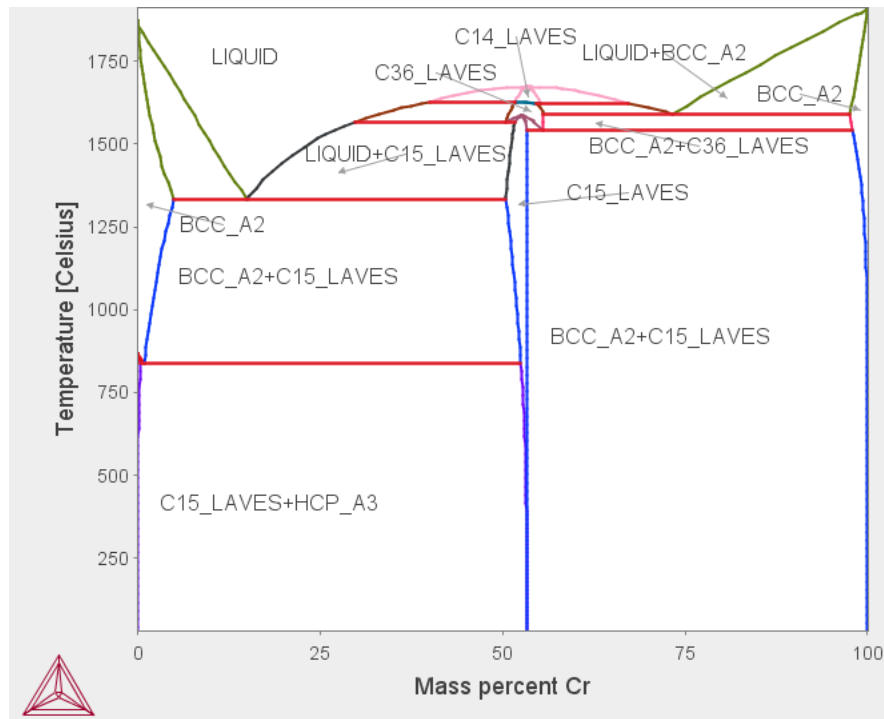
### 3.5.2.2 Low-Temperature Incipient Melting Reactions in the Fe-Cr-Al-Zr Quaternary System

In this part of work our goal was to assess the possibility of low-temperature eutectic and peritectic reactions in the Fe-Cr-Al coating that is supposed to be in contact with Zr cladding. To achieve that, we constructed a number of binary and ternary phase diagrams simulation the behavior of Zr cladding in contact with the Fe-Cr-Al coating. The binary Zr-Fe diagram is presented in Figure 48.



**Figure 48** Binary Zr-Fe phase diagram

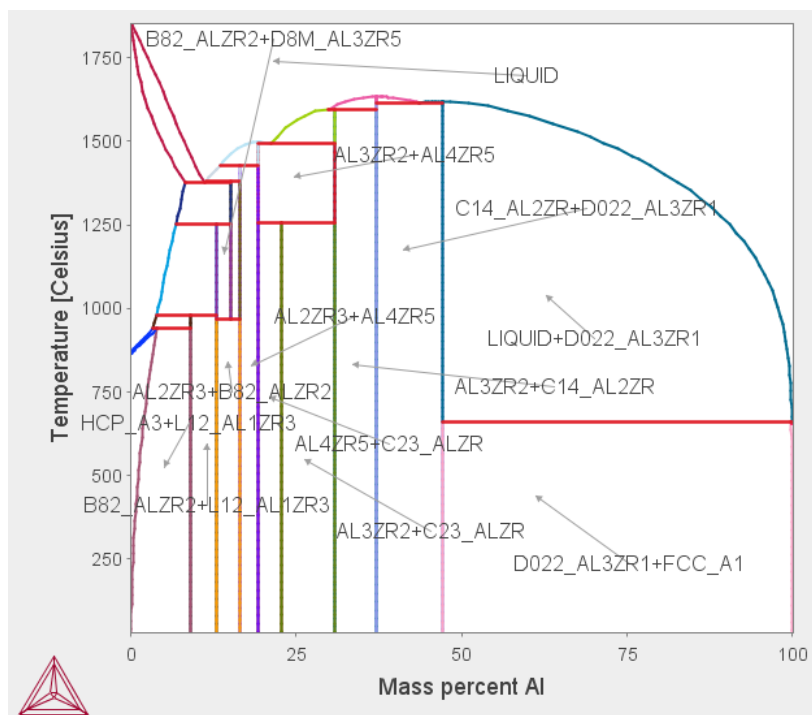
It is characterized by a low-melting eutectic at ~900°C at 18 wt.% Fe. This composition is actually quite possible because of the steep gradient of the Zr and Fe concentrations at the interface between the coating and the Zr clad.



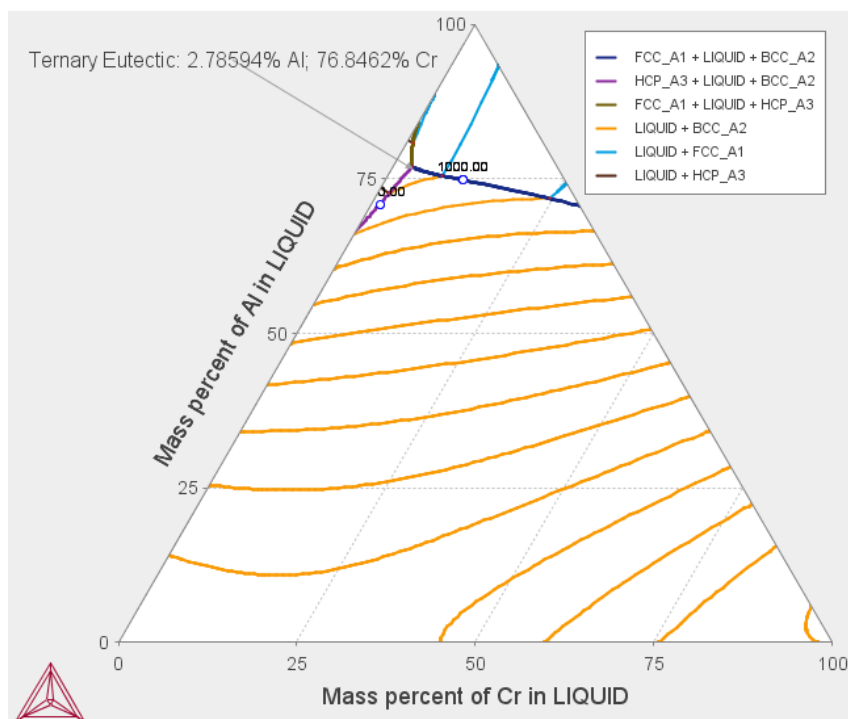
**Figure 49** Binary Zr-Cr phase diagram

In the case of this diagram, the eutectic reactions occurs at  $\sim 1300^{\circ}\text{C}$  and, consequently, does not represent the danger of incipient melting at the clad-coating interface. The last binary phase diagram was Zr-Al, Figure 47. In this case, the Zr-rich eutectic composition is at  $\sim 1350^{\circ}\text{C}$ . This temperature is high enough not to represent the danger of incipient melting for the coated cladding.

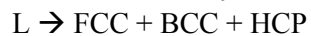
One may conclude that because of the relatively low melting eutectic in the Fe-Zr system, this type of coatings should not be recommended for further experimental work. This conclusion is substantiated even further wne we consider the corresponding ternary phase diagrams, see Figures 51 – 54.



**Figure 50** Binary Zr-Al phase diagram



**Figure 51** Liquidus projection and the ternary eutectic in the Fe-Cr-Al system:



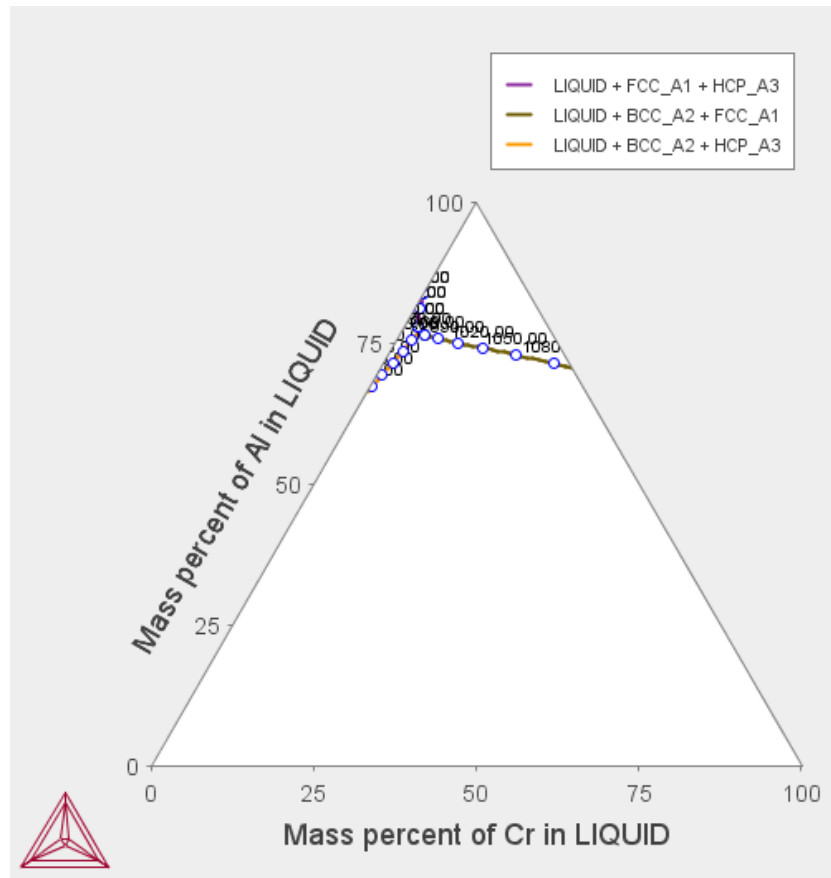


**Figure 52** Monovariant equilibrium lines in the Fe-Cr-Al system

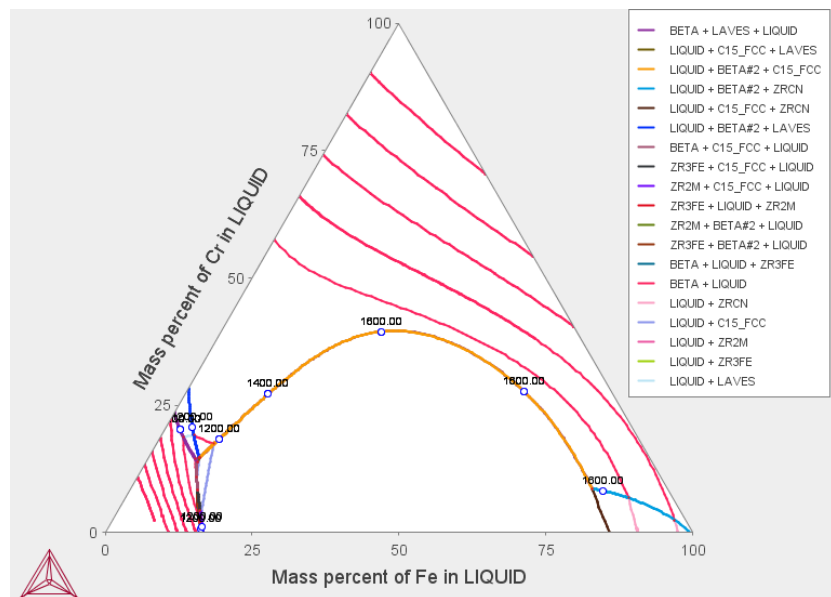


**Figure 53** Liquidus projection in the Fe-Zr-Cr system

Analyzing the liquidus projection for the Fe-Cr-Al system we see the (relatively) low melting phase reaction with the minimum corresponding to  $\sim 880^{\circ}\text{C}$ . Other ternary non-variant and invariant phase reactions take place at higher temperatures. This serves as additional evidence in favor of the conclusion made above, about the significant “hurdle” in developing the Fe-Cr-Al coating(s) for the Zr-based cladding materials.

### 3.6 Conclusions to Chapter 3

In this chapter, three different approaches to increasing thermal stability of zirconium alloy cladding were studied: 1. Coating / braiding with complex silicates ( $\text{SiC}$  and  $\text{ZrSiO}_4$ ); 2. The concept of “self-healing surfaces” and ancillary beryllium additions to zircalloys; and 3. Metallic coatings of the Fe-Cr-Al type.

The most encouraging results, both experimental and computational, were obtained for  $\text{SiC}$  braiding used as a sleeve on the zirconium alloy 704 tubing. It was demonstrated that with such protection, the cladding is capable of withstanding the most aggressive conditions (e.g.,  $950^{\circ}\text{C}$  in the atmosphere of oxygen or steam) for at least 10 minutes without any degradation. This conclusion was confirmed using computational modeling of the oxidation processes.  $\text{ZrSiO}_4$  and  $\text{SiC}$  were proposed as the best possible candidates for ceramic coatings on zircaloy cladding.

Next, the concept of self-healing of the zircaloy clad sputtered with yttria-stabilized zirconia (YSZ) was discussed. It was established that with additions the several ppm's of beryllium to zircaloy this could be a very interesting opportunity for zircaloy modification.

Finally, computational thermodynamics was utilized in order to identify the best process conditions for Fe-Cr-Al coatings and to explore a very important issue of potential incipient melting in such coatings when placed in contact with zirconium. It was established that one of the optimal compositions of the coating should be close to Fe -15wt. % Cr -5 wt.% Al. However, due to the possibility of the formation of a low-temperature eutectic in the Zr-Fe system (around 880°C) a conclusion was made that this is probably not the best path to pursue. Other types of coatings and/or other concentrations of alloying element in the Fe-Cr-Al coatings need to be also explored.

### 3.7 References to Chapter 3

1. E.E. Lewis, Nuclear Power Reactor Safety, John Wiley & Sons, New York (1977)
2. S. Glasstone and A. Sesonske, Nuclear Reactor Engineering, XanEdu Publishing (2010)
3. T. Alam, M.K. Khan, M. Pathak., K. Ravi, R. Singh, and S.K. Gupta, *Nucl. Engin. Design*, vol.241, p.3658 (2011)
4. P. Hofmann, *J. Nucl. Mater.*, vol. 270, p.194 (1999)
5. T. Arima, K. Moriyama, N. Gaja, H. Furuya, K. Idemitsu, and Y. Inagaki, *J. Nucl. Engin. Design*, vol. 241, p.3658 (2011).
6. B.Heuser, G. Was, M. Preuss, M.V. Glazoff, P. Sabharwall, J.Hales, et al., *Funded DOE IRP Proposal (\$3,500,000.00)* by INL, UIUC, University of Michigan, University of Florida, University of Manchester, Engineered Zircaloy Cladding Modifications for Improved Accident Tolerance of LWR Fuel (September 29, 2012)
7. C. Anghel, Q. Dong, J. Rundgren, G. Hultquist, I. Saeki and M. Limbäck, Gas-tight oxides – Reality or just a Hope, Proc. Int. Symp. on High-Temperature Oxidation and Corrosion 2005, Nara, Japan, 30 November – 2 December 2005 *Materials Science Forum*, 522-523, p. 93 (2006)
8. V.S. Zolotarevsky, N.A. Belov, and M.V. Glazoff, *Casting Aluminum Alloys* (monograph), 546pp., Elsevier, Amsterdam (November 2007)
9. J.S. McNatt, M.J. Shepard, N. Farkas, J.M. Morgan, and R.D. Ramsier, *J. Phys. D: Appl. Phys.* vol.35, p.1855 (2002)
10. W.F. Hsieh, J.J. Kai, C.H. Tsai, and X.J. Guo, *Mater. Chem. Phys.*, vol. 50, p.37 (1997).
11. O. Coindreau, C. Duriez, and S. Ederli, *J. Nucl. Mater.*, vol.405, p.207 (2010).
12. C. Gibert, Rapport CEA-R-5848, Influence de l'Irradiation et de la Presence de Lithium sur la Nature Crystallographique de la Zircone Dans le Cadre de l'Etude de la Corrosion du Zr4 en Milieu Rep (1999)
13. B. Cox, Oxidation of Zirconium and Its Alloys, in: *Advances in Corrosion Science and Technology*, vol. 5, ed. by M. G. Fontana and R. W. Staehle (1976) pp.173-391
14. T. Chuto, F. Nagase and T.I Fuketa, *Nucl. Engin. Tech.*, vol.41, p.163 (2008)
15. E.N. Hoffman, D.W. Vinson, R.L. Sindelar, D.J. Tallman, G. Kohse, and M.W. Barsoum, *Nucl. Engin. Design*, vol.244 , p.17 (2012)

16. Kevin M. McHugh, John E. Garnier, Sergey N. Rashkeev, Michael V. Glazoff, George W. Griffith, and Shannon Bragg-Sitton, "High Temperature Steam Corrosion of Cladding for Nuclear Applications: Experimental", ***Ceramic Engineering and Science Proceedings*** (special volume: Ceramic Materials for Energy Applications III), vol.34, issue 9, pp.149-160 (2013)
17. A. F. Brown and T. Healey, "The Kinetics of Total Oxygen Uptake in Steam-Oxidized Zircaloy-2 in the Range 1273-1673 K," *J. Nucl.Mater.* 88 (1980) 1-6.
18. K. Pettersson and Y. Haag, "Deformation and Failure of Zircaloy Cladding in a LOCA. Effects of Preoxidation and Fission Products on Deformation and Fracture Behavior, SKI project B23/78," Studsvik Energiteknik AB, STUDSVIK/K4-80/13, March 1980.
19. J. H. Baek, K. B. Park and Y. H. Jeon, "Oxidation kinetics of Zircaloy-4 and Zr-1 Nb-1Sn- 0.1Fe at temperatures of 700-1200°C," *J. Nucl.Mater.* 335 (2004) 443-456.
20. J. H. Baek and Y. H. Jeon, "Steam oxidation kinetics of Zr-1.5 Nb-0.4Sn-0.2Fe-0.1Cr and Zircaloy-4 at 900-1200OC," *J. Nucl.Mater.* 361 (2007) 30-40.
21. R. R. Biederman, et. al., "A Study of Zircaloy-4 – Steam Oxidation Kinetics," EPRI NP-734 Final Report, April, 1978.
22. E. D. Hindle and C. A. Mann, "An Experimental Study of the Deformation of Zircaloy PWR Fuel Rod Cladding Under Mainly Convective Cooling," Zirconium in the Nuclear Industry: Fifth Conference, 1980, Boston, MA, USA, ASTM STP 754, ASTM, pp. 284-302.
23. S. Sagat, H. E. Sills, and J. A. Walsworth, "Deformation and Failure of Zircaloy Fuel Sheaths Under LOCA Conditions," Zirconium in the Nuclear Industry: Sixth International Symposium, Vancouver, Canada, ASTM STP 824, ASTM pp. 709-733 (1982).
24. T. Forgeron et. al., "Experiment and Modeling of Advanced Fuel Rod Cladding Behavior Under LOCA Conditions: A-B Phase Transformation Kinetics and EDGAR Methodology," Zirconium in the Nuclear Industry: Twelfth International Symposium, 1998, Toronto, Canada, ASTM STP 1354, ASTM pp. 256-278.
25. J. H. Kim et. al., "Embrittlement Behavior of Zircaloy-4 Cladding during Oxidation and Water Quench," *Nuclear Engineering and Design*, 235 (2005) 67-75.
26. T. Furuta et. al., "Zircaloy Clad Fuel Rod Burst Test Behavior under Simulated Loss of Coolant Conditions in PWRs," *J. Nucl. Sci. Technol.*, 15, (1978), 736-744.
27. D.Q. Peng , X.D. Bai, F. Pan, and H. Sun, *Nucl. Instr. and Meth.*, vol.229, p.269 (2005)



28. D.M. Cupid, and H.J. Seifert, Thermodynamic Calculations and Phase Stabilities in the Y-Si-C-O System, *J. Phase Equilib. Diffus.*, vol. 28 (2007) 90-100
29. Lance L. Snead, Takashi Nozawa, Yutai Katoh, Thak-Sang Byun, Sosuke Kondo, and David A. Petti, "Handbook of SiC properties for fuel performance modeling," *J. Nucl. Mater.* 371 (2007) 329-377.
30. P. T. B. Shaffer, Engineered Materials Handbook, Vol 4, Ceramics and Glasses, ASM International, (1991) p. 808.
31. Advances in Silicon Carbide Processing and Applications, Stephen E. Saddow and Anant Agarwal, Eds., Artech House, Inc., Norwood, MA (2004), p. 8.
32. Bind J., Phase transformation during hot-pressing of cubic SiC, *Mater. Res. Bull.*, Vol. 13, 1978, p 91-96
33. J. E. Garnier and G. W. Griffith, "Methods of Producing Silicon Carbide Fibers, and Articles Including Same", USP Docket 2939-10059US (2012).
34. K. M. McHugh, J. E. Garnier, and G. W. Griffith, "Synthesis and Analysis of Alpha Silicon Carbide Components for Encapsulation of Fuel Rods and Pellets," Proceedings ASME 2011 Small Modular Reactors Symposium (Washington, DC, USA, September 28–30, 2011), Paper No. SMR2011-6584, pp. 165-169.
35. N. S. Jacobson, "Corrosion of Silicon-Based Ceramics in Combustion Environments," *J. Am. Ceram. Soc.* **76**, 3-28 (1993).
36. E. J. Opila and R. E. Hann, Jr., "Paralinear Oxidation of CVD SiC in Water Vapor," *J. Am. Ceram. Soc.* **80**, 197-205 (1997).
37. E. J. Opila, "Oxidation and Volatilization of Silica Formers in Water Vapor," *J. Am. Ceram. Soc.* **86**, 1238-48 (2003).
38. B. E. Deal and A. S. Grove, "General Relationship for the Thermal Oxidation of Silicon," *J. Appl. Phys.*, **36**, 3770–78 (1965).
39. E. J. Opila, "Variation of the Oxidation Rate of Silicon Carbide with Water- Vapor Pressure," *J. Am. Ceram. Soc.*, **82**, 625–36 (1999).
40. J. L. Smialek, R. C. Robinson, E. J. Opila, D. S. Fox, and N. S. Jacobson, "SiC and Si<sub>3</sub>N<sub>4</sub> recession due to SiO<sub>2</sub> scale volatility under combustor conditions," *Adv. Composite Mater.* **8**, 33-45 (1999).
41. D. R. Gaskell, *An Introduction to Transport Phenomena in Materials Engineering*; p. 573. Macmillan, New York, 1992.

42. T. Bakos, S.N. Rashkeev, and S.T. Pantelides, "Reactions and Diffusion of Water and Oxygen Molecules in Amorphous SiO<sub>2</sub>," *Physical Review Letters* **88**, 055508 (2002).
43. H.T. Lin, M.K. Ferber, "Mechanical reliability evaluation of silicon nitride ceramic components after exposure in industrial gas turbines," *J. Eur. Ceram. Soc.* **22** (2002) 2789–2797.
44. S. Ueno, D.D. Jayaseelan, T. Ohji, "Development of oxide-based EBC for silicon nitride," *Int. J. Appl. Ceram. Technol.* **1** (2004) 362–373.
45. K.N. Lee, D.S. Fox, J.I. Eldridge, D. Zhu, R.C. Robinson, N.P. Bansal, R.A. Miller, "Upper temperature limit of environmental barrier coatings based on mullite and BSAS," *J. Am. Ceram. Soc.* **86** (2003) 1299–1306.
46. K. N. Lee, D. S. Fox, N. P. Bansal, "Rare earth silicate environmental barrier coatings for SiC/SiC composites and Si<sub>3</sub>N<sub>4</sub> ceramics," *J. European Ceramic Society* **25** (2005) 1705–1715.
47. S. Ueno, D. D. Jayaseelan, T. Ohji, H.-T. Lin, "Recession mechanism of Lu<sub>2</sub>Si<sub>2</sub>O<sub>7</sub> phase in high speed steam jet environment at high temperatures," *Ceramics International* **32**, pp.775–778 (2006).
48. S. Ueno, T. Ohji, H.-T. Lin, "Recession behavior of Lu<sub>2</sub>SiO<sub>5</sub> under a high speed steam jet at high temperatures," *Ceramics International* **37**, pp.1185–1189 (2011).
49. S. Ueno, T. Ohji, H.-T. Lin, "Corrosion and recession of mullite in water vapor environment," *J. European Ceramic Society* vol.28, pp.431–435 (2008).
50. S. Ueno, T. Ohji, H.-T. Lin, "Recession behavior of Yb<sub>2</sub>Si<sub>2</sub>O<sub>7</sub> phase under high speed steam jet at high temperatures," *Corrosion Science* **50** (2008) 178–182.
51. S. Ueno, T. Ohji, H.-T. Lin, "Corrosion and recession behavior of zircon in water vapor environment at high temperature," *Corrosion Science* **49** (2007) 1162–1171.
52. S. Ueno, D.D. Jayaseelan, T. Ohji, H.T. Lin, "Corrosion and oxidation behaviors of ASiO<sub>4</sub> (A = Ti, Zr and Hf) and silicon nitride with an HfSiO<sub>4</sub> environmental barrier coating," *J. Ceram. Process. Res.* **6** (2005) 81–84.
53. ThermoCalc Classic Version S User's Guide, P. Shi and B. Sundman Editors, ThermoCalc Software AB, Stockholm, Sweden (2010)
54. FactSage FACT oxide database (2010)
55. M. C. Payne, M. P. Teter, D. C. Allan, T. A. Arias, J. D. Joannopoulos, J. D., "Iterative minimization techniques for *ab initio* total-energy calculations: molecular dynamics and conjugate gradients," *Rev. Mod. Phys.* **64**, pp.1045-1097 (1992).

56. J. P. Perdew, K. Burke, M. Ernzerhof, "Generalized Gradient Approximation Made Simple," *Phys. Rev. Lett.* **77**, pp. 3865-3868 (1996).
57. P. E. Blöchl, "Projector Augmented Wave Method." *Phys. Rev. B* **50**, pp. 17953-17979 (1994)
58. G. Kresse, J. Joubert, "From ultrasoft pseudopotentials to the projector augmented-wave method," *Phys. Rev. B* **59**, pp.1758-1775 (1999).
59. G. Kresse, J. Furthmüller, Efficient iterative schemes for ab initio total-energy calculations using a plane-wave basis set," *Phys. Rev. B* **54**, 11169-11186 (1996).
60. D. J. Chadi, M. L. Cohen, "Special Points in the Brillouin Zone," *Phys. Rev. B* **8**, pp.5747-5753 (1973).
61. M.V. Glazoff, P. Sabharwall, T.E. Lister, B. Heuser, Beryllium-Doped Zircaloy Rods with YSZ (Ytria-Stabilized Zirconia) Modified Surfaces to Achieve Self-Healing Mode and Protection from High-Temperature Chemical Reactions, INL LDRD Proposal (June 2013).
62. Kevin M. McHugh, John E. Garnier, Sergey N. Rashkeev, Michael V. Glazoff, George W. Griffith, and Shannon Bragg-Sitton, "High Temperature Steam Corrosion of Cladding for Nuclear Applications: Experimental", *Ceramic Engineering and Science Proceedings* (special volume: Ceramic Materials for Energy Applications III), vol.34, issue 9, pp.149-160 (2013)
63. G. Hultquist; Tveten, B.; Hörnlund, E.; Limbäck, M.; R. Haugsrud, *Oxidation of Metals* vol.56, p.313 (2001).
64. G. Hultquist; B. Tveten, B.; E. Hörnlund, *Oxidation of Metals*, vol.54, p.1 (2000)
65. N.B. Pilling, R. E. Bedworth, "The Oxidation of Metals at High Temperatures". *J. Inst. Met* vol.29, p. 529-591 (1923).
66. David H. DeYoung, William F. McGinnis, Ray T. Richter, Jeffrey J. Wiesner, Aluminum Alloys Having Improved Cast Surface Quality, US Patent #6,412,164 (July 02, 2022)
67. S.N. Rashkeev and M.V. Glazoff, Atomic-Scale Mechanisms of Oxygen Electrode Delamination in Solid Oxide Electrolyzer Cells, *International Journal of Hydrogen Energy*, pp.1280-1291, vol.37, issue 2 (January 2012)

68. K.S. Chan, W. Liang, N.S. Cheruvu, D.W. Gandy, Computational Design of Corrosion-Resistant Fe–Cr–Ni–Al Nanocoatings for Power Generation, *Journal of Engineering for Gas Turbines and Power*, vol. 132, p.052101-1 (2010)
69. K.A. Terrani, S.J. Zinkle, and L.L. Snead, Advanced oxidation-resistant iron-based alloys for LWR cladding, *Journal of Nuclear Materials*, vol. 448, issue 1-3, pp. 420-435 (2014).

## **Chapter 4 Development of Plasticity Model Using Non-Associated Flow Rule for Zirconium Nuclear Alloys**

### **4.1 Brief Review of Plasticity Theory Development: Tresca, von Mises Plasticity, Schmid's Law, Normality and Deviations from Them**

Schmid's law states that a slip system will be potentially active when shear stress, resolved on the slip plane and in the slip direction, reaches a certain critical value called critical resolved shear stress (CRSS) [1, 2]. For the uniaxial loading conditions this law implies that (1) CRSS does not depend on the orientation of the load axis, and (2) CRSS is independent of the sign of the loading stress (tension or compression). However, the latter condition does not hold when there is coupling between CRSS and hydrostatic pressure. Schmid's law and the numerous deviations from it have been and remain an issue of considerable interest. There is a general understanding that, on a microscopic scale, plastic flow is controlled by the generation, motion and interaction of dislocations which, to a significant extent, define the macroscopic deformation behavior of a material element [3]. Thus, a physical description of plastic flow must, at least in principle, bridge the entire hierarchy of length scales, from understanding behavior of individual dislocations on the atomistic scale and proceeding up to the characterization of the macroscopic material properties [4]. In his work on the thermodynamics of plasticity Rice emphasized the concept of "structural internal- variables" [5]. This approach views inelastic deformation of a material element as a sequence of constrained equilibrium states: the state at any given time in the deformation history is fully characterized by the corresponding values of stress and

temperature and the collection of internal variables which mark the extent of microstructural rearrangements within the sample. This means that a material subject to plastic deformation is considered simultaneously on two different scales - macroscopic, where straining occurs (internal variables of the averaging type), and microscopic, where structural rearrangements, characterized by the "structural" internal variables, occur<sup>7</sup>. The internal variables are supposed to provide all of the relevant information on microstructure. Rice showed that the general normality structure of the constitutive laws can be recovered if it is assumed that the rate at which a structural rearrangement takes place is governed solely by its associated thermodynamic force. This approach establishes a connection between elementary, e.g. dislocation, mechanisms of plasticity and their macroscopic manifestations rationalized in the form of Schmid's law, and the normality flow rule, and provides clear indications where one should expect these conditions to be violated.

Significant progress in understanding the nature of non-Schmid effects has been achieved for b.c.c. metals. In particular, working with a simple "line-tension" model and considering the rate of kink nucleation on screw dislocations, Seeger reported a quantitative agreement between theoretical predictions [6] and experimental data on the flow stress for several b.c.c. materials (see, e.g. [7] for molybdenum, Ref. [8] for niobium, and Ref. [9] for tantalum). Non-planar spreading of dislocation cores into several planes of the 111 zone explained the non-Schmid behavior of these metals, while the anomalous yield of some  $L_{12}$ -superstructures, e.g. Ni<sub>3</sub>Al (or hexagonal D0<sub>19</sub> Ti<sub>3</sub>Al [10]), was elegantly explained in terms of temperature- and orientation-

---

<sup>7</sup> When applied to metal plasticity this statement simply embodies the conventional notion that slip on a given system within a single-crystalline element is stress-state dependent only through the local resolved shear stress on that system or, at a more fundamental level of modeling, that the velocity of a given segment of dislocation line is stress-state dependent only through the glide force per unit length of that line" [3].

dependent “sessile - glissile” transformations of  $\langle 011 \rangle$  screw dislocation cores in these compounds [10].

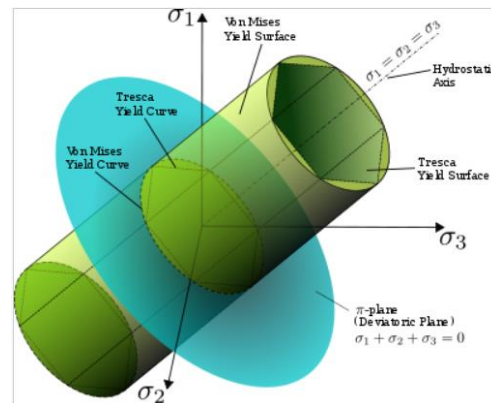


**Figure 54** The von Mises yield surfaces in principal stress coordinates circumscribes a cylinder with radius  $\sqrt{2/3}\sigma_y$  around the hydrostatic axis. Also shown is Tresca's hexagonal yield surface ([http://en.wikipedia.org/wiki/Von\\_Mises\\_yield\\_criterion](http://en.wikipedia.org/wiki/Von_Mises_yield_criterion)) [13]

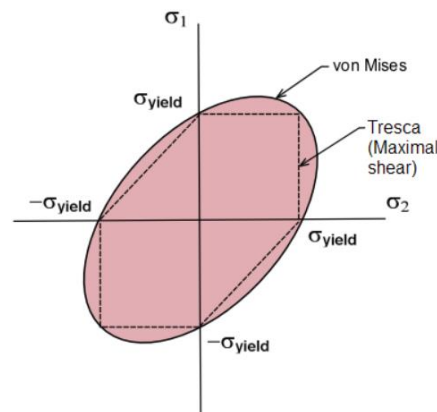


**Figure 55** Intersection of the von Mises yield criterion with the  $(s_1, s_2)$  plane, where  $s_3=0$  [13]

Based on well documented experimental observations, f.c.c. materials (metals: Al, Cu, Ag, etc., and semiconductors: Si and Ge) are thought to epitomize the ideal Schmid behavior in plasticity. The brief analysis of these results, which motivated the present studies on the non-associated flow rule for hcp metals and Zr in particular, of individual dislocations under different loading modes, is given in the next section. Even to a much greater extent, these deviations become quite large in HCP materials like Zr, Ti, and Mg. Using a general scheme similar to the

one given in Figure 54, one can visualize such deviations using the concept of the “Lode angle” [14]

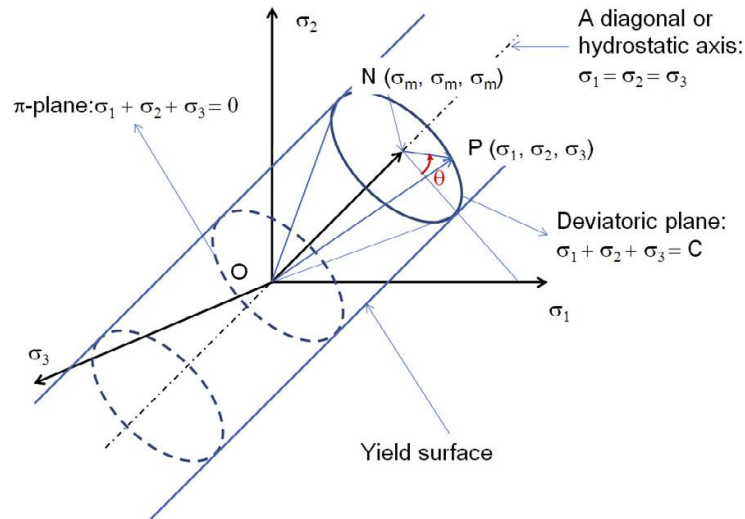


**Figure 56** Deviations from normality and associated flow rule as illustrated by the concept of the so-called “Lode angle” [14]

Richmond and Spitzig [11, 12] convincingly demonstrated for both iron-based materials and aluminum that flow stress exhibits a linear dependence on pressure  $P$ , according to the relation [11, 12]:

$$\sigma = \sigma_0(1 + 3\alpha P)$$

where  $\sigma_0$  is the flow stress at  $P = 0$ , and  $\alpha$  is a pressure coefficient which was found to be approximately the same for all iron-based materials but different for aluminum. Typical results obtained in these experiments are presented in Fig. 1 [12]. Tension and compression tests were performed on AA1100 aluminum at different superimposed pressures, 0.1 MPa (1 atm), 138, 414 and 828 MPa. The difference between the absolute values of flow stress in simple tension and simple compression (the strength differential, SD) was only about 0.3% and, thus, could not be reliably detected in such experiments. However, the effect of



superimposed pressure on the increase of the flow stress was quite substantial, as can be seen from Fig. 1 [12]. That the critical shear stress depends on the superimposed pressure does not yet constitute a violation of the normality flow rule, introduced into mechanics of plasticity by von Mises [15]. The prevailing view based on this rule is that pressure dependent plastic deformation produces an associated permanent volume expansion (dilatation) which is expected to couple to its associated thermodynamic force, i.e. pressure. Indeed, such a volume expansion is likely to be present due to the formation of new lattice defects. However, as was shown in Refs [11, 12], this expansion cannot account for the observed pressure dependence and, thus, can't relate the pressure dependency of yielding to irreversible plastic dilatancy.

Theoretical descriptions of the pressure dependence of yielding have focused on dislocation motion as the source of the observed pressure sensitivity of the flow stress. In particular, Jung [14] derived an expression for the work required to form and move a dislocation in the crystal lattice. This resulted in the following equation for the flow stress,  $\tau$ , as a function of pressure,  $P$  [16]:

$$\tau = \tau_0 \left( 1 + \frac{2}{G_0} \frac{dG}{dP} \cdot P \right)$$

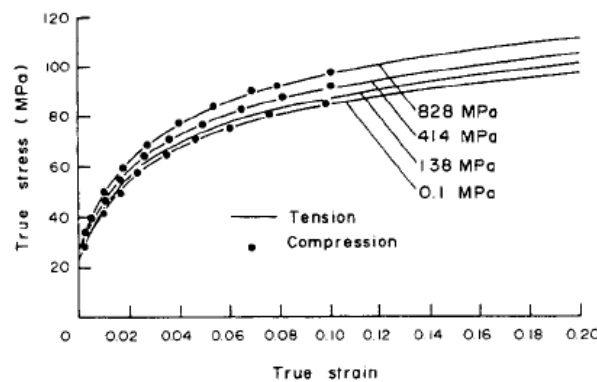


**Figure 57** The results of the tension and compression tests at 1 atm (0.1 MPa) and at superimposed pressures of 138, 414 and 828 MPa, after Spitzig and Richmond [12]

Again, in the case of HCP materials plastic deformation proceeds differently: at lower temperature (including ambient temperature)

In this Chapter (prepared under the guidance of Prof. Jeong - Whan Yoon, Deakin University, Melbourne, Australia) a research effort was made to develop a non-associated flow rule for zirconium. Since Zr is a hexagonally close packed (hcp) material, it is impossible to describe its plastic response under arbitrary loading conditions with any associated flow rule (e.g. von Mises). As a result of strong tension-compression asymmetry of the yield stress and anisotropy, zirconium displays plastic behavior that requires a more sophisticated approach.

Consequently, a new general asymmetric yield function has been developed which accommodates mathematically the four directional anisotropies along  $0^\circ$ ,  $45^\circ$ ,  $90^\circ$ , and biaxial, under tension and compression. Stress anisotropy has been completely decoupled from the r-value by using non-associated flow plasticity, where yield function and plastic potential have been treated separately to take care of stress and r-value directionalities, respectively. This theoretical development has been verified using Zr alloys at room temperature as an example as these materials have very strong SD (Strength Differential) effect. The proposed yield function reasonably well models the evolution of yield surfaces for a zirconium clock-rolled plate during in-plane and through-thickness compression. It has been found that this function can predict both tension and compression asymmetry mathematically without any numerical tolerance and shows the significant improvement compared to any reported functions.

Finally, in the end of this chapter, a program of further research is outlined aimed at constructing tensorial relationships for the temperature and fluence-dependent creep surfaces for Zr, Zircaloy-2, and Zircaloy-4. Recently, hexagonal close-packed (HCP) metals attracted

increasing efforts owing to the high ratio of strength to density. However, the plastic behavior of HCP metals shows noticeable difference between tension and compression, which is referred as the strength differential (SD) effect. SD effect is mainly due to the directional twinning of HCP metals. Cazacu and Barlat [17] restored the asymmetry of the third stress invariant to model SD effect of HCP metals. Cazacu et al. [18] developed another asymmetric yield function for HCP metals which covers the upper and lower bounds of SD effect for pressure insensitive metals. Plunkett et al. [19] applied the CPB'06 yield function to describe mechanical response of high-purity zirconium accounting anisotropic hardening. Nixon et al. [20] successfully modeled the anisotropic-asymmetric behavior of high-purity  $\alpha$ -titanium with the Cazacu-Barlat [1] yield function. Yoon et al. [21] employed the CPB'06 yield function for AZ31 sheet alloy with anisotropic hardening for simulation of axial crushing. Khan and Yu [22] experimentally investigate the anisotropic behavior of Ti-6Al-4V alloy both in tension and compression considering effect of strain rate and temperature. Khan et al. [23] also proposed a yield function with dependence on strain rate and temperature to model both the anisotropy and tension - compression asymmetric characteristics of Ti-6Al-4V alloy.

Advanced plasticity in modeling of plastic behavior of HCP metals poses three new challenges:

- a) Constitutive models of plastic deformation should couple the effect of the through-thickness stress and be developed for metals under spatial loading;
- b) Constitutive models can provide correct description of anisotropic behavior not only in tension but also in compression;
- c) Constitutive functions are capable of modeling strong SD effect of HCP metals since employment of these metals is an efficient way for weight reduction.

However, the yield functions reviewed above do not fully provide satisfactory solutions for all of these challenges. In this work, a general yield function is proposed with dependence on the first, second and third invariants of the stress tensor. The yield function proposed is extended to an anisotropic form by introducing two different linear transformation tensors to the second and third invariants, respectively. Non-AFR is also used where the plastic strain directions are defined by a separate quadratic plastic potential and the directional hardenings are defined by the proposed yield function. So with this change it is possible to precisely reproduce the anisotropy in both yield and plastic strain behaviors, with the latter assumed to be unaffected by plastic deformation. A constitutive model developed in this study substantially improves accuracy in the stress-strain prediction and it is expected to provide significantly more accurate results in applications where isotropic hardening is used and considered to be approximately valid as the case of HCP materials. Finally, the anisotropic form of the yield function proposed is utilized to model the yield surface evolution of a zirconium clock-rolled plate during in-plane and through-thickness compression to validate its flexibility

## **4.2 Development of Plasticity Model Using Non-Associated Flow Rule for HCP Materials Including Zirconium for Nuclear Applications**

### **4.2.1 Plastic Potential for Non-Associated Flow Plasticity**

One of the most common models of metal deformation still widely used in industry is based on the quadratic plastic potential of the form proposed by Hill [24], which for plane stress conditions is often normalized for convenience to uniaxial tension along the 1-axis as follows,

$$\bar{\sigma}_p(\vec{\sigma}) \equiv \sqrt{\sigma_{11}^2 + \lambda_p \sigma_{22}^2 - 2\nu_p \sigma_{11} \sigma_{22} + 2\rho_p \sigma_{12} \sigma_{21}}$$

$$\lambda_p = \frac{1 + 1/r_0(\bar{\epsilon}_p)}{1 + 1/r_0(\bar{\epsilon}_p)} \quad \nu_p = \frac{1}{1 + 1/r_0(\bar{\epsilon}_p)} \quad \rho_p = \frac{1/r_0(\bar{\epsilon}_p) + 1/r_0(\bar{\epsilon}_p)}{1 + 1/r_0(\bar{\epsilon}_p)} \frac{1 + 2r_{45}(\bar{\epsilon}_p)}{2} \quad (4.1)$$

The parameters,  $r_0(\bar{\epsilon}_p)$ ,  $r_{45}(\bar{\epsilon}_p)$ , and  $r_{90}(\bar{\epsilon}_p)$  are the ratios of the plastic strain rate across the width of a uniaxial tension test to the plastic strain rate through the thickness for tension at respectively, 0, 45, and 90 degrees to the rolling direction of the sheet coil aligned with the 1-axis of the coordinate system. The r-values are able to be defined as a function of effective plastic strain (non-constant values) as shown in Eq.4.1.

According to classical plasticity, the plastic potential is used in the flow rule to define the direction of the rate of change of all components of the plastic strain tensor,

$$\frac{dE_{ij}^{(p)}}{dt} = \frac{\partial \bar{\sigma}_p(\vec{\sigma})}{\partial \sigma^{ij}} \dot{\lambda} \quad (4.2)$$

where  $\dot{\lambda}$  is the plastic compliance factor that controls the magnitude of the rate of change of the plastic strain tensor. Since the plastic potential is a linear homogeneous function of the stress, it follows from Eq. 2, and the following sequence, that the rate of plastic work is equal to the product of the magnitude of the plastic potential and the plastic compliance factor,

$$\frac{dw_p}{dt} = \sigma^{ij} \frac{dE_{ij}^{(p)}}{dt} = \sigma^{ij} \frac{\partial \bar{\sigma}_p(\vec{\sigma})}{\partial \sigma^{ij}} \dot{\lambda} = \bar{\sigma}_p(\vec{\sigma}) \dot{\lambda} \quad (4.3)$$

Although it is not necessary to explicitly define the compliance factor for implementation in finite element analysis, it is useful to note that the quadratic form of the plastic potential, with the flow rule, also leads to a specific definition of the plastic compliance factor in terms of the parameters of the plastic potential and the components of the plastic strain rate tensor as follows,

$$\dot{\lambda} \equiv \sqrt{\frac{\lambda_p \left( \dot{E}_{11}^{(p)} \right)^2 + \left( \dot{E}_{22}^{(p)} \right)^2 + 2\nu_p \dot{E}_{11}^{(p)} \dot{E}_{22}^{(p)}}{\lambda_p - \nu_p^2}} + \frac{2}{\rho_0} \left( \dot{E}_{12}^{(p)} \right)^2} \quad (4.4)$$

It is therefore a consequence of the flow rule and the linear homogeneous plastic potential, that the compliance factor is a specific linear homogeneous function of the rate of change of the plastic strain tensor, with parameters of this function determined solely by the parameters of the plastic potential. It is therefore reasonable to identify the plastic compliance as the rate of change of an *effective plastic strain*, and more to the point, the integral of which

$$\bar{\lambda} \equiv \int \dot{\lambda} dt \quad (4.5)$$

can be used as the work hardening variable in the stress-strain relation. This definition was adopted in the works on non-AFR in Stoughton and Yoon [25- 27].

#### 4.2.2 A General Yield Function for the Tension Compression Asymmetry of Yield Stress (SD-Effect)

For an isotropic material under spatial loading of a stress tensor denoted by  $\boldsymbol{\sigma}$  or  $\sigma_{ij}$ , the stress state can be solely determined by three stress invariants expressed as follows:

$$I_1 = \text{Tr}(\boldsymbol{\sigma}_{ij}) = \sigma_1 + \sigma_2 + \sigma_3 \quad (3-6)$$

$$J_2 = \frac{1}{2} s_{ij} s_{ij} = \frac{1}{6} \left[ (s_1 - s_2)^2 + (s_2 - s_3)^2 + (s_3 - s_1)^2 \right] \quad (4.7)$$

$$J_3 = \det(\boldsymbol{s}_{ij}) = s_1 s_2 s_3 \quad (4.8)$$

where  $\sigma_1, \sigma_2$  and  $\sigma_3$  are three principal stresses of the stress tensor of  $\boldsymbol{\sigma}$  and  $s_1, s_2$  and  $s_3$  are three principal values of the stress deviator tensor of  $\mathbf{s}$  or  $s_{ij}$  computed by

$$s_{ij} = \sigma_{ij} - \sigma_m = \sigma_{ij} - \frac{I_1}{3} \quad (4.9)$$

with  $\sigma_m$  as the mean stress.

Based on experimental results of uniaxial tension under a superimposed hydrostatic pressure for aluminum and steel alloys, Spitzig et al. [28] and Spitzig and Richmond [29] formulated the pressure sensitivity of metals by adding the first stress invariant to the von Mises stress as below:

$$f(\sigma_{ij}) = \sqrt{3J_2} + aI_1 = \sigma_{\text{Mises}} + aI_1 \quad (4.10)$$

where  $\sigma_{\text{Mises}}$  denotes the von Mises stress.

Drucker in 1952 [30] proposed a yield function to couple the effect of both the second and third invariants on yielding as below:

$$f(\sigma_{ij}) = J_2^3 - cJ_3^2 \quad (4.11)$$

Cazacu and Barlat [17] restored the asymmetry of the third invariant in Eq. (11) to consider SD effect for pressure insensitive metals in a form of

$$f(\sigma_{ij}) = J_2^{3/2} - cJ_3 \quad (4.12)$$

Here a general yield function is formulated with three invariants as below:

$$f(\sigma_{ij}) = a \left[ bI_1 + (J_2^{3/2} - cJ_3)^{1/3} \right] \quad (4.13)$$

This general yield function assumes a linear dependence of yielding on the first invariant according to experimental results of Spitzig et al. [28] and Spitzig and Richmond [29] and preserves the asymmetry of the third stress invariant to model SD effect of pressure insensitive metals. The material constants of  $b$  and  $c$  modulate the influence of the pressure and the third invariant on yielding of metals while the material parameter  $a$  is determined by experiments used to characterize the strain hardening behavior of metals. Normally, the strain hardening

behavior is measured from uniaxial tensile tests and accordingly the material constant  $a$  is computed in a form of

$$a = \frac{1}{b + \left( \frac{1}{3\sqrt{3}} - \frac{1}{27}c \right)^{1/3}} \quad (4.14)$$

When the material constant  $b$  is zero, Eq. (4.14) reduces to the Cazacu-Barlat'2004 yield function. The von Mises yield function is realized from Eq. (14) when both  $b$  and  $c$  disappear. Moreover, it is easy to prove that the material constant  $b$  does not affect the convexity of the proposed yield function since the Hessian matrix of the proposed yield function is identical to that of the Cazacu-Barlat'2004 yield function. Therefore, the convexity of the proposed yield function in Eq. (4.14) is satisfied when  $c \in [-3\sqrt{3}/4, 3\sqrt{3}/4]$  which is the same as that for the Cazacu-Barlat'2004 yield function.

The effect of pressure sensitivity is modulated by the parameter  $b$  as illustrated in Figs. 1 (a) and (b). It is observed that yield stresses increase with the mean stress when  $b < 0$ , while raising the mean stress reduces the yield stresses when  $b > 0$ . When  $b = 0$ , yielding is independent of the first stress invariant. Effect of  $b$  is also depicted for the yield surface under plane stress in Fig. 2. The ratio of tensile yield stress to compressive yield stress decreases as  $b$  rises from a negative value to a positive one.

The material parameter  $c$  adjusts effect of the third stress invariant on yielding. The material constant  $b$  is set to zero to graphically illustrate influence of  $c$  on the yield surface since the three-dimensional yield surface can be plotted on the  $\pi$ -plane in Fig. 3 for pressure insensitive materials. It is observed that the yield surface is convex when  $c \in [-3\sqrt{3}/4, 3\sqrt{3}/4]$ . In addition, SD effect is correctly modeled without the effect of the pressure sensitivity.



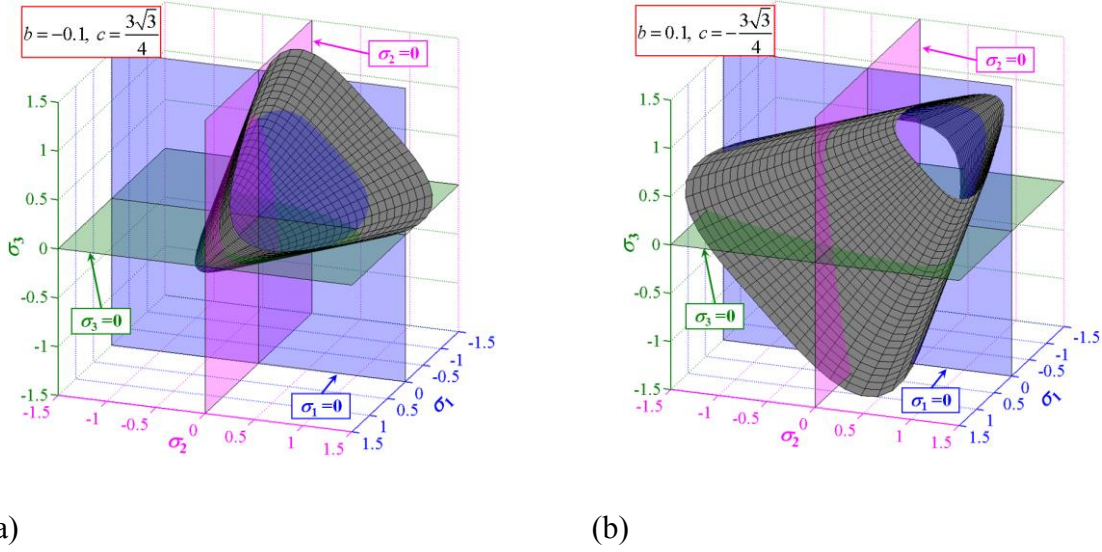


**Figure 58** Effect of the pressure sensitive parameter  $b$  on the yield surface of the proposed yield function constructed in the three-dimensional space of principal stresses: (a) negative  $b$  ; (b) positive  $b$  .

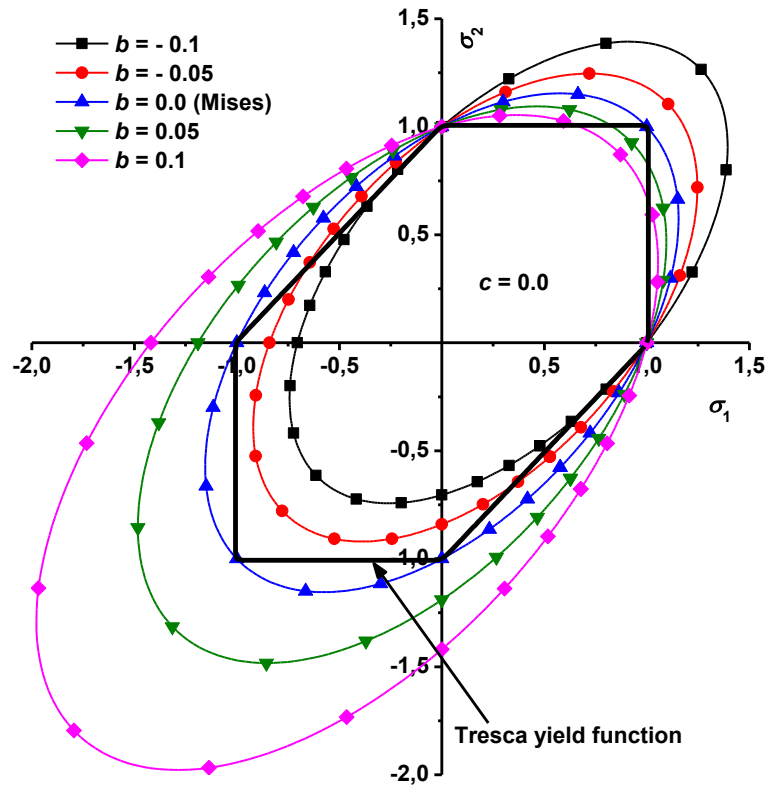


**Figure 59** Effect of the pressure sensitive parameter  $b$  on the yield surface of the proposed yield function constructed in the space of principal stresses under plane stress condition with  $\sigma_3 = 0$

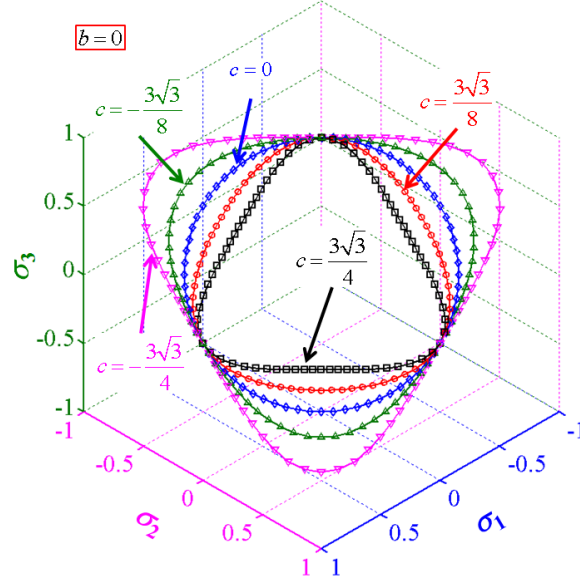


**Figure 60** Effect of the third stress invariant on the yield surface adjusted by the material parameter  $c$  for materials under spatial loading

#### 4.2.3 Extension of the Model for Orthotropic Metals

The yield function proposed can be extended to describe the anisotropic plastic deformation for orthotropic metals in a form of

$$f(\sigma_{ij}) = \tilde{I}_1 + (J_2'^{3/2} - J_3'')^{1/3} \quad (4.15)$$

with

$$\tilde{I}_1 = h_x \sigma_{xx} + h_y \sigma_{yy} + h_z \sigma_{zz} \quad (4.16)$$

$$J_2' = \frac{1}{2} \mathbf{s}' : \mathbf{s}' = \frac{1}{6} \left[ (s_1' - s_2')^2 + (s_2' - s_3')^2 + (s_3' - s_1')^2 \right] \quad (4.17)$$

$$J_3'' = \det(\mathbf{s}'') = s_1'' s_2'' s_3'' \quad (4.18)$$

where  $\tilde{I}_1$  represents the anisotropic-weighted first stress invariant for pressure sensitivity,  $J'_2$  is the second stress invariant of an isotropic plastic equivalent (IPE) transformed stress tensor of  $\mathbf{s}'$ , and  $J''_3$  is the third stress invariant of another IPE transformed stress tensor of  $\mathbf{s}''$ .  $s'_1, s'_2$  and  $s'_3$  are three principal values of  $\mathbf{s}'$  while  $s''_1, s''_2$  and  $s''_3$  are three principal values of  $\mathbf{s}''$ . The axes of x, y and z represent rolling direction (RD), transverse direction (TD), and normal direction (ND) of cold rolled metals, respectively. Two IPE stress tensors of  $\mathbf{s}'$  and  $\mathbf{s}''$  are transformed from the stress tensor  $\boldsymbol{\sigma}$  by two fourth-order linear transformation tensors of  $\mathbf{L}'$  and  $\mathbf{L}''$  as follows:

$$\mathbf{s}' = \mathbf{L}'\boldsymbol{\sigma}, \mathbf{s}'' = \mathbf{L}''\boldsymbol{\sigma} \quad (4.19)$$

with

$$\mathbf{L}' = \begin{bmatrix} (c'_2 + c'_3)/3 & -c'_3/3 & -c'_2/3 & 0 & 0 & 0 \\ -c'_3/3 & (c'_3 + c'_1)/3 & -c'_1/3 & 0 & 0 & 0 \\ -c'_2/3 & -c'_1/3 & (c'_1 + c'_2)/3 & 0 & 0 & 0 \\ 0 & 0 & 0 & c'_4 & 0 & 0 \\ 0 & 0 & 0 & 0 & c'_5 & 0 \\ 0 & 0 & 0 & 0 & 0 & c'_6 \end{bmatrix} \quad (4.20)$$

$$\mathbf{L}'' = \begin{bmatrix} (c''_2 + c''_3)/3 & -c''_3/3 & -c''_2/3 & 0 & 0 & 0 \\ -c''_3/3 & (c''_3 + c''_1)/3 & -c''_1/3 & 0 & 0 & 0 \\ -c''_2/3 & -c''_1/3 & (c''_1 + c''_2)/3 & 0 & 0 & 0 \\ 0 & 0 & 0 & c''_4 & 0 & 0 \\ 0 & 0 & 0 & 0 & c''_5 & 0 \\ 0 & 0 & 0 & 0 & 0 & c''_6 \end{bmatrix} \quad (4.21)$$

$$\boldsymbol{\sigma}^T = (\sigma_{xx} \quad \sigma_{yy} \quad \sigma_{zz} \quad \sigma_{yz} \quad \sigma_{xz} \quad \sigma_{xy}) \quad (4.22)$$

In the extended anisotropic form of the yield function proposed, the material constants of  $a, b$  and  $c$  in the isotropic form of the yield function are implicitly coupled by  $h_x, h_y, h_z$  and anisotropic parameters in two fourth-order linear transformation tensors of  $\mathbf{L}'$  and  $\mathbf{L}''$ .

The anisotropic pressure sensitivity parameters of  $h_x, h_y$ , and  $h_z$  are computed by uniaxial tensile tests in rolling direction (RD), transverse direction (TD), and normal direction (ND) under different hydrostatic pressure. Here the pressure sensitivity is assumed to be isotropic for the simplicity purpose. That is,  $h_x = h_y = h_z = b$ . Then the anisotropic yield function reduces to a form of

$$f(\sigma_{ij}) = bI_1 + (J_2'^{3/2} - J_3'')^{1/3} \quad (4.23)$$

#### 4.2.4 Modeling of Yield Surface Evolution for Zirconium Clock-Rolled Plate

The yield function proposed in Eq. (23) is employed to illustrate the yield surface evolution of a zirconium clock-rolled plate during in-plane and through-thickness compression for various levels of pre-strains. The evolution of yield surfaces is reported by Plunkett et al. [31] using the visco-plastic self-consistent (VPSC) polycrystalline model of Lebensohn and Tomé [32]. In the VPSC model, the initial texture was obtained from experiments. The deformation mechanisms are assumed to be composed of prismatic  $\langle a \rangle$ -slip, pyramidal  $\langle c + a \rangle$ -slip and tensile twinning. The slip and twinning parameters (i.e. critical stresses, hardening coefficients and rate sensitivity exponent) are referred after Tomé et al. [33].

Effect of texture evolution is investigated on the yielding behavior of the zirconium clock-rolled plate using the VPSC polycrystalline model. Yield stresses are depicted as the symbols in Fig. 4 during in-plane compression for various levels of 1 %, 5 %, 25 %, 35 %, 45 % and 60 %. For each level of pre-strain, the material constants of the proposed yield function in Eq. (4-23) are optimized to match with yield stresses with minimum errors as summarized in Table 1. With the material constants optimized in Table 1, the yield surfaces are constructed for

different levels of pre-strains and compared with the stresses computed by the VPSC polycrystalline model in Fig. 58. The comparison reveals that the proposed yield function accurately describes the yielding behavior of the zirconium clock-rolled plate for various levels of pre-strain in in-plane compression.

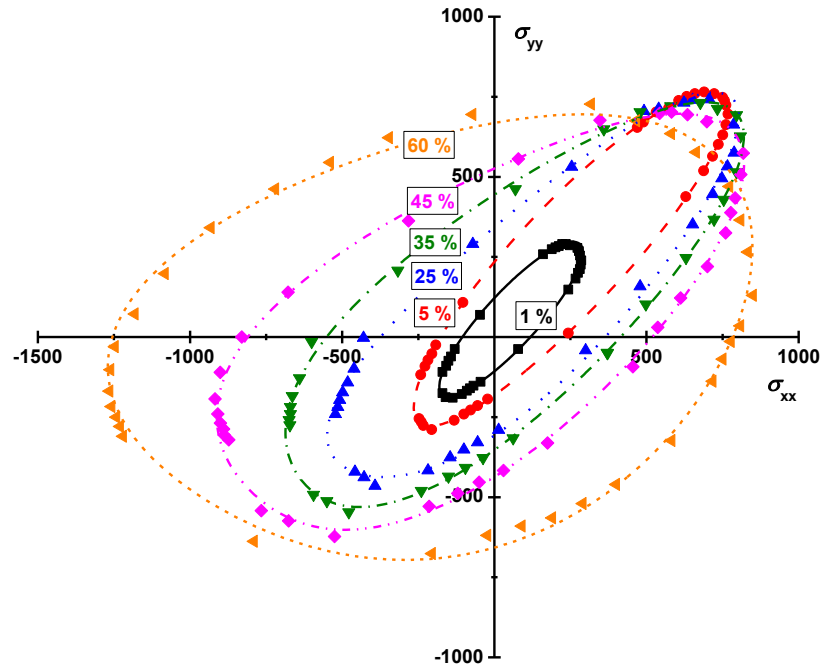


**Figure 61** Comparison of yield surface evolution predicted by the proposed yield function with those computed by the VPSC model for a zirconium clock-rolled plate during in-plane compression for various levels of pre-strain. (units: MPa)

In addition, yield stresses of the identical metals are computed by the VPSC polycrystalline model during through-thickness compression for different levels of pre-strains (0.2 %, 1 %, 5 %, 25 % and 35 %) as illustrated by symbols in Fig. 58.

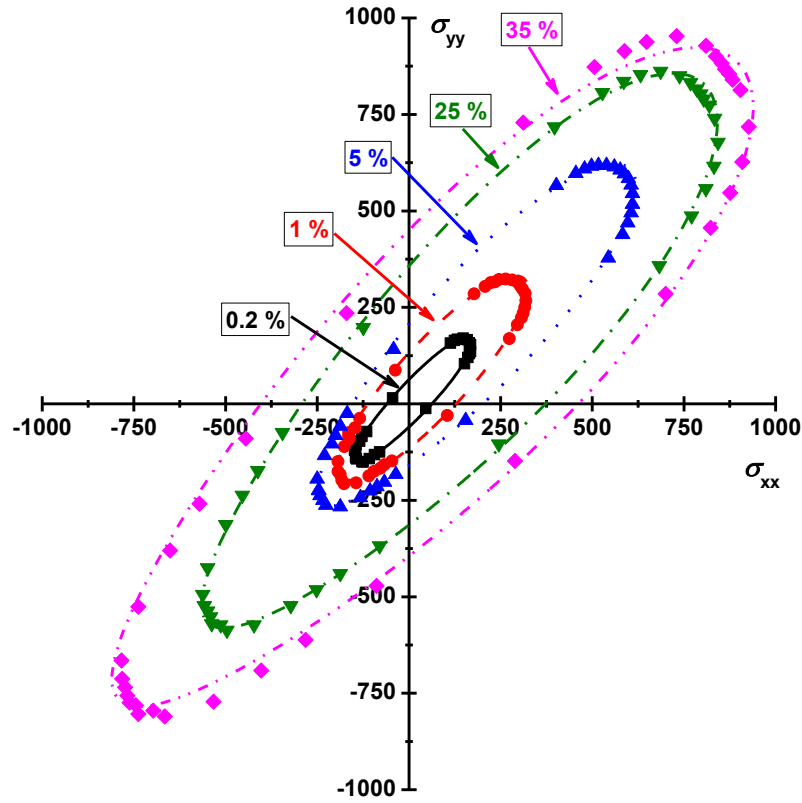


**Figure 62** Comparison of yield surface evolution predicted by the proposed yield function with those computed by the VPSC model for a zirconium clock-rolled plate pre-strained in through-thickness compression for various levels of pre-strain. (units: MPa)

These yield stresses are utilized to optimize the material constants of the proposed yield function as listed in Table 2. The yield surfaces are predicted by the yield function in Eq. (4.23) with the material constants optimized. The yield surfaces predicted are compared with those computed by the VPSC model. It is obvious that the proposed yield function accurately models the evolution of the yield surfaces during through-thickness compression for different pre-strain levels.

#### 4.2.5 Application to High-Purity $\alpha$ -Titanium

Titanium alloys are widely used in aerospace engineering, energy and automotive industries owing to their attractive mechanical properties of elevated strength-to-density ratio, exceptional corrosion and erosion resistance and excellent structural efficiency even at high temperatures. Titanium alloys are also a promising material in body implants and prosthetic devices because of the inherent non-reactivity with tissue and bone: nontoxic, non-allergenic and fully biocompatible. Thus, the proposed yield function is applied to describe plastic behavior of a high purity  $\alpha$ -titanium, Nixon et al. [20]. Yielding of this metal is assumed to be insensitive to hydrostatic pressure because there is no experimental result from uniaxial tensile tests under different hydrostatic pressure indicating that hydrostatic pressure affects plastic deformation of titanium alloys. Moreover, SD effect of high-purity  $\alpha$ -titanium is not severe and can be successfully modeled by the proposed yield function without pressure sensitivity. Therefore, the material constant of  $b$  is set to zero for high-purity  $\alpha$ -titanium. Taking the advantage of pressure insensitivity of high-purity  $\alpha$ -titanium, the three-dimensional yield surfaces are constructed on the  $\pi$ -plane by the yield function proposed for various amount of plastic strain: 0 %, 5 %, 10 % and 20 %. The constructed yield surfaces are compared with experimental data points as depicted in Fig. 3-6. Besides, comparison of the yield surfaces is also carried out under plane stress conditions in Fig. 3-7. The comparison in both spatial loading and plane stress demonstrates that the yield function proposed accurately models the orthotropic behavior of the high-purity  $\alpha$ -titanium not only in tension but also in compression.

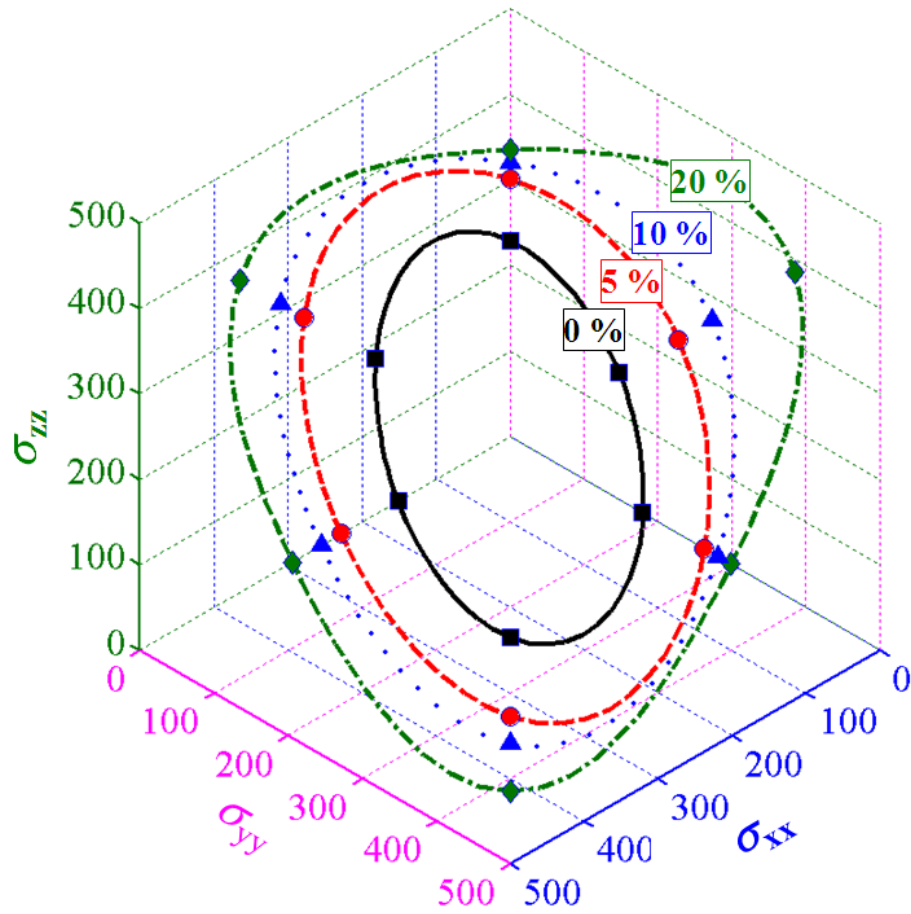


**Figure 63** Comparison the yield surfaces of high-purity  $\alpha$ -titanium constructed by the proposed yield function on the  $\pi$ -plane with experimental results (units: MPa)



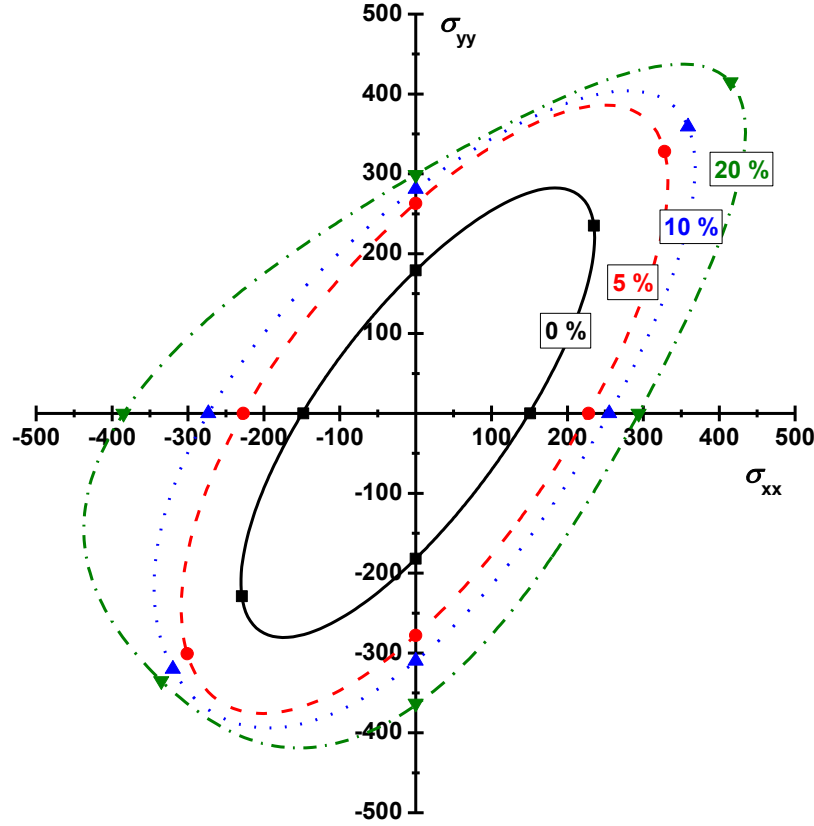


**Figure 64** Comparison the yield surfaces of high-purity  $\alpha$ -titanium constructed by the proposed yield function under plane stress with experimental results (unit: MPa).

### 4.3 Conclusions to Chapter 4

A new general yield function based on non-associated flow plasticity is proposed to extend symmetric yield functions to consider the SD effect for incompressible sheet metals. The SD effect is coupled by considering the hardening curves in both tension and compression. The new yield function is proven to be able to describe both anisotropy and asymmetry of sheet metals from the comparison of predicted yield surfaces for HCP metals with strong SD effect. The anisotropic form of the proposed yield function is validated to be capable of modeling evolution

of yield surfaces for a zirconium clock-rolled plate during in-plane and through-thickness compression for various levels of pre-strain.

#### 4.4 Recommendations and Path Forward: Temperature Dependent Creep Surface under General Loading Conditions

Constitutive laws in materials generally consist of a state equation and evolution equations. The state equation describes the relationship between the strain rate  $\dot{\epsilon}$ , stress  $\sigma$ , temperature  $T$  and state variables  $x^k$ , which represents the microstructural state of the material. The porosity of a material and a measure of the accumulated plastic deformation such as the effective strain or the dislocation density are a few examples of the variables  $x^k$ . The state equation can be expressed mathematically, for instance in a scalar form for uniaxial deformation, as

$$\dot{\epsilon} = \dot{\epsilon}(\sigma, T, x^k) \quad (4.24)$$

The evolution equations describe the development of the microstructure through the change of the state variables and can take the form

$$\dot{x}^k = \dot{x}^k(\sigma, T, x^k) \quad (4.25)$$

In Phase-I, the evolution equation for Zr. has been derived at the room temperature as shown in Figures 3-8. Then, the evolution model was only the function of stress (not a function of temperature)

$$\dot{x}^k = \dot{x}^k(\sigma, x^k) \quad (4.26)$$

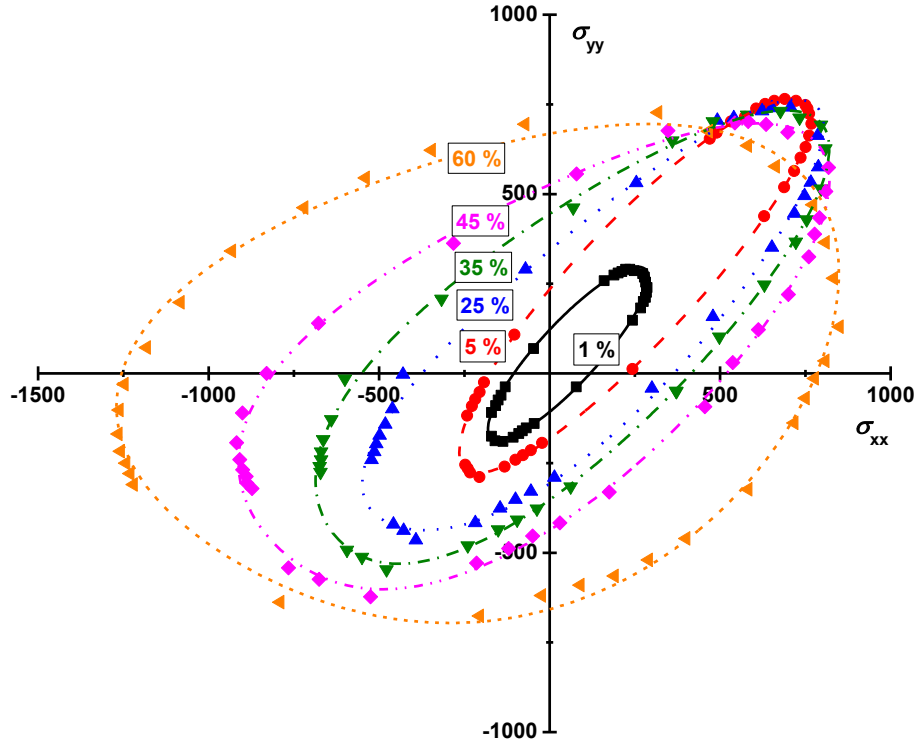


**Figure 65** Comparison of yield surface evolution predicted by the proposed yield function with those computed by the VPSC model for a zirconium clock-rolled plate during in-plane compression for various levels of pre-strain. (units: MPa)

Eq. (4.26) was derived based on non-associated flow plasticity. Also, the VPSC (Visco-Plastic Self Consistent) model utilizing texture measurement was also utilized to replace the extensive experimental testing to calibrate the proposed model.

In Phase-II, a temperature dependent creep evolution model for Zr. alloy is proposed to be developed. As shown in Fig.2, Zr. shows a dramatic decrease of yield stress by increasing temperature. If the critical stress to initiate cracking of Zr. is defined, cracking is assumed to be occurred with

$$\Delta T \geq \frac{2\sigma_{cr}(1-\nu)}{\alpha E} \quad (4.27)$$

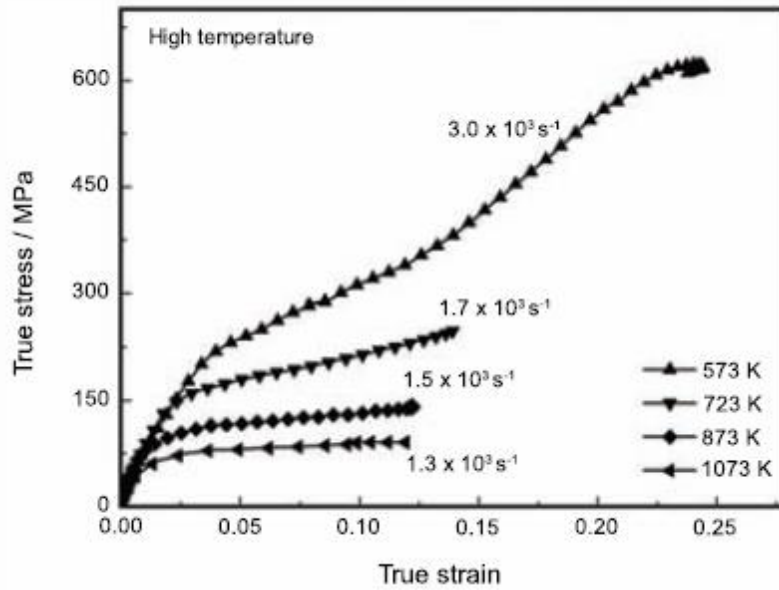


**Figure 66** True stress behavior of Zirconium under compression under various high temperatures

Eq. (4.27) is commonly accepted in nuclear industry. However, since Zr. shows very strong asymmetric and anisotropic plastic behaviors, the simple scalar equation to connect Zr. creep fracture only with temperature and crystal stress is not reliable. The creep criteria in Eq. (4.27) must be represented in a continuous tensor space with temperature dependency as the initiation of creep behavior.

For this purpose, in-situ texture data with various temperatures should be measured for the VPSC crystal plasticity model to calibrate the time dependent coefficients of the constitutive model. Also, one directional in-situ tensile or compression testing under each temperature is recommended for a reference point. Then, it is able to generate a temperature dependent creep model like Eq.2 and to predict the precise creep behavior of Zr, alloy. The merit of this approach is to incorporate minimum experimental data with the help of crystal plasticity modeling. Also, it

is allowed to generate the complete creep space under a general loading condition at any temperature.

**Input data:**

- Tensile testing along one direction for selected several temperatures
- Texture data for selected several temperature.

**Predictions:**

*(VPSC Polycrystal Model for the selected temperatures)*

- Directional properties for any loading condition
- Evolution of r-values with respect to effective plastic strain
- Discrete strain-rate potential.

*(Non-Associated Continuum Model)*

- Yield Surface Evolution as the function of temperature and stress triaxiality
- Dual Creep Surface (Strain-rate potential) from yield surface evolution.

The schematic diagram to explain input and output is presented in Fig.10.

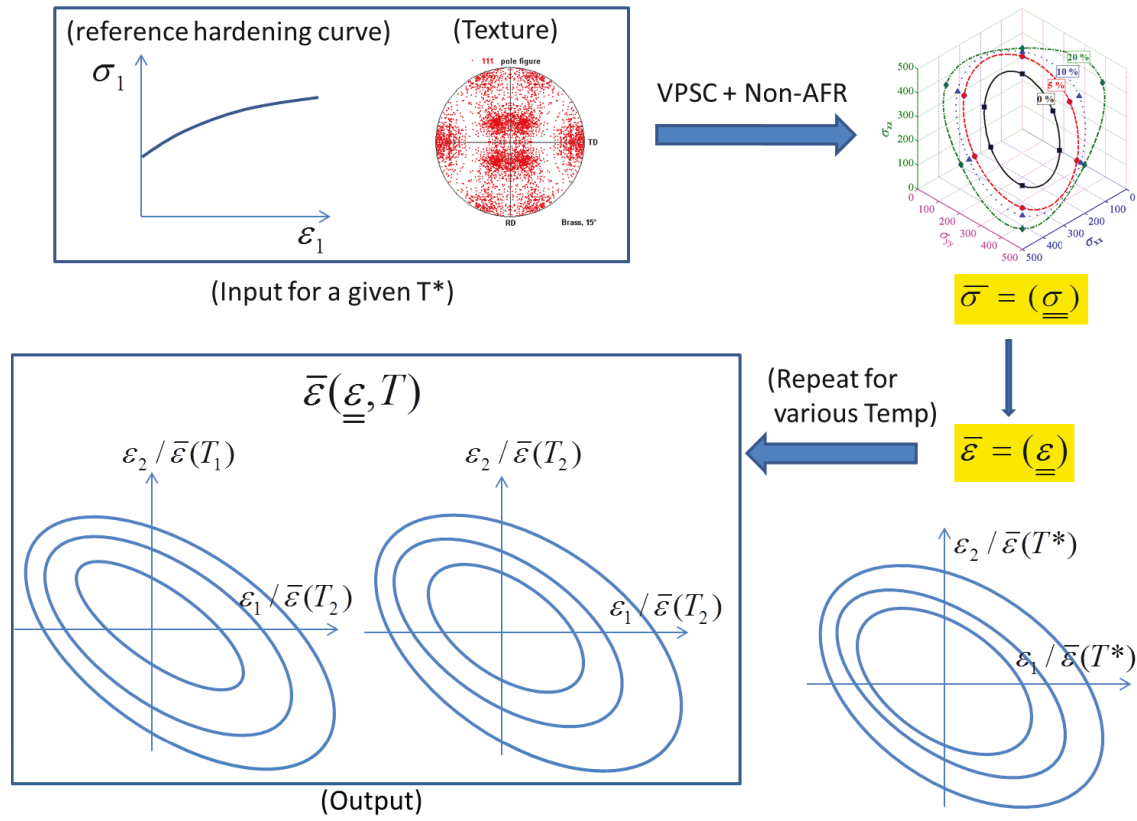


**Figure 67** Schematic view of a proposed general methodology

## 4.5 Tables

**Table 1** Material constants in the proposed yield function in Eq. (23) for a zirconium clock-rolled plate during in-plane compression for various levels of pre-strain

Pre-strain	$b$	$c'_1$	$c'_2$	$c'_3$	$c''_1$	$c''_2$	$c''_3$
1 %	-0.0608	0.8296	0.9253	2.3893	-0.0242	-0.0802	0.0553
5 %	-0.1410	0.9767	1.1056	2.7774	-1.0342	1.3298	0.3355
25 %	-0.0100	1.3992	0.8097	2.2170	-3.7006	-0.3056	0.2823
35 %	-0.0563	1.4783	0.8918	2.2120	1.1077	-0.9910	-2.9780
45 %	-0.0319	1.8039	0.9850	1.9848	0.6250	-0.7562	-3.6015
60 %	0.0003	2.6681	1.5868	1.3944	0.8682	-1.8095	-1.6691

**Table 2** Material constants in the proposed yield function in Eq. (23) for a zirconium  
 clock-rolled plate during through-thickness compression for various levels of pre-strain

Pre-strain	$b$	$c'_1$	$c'_2$	$c'_3$	$c''_1$	$c''_2$	$c''_3$
0.2 %	-0.0178	0.5946	0.6074	2.3372	0.4017	-0.7646	0.2295
1 %	-0.0746	0.9357	1.0463	2.7183	-0.0008	-0.0450	0.0245
5 %	-0.1379	0.9066	1.0312	2.6937	0.5818	1.1102	0.8839
25 %	-0.0685	0.8530	0.9600	2.5815	-1.6096	1.1486	1.6666
35 %	-0.0621	0.9858	0.8798	2.4899	0.9359	1.0635	-1.3575



## 4.6 References to Chapter 4

1. J. Lubliner, J., Plasticity Theory. Macmillan, New York (1990)
2. J.L. Bassani, *Adv. Appl. Mech.*, 30, 191 (1994)
3. J. Rice, *J. Mech. Phys. Solids*, vol.19, 433 (1979)
4. M. Zaiser, M.V. Glazov, L.A. Lalli, and O. Richmond, *Comp. Mater. Sci.*, vol.15, pp.35-49 (1999)
5. Rice, J., Continuum mechanics and thermodynamics of plasticity in relation to microscale deformation mechanisms, in *Constitutive Equations of Plasticity*, ed. A. Argon. MIT Press, Cambridge, MA, pp. 23-75 (1975)
6. A. Seeger, in *Dislocations*, ed. P. Veyssiere, L. P. Kubin and J. Castaing, CNRS, Paris, p. 141 (1984)
7. L. Hollang, L., M. Hommel, M. and A. Seeger, *Physica Status Solidi (a)*, vol. 160, 329 (1997)
8. U. Holzworth, and A. Seeger, in *Proc. 9th Int. Conf. Strength of Metals and Alloys*, ed. D. G. Brandon, R. Chaim and A. Rosen. Freund, London, p. 577 (1991)
9. M. Werner, *Physica Status Solidi (a)* v.104, 63 (1987).
10. V. Vitek, in *Proc. NATO Workshop on the Stability of Materials*, Korfu, Greece, 1995
11. O. Richmond, and W. Spitzig, Pressure Dependence and Dilatancy of Plastic Flow, *Int. Union of Theoretical and Applied Mechanics*, 1980.
12. W.A. Spitzig, and O. Richmond, *Acta Metall.*, (1984)
13. [http://en.wikipedia.org/wiki/Von\\_Mises\\_yield\\_criterion](http://en.wikipedia.org/wiki/Von_Mises_yield_criterion)
14. J.-W. Yoon, Ya. Lou, J.H. Yoon, and M.V. Glazoff, Asymmetric Yield Function Based on the Stress Invariants for Pressure Sensitive Metals, *International Journal of Plasticity*, vol.56, pp.184-202 (2014)
15. O. Cazacu, F. Barlat, A criterion for description of anisotropy and yield differential effects in pressure-insensitive metals, *International Journal of Plasticity* 20, 2027-2045 (2004)
16. O. Cazacu, B. Plunkett, F. Barlat, Orthotropic yield criterion for hexagonal closed packed metals, *International Journal of Plasticity* 22, 1171-1194 (2006)

17. B. Plunkett, R.A. Lebensohn, O. Cazacu, F. Barlat, Anisotropic yield function of Hexagonal materials taking into account texture development and anisotropic hardening, *Acta Materialia* 54, 4159-4169 (2006)
18. M.E. Nixon, O. Cazacu, R.A. Lebensohn, Anisotropic response of high-purity  $\alpha$ -titanium: experimental characterization and constitutive modeling, *International Journal of Plasticity* 26, 516-532 (2010)
19. J.H. Yoon, O. Cazacu, R.K. Mishra, Constitutive modeling of AZ31 sheet alloy with application to axial crushing, *Materials Science & Engineering A* 565, 203-212 (2013)
20. S.K. Khan, S. Yu, Deformation induced anisotropic responses of Ti-6Al-4V alloy. Part I: experiments, *International Journal of Plasticity*, 38, 1-13 (2012)
21. S.K. Khan, S. Yu, H. Liu, Deformation induced anisotropic responses of Ti-6Al-4V alloy. Part II: a strain rate and temperature dependent anisotropic yield function, *International Journal of Plasticity* 38, 14-26 (2012)
22. R. Hill, A theory of the yielding and plastic flow of anisotropic metals", *Proc. Roy. Soc. London, A*193, 281-297 (1948)
23. T.B. Stoughton and J.-W. Yoon, A pressure-sensitive yield criterion under a non-associated flow rule for sheet metal forming, *Int. J. Plasticity*, 20, 705-731 (2004)
24. Stoughton, T. B., and Yoon, A Review of Drucker's Postulate and the Issue of Plastic Stability in Metal Forming, *Int. J. of Plasticity*, 22, 391-433 (2006)
25. Stoughton, T. B. and Yoon, J. W., On the existence of indeterminate solutions to the equations of motion under non-associated flow, *Int. J. Plasticity*, 24, 583-613 (2008)
26. W.A. Spitzig, O. Richmond, The effect of pressure on the flow stress of metals, *Acta Metallurgica* 32, 457-463 (1984)
27. W.A. Spitzig, R.J. Sober, O. Richmond,, Pressure dependence of yielding and associated volume expansion in tempered martensite, *Acta Metallurgica* 23, 885-893 (1975)
28. D.C. Drucker, W. Prager, Soil mechanics and plastic analysis for limit design, *Quarterly of Applied Mathematics* 10, 157-165 (1952)
29. B. Plunkett, O. Cazacu, R.A. Lebensohn, F. Barlat, Elastic-viscoplastic anisotropic modeling of textured metals and validation using the Taylor cylinder impact test, *International Journal of Plasticity* 23, 1001-1021 (2007)
30. R.A. Lebensohn, C.N. Tomé, A self-consistent anisotropic approach for the simulation of plastic deformation and texture development of polycrystals: application to zirconium alloy, *Acta Metallurgica et Materialia* 41, 2611-2624 (1993)
31. C.N. Tomé, P.J. Maudlin, R.A. Lebensohn, G.C. Kaschner, Mechanical response of zirconium-I. Derivation of a polycrystal constitutive law and finite element analysis, *Acta Materialia* 49, 3085-3096 (1993)

## **Chapter 5 Morphological Analysis of Zirconium Nuclear Fuel Retaining Rods Braided with SiC: Quality Assurance and Defect Identification**

### **5.1 Introduction**

In Chapter 3, several potential protection approaches were considered in order to improve the zircalloys' thermal stability. In all such cases, one must be sure that the proposed coating / braiding is chemically inert and would not interact with Zr, that all thermo-mechanical characteristics are compatible enough to provide a good protection for Zr clad, and that it is crack (or, more generally, defect) free.

To be able to identify defects of a cladding or braiding material automatically, without human interference, is a serious technological and mathematical problem. In this Chapter we propose a novel solution for the identification of defects in  $\alpha$ -SiC-braiding obtained at INL using an original process described below. It is based on the so-called “mathematical morphology” and is applied in nuclear materials engineering for the 1<sup>st</sup> time [1, 2]. Before the description of the morphological algorithm, we provide a brief overview of the production process [3, 4].

Currently, alpha - silicon carbide ( $\alpha$ -SiC) is being explored as a cladding or braiding material candidate for fuel rods in water-cooled reactors. The material's combination of high strength and hardness, chemical inertness, and attractive thermal properties (high conductivity, low expansion, and thermal shock resistance) makes it useful for an impressive variety of applications. Unlike most ceramic materials, it also performs well in a nuclear reactor environment (excellent radiation stability, low activation elements; retains its strength and shape

under high dpa conditions) [5, 6]. SiC exhibits polymorphism, and more than 250 polytypes have been identified. One of such crystal stacking arrangements results in the formation of the cubic 3C-SiC ( $\beta$ ) structure. All hexagonal stacking arrangements (2H, 4H, 6H, etc.) are grouped together as  $\alpha$ -SiC with the 6H polytype being the most prevalent [7].

$\beta$ -SiC fibers are very strong ( $\sim 3$  GPa tensile strength) and stiff ( $\sim 420$  GPa tensile modulus), but are quite expensive. These materials are only available from outside the United States in limited quantities and at costs ranging from \$500 to \$6,000 per pound.  $\beta$ -SiC fibers are used in high cost products, including high-temperature semiconductors, abrasives, wear components, armor, rockets, turbine engines plus metal and ceramic matrix composites.

Recently, a novel material processing technology was developed at the Idaho National Laboratory for making alpha silicon carbide ( $\alpha$ -SiC) fibers by low-cost direct conversion of carbon fibers using the SiO vapor, see Figure 1 [Garnier et al., 8].

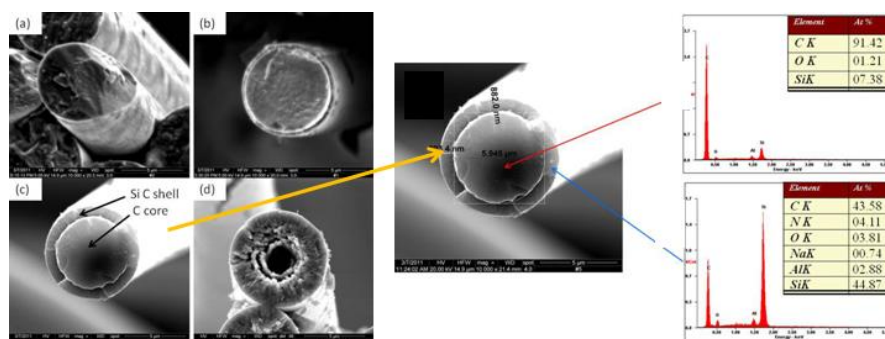


**Figure 68** SEM photomicrographs of cross sections of C fibers filaments during conversion to SiC. **(a)** As-received (unconverted) PAN-based carbon fibers. **(b)** Partially converted carbon filament with  $\sim 200$  nm thick SiC shell. **(c)** Partially converted C filament with  $1\ \mu\text{m}$  thick SiC shell. **(d)** Fully converted SiC tube. SEM/EDS analysis of a partially converted filament (right) indicates stoichiometric conversion of C to SiC, [8].

Different technical solutions may be proposed for developing SiC ceramic based fuel cladding. In one project developed at the INL [8], initial zircaloy cladding tube was braided with fiber, Figure 68, with additional water resistant coating, in order to avoid direct contact of water with zircaloy tube. As demonstrated in [3], this system exhibits excellent corrosion resistance at high temperatures corresponding to emergency conditions (temperatures up to 2200°C, [3]).

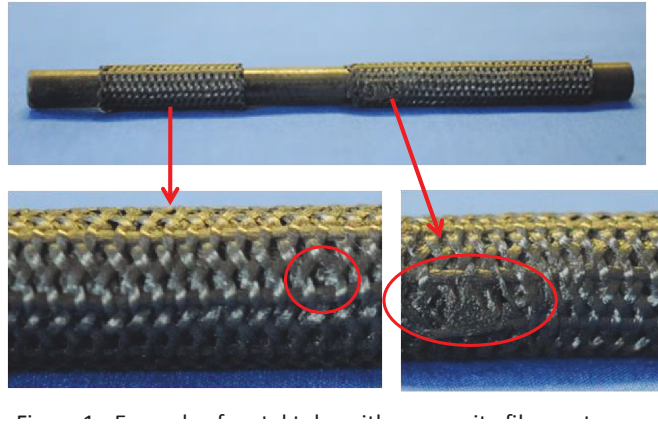


**Figure 69** Zy-4 tube with composite fiber outer wrap. Off-normal braided features are highlighted in red circles.

In this work, we report the results of quality control for SiC-protected Zy-4 material using an original and unique advanced set of mathematical morphology algorithms of mathematical morphology. The paper is organized as follows. Section 2 contains formulation of the problem and a general description of the mathematical morphology approach to quality assurance in industrial applications. A more detailed description of the problem and the algorithms are discussed in Section 3, followed by the main results, their discussion, and conclusions in Section 4.

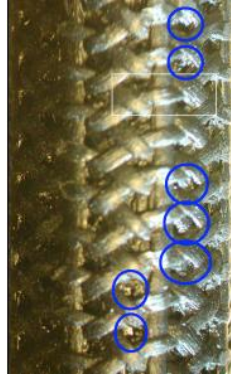
## 5.2 Formulation of the Problem

Figure 70 presents a general view of the ZY-4 tubing braided with SiC fibers. It contains a “standard”, or “reference” area, tentatively without defects of any kind. It conforms to the periodicity rules imposed by the morphology of the coating.



**Figure 70** General view of the analyzed sample (optical - digital photography)

We further analyze this image to identify (extract) those portions of it that contain (relatively) large deviations (with respect to the accepted standard) of the two types: 1. Local defects and non-uniformities in the weaving of the SiC filaments; and 2. Global defects –shifts, stretched areas; rotations, etc. In the second image, Figure 68, we have identified visually local defects (blue ovals) and global defects (lateral shifts of the vertical filaments).



**Figure 71** Local defects (blue ovals) and global defects (lateral shifts of the vertical filaments)

Our goal is to identify possible defects of the braiding comparing the standard area (denoted by white rectangle) to the rest of the specimen surface. While so doing, it is necessary to eliminate the “defects” caused by non-uniformity of the sample illumination, and introduce corrections for its cylindrical shape. However, before proceeding with the description of the developed algorithms, one needs to have a brief introduction on the general subject of mathematical morphology.

### 5.3 What is Mathematical Morphology?

Here we describe an original approach to multi-scale image analysis and segmentation of complex  $N$ -dimensional color images. Unlike any “algebraic” linear integral transform methods (fast Fourier transform or FFT, wavelets etc. [9-11]) it is geometry-based and involves image filtering with simple geometrical figures [12-14]. In this sense, it has some similarities to mathematical morphology proposed by Serra and Matheron [15-19]. However, the approach described below is completely original and was developed independently [12-14, 20].

The key point in any problem of image segmentation, feature extraction, etc., is *the formulation of its mathematical model*. The human visual cortex and rapid processing power of

the human mind are really hard to match - even with fast computers and sophisticated algorithms. On a purely qualitative level, human beings solve many problems of image analysis and recognition almost every waking minute. This implies that the models used in such cases are largely representative of reality. Typically, data inferred from such analysis are compared to the existing knowledge about the studied objects/processes.

Using computers it is currently difficult to analyze a variety of images in a completely automatic mode. One reason is that for “real-time” automatic image processing, substantial supercomputer resources are needed. Perhaps more importantly, in many cases, mathematical models of objects and/or phenomena, which are being studied, are very complex and difficult to build, if at all possible.

On the other hand, a large class of problems exists that can be solved by computers far better than by humans. Typically, these problems include simple models of image formation, which open the possibility of analyzing information about object shape(s) that is contained in images.

From this point of view, one of the most fundamental problems in the general field of image analysis is the construction of such mathematical models that capture the principal features and contents of an image. Such a description (or mathematical model) must include only the most relevant, fundamental information about the image (the ‘signal’) and ignore the less relevant information (subtle details, i.e., ‘noise’). In *morphological analysis* we assume that a suitable image is available; we consider as irrelevant the conditions of image acquisition, or its background, the parameters of registering instruments, or the conditions of illumination. Thus, one could conclude that the methods of morphological analysis are a step on the way towards understanding image semantics. Images of the same scene recorded at different conditions (e.g.,



weather, illumination, time of day, etc.) can differ radically. This fact renders far more difficult the tasks of analysis and feature extraction of “real” images – that ideally should *not* depend on the conditions of their registration.

Among others, one could mention problems of identifying an unknown object on the background of a well-known scene, with uncontrolled illumination. The methods of morphological analysis developed for solving such problems have turned out to be very effective.

Consider the principal idea of such methods using the following example. Assume that a certain image was acquired using a camera in the visible spectral range. As a rule, it carries ‘sufficiently detailed’ information about the geometrical shapes of the objects so that the objects can be detected and identified or classified. This statement is true because object surfaces that possess the same geometrical and optical properties generally have the same brightness. Assume that these properties are conserved even if the spectral range of illumination and its nature are changed. Images of a given scene, even though potentially acquired with different optical techniques and in different conditions, will be connected to the geometrical properties of the objects comprising the scene, and they can (in principle) be obtained (extracted) via image brightness transformation(s). In mathematics it is said that the maximal invariant of such class of transformations will determine all of the objects that are *inherently* present at a given scene and do not depend upon the conditions of image formation. Such an invariant, in analogy to solid-state physics, could be called the “form-factor”, or “form (shape)”. Inasmuch as this invariant does not define the scene completely, it is called the image form for a given scene. The differences between one scene image and the others that are not related to the conditions of image acquisition could be related to the differences in the image content – for example, the appearance of new objects on the scene, or disappearance of old objects. The brightness of

infrared images that carries information on the physical properties of objects (e.g., thermal contrast) could be related to the geometric shape of the images and, thus, firmly connected to specific objects on this scene.

To continue, we introduce the mathematical language used in order to conduct multispectral morphological analysis of different complex objects. By the term *image* we will define a function  $f(\cdot): X \rightarrow R^1$ , given on a discrete set  $X = \{x_1, \dots, x_N\}$ , called the “field of view”. For convenience we will consider that images are just vectors of the  $N$ -dimensional Euclidean space:  $f_i = f(x_i)$ ,  $x \in X$ ,  $i = 1, \dots, N$ . In certain cases (which are important from the practical point of view) a model of image transformation can be described as follows:

$$f = F(h, \nu), \quad h \in V_g \subset R^N, \quad f \in R^N, \quad (5.1)$$

where  $f$  is obtained for different conditions of its acquisition.  $F$  is the function characterizing additional possible distortions introduced in the course of image acquisition. In addition to that, image distortions can be stochastic and depend on a random noise,  $\nu$ . The set  $V_g$  is called the form of image  $g$ . The one, which is minimal with respect to its inclusion into the linear vector space,  $L_g \subset R^N$ , containing that set  $V_g$ , will be called “form - in the broad, or general, sense”. If  $V_a \subset V_b$ , then we will say that image  $a$  is not any more complex in its shape than image  $b$  and will denote this as  $a \prec b$ . If  $a \prec b$  and  $a \succ b$ , then we will say that two images are equivalent with respect to their forms, and will denote that fact as  $a \sim b$ .

Not surprisingly, the case that is most extensively studied is when the image  $f$  is transformed according to the linear scheme given below:

$$f(x) = g(x) + \nu(x), \quad x \in X, \quad g(\cdot) \in V_g, \quad (5.2)$$

In expression (2) it is assumed that the shape  $V_g$  is known, and the first moment  $E\nu(x) = 0$ ,

$x \in X$ , the noise is uncorrelated:  $E\nu(x_1)\nu(x_2) = \begin{cases} \sigma^2, & x_1 = x_2 \\ 0, & x_1 \neq x_2 \end{cases}$ ,  $x_1, x_2 \in X$ , and the dispersion

$\sigma^2$  is unknown. Image  $g$  in expression (5.2), which defines the shape (form),  $V_g$ , is a linear combination of the following type:

$$g(x) = \sum_{i=1}^n c_i \chi_i(x), \quad x \in X, \quad (5.3)$$

In expression (3),  $c_i \in R^1$ ,  $i = 1, \dots, n$ ; and  $\chi_i(\cdot)$ ,  $i = 1, \dots, n$ , – are the characteristic functions of the sets  $A_1, \dots, A_n$ , forming the field of view:

$$X: \chi_i(x) = \begin{cases} 0, & x \notin A_i \\ 1, & x \in A_i \end{cases}, \quad \bigcup_{i=1}^n A_i = X, \text{ and } V_g = \{h_F : h_F(x) = F(g(x)), x \in X, F(\cdot) \in \mathbf{F}\},$$

In this expression, function  $F(\cdot)$  represents the influence of different conditions of the image formation;  $\mathbf{F}$  is a set of functions such that  $F(\cdot): R^1 \rightarrow R^1$ , which describe the variety of conditions of image acquisition and/or formation.

Let's assume that  $h_F(x) = F(g(x)) = \sum_{i=1}^n F(c_i) \chi_i(x)$ , then the form of image  $g$  is just a linear combination of orthogonal<sup>8</sup> vectors  $\chi_i$ ,  $i = 1, \dots, n$ , in Euclidean space  $R^N$  of all images, i.e. it is an  $n$ -dimensional subspace of vector space  $R^N$ , as shown below:

$$V_g = \left\{ h(x) = \sum_{i=1}^n C_i \chi_i(x) \mid C_i \in R^1, i = 1, \dots, n \right\} \quad (5.4)$$

---

<sup>8</sup>  $(\chi_i, \chi_j) \equiv \sum_{x \in X} \chi_i(x) \chi_j(x) = 0$ , if  $i \neq j$ ,  $i, j = 1, \dots, n$

Form  $V_g$  is uniquely defined by the concatenation  $\bigcup_{i=1, \dots, n} A_i = X$ . It is important that the brightness of each image,  $h \in V_g$  on each of the sets  $A_i, i = 1, \dots, n$ , is constant. In other words, a random image formed according to the model  $\{(2), (3)\}$ , obtained at different observation/acquisition conditions (each described by a function  $t(\cdot) \in T$ ), will possess a constant first moment (mathematical average) on each of the sets  $A_1, \dots, A_n$ , and the same dispersion (second moment).

Now consider the problem of approximating an image  $f \in R^N$  by such images

$$h \in V_g \quad (5.5)$$

that the solution of this problem, a vector function  $\tilde{g}$ , is an argument that delivers the global minimum to the energy-like quadratic functional:

$$\tilde{g} = \arg \min_{h \in V_g} \|f - h\|^2. \quad (5.6)$$

It is well known from theory [2] that this problem can always be uniquely solved. The solution is an orthogonal projection

$$\tilde{g} = \Pi_{V_g} f = \sum_{i=1}^n \frac{(f, \chi_i)}{\|\chi_i\|^2} \chi_i \text{ of the image } f \text{ on } V_g, \quad (5.7)$$

By definition,  $(a, b) = \sum_{x \in X} a(x)b(x)$  is the scalar product and  $\|a\|^2 = (a, a)$  is the vector norm squared in the Euclidean space  $R^N$ .

Let the image  $f$  be defined by the equality (2), in which  $g \in V_g$ . Then the following mathematical statement will be true:

$$E \| f - \Pi_{V_g} f \|^2 = E \| g + v - \Pi_{V_g} g - \Pi_{V_g} v \|^2 = E \| (I - \Pi_{V_g})v \|^2 \quad (5.8)$$

In equation (8)  $I : R^N \rightarrow R^N$  – is the unity operator. The value  $\| (I - \Pi_{V_g})f \|^2$ , which is equal to the distance squared between  $f$  and  $V_g$ , is a measure of quality of the approximating solution. It also characterizes the difference between image  $f$  and image  $g$ .

### Example

As an example, we consider the problem of quantitative characterization of metallic surfaces. In the process of rolling metallic sheet it would be desirable to analyze surface quality automatically. On that basis, a positive feedback loop could allow the shop floor operator to make decisions about changing different parameters of the rolling process (e.g., under-lubrication, over-lubrication, rolling speed, etc.). Typically, rolled sheet inherits its thermo-mechanical processing history: rolling results in the appearance of so-called “roll grind imprint”, while stretching – in the appearance of grain roughening or, in industrial parlance, “orange peel”.

The developed algorithms allowed analyzing both quantitative 3D-data on surface heights obtained using a confocal microscope, and conventional 2D digital photographs.

As it was pointed out above, the principal idea of morphological analysis is to extract from an image the maximal amount of information (the ‘signal’) that pertains to the shapes of the objects/features comprising it, while discarding the remaining part of information (‘noise’) related to non-interesting features and the conditions of image acquisition.

In the present work  $f(x, y)$  is directly the height of explored surface at a given point, which gives one a possibility to analyze different surface shapes.

A *Morphological filter* can be considered an operator  $T: R_I \rightarrow R_I$ , where  $R_I$  is the functional space of images. In this work, we will use filter  $T_1$  – it will be called “Filter of the 1<sup>st</sup> order”:

$$T_1 f(x, y) = a_{xy}x + b_{xy}y + c_{xy}, \quad (5.9)$$

The coefficients  $a_{xy}$ ,  $b_{xy}$ , and  $c_{xy}$  for each surface point  $(x, y)$  are found from the condition

$$\int_{Q_{xy}} (f(x', y') - a_{xy}x' - b_{xy}y' - c)^2 dx' dy' \sim \min_{a_{xy}, b_{xy}, c_{xy}} \quad (5.10)$$

In this last expression,  $Q_{xy}$  stands for the domain of the morphological filter that is defined as:

$Q_{xy} = [x-w, x+w] \times [y-h, y+h]$ , where  $w$  and  $h$  are the semi-length and semi-width of the filter

domain. Using this notation, one can write down the formulation of the problem in the following way:

$$\int_{x-w}^{x+w} dx' \int_{y-h}^{y+h} dy' (f(x', y') - a_{xy}x' - b_{xy}y' - c)^2 \sim \min_{a_{xy}, b_{xy}, c_{xy}} \quad (5.11)$$

Another filter that will be used in the present work is called  $T_2$ , or “Filter of the 2<sup>nd</sup> order”

$$T_2 f(x, y) = a_{xy}x^2 + b_{xy}y^2 + c_{xy}xy + d_{xy}x + e_{xy}y + g_{xy}, \quad (5.12)$$

Where the coefficients  $a_{xy}$ ,  $b_{xy}$ ,  $c_{xy}$ ,  $d_{xy}$ ,  $e_{xy}$ , and  $g_{xy}$  for each surface point  $(x, y)$  are found from the following condition

$$\min_a \int_{Q_{xy}^a} (f(x', y') - a_{xy}x'^2 - b_{xy}y'^2 - c_{xy}x'y' - d_{xy}x' - e_{xy}y' - g_{xy})^2 dx' dy' \sim \min_{a_{xy}, b_{xy}, c_{xy}, d_{xy}, e_{xy}, g_{xy}}, \quad (5.13)$$

In this expression,  $Q_{xy}^\alpha$  is the domain of the morphological filter, which depends upon parameter  $\alpha$  in each point  $(x,y)$  of the domain. Parameter  $\alpha$  stands for the angle of filter rotation in the XY plane. We will say that filter  $T_1$  is a filter of the first order, while  $T_2$  is a filter of the second order.

The results of data processing for rolled and stretched metallic sheet are provided in Figure 5. It can be seen that such processing-dependent features as roll grind imprint and grain roughening are extracted and can be quantified with high accuracy [20].

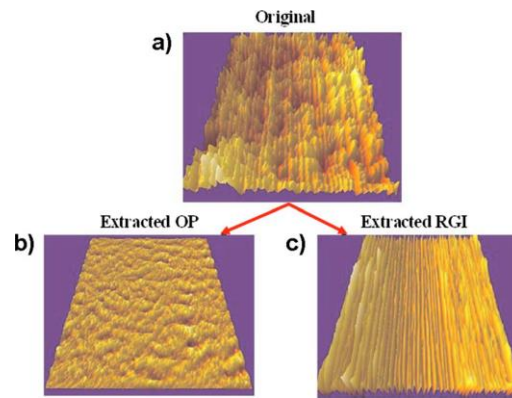


**Figure 72** Three-dimensional (3D) representation of the surface height function  $f(x, y)$  for original rolled and formed aluminum alloy, AA6022. Total surface height function **(a)** and its morphological decomposition into OP (“orange peel”, or grain roughening) **(b)**, and RGI (roll-grin imprint) **(c)** components. The size of the imaged area is  $1.2 \times 1.2 \text{ mm}^2$ , [20]. The original quantitative surface height data for analysis were obtained using confocal microscopy.

Now, that the approach was described and an important example considered in some detail, we are in a position to describe the morphological algorithm for quality assurance of the SiC-braided rodlets made of Zircaloy-4.

## 5.4 Description of the Morphological Algorithm

We used the methods of projectional morphological analysis in order to analyze and extract defects/distortions with respect to the standard, “ideal”, sample, which will be called template. The template is selected from the existing photographs as the area that contains the minimal number of defects.

The data for this morphology study was obtained using conventional digital photography. Each cylindrical sample was rotated  $10^\circ$  and then photographed, for a total of 36 images per sample.

The developed morphological algorithm works as follows. The standard (template) is used to scan the image moving left, right, up, and down. The location of the centers for which the minimal morphological difference is achieved, is stored in the memory. At these points (pixels) the similarity between the template and the studied sample is the highest possible.

The difference between the sample under the template and its projection upon the template is the ultimate result of the algorithm’s work. It can be fine-tuned as a function of the parameter that imposes a certain limit on the absolute value of this difference.

Let us introduce the concept of a local defect, by which we will define those defects of braiding that can be described as the difference between the normalized image under the template (let’s denote this image as ‘ $\varphi$ ’) and its projection upon the template shape, denoted as ‘ $f$ ’.

It is important to note that  $\varphi$  actually represents a vector-function  $\varphi = \varphi(x, y)$ . It can be conveniently defined as the set supporting the template that is run for all points of the sample.



In all further notations we will omit the coordinates (x, y), with the exception of the template, for which the original notation will still be used. Let's also assume the following designations:

- Scalar product of the images -  $(\varphi, f)$ ;
- $L_2$ -norm of a given vector-function:  $\|\varphi\|_{L_2}^2 = (\varphi, \varphi)$ ;
- The average value of the brightness for a given area (limited by the template, at the (x,y) point) -  $M(\varphi) = \sum_{i=1}^N \varphi_i / N$ , where N is the number of points (pixels) in the template;
- An operator which performs normalization of the image:

$$\|\varphi\| = \frac{\varphi - M(\varphi)}{\|\varphi - M(\varphi)\|}; \quad (5.14)$$

- An operator that projects an image upon the template 'f' is denoted as

$$proj(\varphi, f) = norm(\varphi) \cdot (norm(\varphi), norm(f)) \quad (5.15)$$

In this case, the difference of the normalized image under the template and its projection will be presented in the following way (remember about the dependence on the (x, y) coordinates):

$$\begin{aligned} norm(\varphi) - proj(\varphi, f) &= norm(\varphi) - norm(f) * (norm(\varphi), norm(f)) = \\ &= \frac{\varphi - M(\varphi)}{\|\varphi - M(\varphi)\|} - \frac{f - M(f)}{\|f - M(f)\|} \cdot \left( \frac{\varphi - M(\varphi)}{\|\varphi - M(\varphi)\|}, \frac{f - M(f)}{\|f - M(f)\|} \right) \end{aligned} \quad (5.16)$$

As above, all  $\|\cdot\|$  - norms are understood in the sense of  $L_2$  (square-integrable functions).

When the value of the difference  $norm(\varphi) - proj(\varphi, f)$  exceeded a certain threshold value, the corresponding area was declared to contains defect(s), and highlighted in green or in red depending on the defect's severity.

## 5.5 Results and Discussion

Our first challenge was to account for the cylindrical shape of the rodlet that causes its non-uniform illumination and “induced”, non-existent defects (caused by non-uniformities of illumination of the sample in the longitudinal and transverse directions). Additionally, there are illumination artifacts that are associated not with the geometry of the sample, but only with the conditions of illumination. Before morphological techniques could be applied to extract defects on the surface of a rodlet, it was necessary to solve the problem of morphological reduction to uniform illumination. Several simple morphological algorithms allow introducing the required correction, Figure 73.



**Figure 73** The effects of non-uniformity of illumination were removed using a morphological algorithm

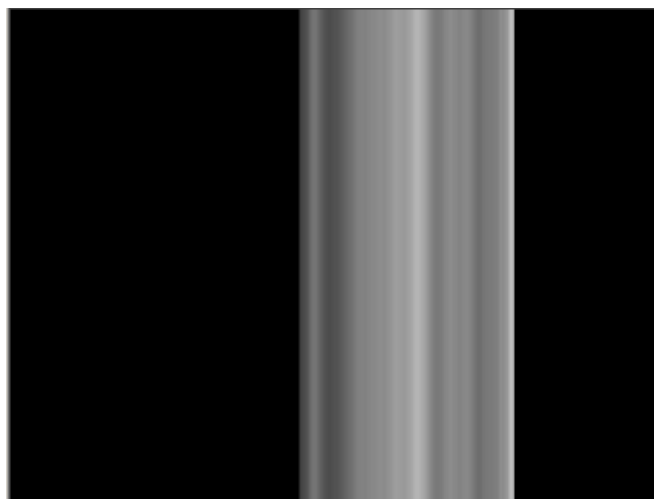


**Figure 74** Equalizing “cylinder of brightness” allowing introducing the non-uniform illumination correction (see Figure 70 above)

The template is used for scanning the sample surface, moving up, down, left, and right. Points are used in order to denote the locations in which the morphological differences are minimal (see graph in Figure 75). This corresponds to the maximal likeness of the template and the scanned surface (under the template) and, correspondingly, to the highest surface quality (i.e., no defects)

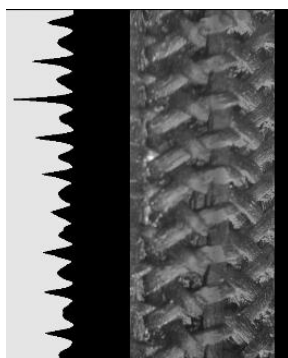


**Figure 75** Minima correspond to the points in which morphological difference between the analyzed sample and the etalon (reference sample) were minimal

However, only those are taken into consideration which corresponds to the periodic structure of the analyzed image. These denoted by small white circles in Figure 75 above. The shifts to the left and to the right with respect to the vertical line drawn across the template center are an indication of the global defects, i.e., shifts of weaving, for the discussed areas. Figure 75 illustrates the local minima for which the maximal similarity of the sample and the template was achieved **locally**. However, only those defects are taken into consideration and counted those correspond to the periodic structure of a given image. The point in the centers of the templates corresponds to these local minima; they are highlighted in green in Figure 76. Finally, Figure 77 illustrates the defects themselves.

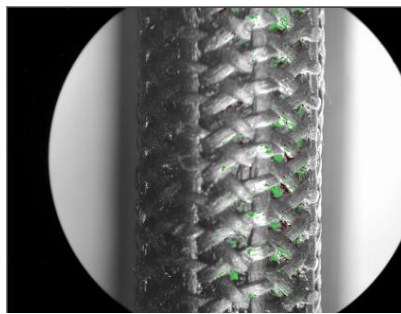


**Figure 76** Major defects are highlighted with green color

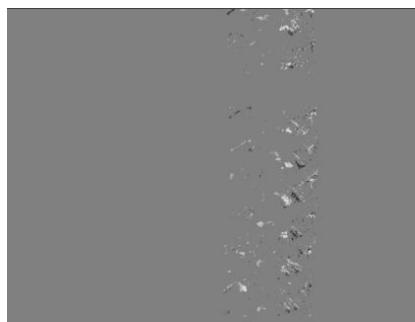


**Figure 77** This Figure corresponds to Figure 73 but illustrates just the defects themselves

The algorithm works in such a way that the locally extracted features (defects) are presented as a function of their magnitude, beginning with the most pronounced defects (with the

highest morphological difference), then those defects are highlighted that are characterized by smaller and smaller values of the morphological difference.

The proposed algorithm was realized on the morphological engine and platform “*MorphoHawk*” (US patent pending) [21]; its general view is presented in Figure 78

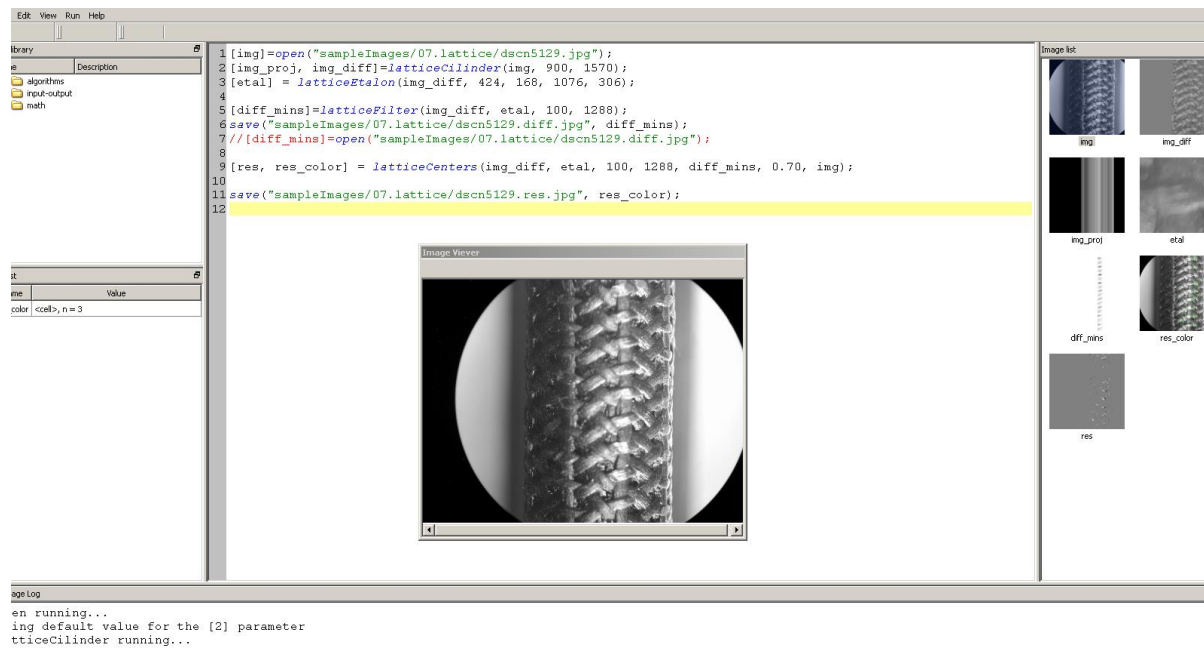


**Figure 75** General view of the *MorphoHawk* platform and of the images generated by the developed MEX modules (the results of morphological processing)

## 5.6 Conclusions to Chapter 5

In conclusion, a new set of morphological algorithms was developed and implemented for quality control and assurance of the zirconium rods braided with SiC fibers. It was demonstrated that the algorithm reliably identifies local areas with imperfections/defects of braiding, thus solving the problem of monitoring of the quality of this protective material. These algorithms now become a part of the morphological platform called MorphoHawk and designed at the Idaho National Laboratory. These algorithms are available for licensing.

## 5.7 Literature to Chapter 5

1. M.V. Glazoff, S.N. Rashkeev, Yu.P. Pyt'ev, J.-W. Yoon, and S. Sheu, Interplay Between Plastic Deformations and Optical Properties of Metal Surfaces: a Multiscale Study, *Applied Physics Letters*, volume 95, issue 8, article 084106 (August 24, 2009)
2. Michael V. Glazoff, Kevin L. Gering, John E. Garnier, and Sergey N. Rashkeev, Methods, Computer-Readable Media for Projectional Morphological Analysis of *N*-Dimensional Signals, US Patent Application Attorney Docket 2939-P11619US(BA-481), June 2013
3. Kevin M. McHugh, John E. Garnier, Sergey N. Rashkeev, Michael V. Glazoff, George W. Griffith, and Shannon Bragg-Sitton, "High Temperature Steam Corrosion of Cladding for Nuclear Applications: Experimental", *Ceramic Engineering and Science Proceedings* (special volume: Ceramic Materials for Energy Applications III), vol.34, issue 9, pp.149-160 (2013)
4. M.V. Glazoff, P. Sabharwall, T.E. Lister, B. Heuser, Beryllium-Doped Zircaloy Rods with YSZ (Yttria-Stabilized Zirconia) Modified Surfaces to Achieve Self-Healing Mode and Protection from High-Temperature Chemical Reactions, INL LDRD Proposal (June 2013).
5. Lance L. Snead, Takashi Nozawa, Yutai Katoh, Thak-Sang Byun, Sosuke Kondo, and David A. Petti, "Handbook of SiC properties for fuel performance modeling," *J. Nucl. Mater.* v.371, p.329-377 (2007).
6. P. T. B. Shaffer, Engineered Materials Handbook, Vol 4, Ceramics and Glasses, ASM International, p. 808 (1991).
7. Advances in Silicon Carbide Processing and Applications, Stephen E. Saddow and Anant Agarwal, Eds., Artech House, Inc., Norwood, p. 8 (2008).
8. John E. Garnier, Kevin McHugh, Idaho National Laboratory, *private communication* (2012)
9. J. K. Beard, The FFT in the 21st Century: Eigen-Space Processing Springer, Berlin, (2003).
10. J. S. Walker, A Primer on Wavelets and Their Scientific Applications,(Studies in Advanced Mathematics), 2<sup>nd</sup> ed., Chapman & Hall/CRC, New York (2008)
11. R. C. Gonzalez, R. E. Woods, and S.L. Eddins, Digital Image Processing using Matlab, 2<sup>nd</sup> ed., Gatesmark (2009)

12. Yu.P. Pyt'ev, "*Methods of Analysis and Interpretation of Experiment*," Moscow State University Publishing Co., Moscow, 1990
13. Yu.P. Pyt'ev, Morphological Analysis of Images, *Reports of the Russian Academy of Sciences*, vol.269, pp.1061-1064 (1983)
14. Yu.P. Pyt'ev, Morphological Notions in Problems of Image Analysis, *Reports of the Russian Academy of Sciences*, vol.224, pp.1283-1286 (1975)
15. J. Serra, *Image Analysis and Mathematical Morphology*" Ac. Press, Volume 1 (1982), Volume 2 (1988)
16. G. Matheron, *Random sets and integral geometry*, John Wiley & Sons, 1975
17. P. Soille, Morphological Image Analysis, Springer, 2<sup>nd</sup> edition, Berlin (2004)
18. F.Y. Shih, Image Processing and Mathematical Morphology, CRC Press, Boca Raton (2009)
19. E.R. Dougherty and R.A. Lotufo, Hands-On Morphological Image Processing, SPIE Press, Washington, DC (2003)

## Appendix A: Thermodynamic Properties of Different Phases in the Zr-H System at Different Temperatures

**Table A1** Gibbs thermodynamic potentials of different phases in the Zr-H system at 300°C

(in J/mole)

X(H)	GMR(GAS)	GMR(IONIC_LIQ)	GMR(BCC_A2)	GMR(C1_FCC)	GMR(HCP_ZR)	GMR(ZRH2_EPS)
0.99975	94.42769	399892.2	11947.52	-28551.1	-11064.1	-30276.6
0.994546	2100.338	397727.4	11947.52	-28551.1	-11064.1	-30276.6
0.969546	11852.58	387562.9	11947.52	-28551.1	-11064.1	-30276.6
0.944545	21663.18	377515.2	11947.52	-28551.1	-11064.1	-30276.6
0.919546	31503.19	367526.2	11947.52	-28551.1	-11064.1	-30276.6
0.894545	41363.64	357578.1	11947.52	-28551.1	-11064.1	-30276.6
0.869546	51240.01	347661.9	11947.52	-28551.1	-11064.1	-30276.6
0.844546	61129.58	337772	11947.52	-28551.1	-11064.1	-30276.6
0.819545	71030.52	327905	11947.52	-28551.1	-11064.1	-30276.6
0.794546	80941.56	318058.1	11947.52	-28551.1	-11064.1	-30276.6
0.769545	90861.74	308229.4	11947.52	-28551.1	-11064.1	-30276.6
0.746623	99964.98	299232.3	9739.014	-28551.1	-11064.1	-30276.6
0.744546	100790.3	298417.6	8485.626	-28551.1	-11064.1	-30276.6
0.721623	109900.8	289434.9	-2427.43	-28551.1	-11064.1	-30276.6
0.719546	110726.8	288621.5	-3208.64	-28551.1	-11064.1	-30276.6
0.696623	119844	279652.4	-10156.3	-28551.1	-11064.1	-30276.6
0.694545	120670.6	278840.1	-10656.6	-28551.1	-11064.1	-30276.6
0.671623	129794.2	269883.9	-15084.1	-28551.1	-11064.1	-30276.6
0.669546	130621.4	269072.8	-15399.6	-28551.1	-11064.1	-30276.6
0.664347	132691.4	267043.5	-16136.1	-28764.1	-11064.1	-30262.2
0.66431	132706.1	267029.1	-16141.1	-28766.9	-11064.1	-30261.5
0.646623	139751.3	260129	-18143.8	-29446.4	-11064.1	-29582.8
0.644545	140579	259319	-18334.2	-29470.5	-11064.1	-29485.6
0.639347	142650.4	257292.4	-18774.2	-29493.4	-11064.1	-29235.3
0.63931	142665	257278	-18777.2	-29493.4	-11064.1	-29233.5
0.621623	149714.8	250387.1	-19927.1	-29240.6	-11064.1	-28332.8
0.619546	150543	249578.1	-20031.1	-29183.2	-11064.1	-28223.8
0.614347	152615.8	247554.2	-20265.9	-29018.1	-11064.1	-27949.3
0.61431	152630.5	247539.9	-20267.4	-29016.8	-11064.1	-27947.3
0.596623	159684.7	240657.8	-20823.6	-28261.1	-11064.1	-26999
0.596623	159684.7	240657.8	-20823.6	-28261.1	-11064.1	-26999
0.594546	160513.4	239849.9	-20867.1	-28155.8	-11064.1	-26886.6
0.589347	162587.5	237828.6	-20958	-27879.4	-11064.1	-26604.9
0.58931	162602.2	237814.3	-20958.6	-27877.4	-11064.1	-26602.9
0.571623	169660.7	230941	-21096.7	-26820.7	-11064.1	-25639.7
0.569545	170490	230134.1	-21097.5	-26686.7	-11064.1	-25526.3
0.564347	172565.3	228115.3	-21086.7	-26343.9	-11064.1	-25242.4
0.56431	172580	228101	-21086.6	-26341.4	-11064.1	-25240.4
0.546623	179642.9	221236.3	-20928.3	-25108.1	-11064.1	-24273.4
0.544546	180472.7	220430.4	-20898.7	-24957.7	-11064.1	-24159.8
0.539347	182549.2	218414.1	-20815.6	-24577.3	-11064.1	-23875.6
0.53931	182563.9	218399.8	-20815	-24574.5	-11064.1	-23873.6
0.521623	189631	211543.6	-20445.7	-23245.4	-11064.1	-22906.8
0.519545	190461.3	210738.7	-20394.5	-23086.6	-11064.1	-22793.3
0.514347	192539.1	208724.9	-20259.9	-22687.5	-11064.1	-22509.4
0.51431	192553.8	208710.7	-20258.9	-22684.6	-11064.1	-22507.3
0.496623	199625.2	201862.9	-19739.5	-21313.3	-11160.1	-21542
0.494546	200455.9	201059	-19673	-21151.4	-11194.2	-21428.6
0.494546	200455.9	201059	-19673	-21151.4	-11194.2	-21428.6
0.489347	202534.9	199047.7	-19501.8	-20746.1	-11250.2	-21145.1
0.48931	202549.7	199033.4	-19500.6	-20743.3	-11250.5	-21143.1
0.478571	206845.2	194880.2	-19128.1	-19906	-11295.7	-20557.7
0.471623	209625.2	192194	-18874.8	-19365.4	-11294.7	-20179.1
0.469546	210456.5	191391.1	-18797.4	-19204	-11291.1	-20066
0.464347	212536.8	189382.3	-18600.5	-18800.9	-11276.2	-19782.8
0.46431	212551.5	189368.1	-18599.1	-18798.1	-11276.1	-19780.8
0.453571	216849.6	185220	-18179	-17969.7	-11223.3	-19195.9
0.446623	219631.3	182537.2	-17898.7	-17437.3	-11175.9	-18817.6
0.444545	220463	181735.3	-17813.8	-17278.8	-11160	-18704.5
0.439347	222544.6	179728.9	-17598.9	-16883.5	-11117	-18421.4
0.43931	222559.3	179714.7	-17597.4	-16880.7	-11116.7	-18419.4
0.428571	226860	175571.8	-17144.4	-16071	-11014.4	-17834.6
0.421623	229643.4	172892.4	-16845.5	-15552.5	-10939.7	-17456.2
0.419545	230475.6	172091.5	-16755.4	-15398.3	-10916.2	-17343.1
0.414347	232558.4	170087.7	-16528.3	-15014.3	-10855.1	-17059.9
0.41431	232573.2	170073.5	-16526.7	-15011.6	-10854.6	-17057.9
0.403571	236876.5	165935.8	-16051.5	-14227	-10718.7	-16472.6
0.396623	239661.6	163259.8	-15740.2	-13725.7	-10624.3	-16093.8
0.394546	240494.3	162459.9	-15646.7	-13576.8	-10595.2	-15980.5



X(H)	GMR(GAS)	GMR(IONIC_LIQ)	GMR(BCC_A2)	GMR(C1_FCC)	GMR(HCP_ZR)	GMR(ZRH2_EPS)
0.389347	242578.4	160458.7	-15411.6	-13206.3	-10520.5	-15696.8
0.38931	242593.2	160444.5	-15409.9	-13203.7	-10520	-15694.8
0.378571	246899.2	156312.2	-14920.4	-12448	-10358.1	-15108.6
0.371623	249686	153639.6	-14601.3	-11965.9	-10248.1	-14728.9
0.369546	250519.3	152840.8	-14505.5	-11822.9	-10214.5	-14615.3
0.364347	252604.7	150842.2	-14265.5	-11467.1	-10128.9	-14331
0.36431	252619.5	150828	-14263.8	-11464.6	-10128.3	-14329
0.353571	256928.2	146701.2	-13765.6	-10739.8	-9945	-13741.1
0.346623	259716.8	144032.2	-13441.9	-10278	-9821.99	-13360.3
0.344546	260550.6	143234.5	-13345	-10141.1	-9784.57	-13246.4
0.339347	262637.3	141238.6	-13102.1	-9800.61	-9689.64	-12961.1
0.33931	262652.2	141224.4	-13100.4	-9798.21	-9688.96	-12959.1
0.328571	266963.7	137103.3	-12597.7	-9105.08	-9487.23	-12369
0.328571	266963.7	137103.3	-12597.7	-9105.08	-9487.23	-12369
0.321623	269754.2	134438	-12271.8	-8663.86	-9352.81	-11986.6
0.319545	270588.6	133641.3	-12174.3	-8533.06	-9312.04	-11872.2
0.314347	272676.7	131648.2	-11930.3	-8207.95	-9208.88	-11585.7
0.31431	272691.5	131634.1	-11928.5	-8205.66	-9208.14	-11583.6
0.303571	277006	127518.9	-11424.1	-7544.16	-8989.96	-10990.8
0.296623	279798.4	124857.4	-11097.7	-7123.28	-8845.25	-10606.5
0.294545	280633.3	124061.9	-11000.2	-6998.53	-8801.45	-10491.4
0.289347	282722.9	122071.8	-10756	-6688.53	-8690.81	-10203.4
0.28931	282737.8	122057.7	-10754.3	-6686.34	-8690.02	-10201.3
0.278571	287055.3	117948.5	-10250.3	-6055.74	-8456.75	-9605.1
0.271623	289849.7	115291.1	-9924.42	-5654.62	-8302.52	-9218.45
0.269546	290685.3	114496.9	-9827.05	-5535.74	-8255.91	-9102.71
0.264347	292776.4	112509.8	-9583.54	-5240.34	-8138.29	-8812.81
0.26431	292791.2	112495.7	-9581.81	-5238.25	-8137.45	-8810.75
0.253571	297112	108393	-9079.4	-4637.4	-7890.02	-8210.53
0.246623	299908.6	105739.9	-8754.81	-4255.2	-7726.77	-7821.13
0.244546	300744.8	104946.9	-8657.84	-4141.92	-7677.49	-7704.55
0.239347	302837.6	102963.1	-8415.37	-3860.43	-7553.21	-7412.49
0.23931	302852.4	102949	-8413.65	-3858.45	-7552.33	-7410.42
0.228571	307176.7	98853.27	-7913.56	-3285.82	-7291.3	-6805.51
0.221623	309975.5	96204.72	-7590.54	-2921.49	-7119.34	-6412.91
0.219546	310812.4	95413.13	-7494.06	-2813.5	-7067.46	-6295.35
0.214347	312906.9	93432.81	-7252.8	-2545.1	-6936.71	-6000.77
0.21431	312921.8	93418.77	-7251.09	-2543.21	-6935.78	-5998.68
0.203571	317249.7	89330.43	-6753.52	-1997.02	-6661.42	-5388.31
0.196623	320051.1	86686.83	-6432.12	-1649.36	-6480.85	-4992
0.194545	320888.7	85896.74	-6336.11	-1546.28	-6426.4	-4873.29
0.189347	322985.1	83920.24	-6096.03	-1290.03	-6289.2	-4575.78
0.18931	323000	83906.23	-6094.33	-1288.23	-6288.22	-4573.67
0.178571	327332	79825.99	-5599.06	-766.459	-6000.5	-3956.96
0.171623	330136	77187.84	-5279.03	-434.096	-5811.23	-3556.3
0.169546	330974.5	76399.41	-5183.41	-335.507	-5754.16	-3436.26
0.164347	333073.1	74427.11	-4944.25	-90.3424	-5610.4	-3135.33
0.16431	333087.9	74413.13	-4942.55	-88.6121	-5609.37	-3133.2
0.153571	337424.4	70341.91	-4448.93	411.0298	-5307.93	-2509.05
0.146623	340231.5	67709.84	-4129.74	729.6481	-5109.64	-2103.28
0.144546	341071	66923.28	-4034.33	824.2181	-5049.85	-1981.66
0.139347	343171.9	64955.73	-3795.62	1059.515	-4899.21	-1676.7
0.13931	343186.8	64941.79	-3793.93	1061.177	-4898.14	-1674.53
0.128571	347528.4	60880.83	-3300.79	1541.325	-4582.2	-1041.54
0.121623	350339	58255.75	-2981.57	1848.002	-4374.26	-629.664
0.119546	351179.5	57471.34	-2886.1	1939.11	-4311.55	-506.156
0.114347	353283.2	55509.3	-2647.07	2165.97	-4153.48	-196.317
0.11431	353298.1	55495.4	-2645.38	2167.573	-4152.35	-194.117
0.103571	357645.7	51446.47	-2150.93	2631.381	-3820.53	449.6403
0.096623	360460.5	48829.71	-1830.31	2928.326	-3601.87	869.0405
0.094545	361302.2	48047.87	-1734.32	3016.662	-3535.87	994.8947
0.089347	363409.2	46092.49	-1493.8	3236.882	-3369.4	1310.811
0.08931	363424.2	46078.63	-1492.09	3238.439	-3368.21	1313.056
0.078571	367779.2	42044.47	-993.481	3689.99	-3018.11	1970.441
0.071623	370599.2	39438.14	-669.257	3980.176	-2786.83	2399.557
0.069545	371442.6	38659.57	-572.028	4066.691	-2716.91	2528.474
0.064347	373553.8	36712.71	-328.046	4282.795	-2540.31	2852.412
0.06431	373568.8	36698.92	-326.313	4284.326	-2539.05	2854.716
0.053571	377933.6	32684.27	181.3886	4729.66	-2166.23	3530.581
0.046623	380760.7	30092.23	513.2232	5017.794	-1918.63	3973.358
0.044545	381606.4	29318.25	613.0512	5104.056	-1843.52	4106.68
0.039347	383723.8	27383.64	864.3096	5320.369	-1653.21	4442.401
0.03931	383738.8	27369.94	866.0989	5321.905	-1651.84	4444.792
0.028571	388118.5	23385.01	1393.343	5772.498	-1246.34	5149.461
0.021623	390957.5	20816.79	1742.471	6068.904	-973.057	5615.488
0.019545	391807.2	20050.94	1848.484	6158.687	-889.275	5756.769
0.014347	393936.2	18139.5	2118.068	6386.722	-674.438	6115.244
0.01431	393951.3	18125.98	2120.005	6388.36	-672.884	6117.814
0.003571	398367.4	14213.87	2710.157	6888.513	-191.829	6894.479
2.50E-04	399746.4	13030.08	2918.055	7067.46	-16.6013	7160.844

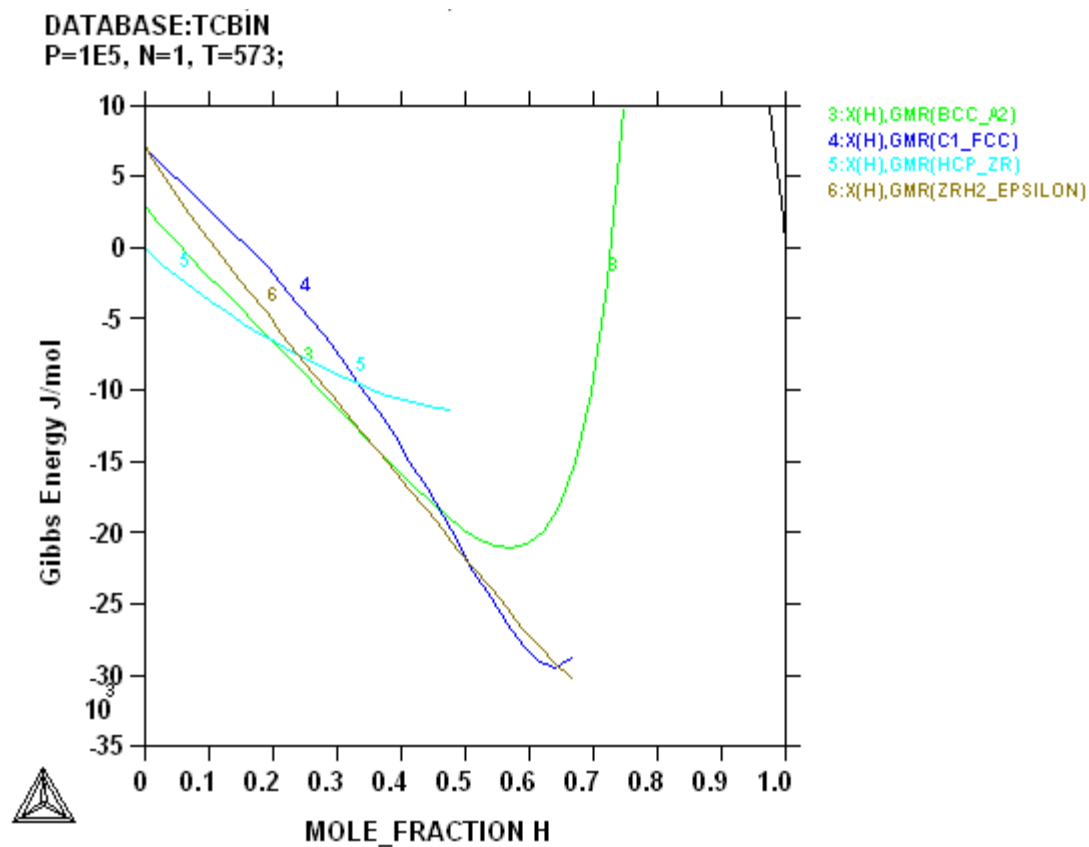


**Figure A-1** Thermodynamic properties of different phases at T=300°C

**Table A2** Gibbs thermodynamic potentials of different phases in the Zr-H system at 350°C  
(in J/mole)

X(H)	GMR(GAS)	GMR(IONIC_LIQ)	GMR(BCC_A2)	GMR(C1_FCC)	GMR(HCP_ZR)	GMR(ZRH2_EPS)
0.99975	92.86265	399891.1	11864.89	-26248	-10024.1	-27958.6
0.994546	2069.708	397710.9	11864.89	-26248	-10024.1	-27958.6
0.969546	11692.54	387492.4	11864.89	-26248	-10024.1	-27958.6
0.944545	21378.83	377400.9	11864.89	-26248	-10024.1	-27958.6
0.919546	31097.11	367373.3	11864.89	-26248	-10024.1	-27958.6
0.894545	40837.6	357390.2	11864.89	-26248	-10024.1	-27958.6
0.869546	50595.4	347441.7	11864.89	-26248	-10024.1	-27958.6
0.844546	60367.55	337521.8	11864.89	-26248	-10024.1	-27958.6
0.819545	70152.08	327626.8	11864.89	-26248	-10024.1	-27958.6
0.794546	79947.58	317753.6	11864.89	-26248	-10024.1	-27958.6
0.769545	89753.02	307900.4	11864.89	-26248	-10024.1	-27958.6
0.746623	98751.7	298882	9749.115	-26248	-10024.1	-27958.6
0.744546	99567.59	298065.4	8553.437	-26248	-10024.1	-27958.6
0.721623	108574.1	289062.7	-1832.52	-26248	-10024.1	-27958.6
0.719546	109390.7	288247.5	-2575.93	-26248	-10024.1	-27958.6
0.696623	118404.6	279259.5	-9195.7	-26248	-10024.1	-27958.6
0.694545	119221.8	278445.6	-9673.32	-26248	-10024.1	-27958.6
0.671623	128242.7	269471.7	-13910.9	-26248	-10024.1	-27958.6
0.669546	129060.6	268659	-14214	-26248	-10024.1	-27958.6
0.664347	131107.4	266625.8	-14922.3	-26471.6	-10024.1	-27968.5
0.66431	131121.9	266611.4	-14927.1	-26474.5	-10024.1	-27968.1
0.646623	138088.2	259698.5	-16861.4	-27208	-10024.1	-27421.3
0.644545	138906.7	258887	-17046.2	-27239.3	-10024.1	-27337.7
0.639347	140955	256856.9	-17474.3	-27281.1	-10024.1	-27120.2
0.63931	140969.5	256842.5	-17477.1	-27281.2	-10024.1	-27118.7
0.621623	147940.8	249939.5	-18605.3	-27104.7	-10024.1	-26322
0.619546	148759.8	249129.2	-18708.4	-27057.3	-10024.1	-26224.7
0.614347	150809.6	247101.9	-18942.3	-26918.2	-10024.1	-25978.7
0.61431	150824.1	247087.6	-18943.8	-26917.2	-10024.1	-25976.9
0.596623	157800.3	240194.3	-19509.8	-26257.9	-10024.1	-25121.6
0.596623	157800.3	240194.3	-19509.8	-26257.9	-10024.1	-25121.6
0.594546	158619.9	239385.2	-19555.6	-26164.6	-10024.1	-25019.8
0.589347	160671	237360.7	-19653.2	-25918.8	-10024.1	-24764.1
0.58931	160685.5	237346.3	-19653.9	-25917	-10024.1	-24762.3
0.571623	167666.5	230462.6	-19823.2	-24968.6	-10024.1	-23885.1
0.569545	168486.6	229654.5	-19828.5	-24847.7	-10024.1	-23781.6
0.564347	170539.1	227632.8	-19829.4	-24537.9	-10024.1	-23522
0.56431	170553.7	227618.5	-19829.4	-24535.6	-10024.1	-23520.2
0.546623	177539.3	220744.1	-19716.7	-23416.2	-10024.1	-22634.1
0.544546	178360	219937.1	-19693	-23279.3	-10024.1	-22529.8
0.539347	180413.8	217918.1	-19625.1	-22932.6	-10024.1	-22268.7
0.53931	180428.4	217903.8	-19624.5	-22930.2	-10024.1	-22266.8
0.521623	187418.6	211038.6	-19310.4	-21716	-10024.1	-21376.9
0.519545	188239.8	210232.7	-19266	-21570.7	-10024.1	-21272.3
0.514347	190295.1	208216.4	-19148.7	-21205.1	-10024.1	-21010.4
0.51431	190309.7	208202.1	-19147.8	-21202.5	-10024.1	-21008.5
0.496623	197304.4	201346.2	-18689.5	-19944.3	-10142	-20116.7
0.494546	198126.2	200541.3	-18630.3	-19795.6	-10187.4	-20011.9
0.494546	198126.2	200541.3	-18630.3	-19795.6	-10187.4	-20011.9
0.489347	200182.8	198527.7	-18477.8	-19423	-10269.2	-19749.6
0.48931	200197.4	198513.5	-18476.7	-19420.3	-10269.6	-19747.7
0.478571	204446.6	194355.7	-18143.2	-18649.8	-10361.8	-19205.5
0.471623	207196.7	191666.7	-17915.5	-18151.6	-10388.7	-18854.4
0.469546	208019.1	190862.9	-17845.8	-18002.8	-10393.1	-18749.4
0.464347	210077	188852	-17668.2	-17631.1	-10397.8	-18486.6
0.46431	210091.6	188837.7	-17667	-17628.5	-10397.8	-18484.8
0.453571	214343.6	184685.6	-17287	-16863.7	-10383.4	-17941.6
0.446623	217095.5	182000.1	-17032.8	-16371.7	-10359.8	-17589.8
0.444545	217918.4	181197.5	-16955.7	-16225.1	-10350.8	-17484.6
0.439347	219977.7	179189.3	-16760.4	-15859.4	-10324.9	-17221.2
0.43931	219992.3	179175	-16759	-15856.8	-10324.7	-17219.4
0.428571	224247.1	175028.5	-16346.5	-15107.2	-10256.6	-16674.9
0.421623	227000.9	172346.7	-16073.8	-14626.6	-10203.2	-16322.2
0.419545	227824.3	171545.2	-15991.5	-14483.6	-10186	-16216.7
0.414347	229885	169539.7	-15783.9	-14127.4	-10140.4	-15952.6
0.41431	229899.6	169525.5	-15782.5	-14124.9	-10140.1	-15950.7
0.403571	234157.3	165384.7	-15347.5	-13396.4	-10035.3	-15404.5
0.396623	236912.9	162706.6	-15062.2	-12930.5	-9960.57	-15050.6
0.394546	237736.9	161906.1	-14976.3	-12792	-9937.23	-14944.7
0.389347	239798.9	159903.5	-14760.5	-12447.4	-9876.91	-14679.6
0.38931	239813.6	159889.3	-14758.9	-12444.9	-9876.47	-14677.7
0.378571	244074.2	155754.3	-14308.9	-11741.2	-9743.51	-14129.3
0.371623	246831.7	153080	-14015.2	-11291.9	-9651.84	-13773.9
0.369546	247656.2	152280.7	-13927	-11158.5	-9623.62	-13667.5
0.364347	249719.7	150280.9	-13705.8	-10826.6	-9551.39	-13401.2
0.36431	249734.3	150266.7	-13704.2	-10824.3	-9550.87	-13399.3

X(H)	GMR(GAS)	GMR(IONIC_LIQ)	GMR(BCC_A2)	GMR(C1_FCC)	GMR(HCP_ZR)	GMR(ZRH2_EPS)
0.353571	253997.9	146137.7	-13244.5	-10147.3	-9394.66	-12848.2
0.346623	256757.4	143467.3	-12945.5	-9715.59	-9288.79	-12490.9
0.344546	257582.5	142669.1	-12855.9	-9587.48	-9256.43	-12384
0.339347	259647.5	140672.3	-12631.4	-9268.85	-9174.07	-12116.2
0.33931	259662.1	140658.1	-12629.8	-9266.6	-9173.48	-12114.3
0.328571	263928.8	136535.2	-12164.3	-8617.25	-8997.22	-11560
0.328571	263928.8	136535.2	-12164.3	-8617.25	-8997.22	-11560
0.321623	266690.2	133868.9	-11862.3	-8203.41	-8878.93	-11200.5
0.319545	267516	133071.9	-11771.9	-8080.65	-8842.94	-11092.9
0.314347	269582.5	131078.1	-11545.5	-7775.39	-8751.63	-10823.3
0.31431	269597.1	131064	-11543.9	-7773.24	-8750.98	-10821.4
0.303571	273866.9	126947.5	-11075.4	-7151.43	-8556.83	-10263.3
0.296623	276630.5	124285.3	-10771.9	-6755.31	-8427.36	-9901.28
0.294545	277456.9	123489.6	-10681.1	-6637.82	-8388.07	-9792.89
0.289347	279525	121499	-10453.9	-6345.72	-8288.63	-9521.33
0.28931	279539.6	121484.9	-10452.3	-6343.66	-8287.92	-9519.41
0.278571	283812.8	117375	-9982.68	-5748.76	-8077.37	-8956.99
0.271623	286578.6	114717.3	-9678.75	-5369.83	-7937.54	-8591.99
0.269546	287405.6	113922.9	-9587.88	-5257.45	-7895.2	-8482.69
0.264347	289475.3	111935.6	-9360.51	-4978.04	-7788.16	-8208.84
0.26431	289490	111921.6	-9358.9	-4976.07	-7787.4	-8206.89
0.253571	293766.7	107818.7	-8889.32	-4407	-7561.45	-7639.52
0.246623	296534.8	105165.6	-8585.59	-4044.49	-7411.83	-7271.16
0.244546	297362.6	104372.7	-8494.81	-3936.96	-7366.58	-7160.84
0.239347	299434.1	102389	-8267.68	-3669.6	-7252.31	-6884.36
0.23931	299448.8	102374.9	-8266.07	-3667.72	-7251.49	-6882.4
0.228571	303729.2	98279.54	-7797.15	-3123.06	-7010.76	-6309.38
0.221623	306499.8	95631.41	-7493.91	-2775.98	-6851.66	-5937.2
0.219546	307328.2	94839.96	-7403.28	-2673.01	-6803.59	-5825.71
0.214347	309401.7	92860.06	-7176.54	-2416.93	-6682.28	-5546.25
0.21431	309416.4	92846.03	-7174.94	-2415.12	-6681.42	-5544.27
0.203571	313700.9	88758.75	-6706.81	-1893.19	-6426.19	-4964.82
0.196623	316474.2	86116	-6404.06	-1560.39	-6257.73	-4588.29
0.194545	317303.4	85326.19	-6313.57	-1461.62	-6206.86	-4475.46
0.189347	319378.9	83350.43	-6087.15	-1215.92	-6078.54	-4192.6
0.18931	319393.7	83336.43	-6085.55	-1214.18	-6077.63	-4190.59
0.178571	323682.6	79257.97	-5617.94	-713.029	-5807.87	-3603.79
0.171623	326458.8	76621.13	-5315.4	-393.182	-5629.95	-3222.26
0.169546	327289	75833.12	-5224.94	-298.21	-5576.24	-3107.9
0.164347	329366.8	73861.95	-4998.56	-61.8437	-5440.78	-2821.11
0.16431	329381.5	73847.97	-4996.96	-60.1744	-5439.81	-2819.07
0.153571	333675.3	69779.32	-4529.14	422.4332	-5155.14	-2223.78
0.146623	336454.8	67149.1	-4226.22	730.8433	-4967.41	-1836.44
0.144546	337286.1	66363.12	-4135.61	822.4854	-4910.74	-1720.29
0.139347	339366.4	64397.11	-3908.76	1050.706	-4767.81	-1428.92
0.13931	339381.2	64383.17	-3907.15	1052.318	-4766.79	-1426.85
0.128571	343680.5	60325.67	-3437.9	1518.985	-4466.35	-821.573
0.121623	346463.9	57703.06	-3133.66	1817.754	-4268.14	-427.349
0.119546	347296.2	56919.41	-3042.6	1906.622	-4208.29	-309.073
0.114347	349379.6	54959.39	-2814.46	2128.129	-4057.28	-12.2381
0.11431	349394.4	54945.5	-2812.84	2129.695	-4056.2	-10.1292
0.103571	353700.3	50901.08	-2340.2	2583.598	-3738.49	607.1974
0.096623	356488.2	48287.51	-2033.19	2874.966	-3528.62	1009.819
0.094545	357322	47506.67	-1941.19	2961.763	-3465.19	1130.708
0.089347	359408.9	45553.87	-1710.49	3178.392	-3305.05	1434.309
0.08931	359423.8	45540.04	-1708.85	3179.925	-3303.91	1436.467
0.078571	363737.7	41511.68	-1229.76	3625.259	-2966.33	2068.927
0.071623	366531.2	38909.43	-917.604	3912.302	-2742.74	2482.311
0.069545	367366.8	38132.15	-823.891	3998.015	-2675.05	2606.589
0.064347	369458.4	36188.63	-588.516	4212.394	-2503.89	2919.056
0.06431	369473.2	36174.86	-586.843	4213.914	-2502.66	2921.279
0.053571	373797.8	32167.71	-96.0059	4657.013	-2140.38	3574.123
0.046623	376599.1	29581.02	225.6262	4944.7	-1899.04	4002.544
0.044545	377437.1	28808.72	322.5214	5030.988	-1825.72	4131.664
0.039347	379535.4	26878.52	566.6954	5247.709	-1639.65	4457.076
0.03931	379550.3	26864.85	568.4358	5249.25	-1638.31	4459.396
0.028571	383891	22890.01	1082.337	5702.366	-1240.5	5143.825
0.021623	386705.2	20329.21	1423.934	6001.778	-971.238	5597.693
0.019545	387547.7	19565.76	1527.901	6092.704	-888.479	5735.518
0.014347	389658.6	17660.74	1792.86	6324.181	-675.745	6085.792
0.01431	389673.6	17647.27	1794.767	6325.846	-674.204	6088.308
0.003571	394053.9	13751.6	2378.827	6836.931	-194.244	6851.265
2.50E-04	395422.9	12575.19	2587.204	7021.72	-17.0472	7115.692

THERMO-CALC (2013.02.07:14.10) :H ZR  
 DATABASE:TCBIN  
 P=1E5, N=1, T=673;

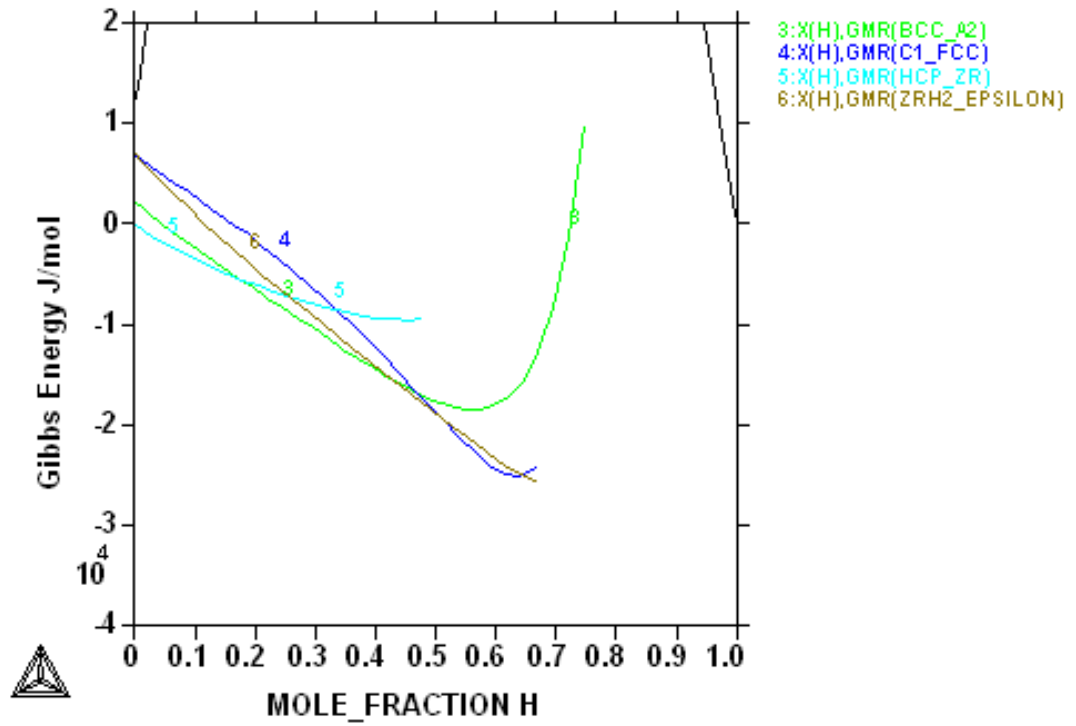


**Figure A2.** Thermodynamic properties of different phases at T=350°C.

**Table A3** Gibbs thermodynamic potentials of different phases in the Zr-H system at 400°C  
(in J/mole)

X(H)	GMR(GAS)	GMR(IONIC_LIQ)	GMR(BCC_A2)	GMR(C1_FCC)	GMR(HCP_ZR)	GMR(ZRH2_EPS)
0.99975	91.30695	399890	11785.57	-23957.6	-8984.1	-25635.4
0.99975	91.30695	399890	11785.57	-23957.6	-8984.1	-25635.4
0.994546	2039.309	397694.3	11785.57	-23957.6	-8984.1	-25635.4
0.979762	7641.181	391594.6	11785.57	-23957.6	-8984.1	-25635.4
0.969546	11533.82	387421.9	11785.57	-23957.6	-8984.1	-25635.4
0.954762	17183.74	381418.3	11785.57	-23957.6	-8984.1	-25635.4
0.944545	21096.89	377286.7	11785.57	-23957.6	-8984.1	-25635.4
0.929762	26769.05	371327.4	11785.57	-23957.6	-8984.1	-25635.4
0.919546	30694.51	367220.4	11785.57	-23957.6	-8984.1	-25635.4
0.904762	36381.69	361291.3	11785.57	-23957.6	-8984.1	-25635.4
0.894545	40316.14	357202.2	11785.57	-23957.6	-8984.1	-25635.4
0.879762	46014.84	351296.1	11785.57	-23957.6	-8984.1	-25635.4
0.869546	49956.46	347221.4	11785.57	-23957.6	-8984.1	-25635.4
0.854762	55664.64	341334.3	11785.57	-23957.6	-8984.1	-25635.4
0.844546	59612.29	337271.7	11785.57	-23957.6	-8984.1	-25635.4
0.829762	65328.58	331400.7	11785.57	-23957.6	-8984.1	-25635.4
0.819545	69281.48	327348.6	11785.57	-23957.6	-8984.1	-25635.4
0.804762	75004.94	321492	11785.57	-23957.6	-8984.1	-25635.4
0.794546	78962.52	317449.2	11785.57	-23957.6	-8984.1	-25635.4
0.779762	84692.45	311605.5	11785.57	-23957.6	-8984.1	-25635.4
0.769545	88654.31	307571.3	11785.57	-23957.6	-8984.1	-25635.4
0.754762	94390.16	301739.5	11785.57	-23957.6	-8984.1	-25635.4
0.746623	97549.43	298531.7	9762.562	-23957.6	-8984.1	-25635.4
0.744546	98355.97	297713.2	8624.618	-23957.6	-8984.1	-25635.4
0.729762	104097.3	291892.4	1796.645	-23957.6	-8984.1	-25635.4
0.721623	107259.5	288690.4	-1233.94	-23957.6	-8984.1	-25635.4
0.719546	108066.8	287873.4	-1939.52	-23957.6	-8984.1	-25635.4
0.704762	113813.4	282063	-6280.14	-23957.6	-8984.1	-25635.4
0.696623	116978.4	278866.7	-8231.13	-23957.6	-8984.1	-25635.4
0.694545	117786.4	278051.1	-8686.04	-23957.6	-8984.1	-25635.4
0.679762	123537.9	272250.5	-11482.5	-23957.6	-8984.1	-25635.4
0.671623	126705.5	269059.4	-12733.5	-23957.6	-8984.1	-25635.4
0.669546	127514.2	268245.2	-13024.1	-23957.6	-8984.1	-25635.4
0.664347	129538	266208.2	-13704	-24191.8	-8984.1	-25669.6
0.66431	129552.3	266193.7	-13708.6	-24194.8	-8984.1	-25669.6
0.654762	133270.3	262454	-14795.2	-24740.2	-8984.1	-25500.4
0.646623	136440.5	259268.1	-15574.3	-24981.9	-8984.1	-25254.8
0.644545	137249.9	258455.1	-15753.5	-25020.2	-8984.1	-25184.7
0.639347	139275.3	256421.3	-16169.6	-25081	-8984.1	-25000.2
0.63931	139289.6	256406.9	-16172.4	-25081.2	-8984.1	-24998.9
0.629762	143010.6	252673.1	-16824.6	-25079	-8984.1	-24634.7
0.621623	146183.3	249492	-17278.5	-24980.6	-8984.1	-24306.4
0.619546	146993.2	248680.3	-17380.6	-24943.2	-8984.1	-24220.7
0.614347	149020.2	246649.6	-17613.6	-24830.1	-8984.1	-24003.3
0.61431	149034.5	246635.2	-17615.2	-24829.2	-8984.1	-24001.8
0.604762	152758.3	242907.1	-17964.7	-24556	-8984.1	-23593.9
0.596623	155933.4	239730.8	-18190.8	-24266.1	-8984.1	-23239.5
0.596623	155933.4	239730.8	-18190.8	-24266.1	-8984.1	-23239.5
0.594546	156744	238920.4	-18238.8	-24184.7	-8984.1	-23148.3
0.589347	158772.4	236892.7	-18343	-23969.4	-8984.1	-22918.8
0.58931	158786.8	236878.4	-18343.7	-23967.8	-8984.1	-22917.2
0.579762	162513.4	233155.8	-18479.4	-23532.7	-8984.1	-22491.8
0.571623	165690.8	229984.2	-18544.1	-23127.4	-8984.1	-22126.1
0.569545	166502	229175	-18553.7	-23019.6	-8984.1	-22032.4
0.564347	168532	227150.3	-18566.4	-22742.6	-8984.1	-21797.3
0.56431	168546.3	227135.9	-18566.4	-22740.6	-8984.1	-21795.7
0.554762	172275.7	223418.8	-18549.9	-22208.4	-8984.1	-21361.9
0.546623	175455.4	220251.9	-18499.2	-21734.7	-8984.1	-20990.6
0.544546	176267.1	219443.8	-18481.3	-21611.2	-8984.1	-20895.6
0.539347	178298.6	217422.1	-18428.4	-21298.3	-8984.1	-20657.6
0.53931	178313	217407.7	-18428	-21296	-8984.1	-20655.9
0.529762	182045	213696	-18302.2	-20708.3	-8984.1	-20217.6
0.521623	185227	210533.7	-18168.8	-20196.6	-8984.1	-19843
0.519545	186039.3	209726.7	-18131.1	-20064.7	-8984.1	-19747.3
0.514347	188072.2	207707.9	-18031.1	-19732.6	-8984.1	-19507.5
0.51431	188086.7	207693.6	-18030.3	-19730.2	-8984.1	-19505.8
0.504762	191821.3	203987.2	-17826	-19114.3	-8984.1	-19064.5
0.504762	191821.3	203987.2	-17826	-19114.3	-8984.1	-19064.5
0.496623	195005.7	200829.5	-17632.9	-18584.7	-9123.9	-18687.6
0.494546	195818.5	200023.7	-17581.1	-18449.1	-9180.63	-18591.3
0.494546	195818.5	200023.7	-17581.1	-18449.1	-9180.63	-18591.3
0.489347	197852.9	198007.8	-17447.1	-18109.1	-9288.11	-18350.2
0.48931	197867.3	197993.5	-17446.1	-18106.7	-9288.75	-18348.5
0.479762	201604.7	194292.5	-17185.2	-17480.7	-9416.26	-17904.8
0.478571	202070.8	193831.2	-17151.5	-17402.6	-9427.97	-17849.5

X(H)	GMR(GAS)	GMR(IONIC_LIQ)	GMR(BCC_A2)	GMR(C1_FCC)	GMR(HCP_ZR)	GMR(ZRH2_EPS)
0.471623	204791.3	191139.3	-16949.3	-16946.8	-9482.63	-17526
0.469546	205604.8	190334.7	-16887.2	-16810.6	-9495.02	-17429.2
0.464347	207640.6	188321.7	-16728.9	-16470.1	-9519.26	-17186.9
0.46431	207655	188307.4	-16727.7	-16467.7	-9519.4	-17185.1
0.454762	211395.1	184611.7	-16426.3	-15843.9	-9542.32	-16739.3
0.453571	211861.4	184151.1	-16387.8	-15766.3	-9543.48	-16683.6
0.446623	214583.9	181463.1	-16159.6	-15314.5	-9543.6	-16358.6
0.444545	215398	180659.7	-16090.3	-15179.8	-9541.59	-16261.3
0.439347	217435.3	178649.6	-15914.5	-14843.7	-9532.75	-16017.6
0.43931	217449.7	178635.4	-15913.3	-14841.3	-9532.67	-16015.9
0.429762	221192.5	174945.1	-15582.9	-14227.6	-9503.46	-15567.7
0.428571	221659.2	174485.1	-15541.1	-14151.5	-9498.74	-15511.8
0.421623	224383.7	171801.1	-15294.5	-13708.7	-9466.76	-15184.9
0.419545	225198.3	170998.8	-15219.9	-13576.9	-9455.79	-15087.1
0.414347	227237.1	168991.8	-15031.9	-13248.4	-9425.69	-14842.1
0.41431	227251.5	168977.5	-15030.5	-13246.1	-9425.46	-14840.3
0.404762	230997	165292.8	-14679.8	-12647.6	-9360.79	-14389.5
0.403571	231464.1	164833.5	-14635.7	-12573.5	-9351.93	-14333.2
0.396623	234190.6	162153.4	-14376.1	-12142.8	-9296.83	-14004.3
0.394546	235005.8	161352.4	-14297.9	-12014.8	-9279.29	-13905.9
0.389347	237046.1	159348.3	-14101.3	-11695.8	-9233.29	-13659.3
0.38931	237060.6	159334.1	-14099.9	-11693.6	-9232.96	-13657.6
0.379762	240808.8	155654.9	-13735.1	-11113.5	-9141.04	-13203.8
0.378571	241276.3	155196.3	-13689.3	-11041.7	-9128.94	-13147.1
0.371623	244004.8	152520.4	-13420.8	-10625	-9055.55	-12816
0.369546	244820.7	151720.6	-13340.2	-10501.2	-9032.72	-12716.9
0.364347	246862.5	149719.6	-13137.7	-10193	-8973.88	-12468.5
0.36431	246877	149705.5	-13136.3	-10190.8	-8973.45	-12466.8
0.354762	250628.1	146031.9	-12761.9	-9630.84	-8859.12	-12009.6
0.353571	251095.9	145574.1	-12715	-9561.57	-8844.31	-11952.5
0.346623	253826.5	142902.3	-12440.6	-9159.76	-8755.58	-11618.9
0.344546	254643	142103.8	-12358.3	-9040.44	-8728.29	-11519
0.339347	256686.4	140106	-12151.9	-8743.54	-8658.5	-11268.7
0.33931	256700.9	140091.9	-12150.4	-8741.44	-8658	-11266.9
0.329762	260455	136424.2	-11769.8	-8202.31	-8524.35	-10806
0.328571	260923.1	135967.1	-11722.2	-8135.66	-8507.2	-10748.4
0.328571	260923.1	135967.1	-11722.2	-8135.66	-8507.2	-10748.4
0.321623	263655.9	133299.8	-11443.9	-7749.07	-8405.06	-10411.9
0.319545	264473.1	132502.5	-11360.5	-7634.32	-8373.84	-10311.1
0.314347	266518.2	130508	-11151.6	-7348.81	-8294.38	-10058.6
0.31431	266532.7	130493.9	-11150.2	-7346.79	-8293.81	-10056.8
0.304762	270289.8	126832.4	-10765.5	-6828.54	-8142.95	-9591.66
0.303571	270758.3	126376	-10717.5	-6764.48	-8123.7	-9533.55
0.296623	273493.4	123713.2	-10436.8	-6392.99	-8009.47	-9193.82
0.294545	274311.2	122917.3	-10352.8	-6282.72	-7974.69	-9092.06
0.289347	276358	120926.3	-10142.4	-6008.42	-7886.44	-8837.06
0.28931	276372.5	120912.1	-10140.9	-6006.48	-7885.81	-8835.25
0.279762	280132.9	117257.1	-9753.87	-5508.61	-7719.16	-8365.43
0.278571	280601.8	116801.5	-9705.57	-5447.07	-7697.98	-8306.72
0.271623	283339.2	114143.4	-9423.47	-5090.21	-7572.57	-7963.42
0.269546	284157.8	113349	-9339.07	-4984.29	-7534.49	-7860.58
0.264347	286206.4	111361.5	-9127.77	-4720.77	-7438.04	-7602.81
0.26431	286220.9	111347.5	-9126.28	-4718.9	-7437.35	-7600.98
0.254762	289984.6	107699.1	-8737.84	-4240.56	-7255.89	-7125.92
0.253571	290454	107244.4	-8689.38	-4181.42	-7232.88	-7066.54
0.246623	293193.9	104591.3	-8406.43	-3838.47	-7096.88	-6719.27
0.244546	294013.2	103798.4	-8321.8	-3736.65	-7055.67	-6615.22
0.239347	296063.8	101814.8	-8109.96	-3483.33	-6951.4	-6354.37
0.23931	296078.3	101800.7	-8108.46	-3481.54	-6950.66	-6352.52
0.229762	299845.6	98159.59	-7719.12	-3021.54	-6754.99	-5871.61
0.228571	300315.4	97705.81	-7670.55	-2964.66	-6730.22	-5811.48
0.221623	303058.1	95058.09	-7387	-2634.69	-6583.99	-5459.77
0.219546	303878.2	94266.8	-7302.2	-2536.7	-6539.72	-5354.36
0.214347	305930.8	92287.31	-7089.92	-2292.84	-6427.85	-5090.06
0.21431	305945.3	92273.28	-7088.41	-2291.11	-6427.05	-5088.19
0.204762	309716.5	88639.87	-6698.26	-1848.05	-6217.46	-4600.72
0.203571	310186.8	88187.07	-6649.59	-1793.24	-6190.96	-4539.75
0.196623	312932.3	85545.17	-6365.4	-1475.16	-6034.61	-4183.05
0.194545	313753.3	84755.64	-6280.39	-1380.66	-5987.32	-4076.12
0.189347	315808.1	82780.62	-6067.58	-1145.4	-5867.88	-3807.94
0.18931	315822.7	82766.62	-6066.07	-1143.74	-5867.03	-3806.03
0.179762	319598.1	79141.66	-5674.8	-715.951	-5643.49	-3311.16
0.178571	320069	78689.95	-5625.98	-662.995	-5615.24	-3249.24
0.171623	322817.7	76054.43	-5340.82	-355.532	-5448.88	-2886.88
0.169546	323639.7	75266.84	-5255.5	-264.137	-5398.32	-2778.22
0.164347	325697	73296.77	-5041.84	-36.471	-5271.16	-2505.61
0.16431	325711.6	73282.81	-5040.33	-34.8622	-5270.25	-2503.68
0.154762	329491.7	69667.25	-4647.26	379.5681	-5032.4	-2000.33
0.153571	329963.1	69216.73	-4598.19	430.9154	-5002.35	-1937.33
0.146623	332715.4	66588.36	-4311.44	729.2496	-4825.19	-1568.46
0.144546	333538.5	65802.97	-4225.6	818.0032	-4771.63	-1457.79

X(H)	GMR(GAS)	GMR(IONIC_LIQ)	GMR(BCC_A2)	GMR(C1_FCC)	GMR(HCP_ZR)	GMR(ZRH2_EPS)
0.139347	335598.6	63838.48	-4010.55	1039.246	-4636.41	-1180.07
0.13931	335613.2	63824.55	-4009.02	1040.81	-4635.44	-1178.09
0.129762	339398.6	60219.66	-3612.98	1444.165	-4382.47	-664.886
0.128571	339870.7	59770.52	-3563.49	1494.2	-4350.51	-600.608
0.121623	342627.1	57150.36	-3274.16	1785.192	-4162.02	-224.089
0.119546	343451.5	56367.49	-3187.47	1871.86	-4105.03	-111.062
0.114347	345514.8	54409.48	-2970.15	2088.113	-3961.07	172.7289
0.11431	345529.4	54395.6	-2968.61	2089.643	-3960.05	174.7458
0.104762	349321.1	50803.22	-2567.77	2484.752	-3690.53	699.7462
0.103571	349794.1	50355.69	-2517.63	2533.846	-3656.46	765.5587
0.096623	352555.4	47745.31	-2224.14	2819.769	-3455.38	1151.348
0.094545	353381.2	46965.46	-2136.1	2905.065	-3394.52	1267.256
0.089347	355448.4	45015.26	-1915.15	3118.202	-3240.7	1558.501
0.08931	355463.1	45001.44	-1913.58	3119.711	-3239.61	1560.572
0.079762	359262.4	41424.39	-1505.08	3510.368	-2951.09	2100.276
0.078571	359736.4	40978.88	-1453.88	3559.034	-2914.55	2168.023
0.071623	362503.8	38380.74	-1153.7	3843.066	-2698.64	2565.621
0.069545	363331.6	37604.73	-1063.47	3928.016	-2633.18	2685.244
0.064347	365403.8	35664.55	-836.635	4140.769	-2467.46	2986.2
0.06431	365418.5	35650.8	-835.021	4142.278	-2466.28	2988.342
0.054762	369228	32093.96	-413.876	4534.298	-2154.2	3547.694
0.053571	369703.3	31651.15	-360.907	4583.346	-2114.54	3618.081
0.046623	372479.1	29069.8	-49.3855	4870.718	-1879.46	4032.091
0.044545	373309.6	28299.19	44.6044	4957.073	-1807.92	4156.995
0.039347	375389	26373.39	281.7625	5174.302	-1626.09	4472.057
0.03931	375403.7	26359.75	283.4545	5175.849	-1624.78	4474.304
0.029762	379228.5	22833.52	727.8063	5580.555	-1278.99	5063.785
0.028571	379705.9	22395.01	784.1545	5631.69	-1234.66	5138.411
0.021623	382495.8	19841.64	1118.313	5934.24	-969.42	5580.066
0.019545	383331	19080.57	1220.26	6026.35	-887.682	5714.419
0.014347	385424	17181.98	1480.664	6261.367	-677.052	6056.453
0.01431	385438.9	17168.56	1482.542	6263.061	-675.523	6058.912
0.004762	389299.9	13714.7	1992.044	6723.095	-254.497	6720.349
0.003571	389783.9	13289.34	2060.651	6785.281	-196.658	6808.079
2.50E-04	391143.2	12120.3	2269.551	6975.975	-17.4931	7070.542

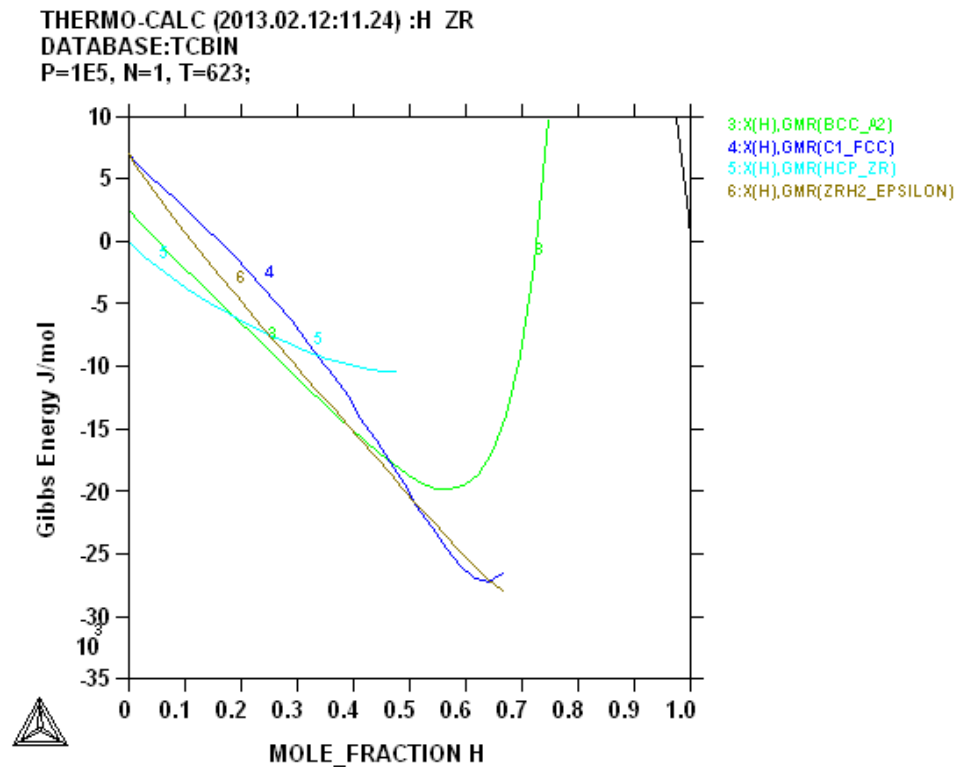


Figure A3 Thermodynamic properties of different phases at T=400°C